FINAL REPORT

Project Title:	Flow Mapping in a Gas-Solid Riser via Computer Automated Radioactive Particle Tracking (CARPT)
Period:	May 5, 2000 – May 4, 2005
Date of Report:	June 04, 2005
Recipient:	Washington University Department of Chemical Engineering, Campus Box: 1198 One Brookings Drive Saint Louis, MO 63130
Award Number:	DE-FC36-01-AL6-7306
Subcontractors:	N/A
Other Partners:	Sandia National Laboratory (SNL), Albuquerque
Principal Investigator:	Al-Dahhan, Muthanna Phone: (314) 935 7187 Email: muthanna@che.wustl.edu
Project Team:	Satish Bhusarapu, Muthanna Al-Dahhan, Milorad P. Duduković – Washington University in St.Louis; Timothy J. O'Hern, Steven Trujillo, Michael Prairie – Sandia National Laboratory, Albuquerque, New Mexico.

Executive Summary

Gas-solid risers are extensively used in many industrial processes for gas-solid reactions (e.g. coal combustion and gasification) and for solid catalyzed gas phase reactions (e.g. fluid catalytic cracking, butane oxidation to maleic anhydride). *Ab initio* prediction of the complex multiphase fluid dynamics in risers is not yet possible, which makes reactor modeling difficult. In particular, quantification of solids flow and mixing is important. Almost all the experimental techniques used to characterize solids flow lead to appreciable errors in measured variables in large scale, high mass flux systems. In addition, none of the experimental techniques provide **all** the relevant data required to develop a satisfactory solids flow model.

In this study, non-invasive Computer Automated Radioactive Particle Tracking (CARPT) is employed to visualize and quantify the solids dynamics and mixing in the gas-solid riser of a Circulating Fluidized Bed (CFB). A single radioactive tracer particle is monitored during its multiple visits to the riser and with an assumption of ergodicity, the following flow parameters are estimated:

a) Overall solids mass flux in the CFB loop.
b) Solids residence time distribution in the riser and down-comer.
c) Lagrangian and Eulerian solids velocity fields in a fully-developed section of the riser. This includes velocity fluctuations and the diffusivity tensor.

The existing CARPT technique is extended to large scale systems. A new algorithm, based on a cross-correlation search, is developed for position rendition from CARPT data. Two dimensional solids holdup profiles are estimated using γ-ray computed tomography. The image quality from the tomography data is improved by implementing an alternating minimization algorithm.

This work establishes for the first time a reliable database for local solids dynamic quantities such as time-averaged velocities, Reynolds stresses, eddy diffusivities and turbulent kinetic energy. In addition, this study also provides global quantities such as solids residence time distribution, first passage time distribution, circulation time distribution and various mixing parameters in the riser. This work advances the understanding of the solids flow pattern and mixing in a well-developed flow region of a gas-solid riser, operated at different gas flow rates and solids loading.

Contents

List of Tables

List of Figures

Nomenclature

A	mean cross-sectional area (m^2)
Ar	Archimedes number, $\rho_g(\rho_p - \rho_g)d_p^3 g / \mu_g^2$
$a(\cdot)$	functional form
$b(\cdot)$	functional form
$\hat{b}$	backprojection of the model employed (-)
$\tilde{b}$	backprojection of the measured data (-)
c	parametric constant in the radial solids holdup profile (-)
C	normalized count data from the detector
C_k	constant in the turbulent transport equation (-)
$\hat{c}$	estimated attenuation parameter (cm^{-1})
d	distance (m)
d_a	detector aperture in a densitometry experiment (m)
d_{eff}	spatial resolution (m)
d_p	particle diameter (m)
D	dispersion coefficient ($m^2 \cdot s^{-1}$)
D_{rr}	radial turbulent diffusivity, $cm^2 \cdot s^{-1}$
D_{zz}	axial turbulent diffusivity, $cm^2 \cdot s^{-1}$
D_{ij}	diffusivity tensor, ($m^2 \cdot s^{-1}$)
$D_{z,ax}$	axial dispersion coefficient, ($m^2 \cdot s^{-1}$)
e	coefficient of restitution (-)
$\hat{e}$	unit vector
E	PDF of RTD (sec^{-1})
E_c,	solids mass flux in the core ($kg \cdot m^{-2} \cdot s^{-1}$)
F	steepness of radial gas holdup profile
f	autocorrelation function (-)
$f_{a,\,c,\,B}$	mass fractions of tracer in annulus, core and bottom zones (dimensionless)
$f(v)$	PDF of solids velocity (dimensionless)

g	gravitational force per unit mass ($m \cdot s^{-2}$)
g_o	radial distribution function (-)
G_s	mass flux ($kg \cdot m^{-2} \cdot s^{-1}$)
H	height along the riser (m)
ΔH	distance between detectors (m)
I_{ca}, I_{ac}	interchange coefficients (core-annulus), ($kg \cdot m^{-3} \cdot s^{-1}$)
I	intensity of radiation ($\# \cdot s^{-1}$)
I_o	intensity of a colliding beam in free space (background)
I_a	intensity with the attenuation of the riser wall
I_s	$I_{s,static}$ or I_{GS}
$I_{s,static}$	intensity with the attenuation of static solids
I_{GS}	intensity during the actual experimental run with moving solids
$I(a//b)$	I-divergence
k	parametric constant in the radial solids holdup profile (-)
l	trajectory length (m)
l_{eff}	intervening chord length between the source and detector (m)
l_d, $l^{'}$	distance the γ-ray traverses in the downcomer wall and in the air (m)
L	length of the riser (m)
m	power law exponent in the radial solids holdup profile
m^*	rate of tracer mass injection ($kg \cdot s^{-1}$)
m_{CT}	number of views (#)
M	macromixing index (-)
M_{CT}	magnification factor, ratio of source-detector to source-object distances
M_d	average number of photons detected per beam (#)
n	occurrences in the interval around t_i(#)
n_{CT}	number of beams in each view(#)
N_d	number of detectors (#)
P	number of discretised intervals (#)
Pe	Peclet number
q	production rate of particles (photons) ($\# \cdot m^{-1} \cdot s^{-1}$)
Q	mass flow rate ($kg \cdot s^{-1}$)

r	radial position (m)
r_c	radius of the core (m)
R	radius of the riser (m)
$R_{12,22}$	element of the correlation matrix
s	focal spot size or source aperture
S	solids inventory (lbs)
t	time (s)
$\langle t \rangle$	ensemble average of "time of flight" (s)
T	total time of data acquisition (s)
U_g^{riser}	superficial gas velocity ($m \cdot s^{-1}$)
$U_{sc,\,t}$	solids velocity in the core and annulus respectively ($m \cdot s^{-1}$)
V^*	dimensionless net superficial gas velocity $\left[\frac{\rho_g^2}{g\mu_g(\rho_p-\rho_g)}\right]^{1/3}\left[U_g^{riser}-\frac{G_s\varepsilon}{\rho_p(1-\varepsilon)}\right]$
V_{CA}	type A choking velocity ($m \cdot s^{-1}$)
W	solids mass flux in the annulus ($kg \cdot m^{-2} \cdot s^{-1}$)
$\bar{x}$	position vector (m)
y	measured data set
Y	finite dimensional space
z	axial distance (m)
Z	scaling function

Greek Symbols

ε	volume fraction (dimensionless)
$\bar{\varepsilon}_s$	mean of the line-averaged solids volume fraction
ε_s'	fluctuating component of the line–averaged solids volume fraction
$<\varepsilon>$	cross-sectional averaged holdup (-)
ν	Courant number (dimensionless)
ν_s	solid phase velocity in axial direction ($m \cdot s^{-1}$)
$\langle \nu_s \rangle$	ensemble averaged velocity of the solids phase ($m \cdot s^{-1}$)
ν_s'	fluctuating component of the solids phase velocity ($m \cdot s^{-1}$)

ρ	density ($kg \cdot m^{-3}$)
ρ_{12}	correlation coefficient
σ^2	variance
σ	attenuation constant (cm^{-1})
μ	viscosity ($g \cdot cm^{-1} \cdot s^{-1}$)
μ_w	mass attenuation coefficient of water ($m^2.kg^{-1}$)
τ	stress tensor per unit bulk density ($m^2 \cdot s^{-2}$)
τ_r	mean residence time (s)
τ_{La}	integral time scale (s)
θ	dimensionless time
Θ_s	granular temperature ($m^2 \cdot s^{-2}$)
ξ	dimensionless radius
β	parametric constant in the solids holdup profile (-)
ψ	density of particles (photons) ($\# \cdot m^{-1}$)
δ	Kronecker delta

Subscripts and Superscripts

a	air
ax	axial
c	transition from bubbling to turbulent fluidization
calib	calibration data
cfb	circulating fluidized bed loop
cs	cross-sectional average
d	downcomer
eff	effective
g	gas
i	inside
p	particle
r	radial
run	experimental run data

x,y,z	three dimensional co-ordinates
s	solid phase
θ	azimuthal

Acronyms

ADM	axial dispersion model
AM	alternating minimization
CARPT	computer automated radioactive particle tracking
CFB	circulating fluidized bed
CFBC	circulating fluidized bed combustor
CFD	computational fluid dynamics
CREL	chemical reaction engineering laboratory
CSTR	continuous stirred tank reactor
CT	computed tomography
CTD	cycle time distribution
DES	discrete element simulation
DPT	dilute phase transport
ECT	electrical capacitance tomography
EM	estimation-maximization
FCC	fluid catalytic cracking
FF	fast fluidized
FPTD	first passage time distribution
GM	Geiger-Muller
HM	harmonic mean
KTGF	kinetic theory of granular flows
LDV	laser-doppler velocimetry
MC	Monte-carlo
PDF	probability density function
PEPT	positron emission particle tracking
PIV	particle imaging velocimetry
PSRI	particulate solids research incorporated

RMS	root mean square
RTD	residence time distribution
TLD	trajectory length distribution
TOF	time-of-flight
SNL	Sandia national laboratory

Acknowledgements

We wish to gratefully acknowledge the financial support of Department of Energy, which has made this research possible. We also wish to thank DuPont for gracefully donating the experimental setup. In addition, we would like to thank Dr. Ted Knowlton and Dr. Reddy Karri at PSRI, Chicago for their suggestions and comments in overcoming the technical difficulties during the operation of the experimental setup. We sincerely acknowledge the assistance provided by Mr. Edward Lau and Mrs. Susan Tucker at MIT nuclear laboratory for irradiating the radioactive particles at free of cost.

Several people at CREL and in Chemical Engineering Department have provided considerable help. In particular, we thank Dr. Pascal Fongarland, Anja Vold and Margaret Frericks for their help and support in conducting experiments on gas-solid riser. Besides, we wish to acknowledge the timely help of all the present and past members of CREL. Our sincere appreciation also goes to Mr. Steve Picker, Mr. Jim Linders, Mr. Pat Harkins and Mr. John Krietler for their help during the fabrication and design of some of the experimental parts.

We wish to acknowledge Ms. Jasenka Benac and Prof. O'Sullivan for helpful discussions on CT algorithms. In addition, we also acknowledge Dr. Miryan Cassanello for collaborative work on further data analysis of the experimental data. We wish to thank the entire Chemical Engineering Department, particularly the secretaries for their help with numerous formalities. Specifically, Mrs. Angela Weatherspoon for her help in different aspects. We also wish to thank Olin Library at Washington University for providing expedited help in procuring several references.

Satish Bhusarapu, Muthanna Al-Dahhan and Milorad P. Dudukovic
Washington University, St. Louis
May 2005

Chapter 1

Introduction

1.0 Scope

The aim of this work is to provide new and as complete as possible information on the flow of solids in Circulating Fluidized Beds (CFB), particularly in the riser section. CFB systems, their historical usage, applications and regimes of operation are briefly reviewed in Chapter 1. The motivation to investigate the gaps in understanding of the solids dynamics in risers is described. The importance of using non-invasive flow monitoring techniques such as Computed Automated Radioactive Particle Tracking (CARPT) and Computed Tomography (CT) is highlighted. Then, the objectives of the work are outlined and discussed. The approach in achieving the objectives by resolving the issues in quantifying the solids dynamics is explained. In the last section of the chapter, the outline of the report is provided.

1.1 Circulating Fluidized Bed (CFB) Systems

1.1.1 Basic CFB Systems

Dealing with solid particles is often a necessity in chemical processes, in the pharmaceutical and metallurgical industries, in mineral processing, energy related processes, and in many other applications. In a number of cases the particles serve as catalysts for reacting gases and/or liquids. In other cases, the particles may be chemically converted, as in ore processing or coal combustion, or may undergo physical transformation, as in drying of particulate solids. Different potential designs are available for carrying out such reactions and contacting operations. Available technologies include fixed beds or moving beds, where the particles move slowly downward in contact with each other, fluidized beds, where the particles are supported by gas or liquid introduced through a distributor at the bottom, and dilute phase transport systems, where the particles are transported by a fluid (gas or liquid or both) via a duct or a pipe.

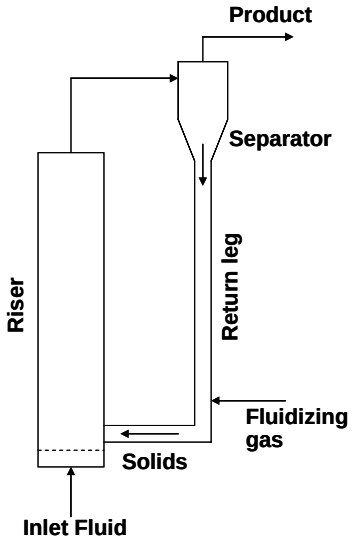

Figure 1-1: Schematic diagram of a typical Circulating Fluidized Bed (CFB) setup

A reactor system which is intermediate between low velocity bubbling fluidized beds and high velocity dilute phase systems is the Circulating Fluidized Bed (CFB). A schematic of a typical CFB is shown in Figure 1-1. The CFB has significant industrial applications because of its efficiency, operational flexibility, and overall profitability

(Berruti *et al.*, 1995). A CFB system consists of a riser, separator, down-comer and feed systems for solids and for the fluid. The riser is a tall column in which solid particles are conveyed upward (with possible backmixing) by the fluid (gas or liquid). Phase separation is accomplished at the top, often via cyclones. The particles and some fluid then flow through a holding tank and are returned via a dense flow down-comer to the bottom of the riser. Fresh fluid is usually introduced at the bottom of the riser, and some may be added to the down-comer. Provisions are made to feed fresh solid particles when needed, often at the bottom of the riser.

1.1.2 CFB Applications in Various Technologies

Fluid bed processing apparently was practiced as early as 1566 as a means for purifying ores (Elmas, 1973). However, fluidization, as it is known today, was introduced commercially in 1937 and was born from the pioneering work of the Standard Oil Development Company (now Exxon-Mobil), which focused on finding a catalytic cracking technology superior to the fixed bed process (Avidan, 1980). In recent years, CFB systems have found a niche in processes where a blend of their features, such as good mixing, good gas-solid contacting at short residence times, excellent heat and mass transfer, and high throughput per unit cross sectional area made their application economically desirable. Operational flexibility is often cited as a benefit over conventional technology. Fluid catalytic cracking (FCC) and circulating fluidized bed combustion (CFBC) are by far the major technologies in terms of through-put of material that utilize CFBs. Other applications have been investigated, and some have been developed commercially or are under development. Table 1-1 lists a few of the applications with key references. Further details regarding the use of CFB technology can be found in Berruti *et al.* (1995) and Grace and Bi (1997).

Based on a qualitative description of the operating regimes for fluidized systems (Kunii and Levenspiel, 1991; Berruti *et al.*, 1995), a CFB is usually operated in turbulent fluidization, fast fluidization, or pneumatic transport regimes. The operating variables typically varied in a CFB are the gas superficial velocity (U_g^{riser}) and the overall solids mass flux (G_s). Generally, risers are operated at gas velocities exceeding 2 $m \cdot s^{-1}$ and

solids mass fluxes greater than 10 $kg \cdot m^{-2} \cdot s^{-1}$. In combustion, and other non-catalytic gas-solid reactions, the solids mass fluxes are generally less than 100 $kg \cdot m^{-2} \cdot s^{-1}$, and particles belonging to Group B of Geldart's classification (Geldart, 1986) are used. In contrast, conditions for applications in solid catalyzed reactions are significantly different: solids mass fluxes are often over 250 $kg \cdot m^{-2} \cdot s^{-1}$, and Geldart's Group A particles are used. In the work reported here, the available experimental set-up in our laboratory (CREL) restricts the operating conditions to a range similar to that of combustion systems. However, additional data have been acquired at Sandia National Laboratory (SNL) to broaden the range of our investigation.

Table 1-1: Key applications of CFB technology with key references

I. Solid–Catalysed Gas Phase Reactions	
Fluid catalytic cracking (FCC)	Squires, 1986; Avidan *et al*., 1990; King, 1992
Fischer-Tropsch synthesis	Dry, 1982; Shingles and McDonald, 1988
Partial oxidation of n-butane to maleic anhydride	Contractor, 1988
Oxidation of o-xylene/naphthalene to phthalic anhydride	Wainwright and Hoffman, 1974
Ethylene epoxidation	Park and Gau, 1986
Anaerobic oxidative dehydrogenation of butane to butadiene	Tmenov *et al*., 1980
Ammoxidation of acrylonitrile from propylene	Beuther *et al*., 1978
Methanol to olefins	Schoenfelder *et al*., 1994
Simultaneous NO_x and SO_2 removal from off-gases	Reh, 1995
II. Gas-Solid Reactions	
Combustion of coal, wood and shale	Reh, 1986; Yerushalmi, 1986
Incineration of solid waste	Chang *et al*., 1987; Hallstrom and Rarlsson, 1991
Gasification of coal, biomass, etc.	Hirsch *et al*., 1986; Suzuki *et al*., 1990
Calcination of alumina, phosphate rock, clay, etc.	Reh, 1971, 1995
Roasting of sulphidic ores (ZnS, Cu_2S, gold ores)	Reh, 1995
Desulphurization of flue gas	Graf, 1986
Reduction of iron ore, nickel ore, etc.	Hirsch *et al*., 1986; Suzuki *et al*., 1990
Cement production	Deng, 1993

1.2 Motivation

"Technology Vision 2020: The Chemical Industry" identifies gas-solid and gas-solid-liquid flows as critical in developing advanced chemical reactors and separators (MFDRC website - http://www.mfdrc.org). Also, statistics show that the production of domestic chemicals which rely on particle technology is valued at $60 billion/year. One percentage point improvement in the efficiency of these operations may achieve savings of $1 billion/year. However, design, scale-up, and performance predictions for a multiphase flow reactor, such as the gas-solid CFB, are still challenging tasks due to the enormous complexity of the interacting phenomena. Reactor scale description of phase distribution, phase recirculation, backmixing, and hydrodynamic and transport parameters are critical in sizing the CFB reactor for achieving optimal performance. They are currently based on empiricism.

Generally, to maximize profitability, gas and solids residence times are chosen to achieve the highest product yield per unit volume. In fluid catalytic cracking (FCC) units, a shorter and a more uniform catalyst residence time in the riser reactor, with reduced backmixing, potentially leads to better reactor performance (larger amounts of desired products and/or a higher conversion) by reducing the inventory of the deactivated catalyst in the riser (Squires, 1986). In other words, a uniform radial profile of solids velocity and little backmixing in the riser are preferred, leading to shorter and more uniform solids residence times. This is the reason for the recent interest in solids "downers" i.e. reactors with downward flow of solids and gas. Solids Residence Time Distribution (RTD) in the riser is also important in non-catalytic gas-solid reactions, as in a combustor, since solids RTD characterizes the degree of solids mixing and can provide information about the physical properties of the solid particles in the riser. In a CFB combustor, lateral mixing and internal recirculation of solids is necessary to maintain uniform temperatures over the entire riser. Hence, lateral and longitudinal mixing is advantageous in a CFB combustor, while in an FCC unit is disadvantageous. The following question arises:

- How do the operating conditions affect the solids axial and radial hold-up distribution, mass flux profiles, and the solids residence time distribution?

In addition, high gas velocities and low solids hold-up are preferred in some applications to minimize compressor costs. However, for many solids catalyzed reactions, lower gas velocities may be preferred because they yield higher solids hold-up, thus maximizing the specific catalyst activity per unit reactor volume (Berruti *et al*., 1995). This raises another question:

- How does one achieve the flow structure required for a specific application by varying the operating conditions, reactor design, or particle characteristics?

To answer such questions, it is necessary to have a fundamental understanding of the particle flow mechanism in risers. Modeling CFBs to produce *ab initio* predictions of their complex fluid and particle dynamics and chemical behavior is not yet possible and such modeling requires experimental validation. Existing models describing this complex flow often lack ***relevant*** experimental data needed for model validation and refinement (Berruti et al., 1995). Moreover, many of the phenomenological and computational fluid dynamic (CFD) models require empirical inputs, and their quality depends on the availability and accuracy of the measurement techniques and data used to obtain model parameters. Hence, to answer the above questions and to thoroughly understand the solids flow inside the risers, it is first necessary to map the solids flow field inside a pilot scale riser at operating conditions relevant to industry. This should provide then the needed database for the CFD modelers.

The first challenge in this approach is identifying suitable and accurate measurement methods. Almost all the experimental techniques used to characterize CFB systems are intrusive (probe techniques), with measured variables having appreciable errors in large scale, and in high mass flux systems (Louge, 1997; Berruti *et al.*, 1995). In addition, none of the experimental techniques provide **all** the relevant data required to develop a satisfactory solids flow model (Sinclair, 2000). Moreover, CFB systems are *opaque* owing to high solids mass fluxes and high solids holdup, and hence, one cannot "*see*" into the risers. Therefore, commonly used sophisticated non-intrusive optical techniques such as Laser-Doppler Velocimetry (LDV) and Particle Image Velocimetry (PIV) cannot be used for investigation of solids flow and mixing in such opaque systems.

Also, these techniques provide only Eulerian measurements, where every local region is characterized independently. A description of solids flow in the whole system is preferred.

To compare the results of various researchers, accurate measurements of gas superficial velocity and solids mass flux are critical in experimental investigations of the riser flow structure. However, quantifying the solids mass flux in CFBs with complete solids recirculation is problematic and has led to different experimental findings under the same operating conditions (Berruti *et al*., 1995). Based on the use of a single particle radioactive tracer, Roy *et al.* (2001) demonstrated an *in-situ* calibration method in a liquid–solid riser, which is sensitive, reliable and, amenable to any equipment scale.

As mentioned earlier, solids RTD is essential for the design of CFB reactors where solids conversion proceeds with time. However, all of the methods described in the literature for measuring solids RTDs have severe limitations and are unable to determine the true RTD of solids (Harris *et al*., 2002). Measurement of the concentration-time response to an impulse injection of tracer, even at two elevations in systems like CFBs **cannot** determine the RTD uniquely (Shinnar *et al.*, 1972; Naumann and Buffham, 1983). Here we show that CARPT can provide the solids RTDs with no ambiguity.

1.2.1 Approach

The non-invasive Computer Automated Radioactive Particle Tracking (CARPT) technique provides complete Lagrangian solids flow field and yields as a bonus the solids residence time distribution (RTD) and eddy diffusivities. With the help of ergodic hypothesis the Eulerian flow field is generated including time average velocity map and various turbulence parameters such as the Reynolds stresses and turbulent kinetic energy. Another radiation based technique, Computed Tomography (CT) yields detailed time averaged local solids holdup profiles in various planes. Together, these two techniques can provide the needed local solids dynamics information for the same setup under identical operating conditions, and the data obtained can be used as a benchmark for development, validation, and refinement of the appropriate riser models. For the above

reasons these two techniques were implemented in this study on a fully developed section of the riser.

To derive the global mixing information in the riser, accurate solids RTD is needed and was obtained by monitoring the times of entry and of exit of a single radioactive tracer. Other global parameters such as Cycle Time Distribution (CTD), overall solids holdup in the riser, and solids recycle percentage at the bottom section of the riser are evaluated from different solids travel time distributions. Besides, to measure accurately the overall solids mass flux, the method of Roy *et al.* (2001) was improved and applied to the down-comer.

1.3 Objectives

The overall objective of this work is to advance the understanding of the solids flow pattern and mixing in a well-developed flow region of a gas-solid riser, operated at different gas flow rates and solids loading. This requires collecting reliable data on solids trajectories, velocities – averaged and instantaneous, solids holdup distribution and solids fluxes in the riser as a function of the operating conditions. Such data is not currently available from one set of operating conditions. This work initiates the creation of a reliable database for solids dynamics in a pilot plant scale CFB, which can then be used to validate/develop phenomenological models for the riser. This study also attempts to provide benchmark data for validation of CFD codes and their current closures. In accomplishing the above objective the following tasks are performed:

- Modification of the pilot scale CFB loop at Chemical Reaction Engineering Laboratory (CREL) is implemented to overcome the technical and operational problems that cause unstable flow.
- Reliable measurements of solids flux at different gas velocities and solids loading were performed. For this purpose, the method of Roy *et al.* (2001) for in-situ calibration of the overall solids mass flux variation with the superficial gas velocity is implemented.

- The effect of operating conditions on the solids velocity field, solids circulation patterns and solids mixing in risers is investigated by varying superficial gas velocity and solids loading. In order to achieve this task, CARPT experiments are designed for obtaining particle trajectories in the fully-developed flow section of the riser. This effort includes development of CARPT hardware and software, and a suitable calibration procedure. It also includes implementation and optimization of the CARPT technique for large-scale risers and validation of the CARPT technique.
- The effects of superficial gas velocity and solids loading on the solids holdup distribution are examined. This requires development of a CT scan measurement for determination of radial solids holdup profiles and with improved accuracy in the wall region. This enhancement in the accuracy is achieved by implementing an improved image reconstruction algorithm.
- True solids RTDs in the riser are obtained for the first time by monitoring the times of entry and of exit of a single radioactive tracer. The difficulties associated with estimation of mixing parameters from a conventional tracer impulse injection-detection method are illustrated as well as the magnitude of the differences in estimated parameters that may arise. This task includes the comparison of the data with the literature findings and appropriate model predictions.
- Solids dynamics and solids holdup distribution obtained via CARPT and CT are illustrated. The new experimental database at high and low solids fluxes is used to study the particle transport mechanism in the riser and understand the mixing mechanisms in different flow regimes.

1.4 Report Organization

Chapter 2 provides a literature survey on solids flow structure in the riser and discusses briefly the findings of previous researchers. Chapter 3 describes the improvements in the algorithms for CARPT and CT accomplished in this work. Chapter

4 provides an outline of the CFB experimental setup and describes the overall solids mass flux measurements. Chapter 5 discusses the solids residence time measurements in "open" systems, such as risers, using single radioactive particle tracking. Chapter 6 provides the details of CARPT and CT experiments in gas-solid risers and describes the time-averaged holdup and velocity fields. In Chapter 7 the effect of operating conditions on the solids velocity field, solids circulation patterns and backmixing is discussed. Chapter 8 summarizes the research findings along with recommendations for future work.

Chapter 2

Background

2.0 Scope

In this chapter, the literature on solids flow and solids residence time measurements in gas-solid risers, pertinent to this study, is briefly reviewed. Studies addressing the phenomenological modeling of the solids flow structure and mixing in risers are also covered.

High solids concentrations, and the size and nature of industrial or pilot scale plants, restricted the range of instrumentation for procuring precise experimental data on solids flow from risers used in CFB systems. However, recent advances in measurement devices, in fast data acquisition boards, in signal processing hardware and software, and in computing machinery have enabled the development of sophisticated experimental methods for probing multiphase reactor systems, often non-invasively, so as not to disturb the flow in any way. For gas-solid flows, most of the experimental techniques reported in the literature deal with probing laboratory scale systems. Cheremisinoff (1986) provided exhaustive descriptions of state-of-the-art instrumentation for gas-solid suspensions and discussed the design, limitations, and advantages of each technique in detail. A similar review by Yates and Simons (1994) is also available. Louge (1997) described the principal devices and experimental techniques used in CFBs, with emphasis on the challenges involved in their implementation and data interpretation. Chaouki *et al*. (1997) focused on non-invasive techniques (especially radioactive) for multiphase flows. Berruti *et al*. (1995) presented various experimental methods and the key findings regarding the parameters that affect the CFB solids flow dynamics.

2.1 Review of Solids Flow Measurements in CFBs

Regarding solids dynamics in CFBs, the work of Yerushalmi *et al.* (1976) is often regarded as the pioneering academic study of the axial flow structure in CFB risers. They discussed the densification at the riser base and elucidated several advantages of operating in the fast fluidization (FF) regime. The decades following this work witnessed hundreds of papers in the open literature, in addition to seven international conferences on CFB technology. The majority of the studies focused on axial and radial solids holdup distribution and flow structure in CFB risers. These studies generated an extensive pool of experimental data covering a wide range of operating conditions and riser dimensions, for both Group A and B powders. The measured variables, the key findings, the employed experimental technique, and the range of used operating parameters are summarized in Tables 2-2, 2-3, 2-4 and 2-5. This review covers exclusively the experimental studies performed on gas-solids flows in three dimensional riser columns. There are numerous other studies on gas-solid fluidized beds, spouted beds, 2D columns, three phase systems, reacting systems, etc. which are not considered in this review. The reviewed studies address the solids dynamics and in particular: a) the solids velocity field, b) the solids concentration distribution, c) the solids mass flux, and d) the solids residence time distribution (RTD).

2.1.1 Solids Dynamics

The gas and solids flow structure in CFB risers is inherently complex. Risers in general exhibit an axial solids holdup distribution, with a certain degree of densification at the bottom of the column where the solids are introduced from the down-comer. As illustrated in Figure 2-1, the solids holdup decreases with height along the riser as the solids are accelerated by the high velocity gas stream (Yerushalmi *et al.*, 1976; Kwauk *et al.*, 1986; Bai *et al.*, 1992a). Provided the riser is long enough, fully developed flow conditions are reached beyond a certain height, corresponding to a mean cross-sectional solids holdup which is approximately invariant with height (Berruti *et al.*, 1995). Experimental observations clearly show that the slip velocities in CFB risers, defined as

the difference between interstitial gas velocity and particle velocity, exceed the single particle terminal velocities by more than two orders of magnitude (Squires, 1986). Berruti and Kalogerakis (1989) explained the high slip velocities by assuming that the flow domain consists of two characteristic regions as shown in Figure 2-1: a dilute gas-solid suspension preferentially traveling upward in the center (core) and a dense phase of particle clusters or strands moving downward along the wall (annulus). Some of the early studies listed in Tables 2-2 to 2-5 provided an experimental basis for the formulation of the core-annulus flow model at different operating conditions (e.g. Bader *et al.*, 1988; Rhodes *et al.*, 1988; Bolton and Davidson, 1988; Brereton and Grace, 1993).

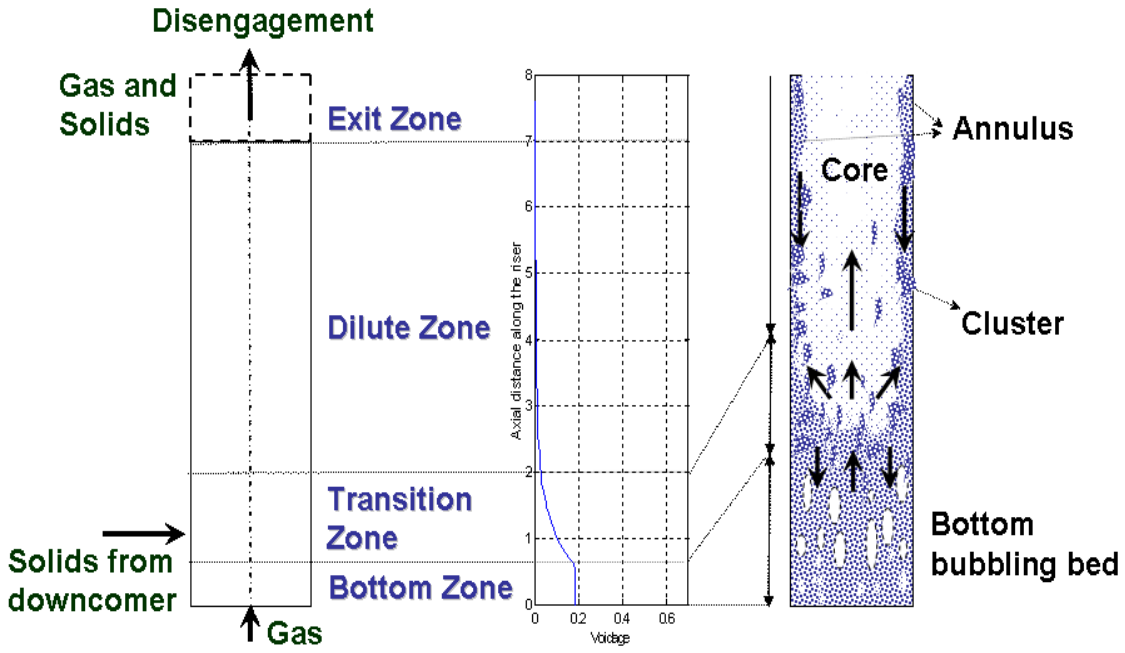

Figure 2-1: Schematic diagram showing the different zones along the riser and a typical axial voidage profile.

The model for the observed core-annulus solids flow structure in the riser can be derived from three different approaches. One relies on gas and solids continuity and the resulting radial and axial gas velocity and particle concentration distributions. The other rests on the concept of solids turbulent diffusion to the wall, while the third involves using energy minimization (Werther and Hirschberg, 1997). The three different

approaches are compared in Table 2-1. An anomaly in the above core-annulus model is that the diffusion of particles occurs towards the region of high solids concentration (annulus). This radial diffusion of particles towards the wall is believed to be due to the concentration gradients in the dilute phase, excluding the 'cluster' phase near the walls (Davidson, 2000). Hence, the phenomenon of clustering is assumed to prevail along with the core-annulus flow. Clustering is termed as a tendency of particles to gather due to externally-imposed effects, most commonly hydrodynamic such as the non-elastic collisions, while 'agglomeration' of particles is due to the adherence in groups, maintained by direct inter-particle forces such as those arising from van der Waals effects or capillary bridges (Horio and Clift, 1992). Thus, the local regions of high particle concentration, or strands, which form as a result of hydrodynamic effects during fluidization at high velocity are termed as clusters. However, groups of adherent particles which form, for example, during lower velocity fluidization of cohesive materials are called agglomerates (Horio and Clift, 1992).

Table 2-1: Different modeling approaches to explain the core-annulus flow structure.

	Key Concepts and Parameters Required	**Pros**	**Cons**	**Key References**
Approach 1	Material balance in core and annulus zones. Solids transfer flux is proportional to concentration in the zone. Requires radial gas velocity distribution, correlations for solids density, velocity in core and/or annulus and axial density profile.	Easy to formulate and solve.	Requires extensive experimental data *a prori*. Gross assumptions. Unreliable for scale-up.	Berruti and Kalogerakis, 1989; Rhodes, 1990; Pugsley *et al*., 1995.
Approach 2	Mass balances in core and annulus with solids interchange mechanism described either by turbulent diffusion or oblique particle-particle collisions. Requires density & velocity for annulus, correlation for axial density, exit factor.	Can explain 'clustering'. Most of the parameters are predicted	Momentum balances are not included. Still requires experimental data to fit parameters.	Bolton and Davidson, 1988; Senior and Brerton, 1992.
Approach 3	Two phase momentum balances in core and annulus with drag, core-annulus solids shear stress, solids-wall shear stress. Energy minimization to predict parameters. Requires slip velocity with drag relation, comprehensive formulation for clustering suspension.	Explains that existence of core-annulus leads to 'clustering'	Reliable slip velocity versus drag force relationship is vital.	Li *et al.*, 1991, 1999; Bai *et al.*, 1995.

2.1.1a Solids Velocity

The motion of solids plays a particularly important role in CFBs, and local solids velocity can provide valuable insights into the behavior of risers. Table 2-2 lists the sources of experimental data for solids velocity in gas-solid risers. The experimental techniques employed are classified as invasive or non-invasive. Invasive methods are optical fiber probes, extraction probes, pitot tubes, iso-kinetic probes, and spatial filter processes. The advantages of using such probes are the ease of experimental measurement and usage at industrially relevant high flux conditions. However, the disadvantages, apart from intrusiveness, are:

a) complicated calibration procedure,

b) manual probe positioning,

c) fouling effects due to the ports on the walls,

d) only point measurements are obtained resulting in only a mean radial profile of axial velocity.

Most of the non-invasive methods are based on optical techniques such as PIV, LDV, and high-speed cameras, while others are based on the use of radioisotopes, such as the Positron Emission Particle Tracking (PEPT) employed by Stellema (1998), and the gamma emitting Radioactive Particle Tracking (RPT) used by Godfroy *et al.* (1999). The RPT technique developed by Larachi *et al.* (1994) and applied by Godfroy *et al.* (1999) in a CFB riser is similar to that of previous researchers (Kondukov *et al.*, 1964; Lin *et al.*, 1985; Moslemian, 1987) who used the RPT technique in fluidized beds. In the open literature, the study of Godfroy *et al.* (1999) is the only work that presents the particle trajectories in a CFB riser in a full 3-D field and gives particle velocities. The solids velocity and solids dispersion coefficient in the longitudinal direction decreased with increasing solids circulation rates due to a decrease in the turbulent axial velocities. Annulus thickness increased with increasing solids circulation rate. However, there are a few shortcomings in their study, as follows:

a) The radioactive tracer particle used by Godfroy *et al.* (1999) is approximately 27 times larger in volume (d_p = 500 μm) than the solids

used in the riser which had a mean particle size of d_p = 150 μm. Due to higher inertia of the tracer particle, the results represent the motion of a large particle among the smaller solids and hence it is likely that smaller fluctuating components of velocity are observed.

b) The data acquisition frequency used by Godfroy *et al.* (1999) was 100 Hz, which might not be sufficient for a good temporal resolution.

c) It is difficult to validate a CFD or mechanistic model for the velocity profiles using the results of Godfroy *et al.* (1999) because no model exists to predict the behavior of a large tracer particle surrounded by smaller particles. This of course in principle can be done but their study does not provide all the required data, for example the solids holdup distribution, required for CFD validation.

A close review of Table 2-2 shows that no experimental study provides all the information for solids velocity field that one requires for CFD model validation. The employed intrusive techniques (e.g. optical probes, sampling probes) provide vast experimental data at wide ranges of operating conditions, but only the time-averaged radial profile of the axial velocity. At best, the modified intrusive techniques with careful experimentation provided standard deviation or the velocity fluctuation profiles in the axial direction. Very few studies provide 3-D velocity components in 3-D columns. The comparison/validation of CFD models with only mean axial velocity profiles is not sufficient and can be misleading. None of the studies report turbulence stresses, turbulent-kinetic energy (granular temperature), diffusivity (axial, radial), return length distribution, or circulation time distributions. All of these are required to fully understand the mechanism of mixing (e.g. lateral segregation) and its variation with the operating conditions. In this work, all the above variables are studied systematically.

Additionally, there is a disagreement among researchers if the radial profiles of the relative axial velocity (w.r.t. the cross-sectional average) have ‘similar’ shapes or the same functional form. Berruti *et al*. (1995) argued that such ‘similar’ profiles are restricted to a narrow range of operating conditions investigated by Monceaux *et al*. (1986) and Rhodes *et al.* (1992).

Table 2-2: Sources of experimental data for solids **velocity** in gas-solid risers

Reference	**Measurement Technique**	**Riser Geometry** * Dia x Height cm x m	**Solids material / diameter**	**Operating conditions** U_g m·s^{-1} G_s kg·m^{-2}·s^{-1}	**Measurement region****	**Measured solids velocity**	**Comments**
Invasive techniques							
Bader *et al.* (1988)	Pitot tube	30.5 x 12.2 Abrupt exit	FCC 76 μm	3.7; 98	H = 4, 9.1 m	Mean radial profile	Core-annulus flow structure with parabolic profile
Fiedler *et al.* (1997)	CCD based spatial filter	40 x 15.6 Abrupt	Sand 120 μm	4 – 6; 28	H= 1.7, 10.7 m	Particle velocity distribution	Two phase flow
Harris *et al.* (1993)	Pitot tube / isokinetic probe	14 x 5.1 Abrupt exit	FCC 60 μm	2.6, 3; 26 - 52	H = 4.4 m	Mean radial profile	Wavy annular structure
Hartge *et al.* (1988)	Optical fiber probe	40 x 8.4 Abrupt exit	FCC, CFBC ash 85, 120 μm	3.8 – 5.4; 27 - 70	H = 0.9 - 4.7 m	Mean radial profile`	Two phase flow
Herbert *et al.* (1999)	Optical fiber probe	41 x 8.5 Abrupt exit	FCC, Glass beads 42 – 300 μm	$\leq$ 13; $\leq$ 250	H = 4, 4.2 m	Mean radial profile	Core-annulus with the influence of particle diameter
Horio *et al.* (1988)	Optical fiber probe	5 x 2.79 Smooth exit	FCC 60 μm	1.17, 1.29; 11.7, 11.25	H = 0.36, 1.06, 1.63 m	Mean radial profile	Annular flow with clusters
Ishii *et al.* (1989)	Optical fiber probe	5 x 2.79 Smooth exit	FCC 60 μm	1.29; 10.7	H = 0.36. 1.06, 1.63	Mean radial profile (clusters)	Cluster velocity profiles
Qian and Li (1994)	Optical fiber probe / dynamic pressure	7.5 x 10 -	FCC 54 μm	2.5; 62	H = 6.5 m	Instantaneous and mean radial	Radial profiles
Miller and Gidaspow (1992)	Extraction probe	7.5 x 6.58 Smooth exit	FCC 75 μm	2.61–3.84; 12 – 32.8	H = 1.86 – 5.52 m	Mean radial profile	Core-annulus flow structure
Parssinen and Zhu (2001 b)	Optical fiber probe	7.6 x 10 Smooth exit	FCC 67 μm	5.5, 8, 10; 100, 300, 400, 550	H = 1.53 – 9.42 m	Mean radial and averaged axial profiles	S-shaped, linear, parabolic in 4 longitudinal sections
Wang *et al.* (1993)	Particle dynamic anlyser (Phase/Doppler)	22.2 x 22.2 x 300 cm^3 Elbow exit	Sand 530 μm	5.85; 25.4	H = 1.19 – 2.24 m	3 components of particle velocities, TKE	Core-annulus flow structure
Zhou *et al.* (1995)	Optical fiber probe	14.6 x 14.6 x 914 cm^3 Abrupt exit	Sand 213 μm	5.5, 7; 20, 40	H = 5.13, 6.2, 8.98 m	Vertical and lateral profiles of particle vel.	Core-annulus flow structure

Table 2-2: Sources of experimental data for solids **velocity** in gas-solid risers – (Cont'd)

Reference	**Measurement Technique**	**Riser Geometry** * Dia x Height cm x m	**Solids material/ diameter**	**Operating conditions** U_g $m \cdot s^{-1}$ G_s $kg \cdot m^{-2} \cdot s^{-1}$	**Measurement region** **	**Measured parameters**	**Comments**
Non-Invasive techniques							
Cody *et al.* (2000)	Acoustic shot noise (ASN) excitation	61 – 274 x -	FCC 60 μm	Q = 233 – 1333 $kg \cdot s^{-1}$ G_s = 152 – 1247 $kg \cdot m^{-2} \cdot s^{-1}$	H = 5 -40 ft. (from feed injection)	Average axial velocities, RMS acceleration (at the wall)	Granular temperature variation with U_g
Donsi and Osseo (1993)	Laser Doppler Anemometer	4 x 10 x 460 cm^3 Smooth exit	Glass 94 μm	10 – 25; 50 -350	H = 270 cm	Mean radial profiles	Turbulent profile with no down flow
Godfroy *et al.* (1999)	Radioactive particle tracking	8.2 x 7 Elbow exit	Sand 150 μm	4; 23 -75	H = 4- 5 m (above distributor)	3-D Eulerian and Lagrangian velocity field (of a large particle)	Clusters formation; dispersion coeff. variation
Li and Tomita (2000)	Photographic imaging technique	8 x 12 Elbow exit	Polyethylene 3.2 mm 946 $kg \cdot m^{-3}$	9 -25; *O* (0.01)	20 cm regions at 0.7, 5.7, 11.7 m from feed	Mean radial profile	Uniform profiles (swirling and axial)
Rhodes *et al.* (1992)	High speed video camera	30.5 x 6.6	Alumina 75 μm	3- 5; 2- 80	0.1 x 0.1 m^2 at 3.5 m from the distributor	Downward velocity of particle swarms near the wall	Three flow forms – dilute, dense and swarm were found near the riser wall
Shi *et al.* (2002)	PIV	20 x 20 x 400 cm^3 Abrupt exit	Sand 382 μm	2.8 – 4; 1.5 – 2.75	H = 166 cm	Axial and lateral velocities in lateral direction	Downward velocities near the wall
Stellema, (1998)	Positron Emission Particle Tracking (PEPT)	10 x 10 x 10 cm^3 (Interconnected Fluidized beds)	Glass 700 μm	U_g = 0.972 $m \cdot s^{-1}$ Q = 0.121 $kg \cdot s^{-1}$	0.1 x 0.1x 0.1 m^3	3-D Eulerian and Lagrangian velocity field	Presence of small vortex in both the beds
Wang *et al.* (1998)	LDV	14 x 10.4 Abrupt exit	FCC 36 μm	3.49 - 4.78; 2.6-78.3	H = 4 - 6 m	Mean radial profile	Radial profile obeys 1/7 power law
Wei *et al.* (1998)	LDV	18.6 x 8 Abrupt exit	FCC 54 μm	2.3 – 6.2; 18 – 200	2.5 x 10^{-4} mm^3 volume at H = 1.5 – 6.2 m	Radial mean and RMS fluctuating profiles	Core-annulus with radial profiles as parabolic and Boltzman function
Zhang *et al.* (2003)	LDV	41.8 x 18 Abrupt	FCC 77 μm	2.7 – 3.7; 29.7 - 44	H = 6, 14 m	Mean radial profile, PDD curves of particle velocity	Dispersed particle and cluster two phase flow

2.1.1b Solids Concentration

Several experimental methods of characterizing the solids concentration in a cross-section of the riser are listed in Table 2-3. The key observations regarding the experimental results of each researcher are also presented in Table 2-3. Strong radial suspension density gradients have been experimentally found and reported, with a maximum at the wall and a minimum at the center, which agrees well with the core-annulus approximate description of the solids flow field. A critical examination of the experimental results for radial solids concentration distribution suggests that neither the core-annular flow theory nor the clustering approach alone can fully describe the riser gas-solid dynamics. For example, instantaneous data indicate intermittent passage of clusters, while time-averaged data, obtained at several radial locations, suggest core-annulus approximation. It is evident that both phenomena coexist and that a rigorous interpretation should take into consideration both clusters and core-annulus flow. In this work, attempt is made to characterize the clustering phenomena using the instantaneous CARPT data and the solids radial segregation using the time-averaged data of CT.

Both the intrusive and non-intrusive techniques reported, characterized only the time-averaged solids holdup profiles. Very few studies, using a carefully manipulated intrusive optical probe, reported solids holdup fluctuations, but with mutual disagreement persisting among the researchers (e.g. Xu *et al.*, 1999; Issangya *et al.*, 2000). Such disagreement could be due to the shortcomings of the optical probe measurements as discussed earlier. Also, none of the studies reported any specific changes in the holdup profiles with the flow regimes, which can be expected. This requires a high resolution of the holdup profile, particularly near the walls. An attempt is made in this work to characterize such differences between the flow regimes, if they exist.

Tomography proved to be a valuable tool for determining the solids concentration non-invasively and was used by several researchers, as presented in Table 2-3. In contrast to ECT and X-ray tomography, γ-ray tomography, with proper source shielding, can be used in dense flows, but the weight of the experimental set-up reduces temporal resolution and also restricts its applicability along the entire riser length. Martin *et al.* (1992) and Azzi *et al.* (1991) are the only studies that present a 2-D solids

Table 2-3: Sources of experimental data for solids **concentration** in gas-solid risers

Reference	**Measurement Technique**	**Riser Geometry** * Dia x Height cm x m	**Solids material/ diameter**	**Operating conditions** U_g m·s^{-1} G_s kg·m^{-2}·s^{-1}	**Measurement region****	**Measured parameters**	**Comments**
Invasive techniques							
Harris *et al.* (1994)	Pitot tube / isokinetic probe	14 x 5.1 Abrupt exit	FCC 60 μm	2.6, 3; 26 - 52	H = 4.4 m	Mean radial profile	Wavy annular structure
Hartge *et al.* (1986, 1988)	Capacitance probes/ Optic fiber probe	40 x 8.4 Abrupt exit	Sand, FCC, CFBC ash 56, 85, 120	3.8 – 5.4; 27 - 100	H = 0.6 - 4.7 m	Mean radial and axial profiles`	Two phase flow
Herbert *et al.* (1999)	Optical fiber probe	41 x 8.5 Abrupt exit	FCC, Glass beads 42 – 300 μm	≤ 13; ≤ 250	H = 4, 4.2 m	Mean radial and axial profile	Core-annulus with the influence of particle diameter
Horio *et al.* (1988)	Optical fiber probe	5 x 2.79 Smooth exit	FCC 60 μm	1.17, 1.29; 11.7, 11.25	H = 0.36, 1.06, 1.63 m	Mean radial profile	Annular flow with clusters
Issangya *et al.* (2000)	Optical fiber probe	7.6 x 6.1 Smooth exit	FCC 70 μm	4 – 8; 14 - 425	H = 0.97 – 5.23 m	Mean and standard deviation profile	Core-annulus structure in 'dense suspension' and FF regimes
Kato *et al.* (1991)	Optical fiber probe	15 x 3 Abrupt exit	FCC 74 μm	2.4 – 4; 9 - 53	H = 70 -230 cm	Mean radial profiles	Core–annulus in turbulent and FF
Parssinen and Zhu (2001 a)	Optical fiber probe	7.6 x 10 Smooth exit	FCC 67 μm	5.5, 8, 10; 100, 300, 400, 550	H = 1.53 – 9.42 m	Mean radial and averaged axial profiles	Constant in the centre and decreasing near the wall with height
Schlichthaerle and Werther (1999)	Optical probe, γ ray densitometry	40 x 15.6 Abrupt exit	Sand 200 μm	3 – 5; 5 – 50	H = 0.29 – 1m	Mean radial and averaged axial	Presence of local acceleration effects
Schuurmans (1980)	γ ray absorption	Cracking unit	-	-	-	Mean radial profile	Near parabolic profile
Tanner *et al.* (1994)	Optical fiber probe	41.1 x 8.5 Smooth exit	Glass beads 110 μm	2.5, 4.5, 6.5; 30, 79, 107	-	Mean radial and averaged axial	Gas and slip velocity profiles estimated
Wang *et al.* (1998)	Optical density sensor	14 x 10.4 Abrupt exit	FCC 36 μm	2.6, 3; 26 - 52	H = 4 - 6 m	Mean radial profiles	Three kinds of profiles: dense, ring and aggregative
Wei *et al.* (1998)	Optical fiber probe	18.6 x 8 Abrupt exit	FCC 54 μm	3.8 – 5.4; 27 - 100	2.5 x 10^{-4} mm^3 volume at H = 1.5 – 6.2 m	Radial mean profiles	Similar profile for all conditions given Boltzman function

Table 2-3: Sources of experimental data for solids **concentration** in gas-solid risers – (Cont'd)

Reference	**Measurement Technique**	**Riser Geometry** * Dia x Height cm x m	**Solids material/ diameter**	**Operating conditions** U_g m·s^{-1} G_s kg·m^{-2}·s^{-1}	**Measurement region****	**Measured parameters**	**Comments**
Xu *et al.* (1999)	Optical probe	9 x 11 Elbow exit	FCC 54 μm	0.11 – 3.15; 0 - 65	H = 3 m	Radial profiles of mean and fluctuations	Two distinctive regions of lateral profiles
Zhang *et al.* (2003)	Optical density probe	41.8 x 18 Abrupt	FCC 77 μm	2.7 – 3.7; 29.7 – 44	H = 6, 14 m	Mean radial profile, PDD curves of conc.	Dispersed particle and cluster two phase flow
Zhang *et al.* (1991)	Optical probe	3.2, 9,30 x 2.8, 10, 12 Abrupt exit	FCC, HGB, ALO	1 – 4; 5 – 300	H = 1.27, 4.27, 3.77 m	Mean radial profiles and wave forms in 3 regimes	Radial profile independent of U_g, G_s, if CS averaged voidage is constant
Zhu *et al.* (1997)	Optical probe	7.6 x 3	Sand 169 μm	6, 8; 71, 214	H = 1.61 – 2 m	Mean radial and axial profiles	Ring internals result in uniform profiles
Non- Invasive techniques							
Azzi *et al.* (1991)	γ–ray densitometry	19 x 11.7; 70 x -	FCC 75 μm	6.1, 21; 150, 1080	H = 3.1 – 4.8 m	Mean radial profile	2-D concentration map
Berker and Tulig (1986)	γ-ray camera	17.8 x -	FCC -	9.4, 15.3; 122, 310	H = 5.34 m	Mean radial profile	k-ε turbulence model
Grassler and Wirth (1999)	X-ray tomography	19 x 15	Glass 60 μm	2.7, 5.6; 195, 415	H = 4.4, 6.8, 11.6 m	2-D holdup maps	Core-annulus structure
Jaworski and Dyakoski (2001)	ECT	3 m Vertical channel	Polyamide 3 x 3 x1mm^3	1 – 5; Q ≤ 900 kg. s^{-1}	-	Instantaneous 2D profiles	Train of plugs with down flow at the wall
Li and Tomita (2000)	Photographic imaging technique	8 x 12 Elbow exit	Polyethylene 3.2 mm 946 kg·m^{-3}	9 -25; *O* (0.01)	20 cm regions at 0.7, 5.7, 11.7 m from feed	Mean radial profile	Symmetric profiles (swirling and axial)
Malcus *et al.* (2000)	ECT	14 x 7 Smooth exit	FCC 89 μm	3.7 - 4.7; 148 - 302	H = 1.55, 2.1 m	Radial, PDD, standard deviationprofiles	Core- annulus structure
Martin *et al.* (1992)	γ–ray tomography	19 x 11.7	62 μm, 1560 kg·m^{-3}	4.2, 6.3; 114, 308, 202	H = 4 m	Mean radial and axial profiles	2-D concentration maps, Core-annulus flow
Miller and Gidaspow (1992)	X-ray densitometry	7.5 x 6.58 Smooth exit	FCC 75 μm	2.61–3.84; 12 – 32.8	H = 1.86 – 5.52 m	Mean radial profile	Core-annulus flow structure

Table 2-3: Sources of experimental data for solids **concentration** in gas-solid risers – (Cont'd)

Reference	**Measurement Technique**	**Riser Geometry** * Dia x Height cm x m	**Solids material/ diameter**	**Operating conditions** U_g m·s^{-1} G_s kg·m^{-2}·s^{-1}	**Measurement region****	**Measured parameters**	**Comments**
Rhodes *et al.* (1998)	ECT	9 x 7.2 Smooth exit	Sand 100 μm	4; 150	H = 2.8 -4.3 m	Contours of constant conc.	Annulus width decreases height
Saxton and Worley (1970)	γ–ray absorption	-	-	-	-	-	Dense wall, dilute core
Weinstein *et al.* (1986)	X-ray absorption	15.2 x 8.5 Abrupt exit	HFZ -33 59 μm	1.1 – 5; 12- 154	H = 1.64 m	Mean radial profiles	3rd order polynomial radial profile

* Risers with circular cross-section are defined by *diameter x height*, while the ones with rectangular are defined by *length x width x height;* 90^{o} exits are termed as *elbow exits*, riser with increased diameter at the exit (disengagement section) are termed as *smooth exits* and others are termed as *abrupt exits*. No attempt is made to quantify the *smoothness* of the riser exit.

** H – height from the distributor, where measurements are reported

U_g – gas superficial velocity (m·s^{-1})
G_s – overall solids mass flux (kg·m^{-2}·s^{-1})
Q – overall solids flow rate (kg·s^{-1})

'-' indicates data not reported

concentration maps using γ ray tomography in CFB risers. However, both studies have used relatively few projections (27 and 21 projections, respectively), which results in a coarse reconstruction. The enhancement of this work is the use of a large number of projections, which improves the spatial resolution.

2.1.1c Solids Mass Flux

Table 2-4 lists different experimental methods for obtaining *first hand* data for the determination of the local solids mass flux, and reviews the results obtained by different researchers. Note that no reported experimental technique estimates the local solids flux non-invasively. Sampling probes based on isokinetic and non-isokinetic sampling seem to be the lone alternative, and they can determine only the time-averaged flux profiles. However, the use of isokinetic sampling methods for dense suspensions in riser flow remains questionable, as discussed by Rhodes and Laussmann (1992). There is only one study in gas-solid risers (Slaughter *et al*., 1993) that reports the time-series of the solids mass flux resulting in the estimation of its fluctuating component. Such instantaneous mass flux profiles can give a handle on estimating the velocity-holdup cross-correlation term and the method for modeling such a term. Such a model is required as a closure for the turbulent transport equations. The technique employed by Slaughter *et al.* (1993) is still an intrusive one, resulting in appreciably high errors. However, there is no other technique available to estimate such instantaneous solids mass flux. In this work, the best available estimate for the instantaneous solids flux was made using the instantaneous velocity data of the CARPT and the time-averaged CT data.

In addition, determination of overall solids mass flux in closed loop systems such as CFB is a non-trivial problem. Breaking the CFB loop, timing the collection of solids and weighing the amount collected is the traditional method practiced in industry prone to large errors. However, to ensure reproducibility of results and for proper comparison of results among various researchers, accurate measurement of overall solids mass flux is critical for riser flow experimental investigations. In Chapter 4 a number of different techniques employed by previous researchers are reviewed and a non-invasive method for overall solids flux estimation is introduced.

Table 2-4: Sources of experimental data for **local solids mass flux** in gas-solid risers

Reference	**Measurement Technique**	**Riser Geometry** * Dia x Height cm x m	**Solids material/ diameter**	**Operating conditions** U_g m·s^{-1} G_s kg·m^{-2}·s^{-1}	**Measurement region****	**Measured parameters**	**Comments**
Invasive techniques							
Azzi *et al.* (1991)	non-isokinetic sampling probe	19 x 11.7; 70 x -	FCC 75 μm	6.1, 21; 150, 1080	H = 3.1 – 4.8 m	Mean radial profiles	Parabolic momentum profiles
Bader *et al.* (1988)	non-isokinetic sampling probe	30.5 x 12.2 Abrupt exit	FCC 76μm	3.7; 98	H = 4, 9.1 m	Mean radial profiles	Core-annulus flow structure with parabolic profile
Bodelin *et al.* (1994)	non-isokinetic sampling probe	14.4 x 10 Smooth exit	Sand 0.2 mm	5.4; 2.6 – 52.9	H = 4 m	Mean radial profiles	Similar in dilute, different in dense
Coronella and Deng (1998)	isokinetic sampling probe	11.5 x 2.7 Abrupt exit	Sand 209 μm	3.4 – 5.4; 10 -30	H = 0.61 – 2.51 m	Total flux radial profiles	Total flux decreases with height and radius
Herb *et al.* (1992)	isokinetic sampling probe	5 x 2.7, 15 x 10.8 Abrupt exit	FCC 125, 276 μm	1 – 8; 10 -70	H = 1.5 m	Total flux radial profiles	Core-annulus flow with clusters
Issangya *et al.* (1998)	non-isokinetic sampling probes	7.6 x 6.1 Smooth exit	FCC 70 μm	4.5, 7, 7.5; 210, 250, 325	H = 2.8 – 4.62 m	Mean radial profiles	Strong radial gradients with no core-annulus flow
Mastellone and Arena (1999)	isokinetic probe	12 x 5.75 Abrupt exit	FCC, Ballotini, Sand; 70, 89, 310 μm	3 – 6; 16 -250	H = 1.22, 4.23 m	Mean radial profiles	Core-annulus flow with varying density and size, no down flow with coarser particles
Miller and Gidaspow (1992)	non-isokinetic sampling probe	7.5 x 6.58 Smooth exit	FCC 75 μm	2.61–3.84; 12 – 32.8	H = 1.86 – 5.52 m	Mean radial profile	Core-annulus flow structure
Monceaux *et al.* (1986)	non-isokinetic sampling probe	14.4 x 8 Smooth exit	FCC 59 μm	3.2; 0.5 – 1.11	Fully developed	Reduced mass flux profiles	Similar profiles regime
Rhodes and Laussmann (1992)	non-isokinetic sampling probe	15.2 x 6.13 Smooth exit	Alumina 71 μm	2.8, 4; 2.8 –62.7	H = 0.935 – 5.83 m	Radial variation with standard deviations	Core-annulus flow
Rhodes *et al.* (1992)	non-isokinetic sampling probe	15.2 x 6.2; 30.5 x 6.6	Alumina 75 μm	3 – 5; 2 – 111	H = 0.935 – 5.83; 2.6 m	Radial variation	Similar profiles regime
Van Breugel *et al.* (1969)	isokinetic sampling probe	30 x – -	Alumina 40 μm	6 – 16.5; 150 – 550	-	Radial variation	Parabolic profile, backward flow at high solids loads, strong variation near the wall

2.1.2 Solids Mixing

Internal recirculation of solids in CFB risers occurs due to the interchange of solids between the heterogeneous flow structures in the riser. As a result, the residence time of any particle in the riser may vary from less than a second to more than a few minutes. Typically, RTD studies are conducted using tracer techniques. A number of different tracer injection–detection methods was employed for determination of solids RTDs summarized in Table 2-5. All the methods for measuring solids RTDs exhibit limitations which hinder their use. These limitations (Harris *et al.*, 2002) are:

a) choice of tracer particles,

b) method of introducing and detecting the tracer,

c) experimental boundary conditions and,

d) invasiveness of the technique, and flow conditions inside the system.

If the boundary conditions are not adequately characterized, the measured concentration-time curve does not mathematically represent the true RTD, but represents some other distribution of solids travel times. In systems with backflow and recirculation such as CFBs, when measurements are made under ‘open’ boundary conditions, the concentration-time curve of transient impulse response does not yield values equal to the mean and variance of the true RTD which requires ‘closed’ boundary conditions (Naumann and Buffham, 1983). Hence, evaluation of the RTD from classical tracer responses to an impulse injection of tracer particles is difficult and often not possible. This work employs a single tracer particle tracking to overcome the above inadequacies in estimating RTDs. An attempt is made in this work to illustrate the differences in the estimation of residence times from the classical injection-detection method and the single tracer particle tracking method.

Besides the above discussed issues, solids backmixing in risers is usually quantified using an axial dispersion coefficient by fitting the RTD data with a 1D axial dispersion model (ADM). However, with low Peclet number (<10) reported, usage of such an ADM model is questionable. Also, since solids diffusion process is time dependent, appropriate diffusion coefficients are required for the particular time scale of

Table 2-5: Sources of experimental data for solids **residence time distribution (RTD)** in gas-solid risers

Reference	**Measurement Technique**	**Riser Geometry** * Dia x Height cm x m	**Solids material**	**Operating conditions** U_g m·s^{-1} G_s kg·m^{-2}·s^{-1}	**Location of injection and detection method**	**Dispersion Coefficients (D_{ax}, D_r) (m^2·s^{-1}) ***	**Comments**
Ambler *et al.* (1990)	Radioactive tracer	5 x 3 Abrupt exit	Sand 103 μm	4.5 – 7.1; 124-305	Bottom zone, NaI (Tl) detector	-	Bimodal RTD
Avidan (1980)	Ferromagnetic	15 x 8.5 Abrupt	FCC 50 μm	2.3 – 5.6; 70 - 150	Dilute zone, Inductance bridge	0.01 – 0.1; -	Core-annulus with same $D_{ax,p}$'s
Bai *et al.* (1992b)	Particles marked with organic substance	14 x 10 Abrupt exit	Silica gel particles 100 μm	2.88 – 9; 20 - 70	Bottom zone, Desorbed organic sub. with GC	-	Axial dispersion
Bader *et al.* (1988)	Salt tracer	30.5 x 12.2 Abrupt exit	FCC 76 μm	4.57; 147	Bottom zone, Sampling at centre-line, walls	-	Substantial backmixing, D_{ax} increases with diameter
Corleen *et al.* (1990)	$CaCl_2$ on alumina	10 x 6.2 Abrupt	Alumina 120 μm	3.5 – 4.5; 7 - 11	Bottom zone, Sampling probe	-	Core-annulus
Du and Wei (2002)	Phosphor tracer (60 -1250 μm)	14 x 10.4 Abrupt	FCC 74 μm	4.15; 9.8 - 39	Dilute zone (H= 2.17m), PMT	-; 0.001-0.0065	Correlation for D_r
Harris *et al.* (2002 a, b)	Phosphorescent tracer	14 x 14 x 580 cm^3	Cu:ZnS 25 μm	1.8 – 2.8; 5.4 - 30	Bottom zone, PMT	-	Core-annulus
Helmrich *et al.* (1986)	Radioactive tracer	$\leq$ 15 x 1 - 2.5	-	-	-	-	Dual peak with solids bypassing
Kojima *et al.* (1989)	Fluorescent dye	5 x 3.6	FCC 60 μm	1.5 – 2.15; -	Dilute zone, optic probe at centre	0.0001 – 0.09; -	Second peak in the response function
Lin *et al.* (1999)	Radioactive tracer	4 x 6.2 x 22.8 m^3 Abrupt exit	Coal -	2.61, 4.05; -	Bottom zone, NaI (Tl) detector	-	Dual peaks, cascade tanks model
Lyngfelt and Leckner (1992)	Sorbent particles (limestone)	11 m^2 x 17 m	Coal 0 – 30 mm	-	Added before the start, sampling	-	Size reduction
Milne and Berruti (1990)	Radioactive tracer	5 x 3 Abrupt exit	Sand 106 μm	5.56; 124.5	Bottom zone, NaI (Tl) detector	-	Core-annulus
Patience *et al.* (1991)	Radioactive tracer	8.3 x 5 Abrupt exit	Sand 277 μm	4.1 – 6.3; 28 -166	Bottom zone, NaI (Tl) detector	0.21 – 1.62; -	Core-annulus
Ran *et al.* (2001)	Phosphor tracer	18.6 x 9 Abrupt exit	Alumina 79 μm	1.5 – 5.5; 10 -180	Dilute zone (H = 3.5 m), PMT	-; 0.0007 – 0.003	Pe_r increases with ε_σ exponentially

Table 2-5: Sources of experimental data for solids **residence time distribution (RTD)** in gas-solid risers – (Cont'd)

Reference	**Measurement Technique**	**Riser Geometry** * Dia x Height cm x m	**Solids material**	**Operating conditions** U_g m·s^{-1} G_s kg·m^{-2}·s^{-1}	**Location of injection and detection method**	**Dispersion Coefficients (D_{ax}, D_r) (m^2·s^{-1}) ***	**Comments**
Rhodes *et al* (1991, 1992)	Salt tracer	15.2 x 6.2; 30.5 x 6	Alumina 71 μm	2.8 – 5; 5 - 80	Bottom zone, Sampling probe	1.9 -31; -	1 D dispersion, similar profiles
Smolders and Baeyens (2000)	Salt tracer	10 x 6.5 Abrupt exit	Sand 90 μm	2.82 – 4.92; 4.03 - 32	Bottom zone, Sampling probe	0.34 – 2.4; -	1D dispersion and core-annulus model
Viitanen (1993)	Radioactive tracer	100 x 39	FCC 70 μm	7; 488	Bottom zone, NaI (Tl) detectors	0.3 – 15.5; -	Dilute phase flow with no clusters
Wei *et al.* (1998)	Phosphor tracer	14 x 10.4 Abrupt exit	Alumina 54, 1810 μm	2.2 – 7.84 ; 3 - 160	Dilute zone, PMT	Pe_a 50 – 100, Pe_r: 70 - 300	Mixing by dispersion of fines and clusters
Weinell *et al.* (1994, 1997)	Single radioactive particle (0.4, 1 mm)	0.14 x 0.18 x 3 m^3 Abrupt exit	Silica sand 210 μm	0 – 3.6; 5 - 25	No need of injection, NaI (Tl) detectors	-	Particle recirculation times, mean upward and downward vel.'s
Zhang and Arastoopour (1994)	Radioactive tracer	Commercial FCC unit	-	-	In the standpipe, NaI (Tl) detectors	0.28 – 104.8; -	Backmixing is large, 1D model is inaccurate

'-' indicates not reported

* All the studies do not report D_{ax}, D_r

the reaction/process for design purposes. A comparison of the solids diffusivities estimated from the Lagrangian CARPT data and the axial dispersion coefficient obtained by fitting the RTD data with an ADM model is presented.

Apart from the disagreement among researchers regarding the experimental data for the solids flow in risers, as discussed in the earlier sections, the demarcation of the flow regime transitions is also debated. In particular, the description of the fast fluidized regime is widely discussed (Rhodes, 2003; personal communication with Dr. Reddy Karri, PSRI). Although no attempt was made in this work to delineate the regime transition, typical characteristics of the solids flow and mixing in the fast fluidized (FF) and in the dilute phase transport (DPT) regimes are discussed in detail.

2.2 Solids Flow Modeling in Gas-Solid Risers

2.2.1 Modeling of Solids Mixing

Several authors have tried to describe the solids motion in the dilute zone of the riser. Helmrich *et al*. (1986) modeled the solids RTD data by using a loop reactor model, which combined plug flow and stirred tank compartments. However, such models do not physically represent the actual mechanism of solids mixing. Therefore, it is desirable to describe solids mixing either by solids transfer between the core and the annulus of the assumed core-annular model or among clusters. Bolton and Davidson (1988) attributed the radially outward flux of core particles to gas induced turbulent diffusion. However, Harris and Davidson (1994) noted an apparent inconsistency in turbulent diffusion from core to annulus, as it would represent mass transfer against the solids concentration gradient. The solids mixing models by Pugsley and Berruti (1995), Harris and Davidson (1994), and Senior and Brereton (1992) are based on inter-particle collisions. Senior and Brereton (1992) postulated that the lateral movement of solids from core to annulus is due to the lateral velocity gained due to the oblique particle-particle collisions and that this flow is proportional to the core solids concentration. In addition, re-entrainment of particles from the annulus to the core is modeled as due to the gas shear. Patience and Chaouki (1992) characterized radial transport of solids by radial dispersion and found

that the value of the solids dispersion coefficient is about 0.0025 $m^2 \cdot s^{-1}$ which is approximately equal to that measured for radial gas dispersion by Martin *et al.* (1992).

2.2.2 Modeling of Two Phase Fluid Dynamics

Many fluid-dynamic models have been proposed to describe the relationship between solids hold-up and gas velocity, solids mass flux, riser geometry, and particle characteristics. Adopting the classification of Harris and Davidson (1994), one can group the models into three categories: Type I models predict only the axial solids suspension density profile; Type II models characterize both radial and axial solids hold-up distribution and velocity profiles; Type III models employ the fundamental equations of fluid dynamics.

Several models dealing with axial solids distribution in the risers have appeared in the literature (e.g., Li and Kwauk, 1980; Rhodes and Geldart, 1986; Kunii and Levenspiel, 1991; Gupta *et al.*, 1999). However, this modeling is not of direct interest to this study. In the type II models, the core-annular approximation to the flow domain has received considerable attention and is constantly being refined as experimental data continue to be published. Hartge *et al.* (1988) adopted this core annular flow structure and used the Richardson and Zaki (1954) correlation to calculate the core and annular slip velocities. Their model required experimentally measured voidages and particle velocities as inputs, in order to calculate local gas and solids flow at various axial locations. Berruti and Kalogerakis (1989) assumed that the slip velocity in the core equals the particle terminal velocity and that the density in the annulus is equal to that at minimum fluidization. Their model also assumes that the particles in the annulus descend at particle terminal velocities. However, neither of the above assumptions agrees with recent experimental evidence (Miller and Gidaspow, 1992; Zhou *et al.*, 1995). Ishii *et al.* (1989) proposed a clustering annular flow model in which the riser is treated as a bed of homogeneously fluidized clusters. Rhodes (1990) presented a similar model requiring as inputs the average solids flux in the core and annulus and the core radius, and the radial distance at which the solids flux equals zero. He quantified the net core to annulus particle flux by a deposition coefficient determined from the best fit. The major limitation

of all the above models is that they require experimental data for input, hence restricting their use as predictive tools.

Wong *et al.* (1992) presented a "fully predictive model" which combined the Berruti-Kalogerakis model with empirical correlations for the length of the acceleration zone and the voidage at the base of the riser. Several other "predictive" models are found in the literature (Horio and Takei, 1991; Senior and Brereton, 1992; Pugsley and Berruti, 1995; Koenigsdorff and Werther, 1995; Patience and Chaouki, 1995; Schoenfelder *et al*., 1996). These models account for the radial variation of the solids velocity profile and hold-up. However, experimental evidence of the complex two-phase flow structure in risers has necessitated a different class of mathematical models, type III models.

Adewumi and Arastoopour (1986) proposed a two-dimensional model consisting of gas and solid phase continuity equations, together with momentum balances in both the axial and radial directions. The constitutive equations require values for the hydrostatic head for both phases, along with the drag force in both axial and radial directions, where the drag coefficient is obtained from the standard drag curve. On the other hand, Berker and Tulig (1986) used constitutive equations that were developed from a simplified k-ε turbulence model. Sinclair and Jackson (1989) focused on the interactions between the mean particle velocity and gas velocity fields, and the mean particle velocity field and the fluctuating particle velocity component. They assumed that the momentum of moving particles was sufficient to carry them through the gas film, so that interaction occurred by direct particle-particle collisions. They noted that the major inconsistency in the formulation was to neglect the random gas velocity component. The Kinetic Theory of Granular Flows (KTGF) was used by Sinclair and Jackson (1989) to model the particle-particle collisions. Their model was found to exhibit extreme sensitivity with respect to the value of the restitution coefficient. Nieuwland *et al*. (1996) also observed such an extreme sensitivity. Pita and Sundaresan (1993), comparing the results with the experimental data of Bader *et al.* (1988), concluded that inclusion of gas phase turbulence is necessary for accurate predictions. Bolio *et al.* (1995) reported that such extreme sensitivity to the restitution coefficient could be overcome by including a gas phase turbulence model. Ding and Gidaspow (1990), Sun and Gidaspow (1999), and

Huilin and Gidaspow (2003) avoid using the turbulence model by introducing solids viscosity, predicted from the kinetic theory of granular flow (KTGF). All of the models available so far use closures for drag and/or for turbulence, lift, etc. Hence, validation of such models is needed before they could be used with confidence to develop a database for development of phenomenological engineering reactor models for the riser.

2.3 Summary

A review of the literature revealed considerable gaps in the available experimental data for both solids flow structure and backmixing. The available experimental information seems both insufficient and inconclusive for systematic validation of riser CFD codes or for definitive estimation of parameters of an engineering type model. Besides, the experimental techniques employed so far were either invasive and/or incurred large errors in dense risers. Hence, this work incorporates non-invasive flow monitoring techniques such as single radioactive particle tracking and γ-ray tomography to overcome these problems and augment the available data set.

Prior to discussing the usage of these two non-invasive techniques on gas-solid risers, improvements made in data processing in the two techniques are elucidated in the next chapter.

Chapter 3

CARPT and CT Reconstruction Algorithms

3.0 Scope

Over the last two decades, there has been a considerable increase in the usage of non-invasive flow monitoring techniques for multiphase flows (Chaouki *et al.*, 1997; Duduković, 2002). In particular, techniques employing gamma ray emitting isotopes have been predominantly used owing to the high penetration capability of gamma rays which enables one to visualize the flow through dense multiphase systems and thick walls of the reactor. Usually, responses from the radiation detection devices (NaI(Tl) scintillation detectors) require a sophisticated analysis in order to obtain the required information needed to visualize the flow. In the CARPT technique, the sequence of instantaneous positions of the radioactive particle needs to be derived from the counts detected by an array of detectors. From such tracer particle trajectories its velocity components are then derived. In this chapter, a position reconstruction algorithm employing a cross-correlation based search, coupled with a semi-empirical model, is implemented and discussed. Details of this new method for identifying the position of the tracer particle are provided in Section 3-2. In the CT technique, a 2-D image of the attenuation distribution needs to be derived from the counts collected by a fan beam arrangement of detectors subject to a source beam emission to obtain the time-averaged cross-sectional solids holdup distribution. In this chapter, an Alternating Minimization (AM) algorithm developed by O'Sullivan and Benac (2001) is implemented to seek improvements in the image quality. Details of the AM algorithm implementation are discussed in Section 3-3.

3.1 Introduction

The use of radioactive isotopes is broadly classified into two modes – (i) emission, and (ii) transmission. In the former radiation is emitted by a source within the system of interest and is being detected outside; in the latter an outside source is used and the intensity of its radiation is detected on the other side of the system being investigated. In the emission mode a detection system consists of an assembly of scintillation detectors placed external to the reactor, such as used in CARPT, and measures the emitted radiation from within the reactor. The transmission mode, as used in a CT scanner, involves placing the reactor between the radioactive source and the detection system and utilizes well collimated source and detectors.

In the emission mode, a labeled radioactive particles can be introduced into the reactor either as a single particle (as done in CARPT) or as a cloud of particles, as done in emission tomography. In residence time distribution experiments for instance, the second kind of introduction (pulse injection of tracer) is well established (e.g. Viitanen, 1993).In contrast, the use of a single radioactive tracer particle is rather uncommon. This is mainly because monitoring a single radioactive tracer, rather than a cloud of tracer particles, requires a more elaborate measuring technique and often cumbersome theoretical treatment of the raw signal (Larachi *et al.*, 1997). Nevertheless, the wealth of transient and steady state information obtainable from tracking a single tracer particle is richer than the conventional tracking of a tracer cloud.

In transmission tomography, usually, a single detector and a single collimated source, with a pencil beam of radiation, which can be moved simultaneously is predominantly used in industrial diagnosis (e.g. Saxton and Worley, 1970). This first generation tomography provided only line averaged attenuation measurements and is commonly termed as translation tomography or densitometry. In the second generation tomography, an array of detectors is placed in the fan beam viewing the source providing a cross sectional distribution of the attenuation. Image reconstruction in fan beam geometry is intricate and is discussed in detail by Kak and Slaney (1988).

To get an understanding of the complexity in the tracer position reconstruction in CARPT or image reconstruction in CT, consider a radioactive source in the plane of view of a detector as shown in Figure 3-1. The mathematical relation can be derived for relating the intensity of the radiation detected by such a detector to the radioactive source's activity and position and the intervening medium attenuation. The intensity of radiation detected is derived from the basic conservation of particles law (in our case photons), which is given by Equation (3-1) (Snyder, 2003):

$$\frac{\partial \psi(\bar{x},t)}{\partial t} = -\bar{V}(\bar{x},t) \bullet \bar{\nabla}\psi(\bar{x},t) - |V(\bar{x},t)| \cdot \sigma(\bar{x},t) \cdot \psi(\bar{x},t) + q(\bar{x},t) \qquad (3\text{-}1)$$

where $\psi(\bar{x},t)$ is the density of particles (in our case photon density) at $(\bar{x},t)$ along a line joining the radioactive source and the detector center with the units of $\#\cdot m^{-1}$,

$V(\bar{x},t)$ is the velocity of the photons at $(\bar{x},t)$ with the units of $m\cdot s^{-1}$,

$\sigma(\bar{x},t)$ is the attenuation coefficient of the medium at $(\bar{x},t)$ with the units of m^{-1},

$q(\bar{x},t)$ is the production rate of photons at $(\bar{x},t)$ with the units of $\#\cdot m^{-1}\cdot s^{-1}$.

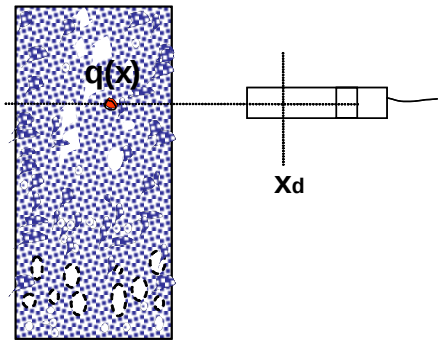

Figure 3-1: Schematic of a radioactive tracer in the plane of the detector

Equation (3-1) can be rewritten into Equation (3-2) for our physical situation with the following three assumptions:

i. constant production rate, $q\left(\bar{x},t\right)=q\left(\bar{x}\right)$ which implies that source activity is constant and results in constant photon density, i.e. $\psi\left(\bar{x},t\right)=\psi\left(\bar{x}\right)$ or, $\frac{\partial\psi}{\partial t}=0$

ii. constant velocity of the photons, $\bar{V}\left(\bar{x},t\right)=|V|\hat{e}$

iii. mono-energetic beam, which means $\sigma\left(\bar{x},t\right)$ does not depend on the incident photon energy.

$$0=-|V|\hat{e}\bullet\bar{\nabla}\psi\left(\bar{x}\right)-|V|\sigma\left(\bar{x},t\right)\psi\left(\bar{x}\right)+q\left(\bar{x}\right) \tag{3-2}$$

$$I_{\bar{x}_d}=\int_0^{\bar{x}_d} q\left(\bar{x}\right)\cdot e^{-\int_{\bar{x}}^{\bar{x}_d}\sigma\left(\bar{x}',t\right)d\bar{x}'}.d\bar{x} \tag{3-3}$$

Equation (3-2) can be simplified to Equation (3-3) by defining the intensity of radiation as $I\left(\bar{x}\right)=|V|\psi\left(\bar{x}\right)$ in (#·s^{-1}) and by noting that

$$\frac{\partial I}{\partial s}=\frac{\partial I}{\partial x}\frac{\partial x}{\partial s}+\frac{\partial I}{\partial y}\frac{\partial y}{\partial s}+\frac{\partial I}{\partial z}\frac{\partial z}{\partial s}=\frac{\partial I}{\partial x}\hat{e}_x+\frac{\partial I}{\partial y}\hat{e}_y+\frac{\partial I}{\partial z}\hat{e}_z=\left\langle\hat{e},\nabla I\right\rangle \tag{3-4}$$

where $\hat{e}$ is the vector and s is the distance along the line $\bar{x}$ to $\bar{x}_d$,

$\bar{x}$ is the position of the radioactive source,

$\bar{x}_d$ is the position of the center of the crystal in the detector

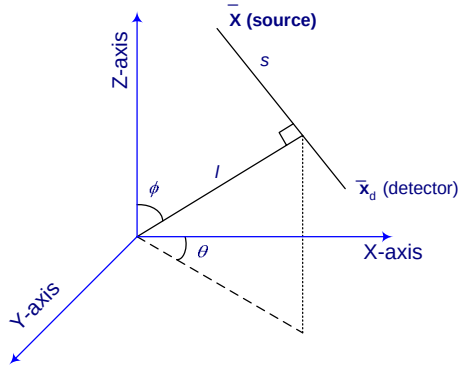

Figure 3-2: Parametric representation of the source-detector lines.

It should be noted that the factors such as detection dead time and buildup (due to scattered photons) were not considered in the above derivation of Equation (3-4) for simplicity. However, for a real physical situation, such as in a CARPT experiment, these effects need to be considered. Now, in a CARPT experiment with a point radioactive source Equation (3-4) can be re-written as:

$$I_{\overline{x}_d} = q\left(\overline{x}\right) e^{-\iiint_{R^3} \sigma(x,y,z,t)\cdot\delta(l - x\cos\theta\sin\phi - y\sin\theta\sin\phi - z\cos\phi)\cdot dx\cdot dy\cdot dz} \tag{3-5}$$

where *x, y* and *z* are the three spatial co-ordinates,

l is the perpendicular distance from the origin to the line joining $\overline{x}$ to $\overline{x}_d$,

θ, ϕ are the angles that the perpendicular makes with the *x* and *z* axes, respectively,

δ is the Kronecker delta.

Note that the expression '$l - x\cos\theta\sin\phi - y\sin\theta\sin\phi - z\cos\phi$' is the parametric representation of the line joining the source at $\overline{x}$ to detector at $\overline{x}_d$.

The inverse problem of position rendition is to evaluate the value of $\overline{x}$, given the values of $I_{\overline{x}_d}$. It can be readily seen that the line integral in Equation (3-4) and the triple integral in Equation (3-5), contains the value of $\overline{x}$ and hence an analytical solution for this inverse problem cannot be accomplished. Also, note that in an actual CARPT experiment the problem is even more complicated because one needs to integrate the intensity values obtained along many different lines connecting the source and each detector within the solid angle subtended by the detector crystal at the source position. Moreover the attenuation coefficient is a function of the distribution of the phases in the system. One intuitive way of facilitating the solution of the inverse problem is by modeling the attenuation coefficient. In other words, the attenuation coefficient can be obtained from the time-averaged holdup profile, as was done by Larachi *et al.* (1997) and Gupta (2002). However, it can be noted that the value of the intensity of radiation, *I*, is highly sensitive to the holdup profile of the phases and the use of a constant time-averaged profile may introduce errors in the results.

In the case of Positron Emission Particle Tracking (PEPT) experiment (e.g. Parker *et al.*, 1993; Stellema, 1998), where the emitted positron gets annihilated with an electron resulting in two counter propagating photons, an analytical solution can be derived. Since the photons are emitted exactly back-to-back, if both the photons are detected by gamma cameras then a line of sight can be determined along which the annihilation has taken place. By recording a number of such lines of sight, the exact particle position can be identified in principle. In fact, the inverse problem of position rendition from the intensity of radiation can be solved with two such lines of sight and is evident from Equation (3-6), derived from Equation (3-3).

$$I_{\overline{x_d}} = e^{-\int_{-\overline{x_d}}^{\overline{x_d}} \sigma \cdot dx'} \cdot q\left(\overline{x}\right) \tag{3-6}$$

$$I_{\overline{x_d}} = I\left(\overline{x_o}\right) \cdot e^{-\int_{\overline{x_o}}^{\overline{x_d}} \sigma \cdot dx'} \tag{3-7}$$

In a CT experiment, the known radioactive source is located outside the reactor and Equation (3-3) is a line integral for the exponential term and is given by Equation (3-7). Here, the objective is to identify the attenuation coefficient, σ. This problem can be solved by a simple back projection method or by other tomographic reconstruction methods (Kak and Slaney, 1988; Snyder and Cox, 1977).

In summary, there are analytical solutions available for CT and PEPT inverse problems, but not for CARPT. However, owing to the stochastic nature of photon emission and detection, and strict requirements in terms of resolution prompts for research in better reconstruction methods in CT. In the case of CARPT, approximate methods/models are required for position reconstruction. These two problems are dealt with in the following sections of the chapter.

3.2 CARPT Position Rendition

Significant progress has been made in the development of advanced non-invasive radioactive particle tracking techniques that can be used for the description of multiphase

flow fields (Duduković, 2002). A single radioactive particle that is neutrally buoyant with respect to the phase being tracked is used with Sc-46 emitting γ radiation employed as the isotope. The particle moves around in the reactor tracking the phase of interest and the position of the particle is determined by an array of scintillation detectors that monitor the γ rays emitted. In order to estimate the position, calibration is performed prior to the CARPT experiment by placing the tracer particle at various known locations, which yield a calibration map relating counts and particle positions for each detector. Now, with the counts detected by each of the detectors during the actual CARPT experiment, the inverse problem can be solved to yield the instantaneous position of the particle. Time differentiation of the successive particle positions yields instantaneous Lagrangian particle velocities as a function of time and position. Hence, it is necessary to have as precise position reconstruction as possible to avoid propagation of error to the velocities and turbulence parameters. However, as discussed in the previous section, an analytical solution can not be obtained for the inverse problem and hence a best possible position has to be found numerically, based on approximate models.

3.2.1 Available Position Reconstruction Methods

Three different classes of methods for identification of particle position in CARPT are available (Chaouki *et al.*, 1997): a) Data reduction scheme; b) Monte-Carlo based model; c) Neural network based model. These methods continue to be updated and improved.

First one is the data reduction scheme (Lin *et al.*, 1985; CREL Annual Reports – 1994-97; Rados, 2003). In this method, it is assumed that the intensity of radiation or counts received by a detector is only proportional to the distance between the center of the detector crystal and the tracer location (since tracer is small it is assumed to be a point source). The calibration curve relating counts versus distance for every detector is fitted with splines as shown in Figure 3-3. While four detectors in principle identify the tracer location exactly, due to the statistical nature of the experiments the redundancy of detectors is used to apply the weighted least-squares method in identifying particle

position. Based on the distances obtained from the spline fit for each detector, the most probable location is identified from a weighted least-squares regression applied to the counts registered by all detectors.

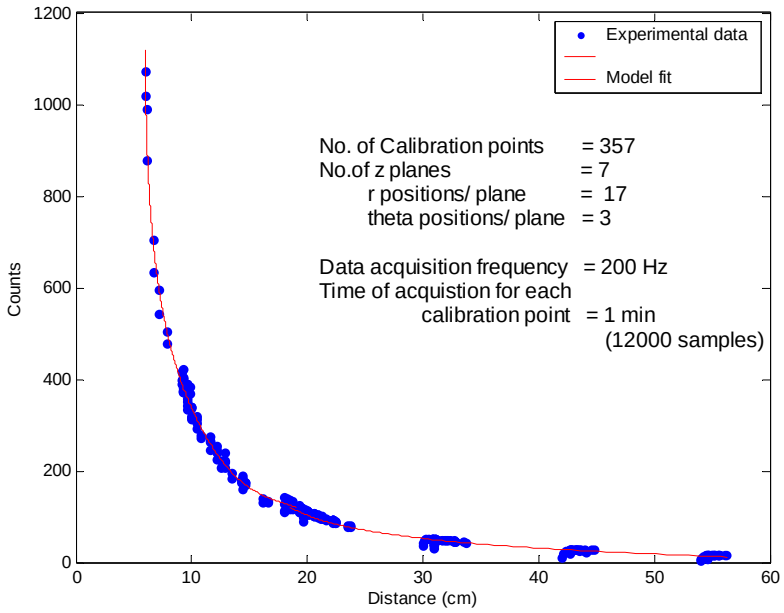

Figure 3-3: Calibration map relating counts versus distance for a detector

This method suffers in accuracy and resolution in dense flows even after improvements (Devanathan, 1991), due to the basic assumption that counts recorded depend only on the particle-detector distance and are independent of the geometry of the system, medium attenuation and solid angle.

The second method available is a model employing Monte Carlo (MC) simulations that accounts for the geometry and radiation effects in a CARPT experiment (Larachi *et al.*, 1994; Yang, 1997; Gupta, 2002). This method generates at very fine grid and the intensity of radiation for each detector is obtained from the calibration data by modeling the intervening medium attenuation with a time-averaged holdup distribution profile. In order to reconstruct the tracer particle position, experimentally obtained detector intensities are compared to those of the model generated by searching for the best grid position with the least error. Larachi *et al.* (1994), Yang (1997) and Gupta (2002) employ a model for the photopeak counts originally proposed by Tsoulfanidis

(1983). This model accounts for the detector dead time, while the detector total efficiencies need to be calculated using Monte Carlo (MC) simulations for given tracer position in the reactor. In order to estimate the total detector efficiency, one needs to evaluate parameters such as the probabilities of interaction of photons with the reactor medium and with the detector crystal and the solid angles. These parameters are evaluated from MC simulations by sampling several thousand directions and assigning a statistical weight to each direction (Larachi *et al.*, 1994). To generate the database for detector total efficiencies with a refined mesh in the reactor is computationally expensive. Alternate methods of approximation are discussed by Larachi et al. (1994) and Gupta (2002). However, the change in the medium attenuation due to the flow is either taken as a constant (Larachi *et al*., 1994) or estimated using a time-averaged holdup profile (Gupta, 2002). A constant holdup profile, where the constants of the holdup profile are obtained by regression, introduces errors into the computationally expensive sophisticated Monte Carlo based model. This is one of the drawbacks of this method. The change in the intensity of counts with changes in the holdup variations is large and this effect is discussed for gas-solid flows later in Chapter 6.

The third method relies on capturing the dependence of radiation intensity with position by a black-box model employing a neural network (Godfroy *et al.*, 1997). In this method, a part of the calibration data is used as training data set to estimate the neural network constants and gain confidence while using the remaining calibration data as test data to check for accuracy achieved. The drawback of this method is that the model used does not have physical significance, and employs a huge number of fitting parameters (~ 160) which can restrict the applicability to a narrow range. However, the method can be used for real time visualization of trajectories.

In conclusion, method b), modeling the detected radiation using Monte-Carlo based model seems to be widely used and/or most tractable. However, there is clearly a need for research on developing accurate and efficient models for position rendition. One approach may be the use of Lie groups and simultaneous identification of position and velocity.

3.2.2 Cross-Correlation Based Search Algorithm

The principle objective here is to develop a method for solving the inverse problem of position reconstruction for the CARPT type experiment. A cross correlation based search for locating the tracer particle position and a semi-empirical model relating the counts recorded (*I)* to the position of the emitting tracer particle ($\bar{x}$), accounting for the geometry and radiation effects are combined in this new approach.

Prior to the actual CARPT experiment, detectors are calibrated. This calibration experiment is performed in-situ (i.e. at the operating conditions of interest), by placing the particle at various known locations and by obtaining the counts for all the detectors (typically N_d = 16 to 30) at the required operating conditions. Hence, each calibration position is mapped to a unique series of counts recorded on N_d detectors. Conversely, an inverse mapping should exist relating a series of counts at N_d detectors to a unique position. Such an inverse mapping will exist if and only if the mapping is one-to-one. Also, note that this is the premise on which a CARPT experiment is founded.

Simple arguments can show that the mapping is one-to-one. Suppose that there exists another tracer position which results in exactly the same series of counts for all the detectors. Then, these two positions should lie on an equi-counts 3-D surface (distorted sphere) for each of the detectors. In other words, there are two points where all such N_d (typically 16 to 30) 3-D surfaces intersect. However, four distinct spheres can at most intersect at a single point. Therefore, for $N_d > 4$ there can be at most one point of intersection, i.e. a unique tracer position. Hence, the assumption that there exist two tracer positions resulting in exactly the same series of counts for all detectors is contradicted and so the mapping is one-to-one. Note that the above arguments are still based on a deterministic approach.

Consider the series of counts obtained on all detectors at a given tracer particle location during calibration $\{C_{calib}(i) : i = 1, N_d\}$, and a similar series of counts obtained during the actual experiment at a given instant $\{C_{run}(j) : j = 1, N_d\}$. The zero lag of the cross-correlation between these two series: $C_{calib}(i)$ and $C_{run}(j)$ provides an estimate of how well the counts from the corresponding detectors match. Note that the zero lag of the

cross-correlation function is the auto-correlation function. The key property exploited here is that the auto-correlation function always peaks at the zero lag. In other words, when the zero lag of the normalized cross-correlation function equals one, the two series: $C_{calib}(i)$ and $C_{run}(j)$ are exactly the same. Hence, the unknown tracer position during the run at that instant is the same as the known calibration position. Therefore, the approach to finding an unknown tracer position is reduced to matching the counts series from that position received by detectors to the counts received from known calibration positions.

The position of the tracer particle during the run should be the nearest to that known position in the calibration data set which has a maximum in the zero lag of the cross-correlation between the two normalized series given by Equation (3-8):

$$R_{run,calib_k}(0) = \sum_{i=1}^{N_d} \frac{C_{calib}(i)}{\sqrt{\sum_{j=1}^{N_d} C_{calib}^2(j)}} \cdot \frac{C_{run}(i)}{\sqrt{\sum_{j=1}^{N_d} C_{run}^2(j)}} \tag{3-8}$$

The values for the cross-correlation function, $R_{run,calib_k}(0)$, are found for the k calibration positions. Hence, the nearest known location is identified to be the calibration position where the series $\{R_{run,calib_k}(0)\colon\ k = 1, N_{calib}\}$ peaks. This gives us the best estimate of the closest known position. Further refinement of this position is performed in the second step by searching around this 'initial best estimate' of the tracer position.

In the second step, all the nearest neighboring positions in the calibration map around this identified 'initial best estimate' of tracer location are located and thus form a closed surface with the identified 'initial best estimate' of tracer location at the center. The method of obtaining the nearest neighbors is discussed later. Using a model for the counts, the mesh is refined within this closed surface and a similar search procedure is followed iteratively until the convergence criterion given by: $R_{run,calib_k}(0) = 1$ is met. The details about the mesh refinement and the iterative procedure are discussed later in

the algorithm implementation. The model for the photo-peak counts is obtained by modeling the total efficiency of the detector, defined as the probability that γ rays will emerge from the reactor without scattering and will interact with the detector. The model for counts recorded (C) is given by:

$$C = \frac{k_1}{d^2} \cdot \exp\left(-k_2 d_x - k_3 d_y - k_4 d_z\right) \cdot \left(1 - \exp\left(-\mu_d k_5\right)\right) \tag{3-9}$$

where d_x, d_y and d_z are the x, y and z directional distances between any position in the reactor and the center of the detector crystal, d is the distance between the tracer position and the center of the detector crystal, μ_d is the attenuation coefficient for the detector material, and $k_{1,2,3,4,5}$ are constants.

The second step provides a new calibration set at a refined mesh level and the cross-correlation based search for the 'best position estimate' is resumed (first step) within this refined mesh. Steps one and two are alternatively followed to meet a set convergence criterion. The flowchart for such an algorithm is provided in Appendix A.

In the counts-position model (Equation 3-9), the solid angle subtended by the detector at any location, varying over small displacements (within the sphere of nearest neighbors) was modeled as $\frac{k_1}{d^2}$, where k_1 corresponds to the view area of the detector from that position. The exponential terms in the three directions correspond to the attenuation due to the medium between the tracer location and the detector, and the constants $k_{2,\,3,\,4}$ correspond to the effective mass attenuation coefficients in the three directions. Following Larachi *et al*. (1997), the probability of interaction of these γ rays, that emerged from the system, inside the crystal of the detector is modeled as $\left(1 - \exp\left(-\mu_d k_5\right)\right)$. Here, k_5 corresponds to the length of the ray along the crystal, which was assumed to be a constant within the sphere of nearest neighbors. Constants are found by an optimization method (discussed later) within the sphere of nearest neighbors.

Algorithm Implementation

To test this new approach, the method and model introduced above were implemented on the CARPT data of Rammohan *et al.* (2001) obtained in a stirred tank. In order to validate the algorithm, few calibration locations were used as test data and the reconstruction errors were evaluated. In other words, few known calibration points are treated as the unknown positions. Also, note that if the predicted calibration positions are included in the calibration data set, the cross-correlation function peaks to one at that position and the second step of refining the calibration mesh within the region of nearest neighbors will become unnecessary. Then the validation for the semi-empirical counts model cannot be achieved. Hence, to avoid this, the positions to be predicted are removed from the calibration data set. The stepwise performance of the algorithm is given below.

i. Identification of peak in the zero lag of the cross-correlation function: Detector counts during calibration at a given tracer location and the detector counts during a CARPT experiment for an unknown tracer location are normalized with the square-root of sum of the squares of the counts from all the detectors (Equation (3-8)). The zero lag of the cross-correlation between the two normalized series corresponding to each calibration location is found and the function variation is illustrated in Figure 3-4. The values of the function $R_{run,calib_k}(0)$ at different calibration positions (N_{calib} = 275) is shown here. The position corresponding to the maximum in this function is the nearest known location which then provides the 'best initial estimate' of the tracer location. It can be noted that the variation of the peaks in the cross-correlation function is very small and a strict convergence criterion needs to be imposed. Note that a location corresponding to $R(0) = 1$ is the exact location of the particle. Hence, a convergence of $1e\text{-}3$ was set for $R(0)\text{-}1$.

ii. Identification of nearest neighbors: Subsequent to identifying the peak in cross-correlation function and checking for the convergence criterion, the next step is to identify the nearest neighbors around the 'initial best estimate'. This can be done in two ways. One way is to locate the positions with highest cross-correlation values as shown in Figure 3-5. Second way is to locate the positions relative to the initial known position

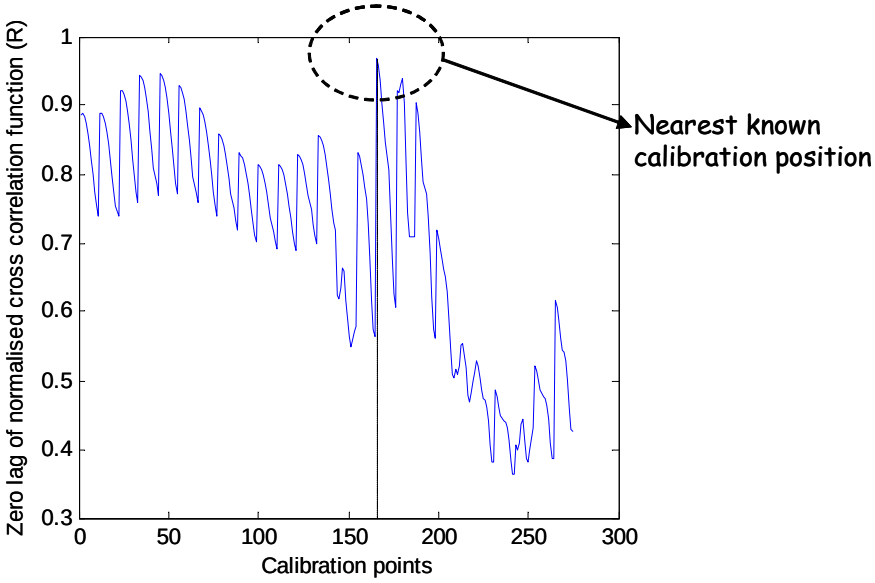

Figure 3-4: Normalized cross-correlation function variation at the calibration points for an unknown location. Note that the calibration points, which are in a 3-D space, are represented in a single sequence (1-275) for the sake of convenience.

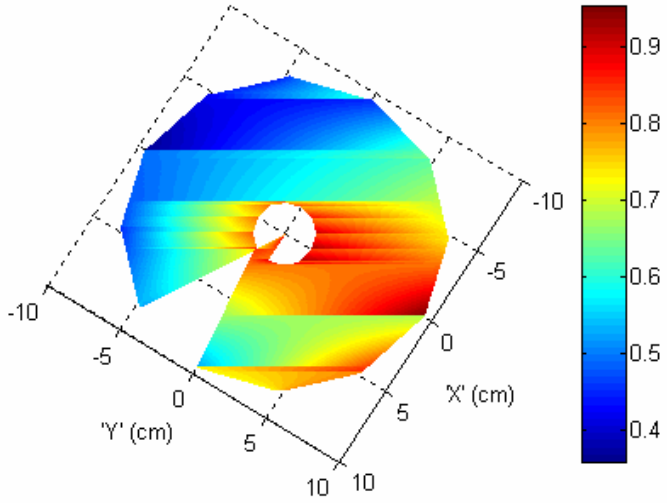

Figure 3-5: Top view of the variation of the cross-correlation function. Note that cross-correlation values are estimated only at discrete points and the colored variation represented (by interpolation) is only for the sake of understanding.

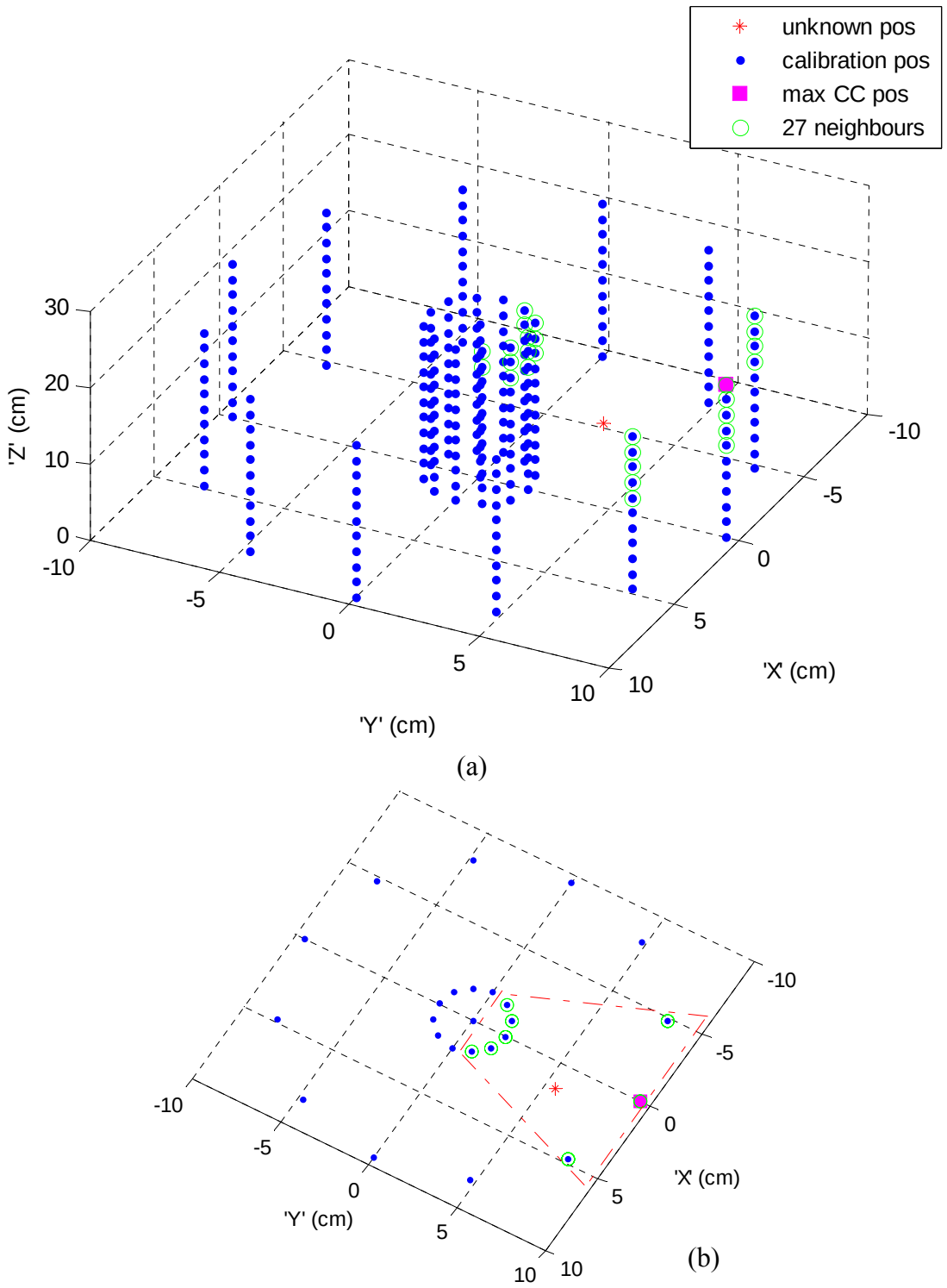

Figure 3-6: a) Relative locations of the calibration positions, nearest neighbors, unknown position and position of peak in the cross-correlation function; b) top view of a)

based on geometry as shown in Figure 3-6. Intuitively, the locations identified by both ways should match. Often, that is not the case. The reason is that the cross-correlation function not only depends on the relative location of the unknown position to the calibration positions, but also on the relative medium attenuation (holdup profile) and the geometry of the system (reactor and the detectors). In a way this is the same argument that the radiation intensity not only depends on the particle-detector distance but also on the direction of the photon detection. A second reason could be due to the variation of the radiation intensity due to the Poisson nature of gamma emission. The effect due to the latter reason is relatively small and one needs a stochastic model to account for this effect. However, it was observed that the volume covered by the nearest neighbors, obtained from geometrical considerations, is invariably larger (i.e. is a superset) and contains as a subset the volume covered by the nearest neighbors obtained from the cross-correlation considerations. This can indeed be observed from the comparison of Figures 3-5 and 3-6b. Hence, the region covered by the nearest neighbors obtained from geometrical considerations is used to refine the calibration mesh for further search.

iii. Mesh refinement and further search: If the convergence criterion is not satisfied in the earlier step, the region covered by the nearest neighbors is refined to search for a better cross-correlation estimate. Having the counts data for each detector at the nearest neighbors (from the calibration data set), the next step is to estimate the counts data for that detector within the region of the nearest neighbors. A simple way of obtaining these estimates of counts is to perform a 3D interpolation. However, it was found that such interpolation does not yield a meaningful variation of the radiation intensity. Probably this is due to the fact that the intensity not only depends on the distance, but also on the direction of the photon detection. Hence, an empirical model given by Equation (3-9) is employed to obtain the variation of radiation intensity within the region of nearest neighbors.

The empirical model requires five constants ($k_{1\text{-}5}$) that need to be estimated for each detector for mesh refinement. These five constants are estimated from the counts data at the nearest neighbors by unconstrained least-squares optimization. The optimization method is discussed here. The optimization uses a modified Levenberg-

Marquardt method of minimization with finite difference Jacobian. It should be noted that the optimization of a non-linear function with three exponentials (Equation 3-9) is highly sensitive and so a robust algorithm (Levenberg-Marquardt) was employed. The plot of the counts variation calculated from the model within the region of nearest neighbors is illustrated in Figure 3-7.

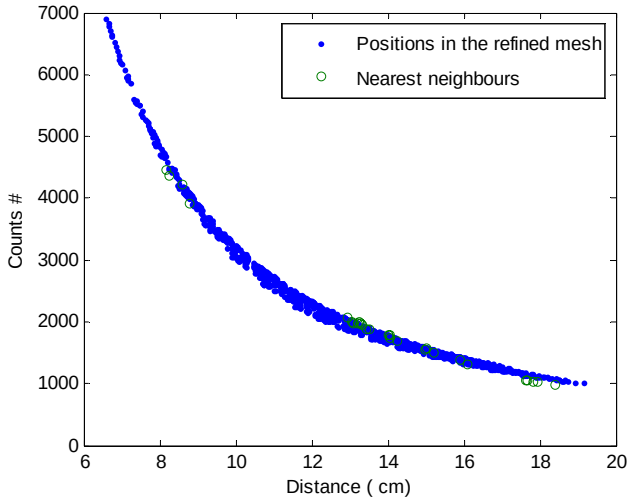

Figure 3-7: Counts variation calculated from the model within the region of neighbors.

A new calibration data set is formed; typically over 1000 positions within the region of nearest neighbors and steps i-iii are repeated until the convergence criterion is met. If the criterion is not met within three such mesh refinement iterations, the 'initial best estimate' (identified in step i) is taken to be the position corresponding to the next highest cross-correlation value. Then, steps ii and iii are similarly performed in an iterative fashion (to a maximum of three) to check for convergence. In the worst case scenario, if the convergence is not met from the highest five such initial known nearest locations, the convergence criterion (*1e-3*) is increased by *1/10*th of its value. Usually, such worst case scenarios occur near the lowest and highest horizontal calibration planes, where the calibration positions are fewer. These are the planes above or below which

there are no more detectors. Hence, the position reconstruction near the lowest and the highest *z* planes are bound to have the largest errors.

One notes that there are few parameters that need to be chosen for the algorithm implementation. For example, the choice of the convergence criterion (e.g. *1e-3*), choice of number of positions for mesh refinement (e.g. 1000), choice of number of mesh refinement iterations (e.g. 3) and the number of initial known location iterations (e.g. 5) . All these factors (in the order listed) can influence the accuracy of reconstruction and the computational time. These factors were varied for each system (stirred tank and gas-solid riser) so as to obtain position accuracy better than 5 mm within reasonable computational time. The flowchart for the described algorithm is provided in Appendix A.

3.2.3 Algorithm Validation

A. Test on calibration data for the stirred tank:

Several known calibration locations, removed from the calibration data set, are reconstructed for the stirred tank reactor. The comparison of the reconstructed data and the actual positions (known) was found to be excellent (mean relative error < 5% for *x, y* and *z* positions) and is shown in Figure 3-8. This excellent reconstruction was possible since the calibration data was obtained with a fine grid, over 400 positions in a 6300 cm^3 vessel. Hence, one can expect even the earlier spline based reconstruction method to perform well with such data. Rammohan *et al.* (2001[a]) used a Monte Carlo based algorithm (Larachi *et al*., 1997) and showed that the reconstruction errors were less than 0.5 cm. However, it is not clear whether the test points used for predicting the reconstruction errors were removed from the calibration data set. One should note that embedding the known data in a calibration set and predicting the same from the set does not give valid error estimates.

B. Test on calibration data for the gas-solid riser:

To compare the performance of the position identification algorithms, few calibration points (removed from calibration data set) were reconstructed for the

calibration data from the gas-solid riser. Monte Carlo based algorithms developed by Yang (1997) at CREL and the present cross-correlation based search algorithm were employed to reconstruct the particle positions. The comparison of the actual and the reconstructed positions of x, y, z coordinates is shown in Figure 3-9. In the case of Monte Carlo based search, the mean and standard deviation of the errors in reconstruction are appreciable (>1 cm) and would lead to large errors in velocity calculations. The downside of this algorithm was the use of an intensive model with Monte Carlo calculations on one hand, and on the other hand use gross empiricism to estimate some of the parameters in the model. The parity plots shown in Figure 3-9 with the cross-correlation based search algorithm illustrate a better reconstruction by the latter with errors less than 5 mm. One should note that the calibration data in the gas-solid riser was obtained on a coarse grid, over 300 positions in a 12,750 cm^3 section of the riser.

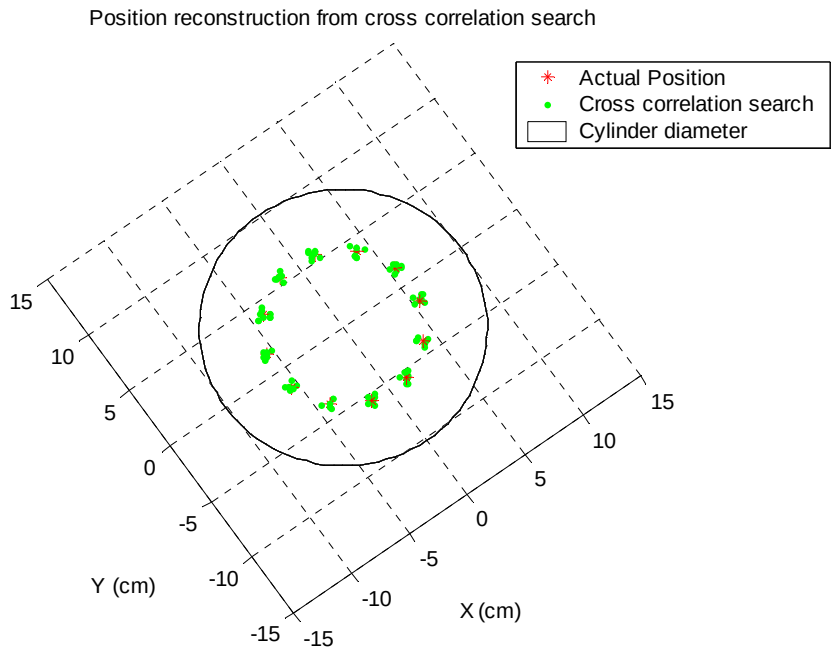

Figure 3-8: Comparison of the reconstructed position from cross correlation search with the actual positions for the calibration data from a stirred tank reactor.

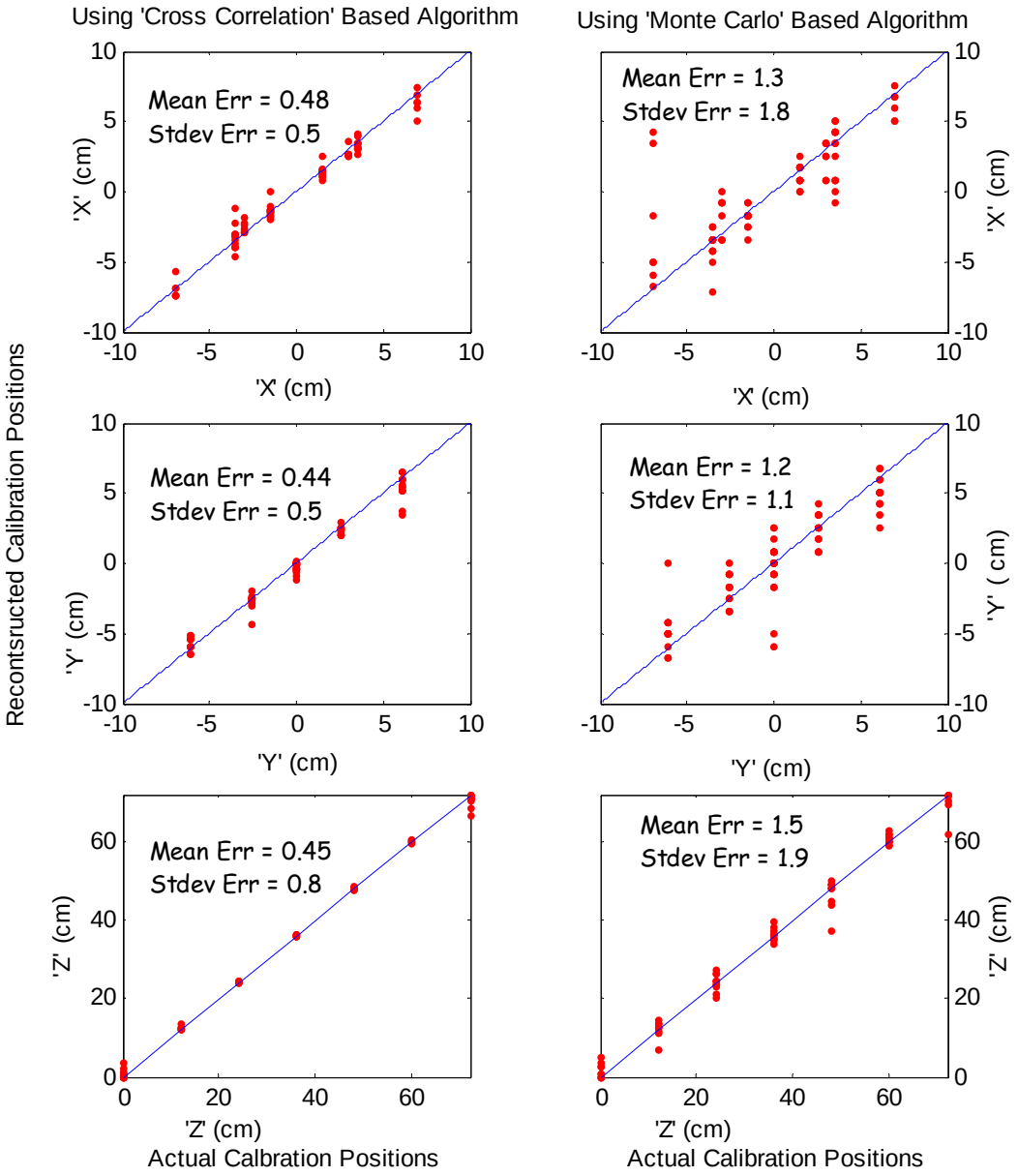

Figure 3-9: Parity plots of the reconstructed and the actual calibration points from Monte Carlo based algorithm and the cross correlation based search algorithm.

C. Test on instantaneous calibration data for the gas-solid riser:

It should be noted that in all the previous comparisons, time-averaged calibration data was used for position reconstruction. However, the actual CARPT data consists of instantaneous counts from the detectors and not the time-averaged data set. Hence, to evaluate the performance of the algorithm on instantaneous counts, individual samples of the calibration data without averaging were used to reconstruct the calibration position. In the calibration experiment in the gas-solid riser, 1 min data was acquired at 200 Hz and was time averaged. 120 samples at one such arbitrarily selected calibration position were reconstructed and the comparison with the actual positions is shown in Figure 3-10. It can be noticed that the reconstructed positions are bound within 0.5 cm from the actual positions, barring few outliers. Similar errors were seen at other calibration positions. This provides reassurance that the reconstruction error for the gas-solid riser CARPT data using cross-correlation based search algorithm is within 5 mm for most of the data.

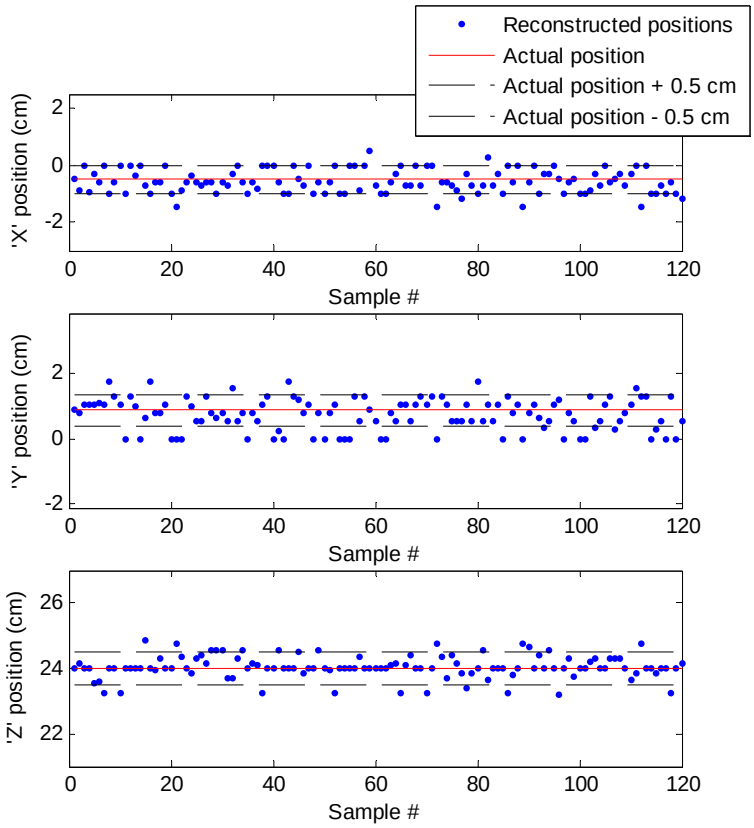

Figure 3-10: Comparison of the reconstructed positions of instantaneous samples from the gas-solid riser calibration data.

3.3 CT Image Reconstruction

3.3.1 Introduction

Computed Tomography (CT) has been successfully used for more than 50 years in the medical field for radiology diagnostics. Recently its use has been expanded to process engineering for industrial applications, in particular for visualizing the distribution of phases in multiphase reactors (Kumar and Duduković, 1997). One key area of research addresses the improvement of image reconstruction algorithms. Several authors have made contributions to the theory of reconstructive tomography and an overview of such algorithms has been presented by Snyder and Cox (1977).

Lange and Carson (1984) defined the image reconstruction for tomography as a maximum likelihood estimation problem and derived an estimation-maximization (EM) algorithm to obtain the maximum likelihood image estimate. The EM algorithm found extensive applications in emission tomography and a comprehensive description of the algorithm has been presented by Dempster *et al.* (1977). Such EM reconstruction algorithms are based on the proper stochastic model of the projection measurements and are superior to other algebraic algorithms such as Fourier/convolution techniques which are deterministic in nature and completely ignore the stochastic element of the data. In experiments where counting statistics are high (~ 500 counts/projection), ignoring the true statistical nature of the observations is not a serious limitation because Poisson counting noise is only a component of the total system noise (Lange and Carson, 1984). It is precisely in the low counts experiments (<100 counts/projection) that the EM algorithms are expected to provide the greatest improvement in the reconstruction quality. Usually in the transmission tomography experiments with the amount of shielding provided at the detectors end (to increase the spatial resolution), the counts recorded are bound to be small (~ 100 counts/projection), which forces one to use an EM algorithm.

However, in the maximization step or M-step of the EM algorithm, an approximation is made in the solution, which can affect the image quality. The M-step results in a transcendental equation, which cannot be solved exactly. Hence, the following approximation is employed to simplify the solution.

$$\frac{1}{e^s - 1} = \frac{1}{s} - \frac{1}{2} + \frac{s}{12} + O\left(s^3\right) \tag{3-10}$$

In the transcendental equation above, $s = l\mu$, where l is the length of a projection in a pixel and μ is the attenuation parameter to be estimated. The above approximation is valid for small values of s. However, in the regions of high density or high μ, the approximation is not justified and may lead to a decrease in the log-likelihood from one iteration to the next.

O'Sullivan and Benac (2001) reformulated the maximum likelihood problem as a double minimization of an I-divergence to obtain a family of image reconstruction algorithms. I-divergence, introduced by Csiszár (1991), is a measure of discrepancy between two functions $a(\cdot)$ and $b(\cdot)$, which is given as (Snyder *et al.*, 1992):

$$I\left(a\|b\right) = \sum_{y \in Y} a(y) \ln\left[\frac{a(y)}{b(y)}\right] - \sum_{y \in Y} \left[a(y) - b(y)\right]. \tag{3-11}$$

where Y is a finite dimensional space

Each step of minimization in the algorithm is claimed to be exact, without any approximation, as compared to the other standard techniques in the literature. The Alternating Minimization (AM) algorithm formulated by them is guaranteed to monotonically increase the log-likelihood function after every iteration. The objective of this work is to implement the AM algorithm (O'Sullivan and Benac, 2001) for the reconstruction of the CT data obtained in the gas-solid riser and to seek improvements in the image quality.

3.3.2 Alternating Minimization Algorithm

The image reconstruction algorithm is based on a statistical model for the measured data. This model includes the poly-energetic nature of the γ-ray beams, the existence of background events, Beer's law and a realistic model for the known point spread function (O'Sullivan and Benac, 2001). Then the reconstruction problem is

formulated as an optimization (maximum likelihood) problem in statistical estimation theory. A brief outline of the algorithm is described below. In the expression for the I-divergence (see Equation 3-11), the function $a(\cdot)$ is taken to be the measured data and $b(\cdot)$ is taken to be a nonlinear model accounting for the Poisson data which includes the parameter space to be estimated. The AM algorithm relies on a transformation of the maximum likelihood estimation problem into a double minimization of an I-divergence between two functions. The first function belongs to a linear family that enforces the constraints imposed on the measured data, while the second function is constrained to have values in an exponential family, where it is the mean of the data. The resulting iterative algorithm alternates between updating these two functions. The terms in the log likelihood function that depend on the parameter space (to be estimated) are negative of the corresponding terms in the I-divergence. Thus, minimizing the I-divergence over the parameter space is equivalent to maximizing the log-likelihood function. The derivation of the iterative algorithm and proof of convergence have been presented by O'Sullivan and Benac (2001).

The final expression for updating the parameter space (attenuation constants) with a model relevant to our CT setup can be derived from the algorithm as follows:

$$\hat{c}_k^{(n+1)} = \hat{c}_k^{(n)} - \frac{1}{Z_k} \ln\left(\frac{\tilde{b}_k^n}{\hat{b}_k^n}\right) \tag{3-12}$$

If $\hat{c}_k^{(n+1)} < 0,$ set $\hat{c}_k^{(n+1)} = 0.$

Set $n = n+1$. Check for convergence and iterate.

where, $\tilde{b}_k^n$ and $\hat{b}_k^n$ are the back-projections of the current estimates in the linear and exponential families. In other words, they are the backprojections of the measured data and the nonlinear model employed and their expressions are given by:

$$\tilde{b}_k^n = \sum_i y_i l_{ik} \tag{3-13}$$

$$\hat{b}_k^n = \sum_i l_{ik} d_i \exp\left(-\sum_{k'} l_{ik'} \hat{c}_{k'}^n\right) \tag{3-14}$$

Z_k's are appropriate scaling functions chosen for the k^{th} pixel such that the following criteria are satisfied:

$$\sum_k \left(\frac{l_{ik}}{Z_k} \right) \leq 1 \quad \forall i \tag{3-15}$$

$\hat{c}_k^{(n)}$ is the attenuation estimate at the n^{th} iteration for the k^{th} pixel.

y_i is the measured counts data at the i^{th} projection.

l_{ik} is the length of the i^{th} projection in the k^{th} pixel (Figure 3-11), and

d_i is the measured counts at the i^{th} projection during a base scan.

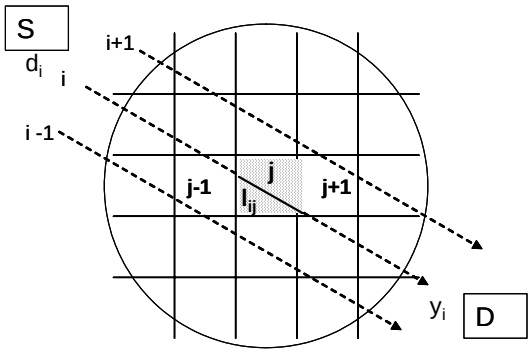

Figure 3-11: Sketch illustrating the employed notation in the AM algorithm.

3.3.3 Algorithm Validation

The above-described AM algorithm was implemented to process the data from our CT scanner (Kumar and Dudukovic, 1997) and as a preliminary validation a phantom image was reconstructed. The image was compared with that obtained from the earlier algorithm of Lange and Carson (1984), implemented by Kumar (1994). The phantom was a beaker filled with water and the data was acquired with the CT scanner at CREL. Figure 3-12 shows the comparison of the reconstructed image of the experimental data from the two algorithms with the same convergence criteria. Certainly, the image quality with the AM Algorithm has improved near the walls and also in few pixels near the center. Quantitative comparison was done by plotting a histogram of the attenuation values, which showed a very narrow spread when calculated by the AM algorithm and a larger spread when obtained by the previous algorithm (Figure 3-13). However, the mean

values of attenuation from both algorithms match closely the theoretical value for water of 0.0857 cm^{-1}.

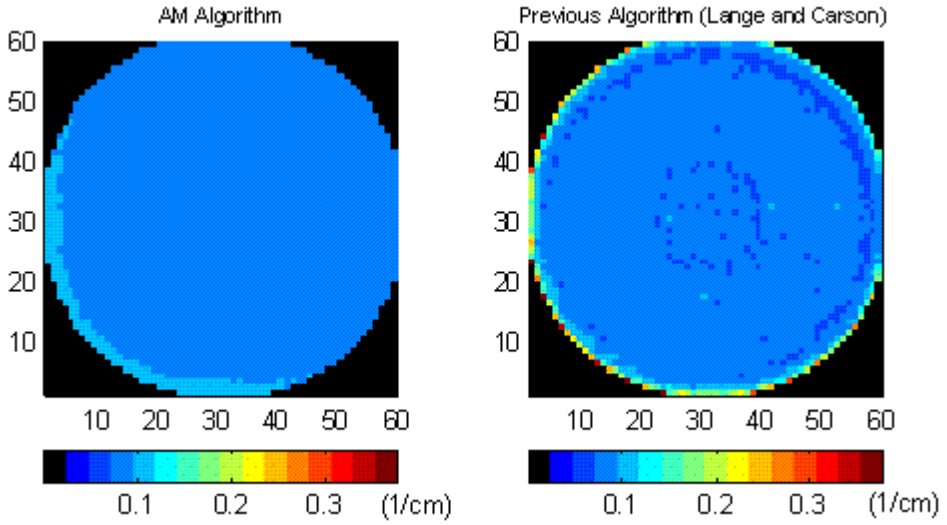

Figure 3-12: Reconstructed water phantom scans from AM and previous algorithms.

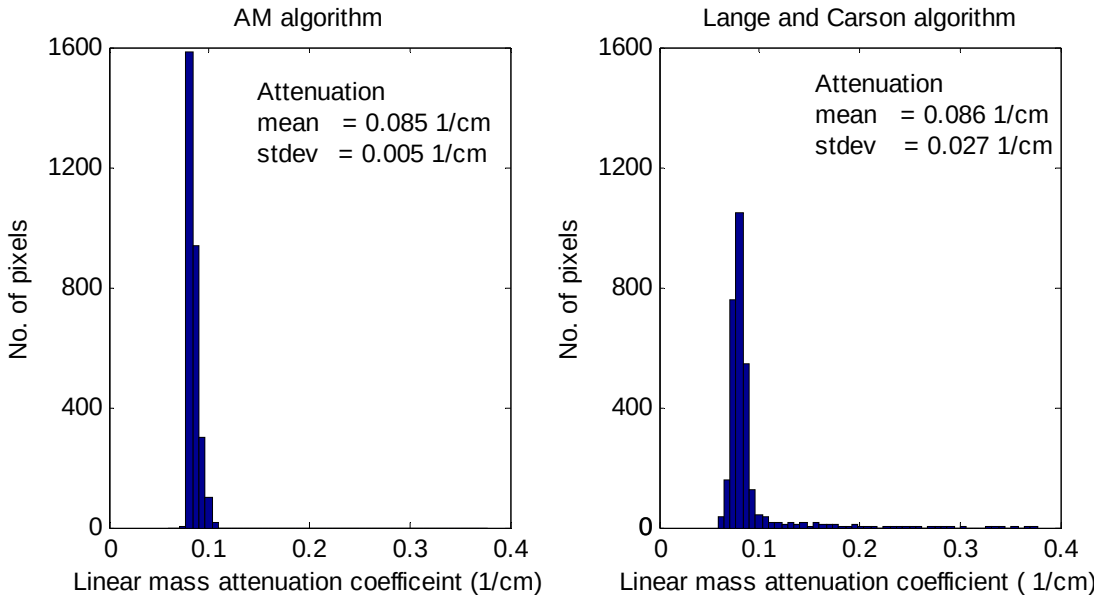

Figure 3-13: Spread of attenuation for water phantom reconstructed from AM algorithm and previous algorithm by Lange and Carson (1984).

In order to check the reconstruction with a high-density attenuator, a stirred tank with internals was used as phantom. The scan was performed of an empty cylindrical vessel with four baffles and an impeller consisting of six blades with a stainless steel shaft, placed in the center of the vessel. The experimental data of the scan was taken from Rammohan *et al.* (2001[b]). Figure 3-14 presents the comparison of the reconstructed images from AM and the previous algorithm. A close observation reveals that reconstruction of the stainless steel shaft is well captured by the AM algorithm as compared to that of the previous algorithm by Lange and Carson (1984). Also, similar to the previous result, the variation of the attenuation values near the wall seems to be more uniform in the reconstruction by the AM algorithm. However, the Plexiglas baffles and the blades seem to have been captured equally poorly by both algorithms owing to the poor spatial resolution of the CT setup. The scanner resolution was estimated to be 1.7 mm at the center of the vessel, following the expression given by Yester and Barnes (1977). Considering the fact that the impeller blades and the baffles are only 1.5 mm thick, we can expect the reconstruction of these parts to be poor.

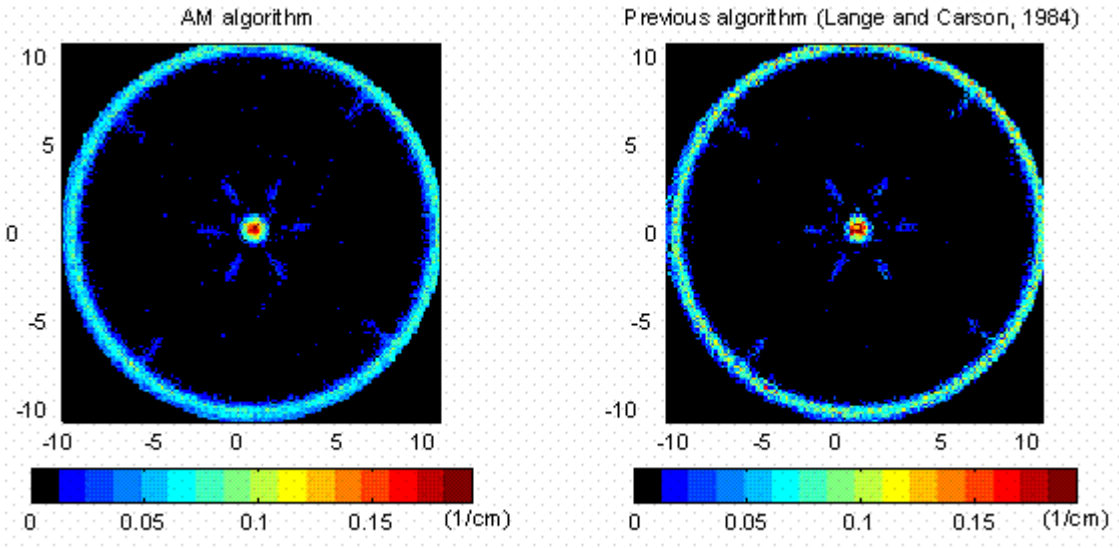

Figure 3-14: Phantom scan of a stirred tank with internals from AM and previous algorithms.

In conclusion, AM algorithm seems to perform well as compared to the previous algorithm of Lange and Carson (1984). However, the improvement in the image quality is marginal. The application of this AM algorithm in systems with stainless steel internals seems to be yielding the maximum improvement.

For the sake of clarification, it is noted here that the term 'radiation intensity' used throughout this chapter represents the counts recorded by the electronic equipment (Scalar) as the photons are counted as discrete particles.

3.4 Summary

Improvements in the reconstruction algorithms for the non-invasive flow monitoring techniques – CARPT and CT were achieved.

i. Analytical solution can not be accomplished for tracer position rendition from CARPT data.

ii. A new approach for tracer position rendition was developed by coupling a cross-correlation based search algorithm for identifying the unknown tracer particle position and a semi-empirical model for relating the counts received to the particle position. The new approach gave better reconstruction of particle position from CARPT data.

iii. The semi-empirical model was found to simulate well the radiation intensity detected by a detector, given the position of the radioactive particle within a small region (within the region of nearest neighbors).

iv. The developed algorithm for identification of CARPT particle position was validated by reconstructing particle positions from both the time-averaged and instantaneous calibration responses. Error in the position reconstruction was evaluated to be around 5 mm.

v. An alternating minimization algorithm for transmission tomography by O'Sullivan and Benac (2001) was implemented with a suitable model for the CT image reconstruction and was found to give marginal improvements in the image quality. The improvement seems to be better near the walls of the column and in systems with stainless steel internals.

Chapter 4

CFB System and Overall Solids Mass Flux Measurements

4.0 Scope

In this chapter, operational difficulties involved in running CFB system and remedies undertaken are discussed. Next, part of the tracer studies are analyzed in which overall solids mass flux measurements are described.

Quantifying the solids mass flux in CFBs with complete solids recirculation is problematic and has led to different experimental findings under the same operating conditions (Berruti *et al*., 1995). Although conceptually simple, estimating the solids mass flux in the closed loop systems, either via experiments or by using a model, is a non-trivial problem. In the present work, a non-invasive in-situ technique is applied, which is sensitive, and can be used on a large scale circulating flow system. The technique is based on estimating the solids velocity and volume fraction distribution in a section (down-comer) of the CFB loop. Solids velocity is obtained by tracking a single radioactive particle as tracer, using a two detector setup, and the volume fraction distribution is obtained by γ-ray densitometry measurements.

4.1 CFB Setup

In this study, the pilot plant scale gas-solid CFB shown in Figure 4-1 was used. The total height of the glass riser is 26 ft. (7.9 m) and the internal diameter is 6 in. (15.2 cm). The solids are soft, approximately spherical glass beads with a mean diameter (d_p) of 150 μm and a particle density (ρ_p) of 2550 $kg \cdot m^{-3}$, which fall into Group B of Geldart's classification (Geldart *et al.*, 1986). The secondary fluid (air) enters the system at the base of the riser, and flow is regulated by a standard air flow meter. The two phase gas-solid suspension in the riser exits into an axi-symmetric disengagement section. Air exits from the disengagement section to a cyclone, connected to the hopper at its bottom. Air from the top of the cyclone exits into a dust collector. The hopper is flexibly connected to the return leg (down-comer), and the solids return to the base of the riser through the down-comer. The glass down-comer is 18 ft. tall with a 2 in. (5.1 cm) internal diameter. The base of the down-comer is connected to the base of the riser with a 45^o angled standpipe of 2 in. (5.1 cm) diameter, made of glass. To regulate the flow of solids into the riser, a mechanical ball valve is placed between the base of the down-comer and the 45^o standpipe.

4.1.1 Modifications Needed to Achieve Stable Operation of the CFB Loop

Originally, the CFB setup had a 90^o elbow at the exit, as shown in the Figure 4-2a. To avoid the expected influence of this exit on the two phase fluid-dynamics inside the riser, we implemented an axi-symmetric disengagement section. The design for this section is based on the already existing riser at Sandia National Laboratory (SNL), which is a 24" diameter PVC column with a splash plate at the top. This splash plate is placed perpendicular to the riser flow. It is intended for the gas-solid mixture separation, and the impact surface is made of thick rubber to reduce the attrition of solids. Schematic diagrams of the original set-up and the modified set-up are shown in Figure 4-2.

After these modifications, the CFB loop was tested for stable operation, meaning that the unit can be operated for more than 8 hours with a constant bed height of solids inside the down-comer and an insignificant amount of solids in the bag filter.

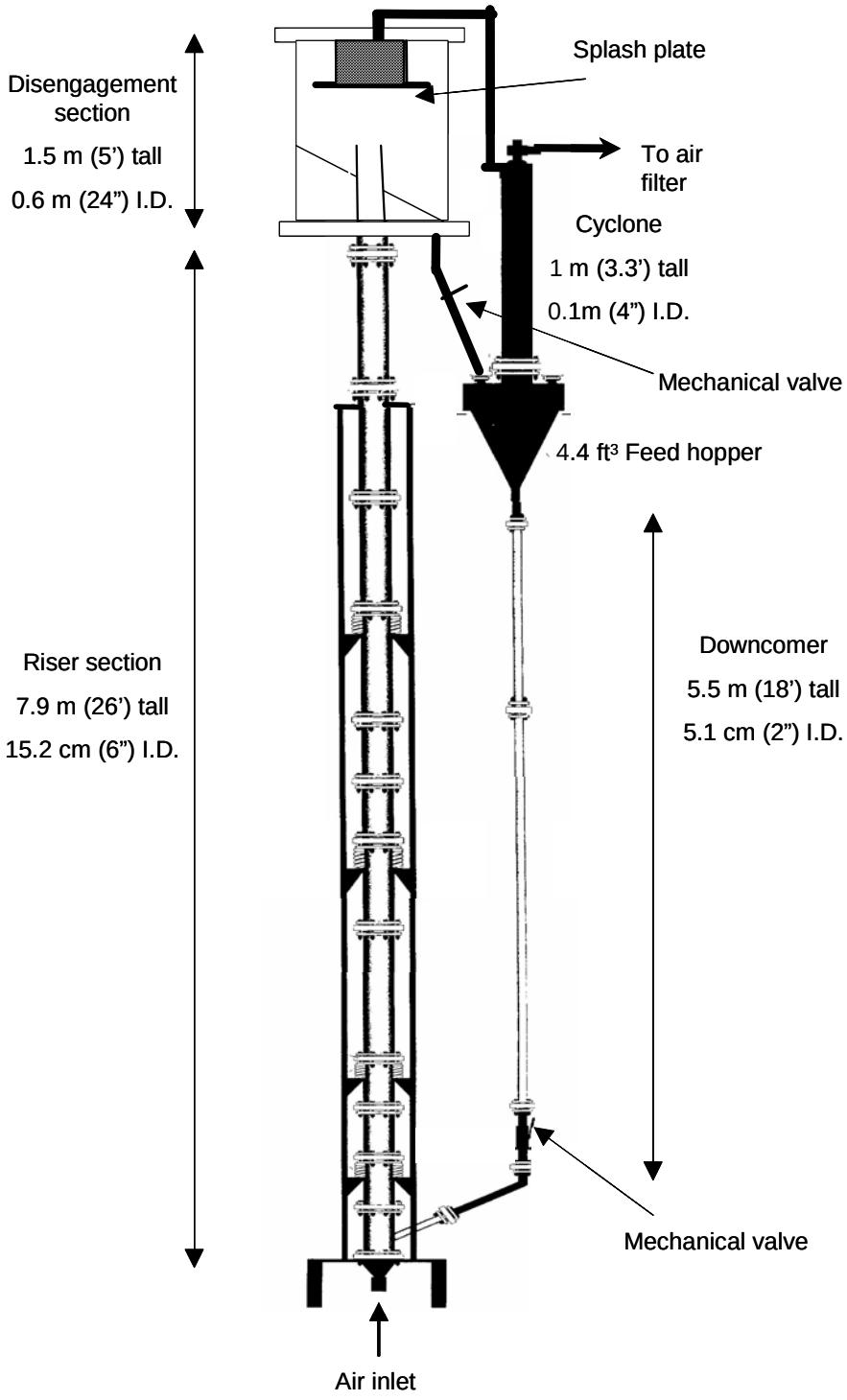

Figure 4-1: Schematic diagram of the CFB setup

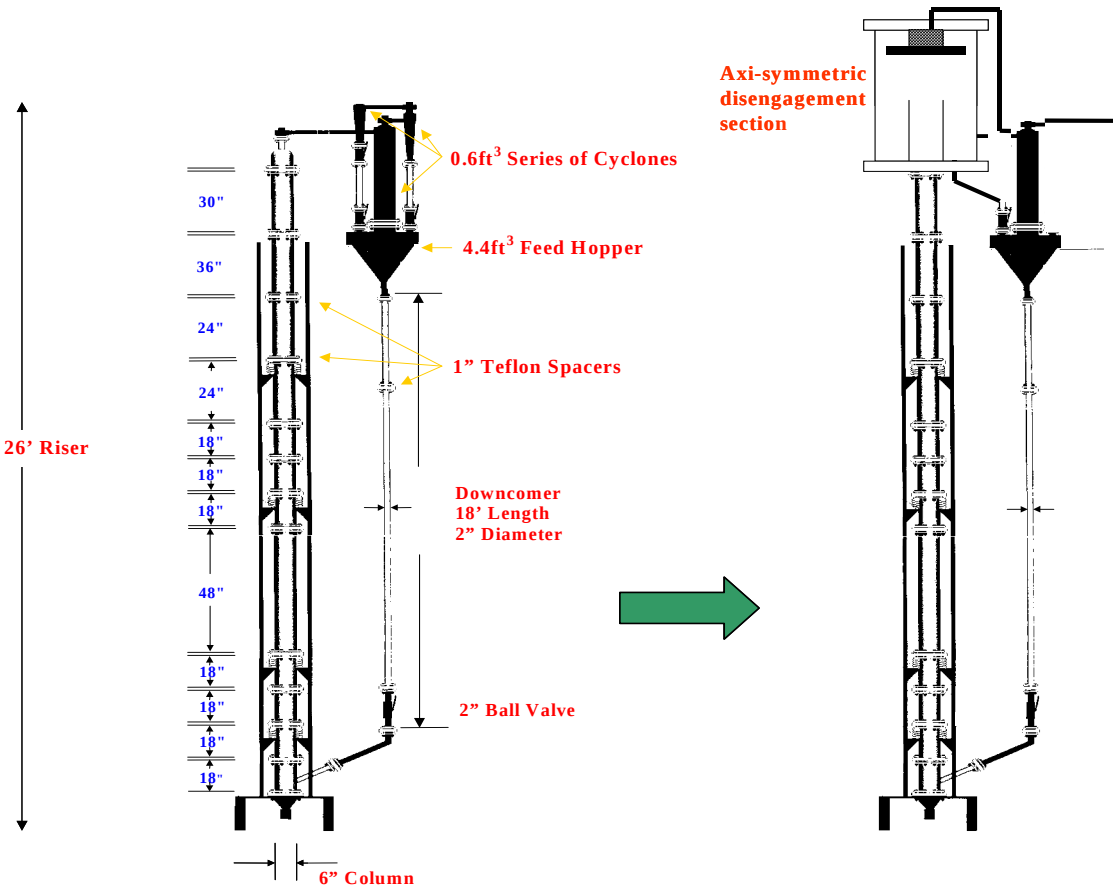

Figure 4-2: (a): Original gas-solid riser. (b): Modified set-up with axi-symmetric disengagement section.

It is noteworthy that in order to reduce the recirculation time for the radioactive particle during tracer studies, we should not have solids inventory in the disengagement section and should try to maintain a constant level of solids at the top part of the down-comer. At low gas superficial velocity (U_g^{riser} = 2.6 m·s^{-1}) and a low solids inventory of 90 lbs, it was observed that the CFB loop was stabilized meaning that the unit can be operated for more than 8 hours with almost a constant height of solids inside the down-comer and insignificant amount of solids in the bag filter.

In order to obtain high solids flux in the riser, the superficial gas velocity is increased to U_g^{riser} = 4.5 m·s^{-1}. At this velocity, the solids height inside the down-comer

could not be maintained and the level was decreasing gradually as a moving packed bed. After 25 min, there was no more "moving packed bed" inside the down-comer. This un-stabilized mode of operation was initially articulated to be occurring due to the accumulation of solids on the bottom plate of the disengagement section, due to the small value of the angle of the slope (14^{o}). The section was fluidized, however unsuccessful in overcoming the un-stabilized flow. Therefore, an increase in the slope of the disengagement bottom plate to 40^{o} has been made. Despite this modification, and even with increasing the initial loading of solids, the height of the solids bed in the down-comer was found to still decrease continuously and become empty after 4 hours of experiment. Also, a significant amount of solids (25 lbs with an initial solids loading of 125 lbs) was retrieved in the bag filter. Hence, to evaluate the stability and possible trouble shootings systematically, and to establish a protocol for the safe introduction and recovery of the radioactive tracer from the unit, a "weak" ^{46}Sc tracer particle (similar to the tracer studies discussed later) was introduced into the CFB unit. The radioactive tracer was tracked using a two detector set-up parallel to the axis of the down-comer.

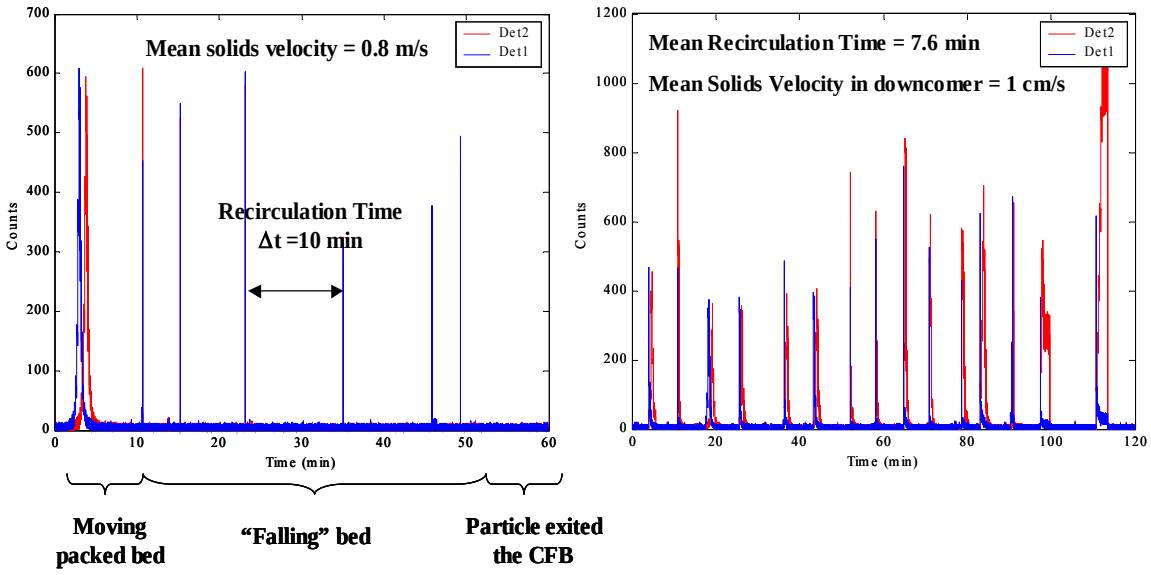

Figure 4-3: Part of the raw data from the two-detector set-up during: a) Un-stabilized run; b) Stabilized run.

Two different kinds of flow patterns were observed from the results, a moving packed bed, where the tracer velocity range was 1-10 $cm \cdot s^{-1}$ and a 'falling' bed, where the tracer velocity range was 1-2 $m \cdot s^{-1}$, as shown in the Figure 4-3. Some of the observations and reasons for the un-stabilized run are:

a) Solids flow from disengagement is in a discontinuous slugging mode oscillating between no solids flow and bursts of solids, resulting in two different flow patterns in the down-comer.

b) Significant air backflow is seen periodically in the standpipe and down-comer which causes solids to flow in the wrong direction through the cyclone and get collected in the filter.

c) When certain bed height was maintained inside the down-comer preventing backflow, only a small amount of solids gets collected in the filter implying a high efficiency of the disengagement section and the cyclone.

d) No significant attrition of the radioactive particle was observed after 7 hours of operation.

In addition to the previous changes made to the slope inside the disengagement section, the following two modifications have been made to stabilize the operation of the loop in order to balance the pressure drops across the loop:

a) An internal standpipe for the solids return leg from the disengagement section to the hopper, as shown in Figure 4-4, was added. This resulted in the solids flowing continuously from the disengagement section into the hopper.

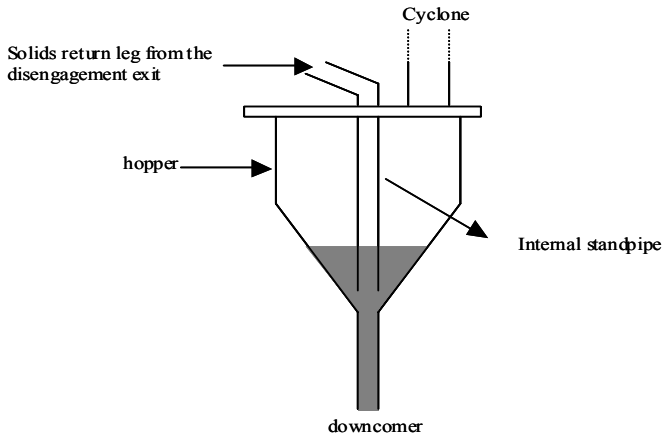

Figure 4-4: Schematic sketch of the modification

b) The diameter of the air exit pipe of the disengagement section (connected to the cyclone inlet) was increased from 2" to 3". This reduces the pressure drop and the back mixing of the air inside the disengagement section.

After these modifications, tests showed that the operation of the loop was fully stabilized. Tests were performed with a superficial gas velocity in the riser $U_g^{riser} < 4.5$ $m \cdot s^{-1}$ with the solids control valve (at the bottom of the down-comer) completely open. These test runs were conducted for 36 hours and the amount of the solids collected inside the filter was less than 500 gm. Subsequent to obtaining a stable flow, tracer studies were performed that are described in the next section.

4.2 Tracer Studies

A single radioactive particle (^{46}Sc) was used as a tracer. It was tailored by coating a layer of polymer (Parylene N) on the Scandium particle to achieve the same density as the solids used (glass beads) and the same diameter (150μm) as the mean particle size of glass beads. By tracking this single radioactive tracer at different sections along the CFB loop, the following measurements were made:

a) overall solids mass flux,

b) solids RTD for the entire riser, and

c) instantaneous solids velocity field in a developed flow section.

The experimental conditions for the tracer studies include: (i) three different superficial gas velocities varying from 3.2 to 4.5 $m \cdot s^{-1}$, (ii) two different solids loading of 140 lbs and 190 lbs, and (iii) ambient conditions (atmospheric pressure and room temperature). This chapter describes the first part, overall solids mass flux measurements.

4.2.1 Overall Solids Mass Flux Measurements - Literature Survey

Direct determination of the solids flow rate usually relies on detection of particle motion. Methods for detection of particle movement can be categorized into optical, radioactive, electrical, tracer, acoustical, heat/mass transfer and mechanical (Jaworski and Dyakowski, 2001; Malcus *et al.,* 2000; Burkell *et al*., 1988; Patience *et al.*, 1990). Mechanical methods include those based on flow separation, such as particle sampling

probes, as well as those based on determination of momentum by means of differential pressure measurements, such as Pitot tubes. Furthermore, these methods can be divided into invasive and non-invasive, where the invasive methods interfere with the normal flow in the systems. A perfect technique for measuring the solids circulation rate would be on-line, non-invasive, capable of operating at high temperatures and in large units, and be able to cover a broad range of circulation rates (Zhang *et al.,* 1997, Wu *et al.,* 2001, Roy *et al.,* 2001).

Many techniques have been introduced for measurement of solids recirculation flow in a closed loop. An obvious method would be to break the loop and estimate the time-averaged solids flow rate across a given section, assuming it to be an estimate of the overall solids circulation rate in the closed loop. Other techniques that are widely used are the introduction of probes into the riser. These invasive methods introduce a device into the flow, which may change the flow itself, leading to a systematic error in the measurement.

Miller and Gidaspow (1992) measured solids flux profiles by means of an extraction probe. Due to a 90-degree bend in the probe, it could not be pulled back flush with the near riser wall. Therefore, the flux measurements could not be performed close to the wall. The radial solids volume fraction was measured with X-ray densitometry, while the solids flow rate was metered by injecting color tracer particles into the hopper. The rate of descent of the particles was measured through a clear PVC pipe with a ruler and stopwatch, assuming plug flow. Herb *et al*. (1992) developed an iso-kinetic sampling probe to measure the axial component of the time-averaged solids mass flux locally within the CFB. The total mass flux in the riser was metered by temporarily closing a butterfly valve above the particle storage vessel, and then measuring the time to accumulate a known packed bed volume in the transparent standpipe. Hartge *et al*. (1988) used fiber optic probes to measure local instantaneous solids concentrations and local solids velocities in a CFB. The solids flow rate was measured by weighing a section of the downcomer after closing a butterfly valve. Solids holdup, averaged over the whole bed cross-section, was determined from differential pressure drop measurements. The local solids concentration inside the bed was obtained by an opto-electronical measuring system with a fairly tiny velocity measuring probe. Disregarding acceleration and wall

friction contributions, Mastellone and Arena (1999) determined solids holdup by measuring the pressure drops between the successive pressure taps. An iso-kinetic probe was used to measure the local solids flux profiles in upward and downward directions. Pugsley *et al*. (1997) determined the solids circulation rate by closing a butterfly valve installed in the return leg, and then timing the accumulation of solids to a certain level. Liu and Huan (1995) measured the bulk solids flow rate by using the rotation rate of a turbine. This method has the advantage that the device is on-line, sensitive, and can be scaled up; however, it requires calibration.

Burkell *et al*. (1988) reviewed and tested five methods for determining the solids circulation rates in CFB systems:

(i) a permeable butterfly valve, upon which the solids were collected while the valve was closed,

(ii) a time of descent technique that measured the time for identifiable particles to fall through a fixed length of a transparent down-comer,

(iii) an impact flow meter,

(iv) a modified orifice meter, and

(v) a calorimetric method based on the heat balance between the high temperature solids in the standpipe and a water-cooled jacket.

The modified orifice meter was found to be the least reliable for circulation rate measurements in CFB systems. The impact flow meter (iii) provided sensitive measurements over a limited range, but time variations in the force signals limit its applicability. The permeable valve technique (i) is useful in small-scale experimental CFB equipment where it causes little interference. Time of descent measurements (ii) are not on-line and may be difficult to execute for very small particles, but they are convincingly reliable. The calorimetric method (v) requires extensive calibration, especially for large systems, but it can provide on-line measurements over a broad range of conditions.

Wu *et al*. (2001) developed a solids flow meter, which is effectively a non-invasive and on-line device. In a section above the down-comer, where the solids are stored prior to re-injection into the CFB system, the solids pass through a short inclined chute and collide with an impact meter. The force of collision is correlated to solids flow

rate, which requires a prior calibration. Patience *et al.* (1990) developed a simple circulation rate measurement technique, where the experimentally measured pressure drop in the horizontal section between the riser and cyclone of the CFB, together with the gas velocity, is correlated with the solids mass flux. This technique is on-line, effectively non-interfering with the flow in the riser and sensitive. However, the technique needs calibration, by estimating the solids mass flux independently from the time-of-descent method (Burkell *et al*., 1988). Jaworski and Dyakowski (2001) investigated the complexities of flow morphology in dense pneumatic conveying systems by using two complementary techniques: a high-speed video camera and a twin-plane electrical capacitance tomography (ECT) system. The latter technique required complicated calibration and underestimated the solids mass flow rate typically by 20-30%, but it is non-invasive. Malcus *et al.* (2000) investigated the hydrodynamics in the bottom region of a CFB riser by electrical capacitance tomography (ECT). Pressure transducers profiled the axial pressure and permitted the determination of the solids mass flux on-line.

Use of extraction probes, fiber optic probes, and most other methods for estimating solids flux in an industrial scale CFB are invasive. Among these, pressure transducers stand out as sensitive, on-line, and highly scaleable. Of the presently available non-invasive methods, all require calibration, which is either complicated, sensitive, or both. The timing and weighing technique involving closing a valve is simple, but insensitive and not on-line. However, it seems to be predominantly used in industry.

In this work, a simple technique is implemented, which is non-invasive, in-situ, sensitive, highly scalable, and usable over a broad range of operating conditions. The technique does not require any calibration and has been demonstrated in a cold-flow CFB setup. The technique consists of tracking a single radioactive tracer particle by using two NaI (Tl) scintillation detectors to estimate the solids velocity in a section of the down-comer and measuring the solids holdup in the same section by γ-ray line densitometry. This method was introduced by Roy *et al.* (2001) for measuring solids recirculation rate in a liquid-solid riser. The differences in this work, apart from the scale of the experimental setup and the system itself, are three fold. First, quantitative method was incorporated to select the best distance between the detectors. Secondly, extensive line

densitometry was performed, which was not deemed necessary for the system used by Roy *et al.* (2001). Finally, the data processing is carried out by a more accurate and powerful cross-correlation technique. In summary, this work describes the improvement and novel application of the method suggested by Roy *et al.* (2001) in a gas-solid circulating flow system.

4.2.2 Measurement Technique

To obtain the overall solids mass flux in the Circulating Fluidized Bed (CFB) loop, two different sets of experiments need to be performed. One set of experiments is to obtain the cross sectional averaged solids holdup, $\bar{\varepsilon}_s$, in the section where the solids mass flux is to be evaluated. The second set of experiments is to obtain the solids velocity from the "time of flight" measurements of the radioactive tracer traversing the axial distance between the detectors. Hence, by representing both the solids velocity and holdup by the sum of deterministic and fluctuating components, and given a cross-sectional area (A) of the section, the ensemble averaged solids mass flux $\langle G_s \rangle$ in the section can be defined as:

$$\langle G_s \rangle = \frac{\rho_s}{A}\left[\int_A \langle v_s \rangle \cdot \langle \varepsilon_s \rangle dA + \int_A \langle v_s' \varepsilon_s' \rangle dA \right] \tag{4-1}$$

$$\langle G_s \rangle \approx \rho_s \cdot \langle v_s \rangle \cdot \langle \bar{\varepsilon}_s \rangle \tag{4-2}$$

The following assumptions are needed to arrive at Equation (4-2):

a) $\varepsilon_s'(t)$ and $v_s'(t)$ profiles are uncorrelated over the whole cross section,

b) they are averaged values,

c) $\langle v_s \rangle \neq f(r,\theta)$, and $\langle \varepsilon_s \rangle \neq f(r,\theta)$.

Essentially plug flow condition for solids in the cross section of interest is required. The down-comer section (2" column) of the CFB loop was used, since it was observed during operation that this section was always filled with a bed of solids moving in a state close to a packed bed.

In order to check the above approximation and to get the value of $\bar{\varepsilon}_s$, γ-ray line densitometry experiments were designed, constructed and performed at different superficial gas velocities in the riser and with different solids valve openings at the base of the down-comer. To perform the measurements of $\langle v_s \rangle$ and $\bar{\varepsilon}_s$, it is critical to select a section in the loop where the above assumptions are valid. In any circulating flow system, a narrow standpipe with a high solids hold up is preferred. In the present work, the down-comer section (2" column) of the CFB loop was used.

4.2.3 Densitometry Experiments

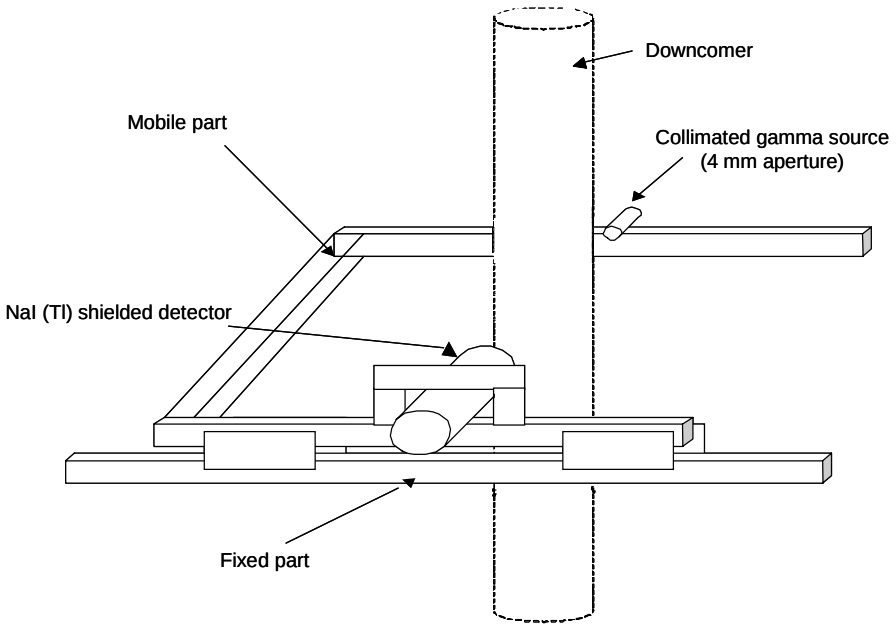

Figure 4-5: Schematic diagram of the densitometry experimental set-up

The experimental setup used to perform the line densitometry measurements is described in Figure 4-5. A single detector and a single source were aligned on a carriage that moves across the diameter of the down-comer to scan different chords through the cross-section of the column. The source (^{46}Sc) was collimated by a lead cylinder with 1.2-cm thick walls and a 4-mm aperture in the center of the cylinder. A NaI (Tl) scintillation detector was used to measure the intensity of the γ-ray photons emitted. The

detector was connected to a photomultiplier tube, pre-amplifier, timing filter amplifier, scalar, and discriminator. A data acquisition system captures the detector output and feeds it to a personal computer. The electronics are standard for photon counting, and further details can be found elsewhere (Devanathan, 1991). It is noteworthy that the data were acquired only at the photo-peak of the energy spectrum. Hence, only unscattered photons were counted, which improved the resolution. However, the intensity of the source is high enough for such measurement (~ 500 μCi) that the error introduced due to the Poisson nature of the photon emission is small. This is an improvement on the technique of Roy *et al.* (2001), who used all the counts, not just the photopeak fraction. The carriage (shown in Figure 4-5) was moved manually along the diameter of the down-comer to scan 11 different chordal lengths through the 2-inch down-comer column. This scanning was initially performed on an empty down-comer to account for the attenuation properties of the column and also for the air between the detector and the source. Next, the scan was performed with the down-comer filled with solids in a known packed bed (static) condition. Finally, the scan was performed for down-comer under operating conditions. By applying Beer-Lambert's law to the above three scanning conditions, the expressions (4-3) to (4-5) can be derived to evaluate the line averaged solids holdup at each chordal length or projection.

$$-\ln\left(\frac{I_a}{I_o}\right) = \mu_a \cdot \rho_a \cdot l_{eff} + \mu_d \cdot \rho_d \cdot l_d + \mu_a \cdot \rho_a \cdot l' \tag{4-3}$$

$$-\ln\left(\frac{I_s}{I_o}\right) = \left[\left(1-\bar{\varepsilon}_s\right)\mu_a \cdot \rho_a + \bar{\varepsilon}_s \cdot \mu_s \cdot \rho_s\right] \cdot l_{eff} + \mu_d \cdot \rho_d \cdot l_d + \mu_a \cdot \rho_a \cdot l' \tag{4-4}$$

$$-\ln\left(\frac{I_s}{I_a}\right) = \bar{\varepsilon}_s \left(\mu_s \rho_s - \mu_a \rho_a\right) l_{eff} \tag{4-5}$$

where I_o, I_a, I_s are the intensities of the radioactive source with background, air and down-comer, and air, down-comer and solids;

μ_d, μ_a, μ_s are the γ-ray attenuation coefficients of the downcomer, air and solids;

l_{eff}, l_d, l' are the projection lengths inside the down-comer, through the down-comer and the remaining length between the source and the detector, respectively.

Hence, I_a was measured at each projection only once which was used for all the experimental conditions. However, I_s was measured in two different modes of operation for every experimental condition. One, in a static mode ($I_{s,static}$), with solids in a packed bed condition whose holdup ($\bar{\varepsilon}_{s,static}$) was determined independently by a standard weight by volume ratio of solids in a 2-inch tube. Second, under the experimental operating conditions (I_{GS}). Expression (4-5) when applied to these two modes gives the solids holdup at each projection ($\bar{\varepsilon}_s$) under the operating conditions as given by expression (4-6). Note that radiation intensity of the background (I_o) is not required to determine the holdup.

$$\overline{\varepsilon_s} = \bar{\varepsilon}_{s,static} \cdot \frac{\ln\left(\frac{I_{GS}}{I_a}\right)}{\ln\left(\frac{I_{s,static}}{I_a}\right)} \tag{4-6}$$

Each of the projection data was acquired for a time span of 1 min (at a frequency of 50 Hz), which proves to be a sufficiently large time interval for proper ensemble averaging of the fluctuations in the photon emission and also of the fluctuations in the holdup values. To estimate the time needed for acquiring the data (1 min), the densitometry scan was performed for one of the experimental conditions (highest U_g^{riser}) for a time span of 5 min, which is 2-3 times the system time scale. Comparing the mean and variance of the data for different time spans, it was determined that 1 min statistics are sufficient to maintain the needed relation of equality between the mean and variance for a Poisson process. The scanning experiments were performed at the same axial height for all the experimental conditions mentioned earlier. In addition, the carriage was turned by 90^o and the experiment was repeated for one condition to check for the axial symmetry of the holdup profile.

The resolution for such a line densitometry experiment can be estimated by evaluating the point spread function for the present setup to calculate the effective detector aperture width (d_{eff}), which is related to the width of blurring. The expression, derived by Yester and Barnes (1977), is given in Equation (4-7), which yields a resolution of 4-mm at the center of the column.

$$d_{eff} = \frac{1}{M}\sqrt{d_a^2 + (M-1)^2 s^2} \tag{4-7}$$

where d_a is the detector aperture, M is the ratio of source-detector to source-object distances, and s is the focal spot size or source aperture.

This value was used as a lower bound to select the spacing between the projections or chords across the diameter of the down-comer and represents an improvement on the method of Roy *et al.* (2001).

4.2.4 Time of flight Experiments

The second type of experiment determines the "time of flight" of the solids in a section of the down-comer located 2.2 m above the base of the riser, which is also the same section where densitometry was performed. To perform this measurement, a procedure similar to that employed in the Computer Automated Radioactive Particle Tracking (CARPT) technique (discussed later in Chapters 6&7) was followed. The density and the size of the single tracer particle are 2550 kg·m^{-3} and 150 μm, respectively. This particle size differs from that in the method of Roy *et al.* (2001), which used a 2.3-mm diameter particles and tracer. The CFB with larger diameter particles and liquid as the fluid exhibited smaller fluctuations in holdup (due to high inertia), and also in the solids velocity.

A two-detector setup, with the centers of the detectors aligned and 40 cm apart (ΔH), was used to track the radioactive tracer particle in the down-comer. Each detector recorded the maximum counts when the radioactive particle moved across the middle plane of the detector. The time difference between the maxima for the two detectors is defined as the "time-of-flight", t. To obtain this accurately, the cross-correlation of the time series from the two detectors used to estimate t is given by:

$$R_{12}(\tau) = \frac{1}{T}\lim_{T\to\infty}\int_0^T C_1(t)\cdot C_2(t-\tau)\cdot dt \tag{4-8}$$

The time lag at the peaks of the normalized cross-correlation series (normalized with the maximum counts for each detector) gives the "time of flight" or residence time between the detectors.

The radioactive tracer is left to circulate in the loop for a long time, typically around 8 hrs, so that the tracer passes through the down-comer section many times. An ensemble average of the "time of flight" ($\langle t \rangle$) between the detectors can be found, along with the variance. Hence, the mean velocity in the section of the down-comer can be defined as:

$$\langle v_s \rangle = \frac{\Delta H}{\langle t \rangle} \tag{4-9}$$

Alternatively, velocity for each tracer passage can be estimated, and hence, the mean and variance of the velocity distribution. The differences in estimating the mean velocity from the above two different means is discussed in the next section.

In each pass, the radioactive tracer may traverse the cross section in front of each detector at a different radial position in the down-comer, following a possibly tortuous path between the measurement planes. From this data, distributions can be derived for "time of flight" (termed as residence time distribution) and for tracer velocity in the down-comer section. The variance of these distributions can be used to quantify the dispersion of the tracer, which can be used as a measure of validation for the assumption of nearly plug flow behavior in the down-comer.

To minimize the error in the calculation of residence times and to increase the resolution, the distance between the detectors must be carefully selected. The correlation coefficient of the time series between the detectors should satisfy the condition:

$$\rho_{12}(\tau) = \frac{R_{12}(\tau)}{\sqrt{R_{11}(0) \cdot R_{22}(0)}} > 0.9 \tag{4-10}$$

Hence, four different ΔH values were tested 20cm, 40cm, 65cm and 82cm at the lowest U_g^{riser} = 3.2 m·s^{-1}, where the mean correlation coefficients were found to be 0.96, 0.93, 0.84 and 0.7 respectively. Accordingly, ΔH = 40cm was fixed for all the experimental conditions.

To verify the solids mass flux measurements obtained in-situ by the densitometry and "time-of-flight" techniques, a simple timing and weighing procedure was performed for varying intervals. The solids were collected at the bottom of the riser by opening the mechanical valve at the bottom of the down-comer. The length of time the valve was open was varied, and the solids collected each time were weighed. Hence, a time versus weight of solids curve was obtained without introducing any air in the riser. To estimate the total solids mass flux, under the experimental conditions, a mechanical valve on the standpipe between the disengagement section and the hopper was closed. The time for all of the solids to empty the down-comer was recorded. From the time for the solids to empty, and the mass of solids collected for this time, obtained from the time versus weight curve, an approximate solids mass flow rate was found. Using the known area of the riser, the solids mass flux was calculated. It must be noted that this procedure gives just a rough estimate, because of the human error involved in the collection of solids and the timing of the valve closing. The values can only be used to check whether the trends of solids flux values vary consistently with operating conditions.

4.3 Results and Discussion

4.3.1 Solids Holdup Measurements

Figure 4-6 shows the radial variation of the line-averaged solids holdup in the down-comer for the conditions used. As can be seen from the plot in Figure 4-6a, the variation is relatively small, and the values lie within the 95% confidence intervals shown as error bars. The error bars are obtained from the variance of reproduced experimental runs (three). Other sources of variance in the results obtained are due to the statistical nature of the photon emission and due to the physical nature of the system, and these sources are discussed separately below. The large error bars and variations near the wall of the down-comer occur because the down-comer, which is held by flexible connection, vibrates during the actual run. Hence, during the scans at the chords close to the wall, either part of the glass column or ambient air is in the field of view instead of the solids and air inside the column. This vibration, observed during the scan, is most likely caused by solids flow choking in the down-comer.

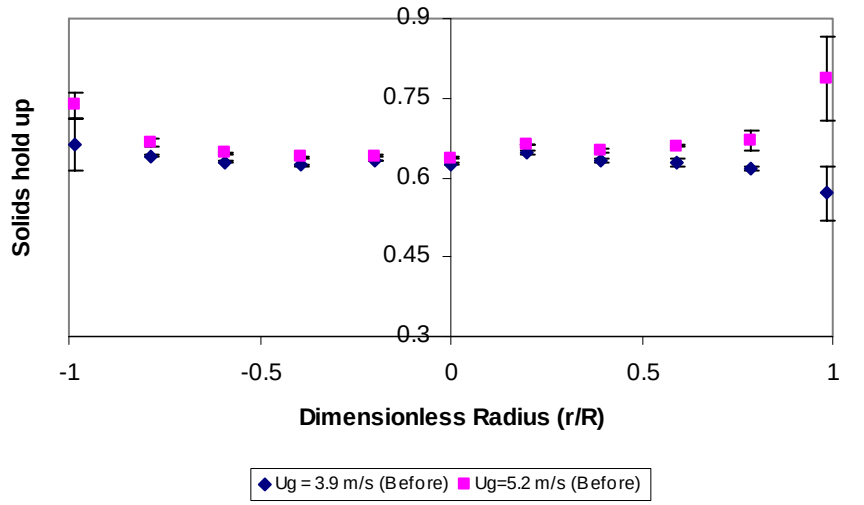

(a)

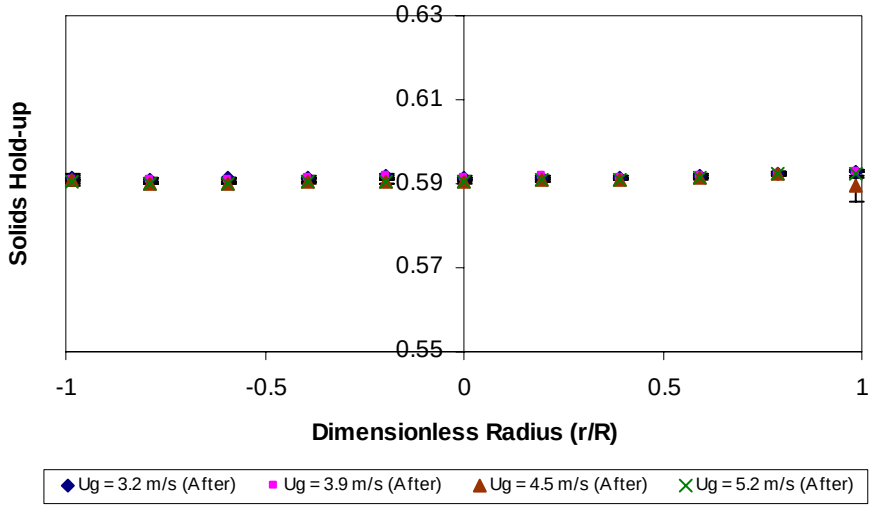

(b)

Figure 4-6: Line-averaged radial solids holdup profiles in the down-comer: a) Before denotes the runs without introduction of secondary air – i.e., runs subject to down-comer vibration; b) After denotes runs with secondary air which decreases the vibration. Note that ordinate scale for the two plots are different.

To avoid choking in the down-comer, secondary air was introduced in the down-comer (shown in Figure 4-7) at the its base and at a distance of 39" below the base of hopper, which resulted in a change in the holdup profile and hence the solids flux values. Also, this secondary air was introduced uniformly along the diameter of the down-comer. As shown in Figure 4-6b, after the modification of introducing the secondary air, the radial holdup profile is flat even near the walls, and the mean value of the holdup decreased from 0.64 to 0.59. Now that we know that the solids holdup profile is uniform, the assumption of plug flow in the down-comer can be verified by evaluating the Residence Time Distribution (RTD) curve from the "time of flight" measurements obtained from the two-detector setup presented subsequently.

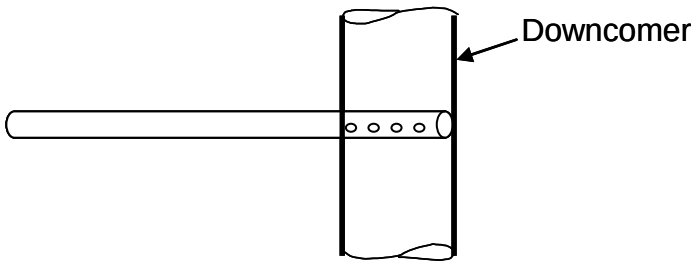

Figure 4-7: Schematic of the introduction of secondary air in the down-comer

Solids holdup profiles presented in Figure 4-6 represent line-averaged values (i.e. average holdup along the source-detector line). Now, one can estimate the actual radial solids hold-up profile from the line-averaged values using an inverse Radon transform (Kak and Slaney, 1988) by assuming a circularly symmetric cross-sectional distribution. However, the line-averaged holdup values were found to be within 3% of the mean value (except at r/R=0.98). Thus there was no necessity to obtain a radial profile for calculating the true cross-sectional holdup average. The line average value with the present method was found to be satisfactory.

An important part of reporting the results of any experiment is an indication of the accuracy of the results. Also, a measure of the variance in the solids holdup from a densitometry experiment can produce an upper bound for the holdup fluctuations, which is necessary to validate the basic assumption of neglecting the mean of the cross

correlation $\left\langle v_s^{'} \varepsilon_s^{'} \right\rangle$. The variance in the solids holdup arises from two different sources. One source of the variance was identified by assessing the reproducibility of the experimental values obtained from a repeated set of runs. These values include variations arising from common laboratory manipulations in the repeated experiments and are shown as error bars in Figure 4-6. A second source of variance was identified within each of the experimental runs (here, from 1 min data). This variance is due to the characteristics of radioactivity measurements and to fluctuations of the holdup arising due to the physical nature of the solids motion. There are three characteristic sources of errors in radioactivity measurements:

a) random emission from the radiation source,

b) detection of nuclear radiation, which will involve errors in the performance of the detector and the performance of the auxiliary equipment, and

c) radiation measurement technique which involves variation due to interaction with matter, resulting in scattering or absorption.

However, the sources of the variance in each individual run cannot be decoupled to obtain the holdup fluctuations separately. For example, the mean total counts obtained in the state of empty down-comer (I_a) was 861 (at a sampling frequency of 50 Hz), while in the state of a static packed bed ($I_{s,static}$) was 681, and in the condition of solids flowing (I_{GS}) was 692. Thus, the mean total counts of 692 will involve the three sources of variance mentioned above, but cannot be decoupled to obtain the holdup fluctuations. Using the standard error analysis using an *error propagation formula* (Knoll, 1989) for Equation (4-6), variance for the solids hold up, which represents an upper bound for the holdup fluctuations ($\varepsilon_s^{'}$) can be derived as:

$$\sigma_{\varepsilon_s}^2 = \frac{\varepsilon_{s,static}^2}{\ln^2\left(\frac{I_{s,static}}{I_a}\right)}\left[\frac{\sigma_{I_{GS}}^2}{I_{GS}^2} + \frac{\ln^2\left(\frac{I_{GS}}{I_a}\right)\cdot\sigma_{I_{S,static}}^2}{I_{s,static}^2\ln^2\left(\frac{I_{s,static}}{I_a}\right)} + \frac{\sigma_{I_a}^2}{I_a^2}\left(\frac{\ln\left(\frac{I_{GS}}{I_a}\right)}{\ln\left(\frac{I_{s,static}}{I_a}\right)} - 1\right)^2\right] + \frac{\ln^2\left(\frac{I_{GS}}{I_a}\right)\cdot\sigma_{\varepsilon_{s,static}}^2}{\ln^2\left(\frac{I_{s,static}}{I_a}\right)} \tag{4-11}$$

Table 4-1 gives an estimate for this variance at each radial location for one of the operating conditions. As can be seen from the table, the maximum variance is 8% of the mean value, excluding the near wall data (r/R = 0.98). This variance represents a relatively small upper bound for the holdup fluctuations. Hence, the assumption of neglecting the cross correlation term between solids velocity and holdup fluctuations is justified. However, the fluctuating component of solids velocity needs to be treated similarly, as described in the next section. To ensure that the fluctuations in the holdup are captured during the scan, an assumption was made that the time scale of data acquisition or photon counting, (50 Hz sampling rate) is smaller than the time scale of the fluctuations in the hold up. This assumption is based on the fact that solids motion in the down-comer is nearly a plug flow with a velocity of the $O(10)$ cm·s^{-1}. However, to estimate the minimum frequency for data acquisition or to characterize the 'errors' in the measured values due to the frequency of acquisition ("dynamic bias"), as done by Rammohan *et al*. (2001[a]), an independently measured time series of the holdup would have been required. This was not attempted in this work.

Table 4-1: Mean and standard deviation of solids hold-up at U_g^{riser}= 3.9 m·s^{-1} and 100% valve opening prior to the modification.

r/R	Mean Hold up ($\bar{\varepsilon}_s$)	Standard deviation (Upper bound for ε_s')
-0.98	0.66	0.373
-0.79	0.64	0.051
-0.59	0.63	0.027
-0.39	0.62	0.029
-0.2	0.63	0.049
0.0	0.62	0.047
0.2	0.65	0.04
0.39	0.63	0.033
0.59	0.63	0.02
0.79	0.62	0.108
0.98	0.57	0.181

4.3.2 Time-of-flight Measurements

Figure 4-8 displays a section of the raw data for the "time of flight" experiments obtained from the two-detector set-up at U_g^{riser} = 3.9 m·s^{-1} after the introduction of the secondary air in the down-comer to avoid choking. During a run of 370 minutes, the tracer particle made 280 trips past the two-detector setup. The raw data shows that there were some "dead-times" in between the occurrences, which are probably due to the particle getting trapped in the hopper for a period of time. This was confirmed during the experiments. A Geiger-Muller counter was used to keep track of the particle, and several times the particle could be found in the hopper, where it stayed for a while before again entering the circulating loop through the down-comer. The correlation coefficient (ρ_{12}) obtained for this condition was 0.93, which is clearly reflected in the degree of separation between the two peaks in Figure 4-8b. As shown in Table 4-2, the total number of occurrences for each of the experimental runs is sufficiently high, i.e., greater than 100 to obtain an ensemble average of the "time-of-flight", the circulation time, and hence the solids velocity.

Using this time difference between the spikes (Figure 4-8a), total recirculation time of the tracer or Cycle Time Distribution (CTD) was also calculated and is shown in Figure 4-8c. CTD is defined as the time elapsed between consecutive passages of a certain fluid element past the cross section through which all the fluid passes (Mann and Crosby, 1973). It was noticed from the raw data that the peak of the counts varied from 550 to 1760, indicating that the tracer particle was traversing at different radial and azimuthal positions in the cross section of the down-comer (thus representing statistically "all" the possible solid particles in the system). This variation in the counts can in fact be verified by a simple calculation based on the attenuation of the gamma radiation by the glass beads following Beer-Lambert's law.

Table 4-2: Results from "time of flight" measurements for different operating conditions

Operating Condition (U_g^{riser}) ($m \cdot s^{-1}$)	***No. of Occurences**	**Ensemble average of "time of flight" (sec)**	**Standard deviation of "time of flight" (sec)**	**Mean of solids velocity (from Equation 4.9) ($m \cdot s^{-1}$)**	**Standard deviation of solids velocity (based on Equation 4.9) ($m \cdot s^{-1}$)**	**Mean of solids velocity (from velocity P.D.F.) ($m \cdot s^{-1}$)**	**Standard deviation of solids velocity (from velocity P.D.F) ($m \cdot s^{-1}$)**	**Solids mass flux ($kg \cdot m^{-2} \cdot s^{-1}$)**	**Standard deviation solids mass flux ($kg \cdot m^{-2} \cdot s^{-1}$)**
Solids Inventory (*M* = 140 lbs), before the modification									
3.9	163	3.76	0.37	0.106	0.01	0.108	0.011	19.3	1.8
4.5	195	4.0	0.54	0.1	0.013	0.102	0.014	18.2	2.4
5.2	102	3.6	0.51	0.11	0.016	0.114	0.015	20.2	2.8
Solids Inventory (*M* = 190 lbs), after the modification									
3.2	257	2.2	0.19	0.182	0.016	0.187	0.02	30.7	1.1
3.9	280	1.95	0.13	0.205	0.01	0.206	0.013	33.7	0.53
4.5	167	1.78	0.12	0.225	0.02	0.227	0.008	36.8	1.3
Solids Inventory (*M* = 190 lbs), after the modification (reproduced results)									
3.2	1379	2.31	0.38	0.173	0.029	0.184	0.06	30.2	1.4
3.9	1023	2.02	0.21	0.198	0.021	0.201	0.02	32.9	1.2
4.5	1389	1.77	0.16	0.225	0.021	0.226	0.018	36.9	0.9
Solids Inventory (*M* = 140 lbs), after the modification									
3.2	1643	2.47	0.34	0.162	0.02	0.165	0.024	26.6	1.1
3.9	1137	2.19	0.2	0.183	0.016	0.184	0.02	30.2	0.8
4.5	2342	2.04	0.24	0.196	0.024	0.2	0.02	32.7	1.3

* Duration of data acquisition for all the operating conditions is not the same

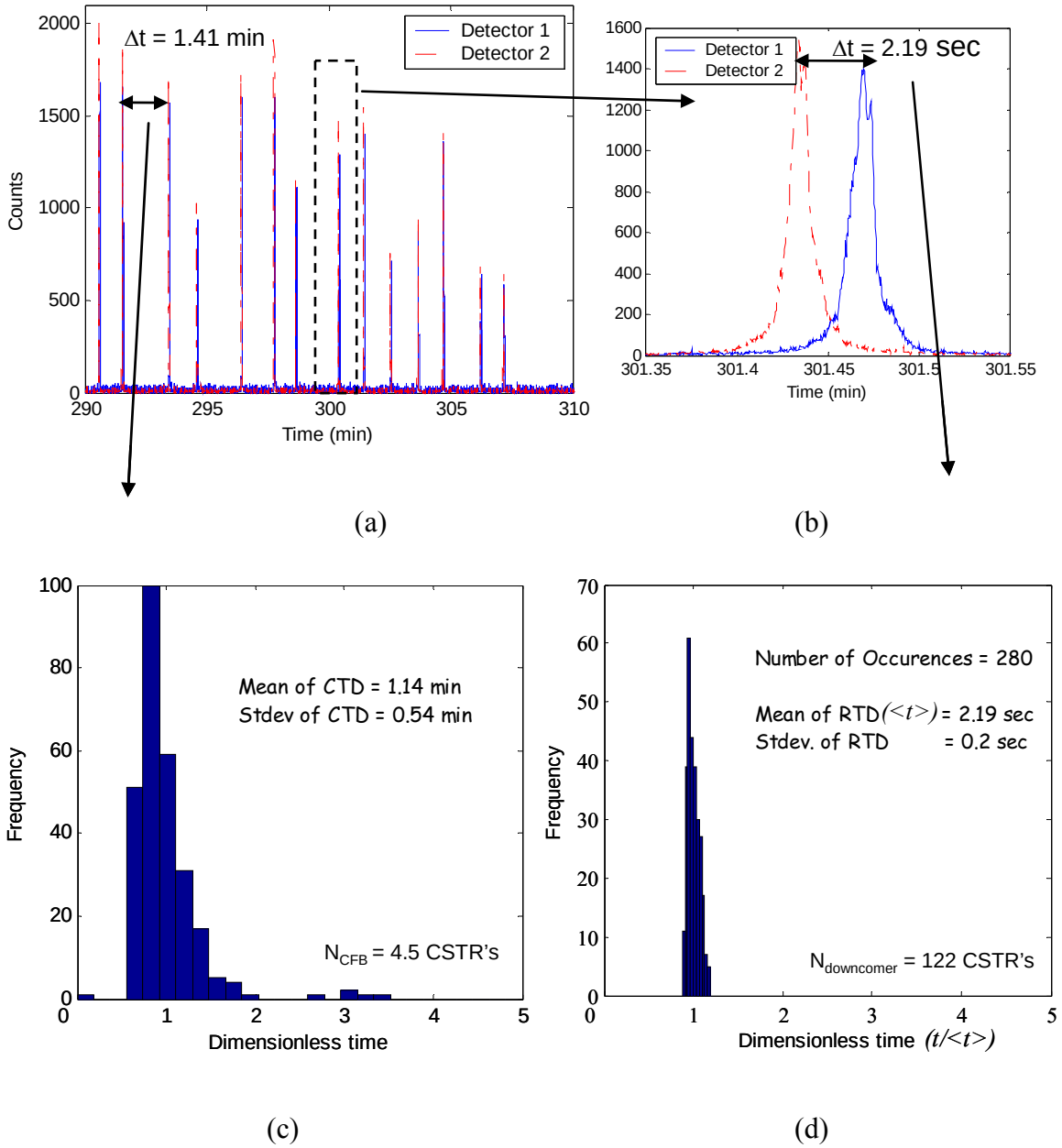

Figure 4-8: Data from "time of flight" measurements at U_g^{riser}= 3.9 m·s^{-1} after the introduction of secondary air. a) Part of the raw data from the two detectors; b) Zoomed in data with correlation coefficient ρ_{12} = 0.93; c) Circulation Time Distribution for the CFB loop; d) RTD between the two detectors (down-comer)

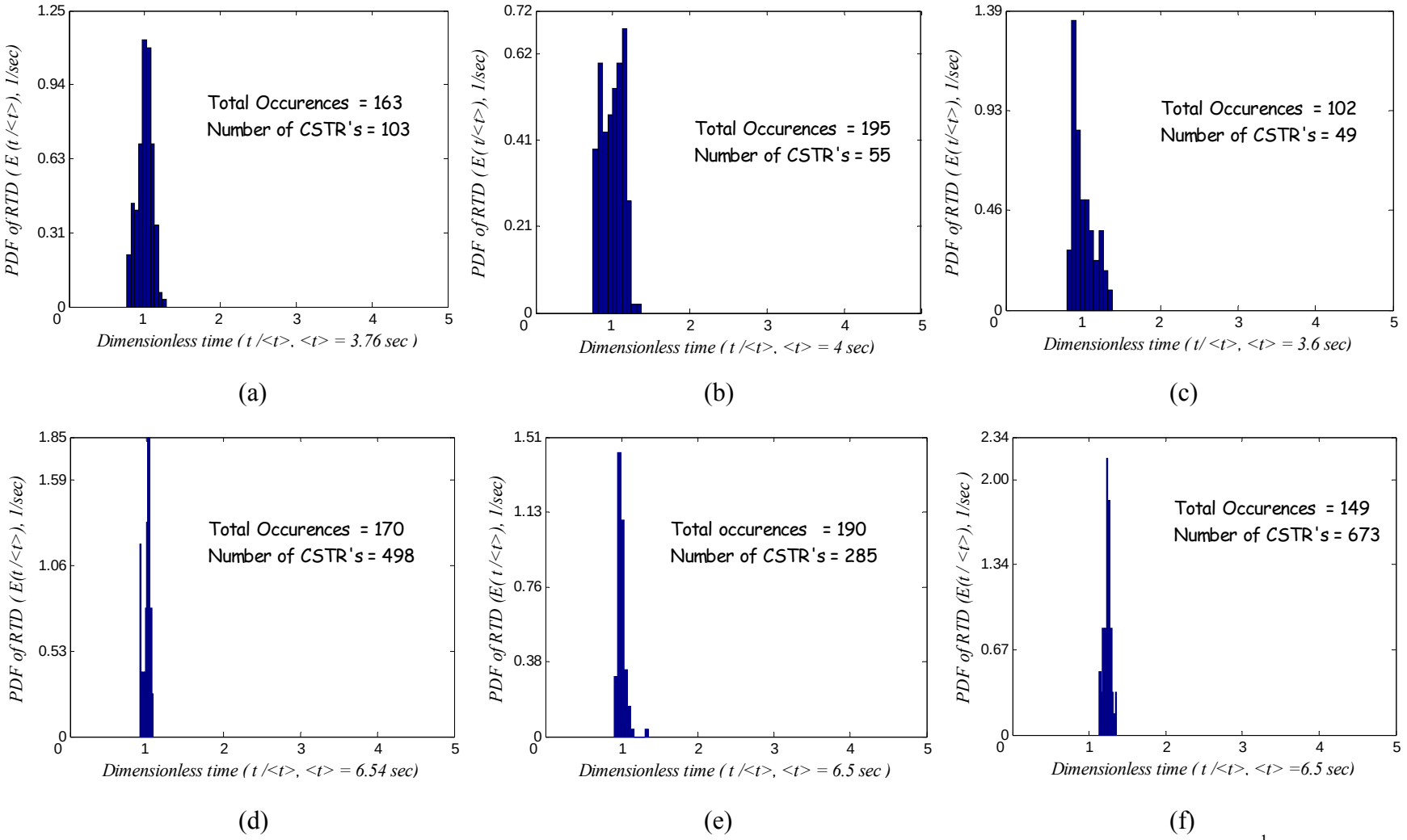

Figure 4-9: PDF of RTD (down-comer) plots for varying valve opening and superficial gas velocity as: a) 100%, 3.9 $m \cdot s^{-1}$; b)100%, 4.5 $m \cdot s^{-1}$; c) 100%, 5.2 $m \cdot s^{-1}$; d) 61%, 3.2 $m \cdot s^{-1}$; e) 61%, 3.9 $m \cdot s^{-1}$; f) 61%, 5.2 $m \cdot s^{-1}$. Note that abscissa is different for each plot.

Using a theoretical photon mass attenuation coefficient for glass beads, the least counts recorded at the farthest point in the plane of the detector is 710, which is comparatively larger than the smallest peak in the counts (550). This discrepancy is possibly due to the calculation method, where the counts were estimated from the mass attenuation coefficients and the maximum counts at the single photon energy (at the photopeak of ^{46}Sc). Also, a small difference from the theoretical mass attenuation coefficient in the actual material can affect this estimate adversely. However, this estimate of the least counts in the plane of the detector gives a counter check that the particle is actually traversing at different radial locations during each different passage. Hence, radiation from the tracer particle gets attenuated differently during each pass.

Besides, another reason for the variation of the peak in the counts might be due to the lateral movement of the particle. This movement may result in the detector recording the maximum counts at an instant later than the instant when the tracer particle first hits the plane of the detector. However, RTD plots in Figure 4-8d and Figure 4-9 show that the flow in the down-comer is predominantly convective with a large Peclet number. This can be verified by the small variance of the solids RTD shown in Table 4-2. The tanks-in-series model was used to determine the flow pattern in the down-comer, and the number of CSTR's obtained from the model (refer to Figure 4-9) was high enough (*O (100)*) to assume that the flow is close to a plug flow condition for all the experimental runs. This assumption is possible if the down-comer is packed tightly with moving solids, which restricts the lateral movement of the particles. That indeed is the case, as verified previously by the line densitometry experiments.

In all of the above calculations, the ensemble average of the tracer velocity is obtained from the mean of the RTD in the down-comer section. Taking a different point of view, each pass of the tracer through the down-comer section will define a velocity using Equation (4-9) where, "time of flight" t can be substituted for mean time $\langle t \rangle$. Hence, a distribution of velocities for all the N passes of the tracer can be developed, and so the mean and the variance for the velocity PDF can be obtained. To compare the mean solids velocity obtained from these two different approaches, consider the discretized form of Equation (4-9).

$$\langle v_s \rangle_t = \frac{\Delta H}{\langle t \rangle} = \frac{\Delta H \cdot \sum_{i=1}^{P} n_i}{\sum_{i=1}^{P} n_i \cdot t_i} \tag{4-12}$$

Similarly, the mean velocity can be obtained using a discretized form of the velocity PDF as:

$$\langle v_s \rangle_\nu = \int f(\nu) \cdot \nu \cdot d\nu = \frac{\sum_{i=1}^{P} n_i \cdot \nu_i}{\sum_{i=1}^{P} n_i} = \frac{\Delta H \cdot \sum_{i=1}^{P} \frac{n_i}{t_i}}{\sum_{i=1}^{P} n_i} \tag{4-13}$$

where n_i is the occurrences around the interval t_i, P is the number of discretized intervals, and f is the PDF of solids velocity.

Certainly, the mean solids velocities obtained from Equations (4-12) and (4-13) will not be equal. To determine which of the two mean velocities is larger, consider a series of residence times $\{t_i\}$. The mean velocity from Equation (4-12) will be ΔH times the inverse of the arithmetic mean (A.M.) of the series, and the mean velocity from Equation (4-13) will be ΔH times the inverse of the harmonic mean (H.M.) of the series. Since for a positive series A.M. $\geq$ H.M., the mean velocity obtained from Equation (4-13) will be larger (in fact, an upper bound) than the mean velocity from Equation (4-12). This can indeed be observed in Table 4-2. The equality sign holds true only when all the values of the series $\{ t_i \}$ are equal, in other words, in a perfect plug flow condition. Also, Figure 4-10 shows the plot for solids velocity PDF and compares the mean and variance estimates obtained from Equations (4-12) and (4-13). It can be observed that the differences in mean and variance are very small, indicating nearly plug flow condition in the down-comer. The maximum difference in the ensemble average of the tracer velocities obtained from the velocity PDF and that from the mean of the RTD is 0.6% (refer to Table 4-2). The difference in the mean of the solids flux measurements is 1%, whereas the difference in their standard deviations is 6%. Hence, either of the above methods for calculation can be employed, if a nearly plug flow condition can be verified.

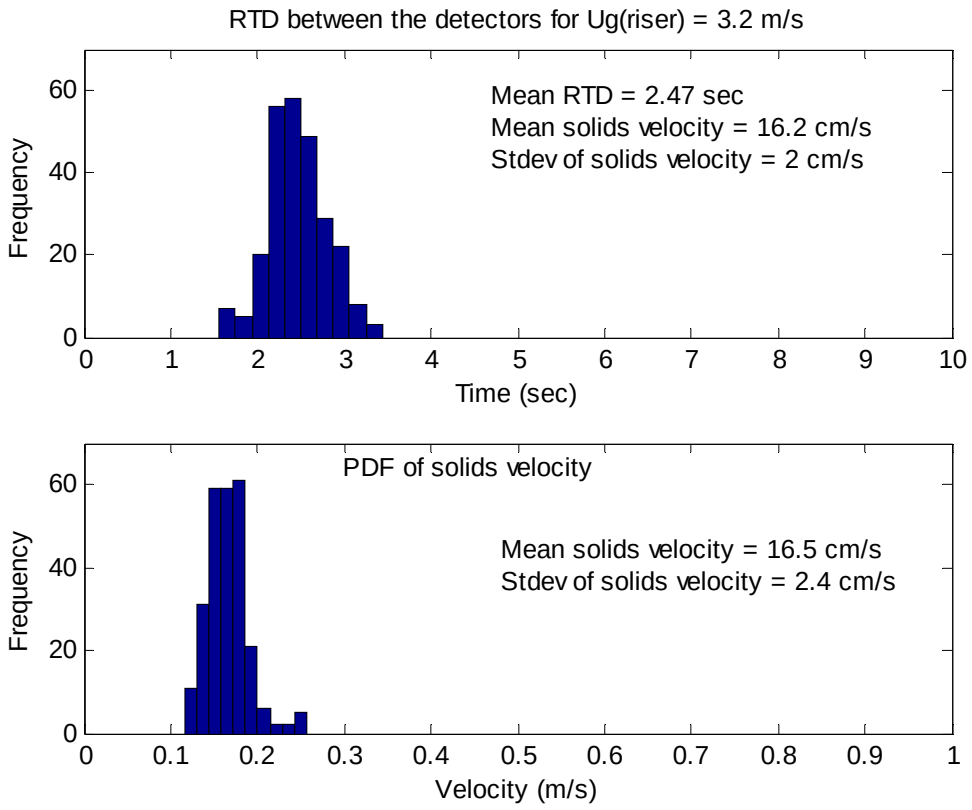

Figure 4-10: Comparison of the mean and variance in solids velocity from two different calculation methods for the condition of U_g^{riser} = 3.2 m·s^{-1} after the modification.

Figure 4-11 displays the solids flux as a function of superficial gas velocity. As shown in Figure 4-11, the effect of superficial gas velocity on overall solids flux was insignificant (within the error limits) for the conditions prior to the modification of introducing secondary air (denoted as "before" in Figure 4-11). In addition, as Figure 4-8c and 4-7d show, the total recirculation time of the tracer or the Cycle Time in the system was also found to be constant (within the error limits). This finding confirms that the down-comer (2 in. column) is choked and thus represents the rate limiting section in the loop. To identify those operating conditions where the solids flux variation is dependent on superficial gas velocity, similar experiments were performed by varying the solids valve opening. As shown in Figure 4-11, analogous invariance of solids flux with the gas superficial velocity was obtained. However, subsequent to the introduction of the secondary air in the down-comer, both the solids mass flux values and trend seem to be

increasing. This significant change is because the secondary air fluidizes the choked down-comer, which results in the increase of the solids velocity and decrease in the solids holdup values. The relative increase in the solids velocity seems to be high enough to counter the decrease in the solids holdup and resulted in increased solids mass flux values. Thus with the introduction of secondary air in the down-comer, the solids mass flux was seen to be increasing with increasing gas superficial velocity, though this increase seems to be decreasing. A calibration curve for solids mass flux with gas superficial velocity was established

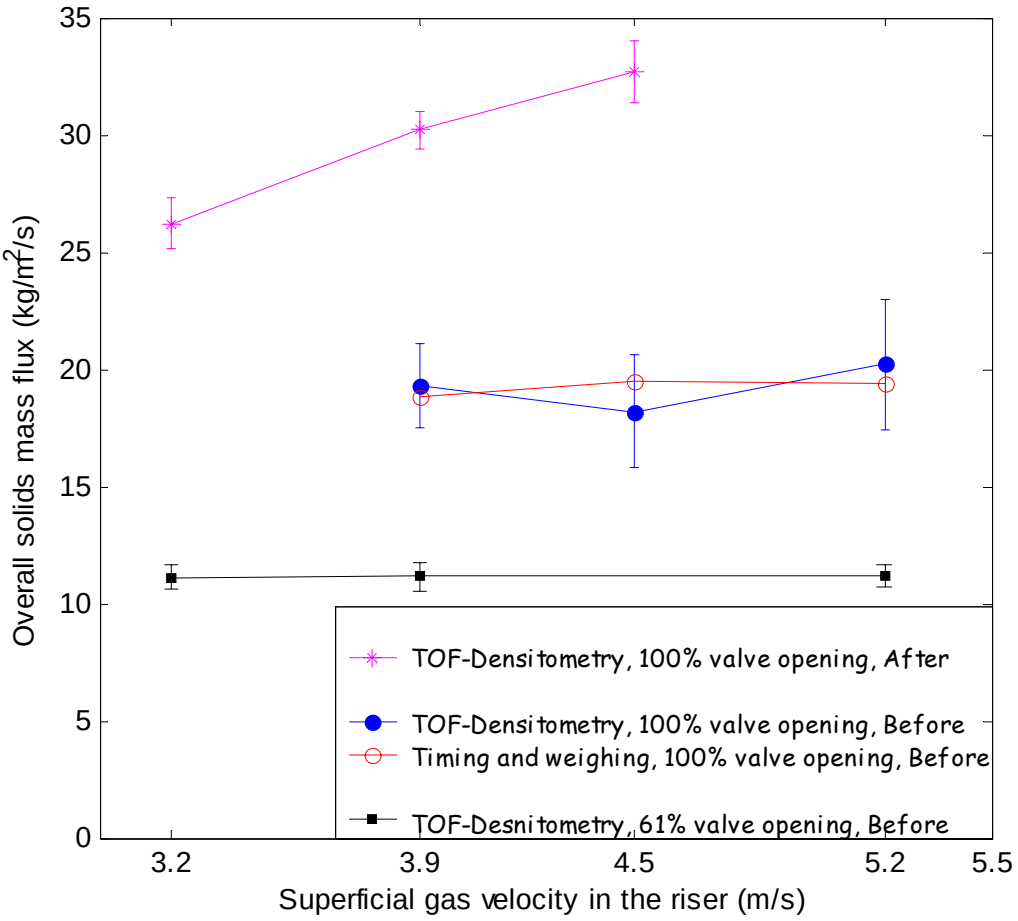

Figure 4-11: Calibration curve for overall solids mass flux variation with gas superficial velocity. Before denotes the runs without introduction of secondary air. After denotes runs with secondary air. "TOF" – time-of-flight.

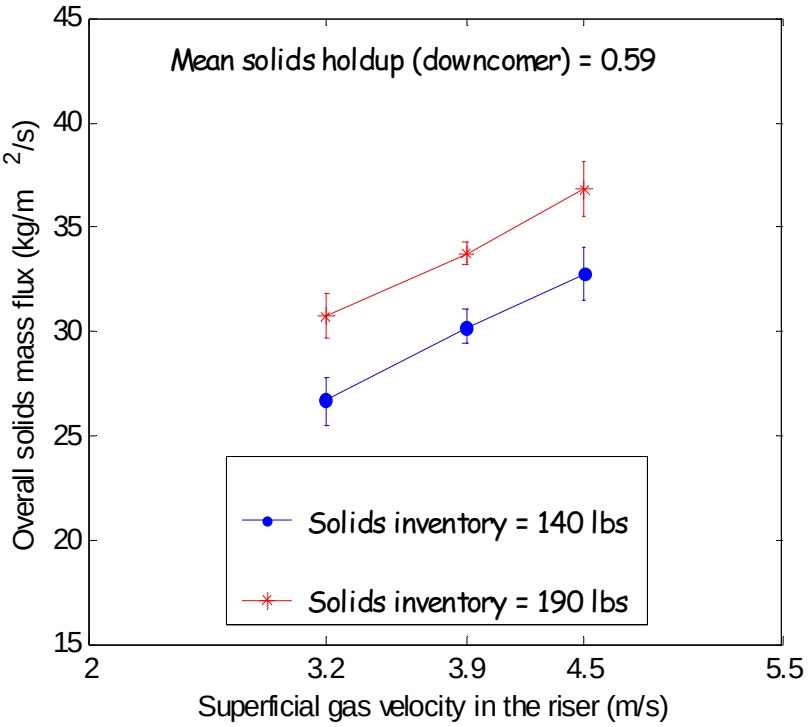

Figure 4-12: Calibration curve for overall solids mass flux variation with gas superficial velocity (reproduced).

To check the reproducibility of the data, both densitometry and "time-of-flight" experiments were repeated. Time-of-flight experiments were performed with another ^{46}Sc tracer particle for a longer duration of data acquisition, which resulted in a higher number of occurrences (refer to Table 4-2). Figure 4.12 shows the calibration curves for overall solids mass flux with gas superficial velocity obtained at two different solids inventory. It can be seen from Table 4-2 that the reproducibility of the overall solids mass flux values is within the error limits. A plot of overall solids mass flux variation with total occurrences showed that the mass flux values reached within 95% confidence intervals by 100 occurrences. Hence, overall mass flux profiles reported are occurrence independent.

Using the overall solids flow measurement procedure described in the previous section, a time versus weight curve was derived and is shown in Figure 4-13. The curve was determined by timing and weighing the solids collected. A linear fit to the data was used to interpolate for the solids mass flux from the experiments. Figure 4-11 shows the

solids mass flux calculated as a function of the superficial gas velocity in the riser for a full valve opening, prior to the modification. It shows no effect of the gas velocity on mass flux as determined by "time of flight" and densitometry measurements

This overall solids flow measurement method probably underestimates the solids mass flux values. The time versus weight curve was obtained with the system turned off (no air introduction in the riser) and the solids would therefore take longer to empty the down-comer than in a system with the air turned on. The time versus weight curve for the actual circulating system would then be steeper, which would give higher solids mass fluxes. It should also be noted that the time versus weight curve should ideally pass through zero, but instead has a constant around 1 kg, which can be attributed to human error in synchronizing actions. With an error of 4%, the results from this procedure are lower (19 $kg \cdot m^{-2} \cdot s^{-1}$) than the values obtained from the "time of flight" and densitometry experiments. However, they confirm that the down-comer was restricting the flow through the loop for the conditions before the modification.

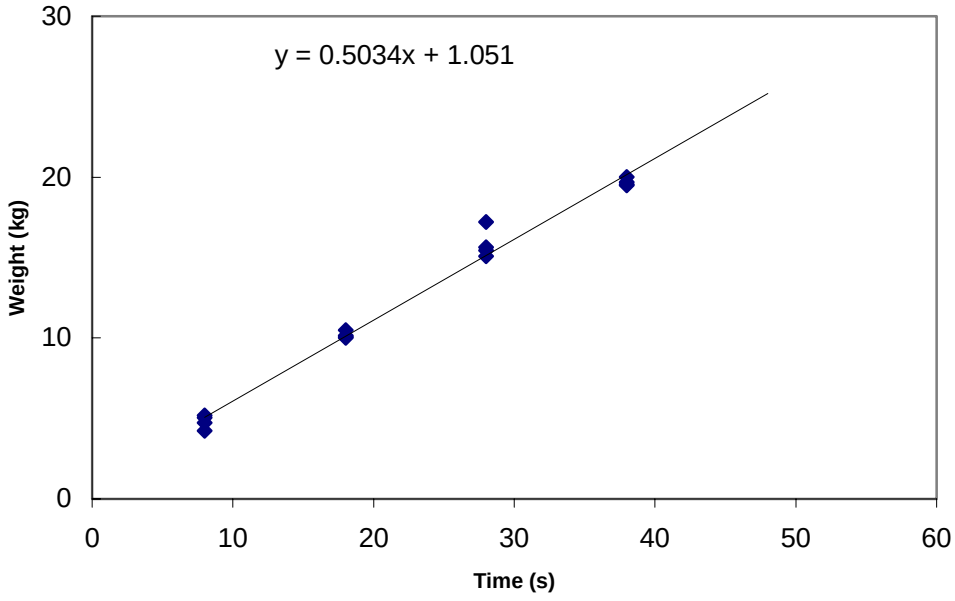

Figure 4-13: Time versus weight of solids fit for the "timing and weighing" procedure.

4.4 Flow Regimes

Once the operating parameters such as superficial gas velocity (U_g^{riser}) and overall solids mass flux (G_s) have been found, one can determine the flow regime of operation. A circulating fluidized bed is generally operated between the choking velocities (Bi *et al.*, 1994) and with gas velocity close to the minimum pressure gradient point, V_{mp} (discussed later). Based on the idealized flow regime map (with no equipment related restrictions) of Bi and Grace (1995), it can be considered to cover from dense phase flow, to fast fluidization and to pneumatic transport. Figure 4-14 shows modified maps for typical circulating fluidized beds and transport riser operation. In this map, the classical choking velocity is obtained from the correlation by Yousfi and Gau (1974) given by:

$$\frac{V_{CC}}{\sqrt{gd_p}} = 32\,\mathrm{Re}_t^{-0.06}\left(\frac{G_s}{\rho_G}V_{CC}\right)^{0.28} \tag{4-14}$$

While the minimum transport velocity, V_{CA}, also called type A choking velocity and defined as the point where the uniform suspension collapses, is obtained from the correlation of Bi and Fan (1991), given by:

$$\frac{V_{CA}}{\sqrt{gd_p}} = 21.6Ar^{0.105}\left(\frac{G_s}{\rho_G}V_{CA}\right)^{0.542} \tag{4-15}$$

The minimum pressure drop point denotes the transition from homogeneous dilute flow to core-annular dilute flow (Leung, 1980). Accurate quantitative determination of this transition is difficult and as a first approximation Bi and Fan (1991) provides a correlation to estimate this transition, given by:

$$V_{mp} = 10.1\left(gd_p\right)^{0.347}\left(\frac{G_s}{\rho_G}\right)^{0.31}\left(\frac{d_p}{D}\right)^{-0.139}Ar^{-0.021} \tag{4-16}$$

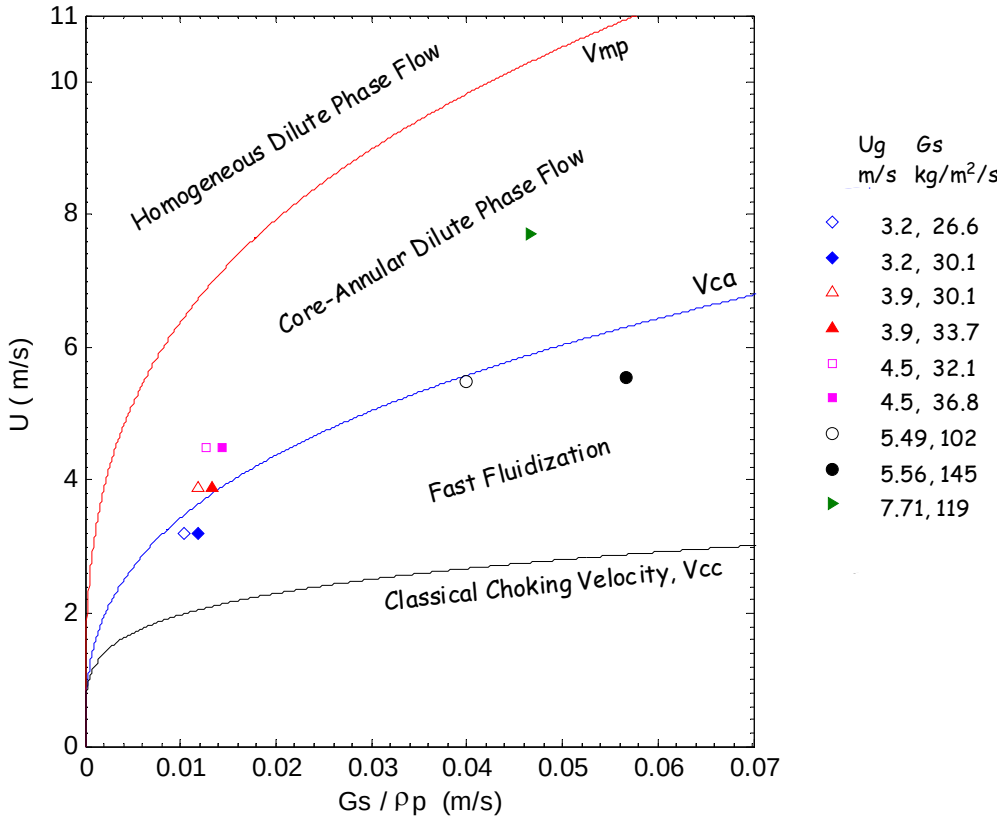

Figure 4-14: Practical flow regime map for gas-solid upflow transport for Group B glass beads, d_p = 150 μm, ρ_p = 2550 kg·m^{-2}·s^{-1}, D = 0.152 m. Symbols indicate the flow conditions in this work

Table 4-3 summarizes key characteristics of different high velocity fluidization regimes. In the fast fluidization regime, axial solids segregation exists, resulting in a dense lower region and dilute upper region. Particle streamers form close to the riser wall, leading to a core-annulus structure in the upper dilute region. Net solids flow at the riser wall is downward in the upper dilute region could be either downward or upward in the lower dense region (Bi and Grace, 1999). While in the heterogeneous dilute phase flow, average solids flux in the annular region is downward with little axial segregation of particles. In this regime too, particles streamers form close to riser wall leading to a core-annulus structure (Bi and Grace, 1999). In contrast, homogeneous dilute flow is characterized by dispersed solids flowing with little particle-particle interaction. Also, radial and axial segregation is small in this regime (Bi and Grace, 1999).

Table 4-3: Key characteristics of the flow regimes (from Bi and Grace, 1995, 1999)

Characteristic	Fast Fluidization	Core-annular dilute transport	Homogeneous dilute transport
Gas velocity range	$U_{se} < U < V_{CA}$	$V_{CA} < U < V_{mp}$	$U > V_{mp}$
Solids flux range	$G_s > G_{s,\,CA}$	$G_s < G_{s,\,CA}$	$G_s << G_{s,\,CA}$
Overall voidage	$\varepsilon = 0.85 - 0.97$	$\varepsilon = 0.97 - 0.99$	$\varepsilon > 0.99$
Axial particle gradients	High	Low	None
Radial particle gradients	High	High	Low
Gas-solids relative velocity	High	Low	$\approx U_t$
Particle backmixing	High	Low	None

$G_{s,\,CA}$ – saturation carrying capacity ($kg \cdot m^{-2} \cdot s^{-1}$)

For flow conditions under investigation throughout this work, flow regimes were identified and are indicated in Figure 4-14. It can be observed that in the fast fluidization regime, there are two flow conditions at low flux and two at high flux. Also, there are four low flux conditions in the core-annular dilute phase transport and one at high flux condition. One should note that none of the flow conditions are nowhere near to the dense phase flow and hence its characteristics are not discussed here. Hence, the subsequent chapters will deal with the solids mixing, velocity fields and holdup profiles under fast fluidization (FF) and dilute phase transport (DPT) regimes.

4.5 Summary

Following are the key conclusions in this chapter:

i. The use of single radioactive particle tracking and densitometry, both of which are non-invasive and in-situ techniques, was demonstrated to give an accurate measurement of the overall solids mass flux in a gas-solid CFB.

ii. Quantitative and qualitative improvements in densitometry, and "time of flight" experiments, as well as in data processing, were recommended and applied.

iii. It was also confirmed that the flow in the down-comer (2" column) is predominantly plug flow.

iv. Using a simple timing and weighing method, solids flux values were underestimated and compared to values obtained from the “time of flight” and densitometry method. However, choking in the down-comer, prior to the introduction of secondary air was confirmed.

v. A calibration curve for overall solids mass flux as a function of the superficial gas velocity in the riser was established.

vi. The overall solids mass flux data reported was proved to be reproducible and occurrence independent.

vii. Flow conditions under investigation were identified to be in fast-fluidization (FF) and in core-annular dilute phase transport (DPT) regimes

Chapter 5

Solids Residence Time Distribution Measurements

5.0 Scope

In this chapter, the quantification of solids residence time distributions (RTD) in the riser using a single radioactive particle is discussed. The wealth of solids mixing information obtained is described. Solids RTD measurements were obtained at high (>100 $kg \cdot m^{-2} \cdot s^{-1}$) and low solids mass fluxes (< 40 $kg \cdot m^{-2} \cdot s^{-1}$) and in two different flow regimes – a) Fast Fluidization (FF), and b) Dilute Phase Transport (DPT).

Solids in CFB risers exhibit local backflow and recirculation which renders a riser to be a system with 'open boundaries' (Naumann, 1981) since the particles can cross both the inlet and exit plane in both vertical directions by convection as well as by dispersion. Hence, the measurement of the concentration-time response to an impulse injection of bundle of tracer particles, even at two elevations, cannot determine the true RTD of solids uniquely (Shinnar *et al.*, 1972; Naumann and Buffham, 1983). The problem is that one cannot distinguish whether the particles being recorded at that moment are entering or leaving the system at the inlet plane and exit plane. Hence, the evaluation of solids RTD in risers from conventional tracer responses is not possible. By invoking ergodicity, a single radioactive particle in the CFB loop is tracked during its multiple visits to the riser. Now the time of residence of that particle between the inlet and exit plane can be uniquely defined and accurate solids RTDs obtained. Such individual radioactive particle tracking provides additional information on the solids flow pattern in the riser that is discussed in this chapter.

5.1 Introduction

In operation and design of Circulating Fluidized Beds (CFB), it is important to know the residence time distribution (RTD) of solids in various segments of the CFB loop and the flow pattern and mixing of solids in the riser. Tracer techniques were employed to determine the solids RTD, and many methods were used in the literature (Avidan, 1980; Bader *et al.*, 1988; Kojima *et al.*, 1989; Ambler *et al.*, 1990; Patience *et al.*, 1990; Wei *et al.* 1998; Harris *et al.*, 2002). For further details refer to Table 2-4.

All tracer impulse response based measurements of the solids RTD have limitations, which were discussed in Section 2.1.2. In systems like risers and fluidized beds where strong dispersion fluxes are present, finding a true RTD with its proper mean and variance is a non-trivial matter (Naumann and Buffham, 1983). The measured impulse responses are not representative of the RTD probability density function (PDF), which requires that the system be "closed" at injection and measurement planes (i.e. at those planes convective flow should dominate). Moreover, in systems with total recirculation, like in CFBs, it is well known that the PDF of the first passage times in the riser cannot be found uniquely even from impulse response measurements at a few locations (Shinnar *et al*., 1972).

Various investigators often matched simple models to the observed impulse solid tracer responses and evaluated axial dispersion coefficients as measures of solids mixing. The experimental conditions, however, often did not satisfy the assumptions of the models and solids circulation rates were not known with certainty. This casts doubts on the evaluated axial dispersion coefficients. Avidan (1980), Patience *et al*. (1990), and Rhodes *et al.* (1991) studied the effects of operating conditions on axial solids mixing in risers. Avidan (1980) observed a maximum in the effective axial solids dispersion coefficient as a function of gas superficial velocity and solids circulation rate (i.e. solids flux in the riser) and attributed this maximum to transition from turbulent to fast fluidization (FF) regime. Similarly, Bi (2004) reports a minimum in the axial Peclet number corresponding to the transition from FF to dense suspension up-flow regime. At higher gas velocities, axial solids dispersion decreased, indicating a reduction in the internal solids recirculation in the risers. Experimental results and a correlation by

Rhodes *et al.* (1991) indicate that the axial solids dispersion decreases with increasing riser diameter, supporting the notion that the annular region is in fact a wall effect. They also showed that the axial solids dispersion decreased with an increase in the solids mass flux. Contrary to this result, Patience *et al.* (1990) found that the solids axial dispersion increased with increased solids mass flux. Ambler *et al.* (1990) found that the internal solids recirculation is greater for larger particles, while the breakthrough times, the time at which solids tracer particles are first detected at the exit, are shorter.

Numerical values of the axial dispersion coefficient D_z in risers often include the bottom zone of the denser fluidized bed. The large range of D_z values recorded (10^{-4} to 31 $m^2 \cdot s^{-1}$) reflects the broad range of solid fluxes used but is also due to the fact that different investigations included different mixing regions to a different extent and used differently executed experiments and models. Experimental conditions and riser diameters were also varied. Hence, the axial dispersion coefficient, $D_{z,}$ values often represent the solids mixing averaged over the bottom zone, transition zone and the dilute zone and are influenced by the proportions of the different regions included in the measurements. The larger values of D_z ranging from 0.1 to 31 $m^2 \cdot s^{-1}$, were thought to be due to the enhanced mixing in the bottom denser fluidized zone.

In this chapter we show that by tracking a single radioactive particle, which is identical in size and density to the solids in the system, one can obtain solids RTDs and additional detailed information on the solids flow pattern in the riser.

5.2 Measurement Technique

Three shielded (collimated) detectors, used for tracking the particle (as indicated in Figure 5-1a), were placed along the CFB loop:

i) at the base of the riser, at 5" above the solids entry zone into riser, and 15" above the air entry,

ii) at the riser exit, 3" below the disengagement section,

iii) at the start of the down-comer, 10" below the hopper section.

The underlying conjecture in this technique that monitors the residence time of a single particle in the system of interest, e.g. in the riser, is the assumption of ergodicity.

Ergodicity is defined in regards to a statistical parameter as relating to a process in which every sizable sample is equally representative of the whole. Hence, by tracking a single radioactive tracer during its multiple visits to the riser in the CFB loop is equivalent to tracking "all" the solids in the riser. From the detector responses, the time spent by the tracer between the cross-sectional planes of the detectors at the riser inlet and riser exit plane can be found and represents the residence times in the riser. Similarly using the other pairs of detectors the residence time in the disengagement and hopper, and in the down-comer can be obtained. Thus, in this method, which is non-invasive, the problem of introducing and detecting the numerous 'tagged' tracer particles is eliminated, and no artificial experimental boundary conditions need to be imposed. In fact, true "open-open" boundaries of the system remain undisturbed. Since only a single tracer particle is being tracked, one obtains the precise "time of passage" of the tracer at the cross sectional planes of the detectors.

A complete and rigorous treatment of "open-open" systems like risers would have to consider all different situations. One kind of openness, where reverse flow is caused by diffusion or a diffusion-like mechanism is considered here. Particles that are in the system may temporarily leave via reverse movement through the inlet plane. However, such particles must finally return to the system since their backward movement is only a random process superimposed on a net positive flow. Similarly, the particles that have left the system at the exit boundary may temporarily return via reverse movement but will eventually leave. The net positive flow will cause all particles that have once entered the system to leave eventually, to return only in their next passage through the CFB loop. The time between the first entry of a particle at the inlet plane and its final exit at the exit plane is some total time, θ_t. This total time will often be different from the residence time t, since time spent on temporary excursions outside the system boundaries contributes to θ_t, but not to t. It turns out that transient response techniques, typically represented by the convolution Equation (5-1), can at best measure the distribution of θ_t (discussed later).

$$C_{out}(\theta) = \int_{-\infty}^{\theta} C_{in}(t-\theta)\cdot g(t)dt \qquad (5\text{-}1)$$

More subtle ways are required to obtain the distribution of *t*. Hence, the distribution obtained from the convolution Equation (5-1) in 'open-open' systems such as risers does not represent the residence time distribution, but would be a distribution of some other travel time.

In systems such as CFB risers, where backflow is significant, especially at the inlet (bottom) of the riser, the tracer particle might pass back and forth across the plane of the detector at the inlet many times before it flows through the riser to be detected by the detector above the riser at the exit plane. Figure 5-1a shows the schematic of a typical trajectory of the tracer particle in the riser. Hence, we can expect to have many peaks in the detector response as the tracer particle passes the detector plane. This is shown in Figure 5-1b, which displays a part of the raw data from the detectors located at the riser inlet, exit and top (entry) of the down-comer. The time elapsed between spikes recorded at different detectors allows us to determine whether the tracer passed the inlet detector several times entering and exiting the system at the inlet, or whether it passed the detector at the riser exit after passing by the inlet detector. The different magnitude of the spikes detected (see Figure 5-1b) indicates that the tracer crossed the detector plane at different distances from the detector face. In order to ensure that the detectors view only the cross-sectional plane of interest, they were heavily shielded by wrapping the column above and below the cross-section with a lead sheet. Therefore, by counting in pairs, the entry and exit of the tracer into the system (region of the riser between the cross-sectional planes viewed by the detectors), we can precisely calculate the time that the tracer particle spent inside the system and outside the system.

In the typical trajectory shown in Figure 5-1a, the tracer enters the system at point A, corresponding to spike 1 in Figure 5-1b, then exits at point B at the same plane, corresponding to spike 2, and re-enters the system again at C, corresponding to spike 3, and then leaves the riser at the time indicated by spike D at the exit detector. Hence, the time spent by the tracer between spikes B and C should not be counted as residence time in the riser and only the time spent between A and B and between C and D is taken as the residence time. The same approach is applied near the exit of the riser at the exit cross-sectional plane. In this way, we can accurately estimate the RTD of the solids in the riser.

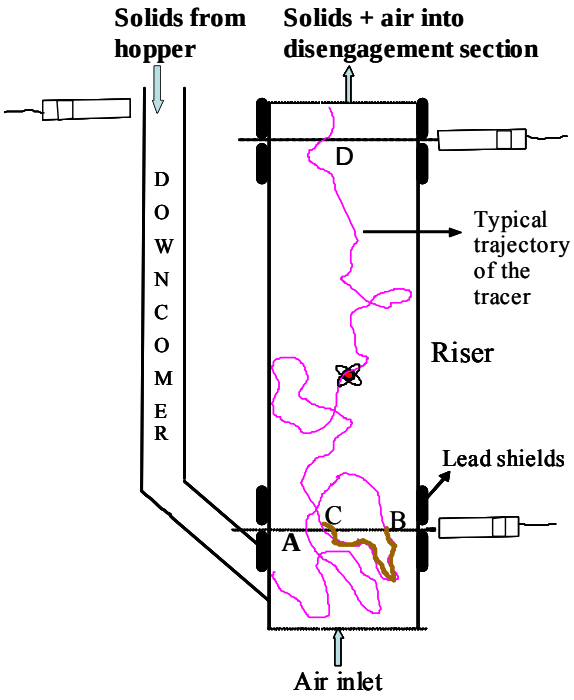

(a)

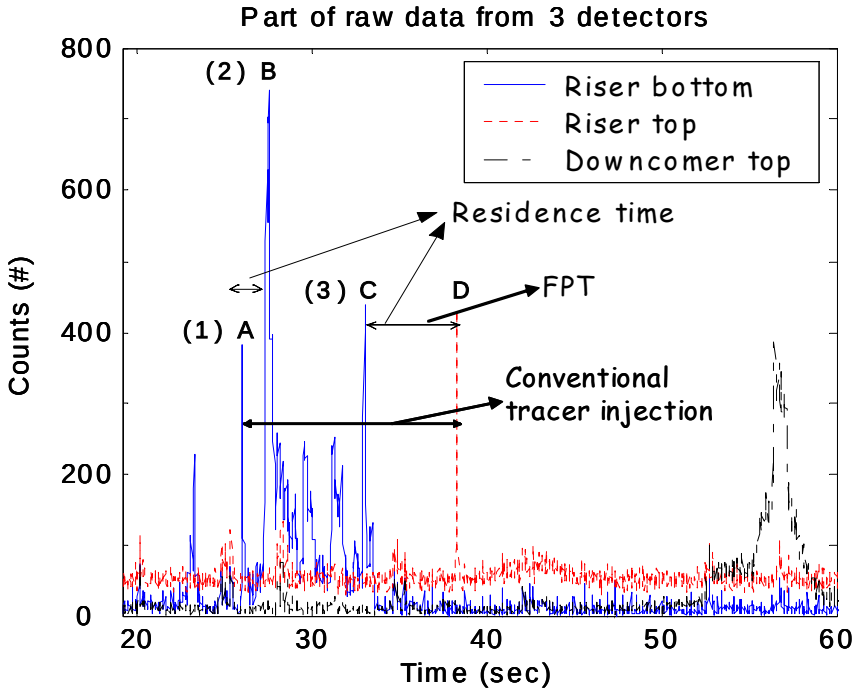

(b)

Figure 5-1: a) Schematic of the three detectors along the CFB loop with a typical trajectory; b) Part of the raw data obtained from the three detectors. A, B, C and D correspond to detection events on the typical trajectories shown in (a).

Single particle tracking in systems with high backmixing, like in the gas-solid riser with "open-open" boundaries allows us to interpret the detector responses in different ways. For example, two different distributions are readily obtained. One is the distribution of total residence times (RTD) in the system (e.g. time between A and B, and C and D, Figure 5-1). The other, the distribution of sojourn times for the first passage of particles that go directly from the inlet to the exit plane, is named first passage time distribution (FPTD). In other words, true solids RTD results by allowing for "open-open" boundaries of the system, while solids FPTD is obtained by imposing "closed-closed" boundaries. Now, if one injects a bunch of tracer particles at the bottom and detects them at the top, the distribution obtained will neither represent the RTD nor FPTD, but will be a distribution of some other solids travel time. Indeed, this can be readily observed in Figure 5-1b. In the typical trajectory shown in Figure 5-1a, the time spent by the tracer between C and D will represent the first passage time, while that between A and D will represent total solids travel time. That total travel time is not reflected in the conventionally measured impulse responses for two reasons. The input can never be a perfect delta function due to the backflow of solids at the entry plane and subsequent re-entry. The measured response at the exit records particles that are leaving and slipping temporarily back into the system. The measured exit concentration-time curve is thus not a convolution of the inlet curve with the E- curve or impulse response of the system. Therefore, distributions of first passage time and that from a conventional injection-detection method will be in error in estimates of mean residence times as well as of the variance of the PDF curve which is related to axial dispersion.

5.3 Results and Discussion

Following the procedure discussed earlier to obtain residence times from the detector responses, the solids RTDs were obtained at various operating conditions. Figure 5-2a shows the PDF of the residence times of the tracer inside the riser section of the CFB loop at a superficial gas velocity (U_g^{riser}) of 3.2 $m \cdot s^{-1}$ and solids mass flux (G_s) of 26.6 $kg \cdot m^{-2} \cdot s^{-1}$, which corresponds to the FF regime. The mean (τ) and standard deviation of solids the RTD are 42.8 sec and 36.2 sec, respectively.

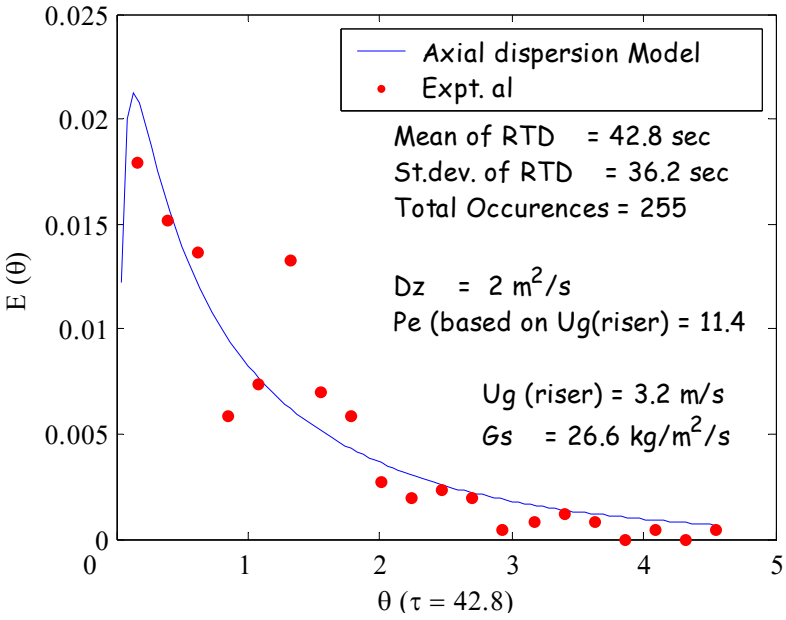

(a)

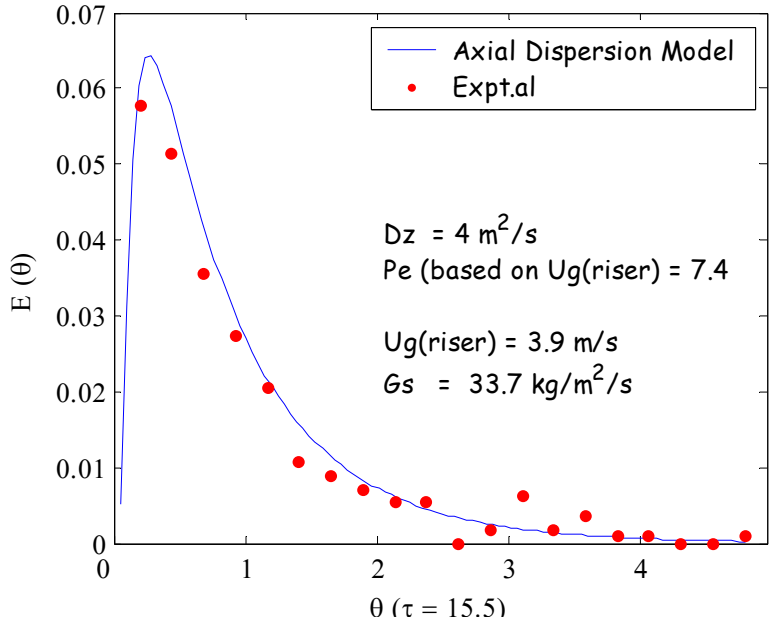

(b)

Figure 5-2: Experimental and simulated solids RTD in the riser at: a) U_g^{riser} = 3.2 m·s^{-1} and G_s = 26.6 kg·m^{-2}·s^{-1} (FF regime); b) U_g^{riser} = 3.9 m·s^{-1} and G_s = 33.7 kg·m^{-2}·s^{-1} (DPT regime).

The occurrence of the second peak in the RTD curve is suggested at 1.2 τ. The PDF of the RTD curve has a long tail, which is a typical characteristic of a system with internal recirculation. By ignoring the possibility of the second peak and by fitting the data with a simple axial dispersion model (ADM), the axial dispersion coefficient, D_z, was found to be 2 $m^2 \cdot s^{-1}$. Here, the dispersion coefficient was obtained by regression when fitting the ADM model in time domain to the E-curve. The dimensionless Peclet number (Pe) for the solids, based on superficial gas velocity in the riser (U_g) is 11.4. This value is reported as this definition of solids axial Peclet number has been used customarily in the literature. This was done for convenience since gas superficial velocity is a directly measurable quantity. An estimate of the solids superficial velocity can be obtained by dividing the length of riser with the mean residence time. Other possibilities of estimating an average solids superficial velocity are discussed later. The Peclet number (Pe_s), based on solids superficial velocity, obtained from τ, was found to be 0.6. Clearly, ADM model can never predict a second peak in the RTD curve. In addition the low value of Pe_s raises doubts about the use of ADM.

Figure 5-2b shows a comparison of the experimental PDF of the RTD and a fitted ADM model at a superficial gas velocity in the riser of 3.9 $m \cdot s^{-1}$ and solids mass flux of 33.7 $kg \cdot m^{-2} \cdot s^{-1}$. These operating conditions correspond to the dilute phase transport (DPT) regime. At this condition, the total number of tracer particle visits was 277 which is equivalent to introducing 277 tagged tracer particles. The second peak cannot be seen, although the E-curve has a long tail. The dispersion coefficient (D_z) was found to be 4 $m^2 \cdot s^{-1}$ and the Peclet numbers, based on the gas superficial velocity and on the solids superficial velocity in the riser, are 7.4 and 0.8, respectively. The ADM seems to fit the data well.

The bimodal RTD as indicated in Figure 5-2a in FF regime was also reported by several other researchers (Helmrich *et al.*, 1986; Kojima *et al.*, 1989; Ambler *et al.*, 1990; Lin *et al.*, 1999). The bimodal PDF of the solids RTD indicates that two flow phenomena occur in the riser. It is assumed that the first peak corresponds to the fraction of the solids which passes rapidly through the riser, while the second peak represents the bulk of the solids delayed by backmixing and internal recirculation within the riser. For comparison, typical results reported by Ambler *et al.* (1990) and Kojima *et al.* (1989) are illustrated in

Figure 5-3. Both of the above studies have used the classical injection-detection methods for obtaining the solids RTD curves shown in Figure 5-3. While Ambler *et al.* (1990) used a bunch of radioactive tracer particles and characterized the whole riser including the bottom zone, Kojima *et al.* (1989) used fluorescent dyed particles and characterized only the upper dilute zone of the riser. Also, Kojima *et al.* (1989) sampled only at the centerline using an optical probe, while Ambler *et al*. (1990) sampled at the cross-section with a NaI detector. Despite the fact that both the reported results are confounded by problems as discussed for the conventional injection-detection methods, bimodality in RTDs can be clearly observed.

Bimodal PDFs of solids RTDs have been reported in the literature for a number of reactor configurations where some bypassing occurs (Levenspiel, 1999). However, in backmixed systems like the riser, it is physically unacceptable to have the second peak higher than the first as reported by Ambler *et al.* (1990). This discrepancy is attributed to the insufficient time resolution of the measurement technique. Although the experimental conditions reported by the above researchers do not match with those shown in Figure 5-2a, their conditions do seem to be in the FF regime. This result suggests that bimodal RTD is a characteristic of the FF regime.

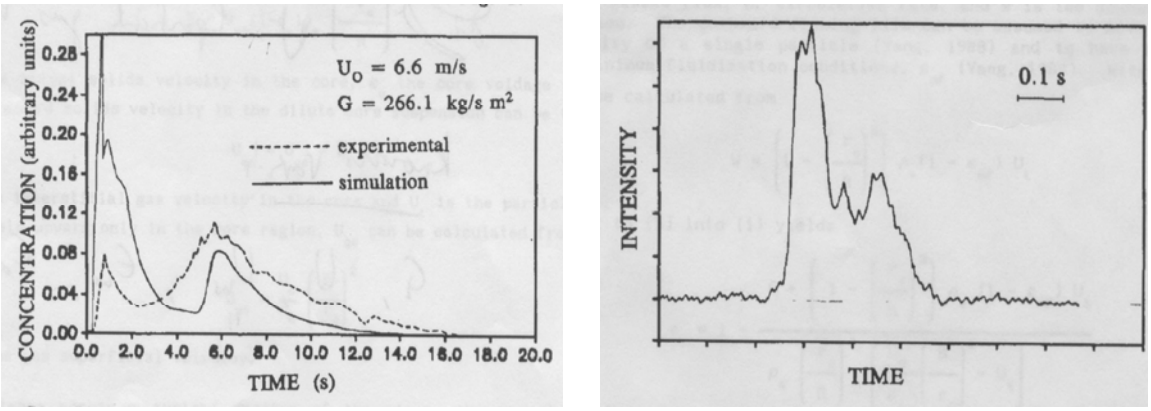

(a) (b)

Figure 5-3: a) Typical tracer response reported by Ambler *et al.* (1990); b) Tracer response obtained by Kojima *et al.* (1989), detected in the dilute zone.

5.3.1 Reproducibility and Occurrence Independence

To check the reproducibility, solids RTD data was obtained with another similar tracer particle with fresh solids inventory at the identical operating conditions (U_g^{risr} = 3.2 m·s^{-1}, G_s = 26.6 kg·m^{-2}·s^{-1}; U_g^{riser} = 3.9 m·s^{-1}, G_s = 33.7 kg·m^{-2}·s^{-1}). Figures 5-4a and 5-4b show the solids PDFs of residence times and the E-curve obtained after a longer data acquisition with higher number of occurrences for each of the conditions. The percentage difference in the mean residence times obtained from the repeated experiments was 2.8% and that of the dispersion coefficients was 5%. This confirms that solids RTD experiments are reproducible within engineering accuracy. However, one can observe that there are changes in the peak heights for both the conditions. This change is due to the change in the number of occurrences and the corresponding change in the time interval used for binning the residence time data. It is noteworthy that the time interval for binning was selected to be the minimum interval for which the area under the E-curve converges to one. Hence, in the non dimensional coordinates (dimensionalized with the maximum value), the PDF curves from the repeated experiments match.

To validate the assumption of ergodicity, the mean residence times at given operating conditions were examined as a function of total tracer occurrences, shown in Figure 5-5. For all the experimental conditions, the mean residence time converges to within the 95% confidence interval after about 300 occurrences except at U_g^{riser} = 3.9 m·s^{-1} and G_s = 33.7 kg·m^{-2}·s^{-1}, when about 1,000 occurrences are needed. Hence, the presented RTDs are number of occurrences independent.

5.3.2 FF and DPT Regimes

Overall solids holdup ($\varepsilon_s^{overall}$) in the riser can be obtained from the knowledge of the mean residence time (τ) and overall solids mass flux (G_s). An $\varepsilon_s^{overall}$ value of 6% is obtained at U_g^{riser} = 3.2 m·s^{-1} and G_s = 26.6 kg·m^{-2}·s^{-1}, which is a typical FF regime holdup. A value of 3% is found at U_g^{riser} = 3.9 m·s^{-1} and G_s = 33.7 kg·m^{-2}·s^{-1}, which is close to the DPT regime holdup (<2%).

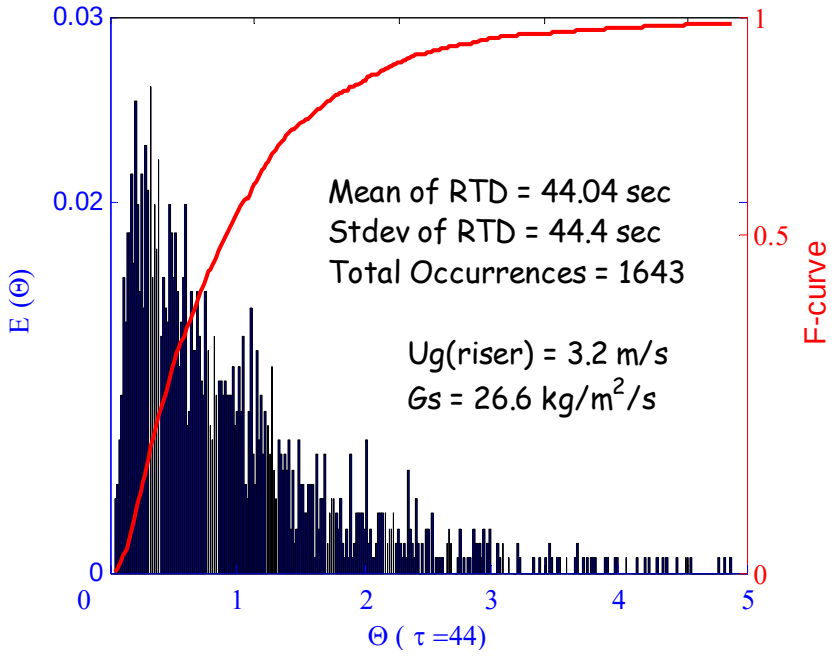

(a)

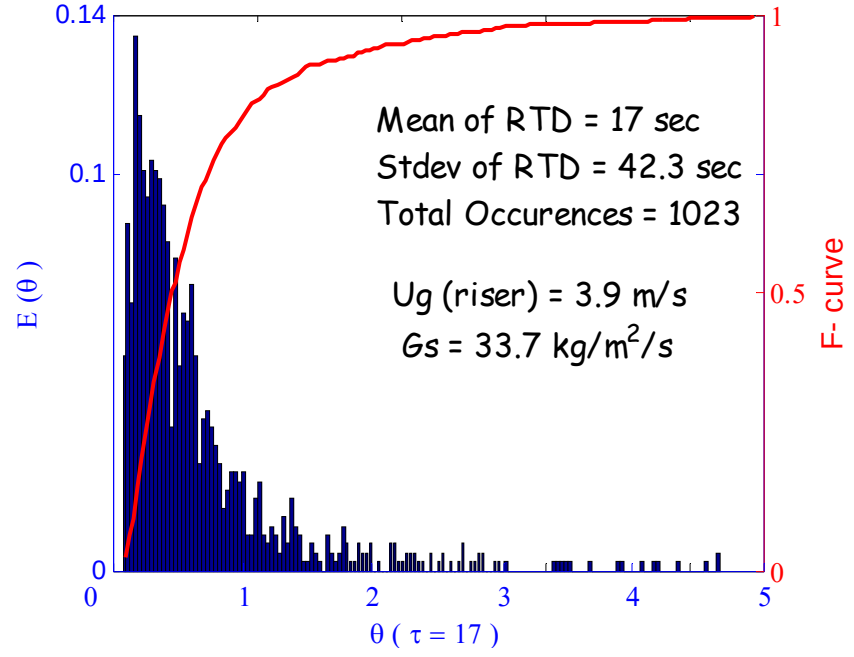

(b)

Figure 5-4: Solids RTD and its E-curve at U_g^{riser} and G_s of: a) 3.2 m·s^{-1}, 26.6 kg·m^{-2}·s^{-1} (FF regime); b) 3.9 m·s^{-1}, 33.7 kg·m^{-2}·s^{-1} (DPT regime). Note that abscissas for each plot are different.

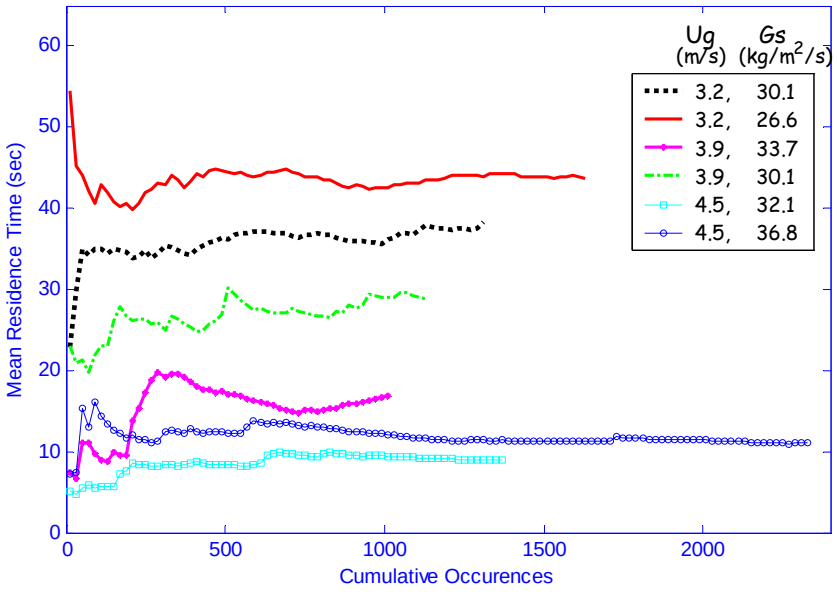

Figure 5-5: Convergence of mean residence time with total occurrences

However, one should note that the value of overall solids holdup is profoundly influenced by the method for the calculation of the overall mean solids velocity ($\overline{V_p}$). One method is to divide the length of the riser by the mean residence time as is done above. Second is to define a solids velocity for each passage of the tracer and obtain a PDF of the solids velocity in the riser. Then, one can use the first moment of this PDF to obtain the overall mean solids velocity. The comparison of the velocities between these two methods was done in Chapter 4 (Section 4.3.2) for RTD in down-comer. An assessment of these two velocities for the condition in FF regime shows a difference of 56%, which suggests that $\varepsilon_s^{overall}$ value can be influenced by more than 50%. Alternatively, one can also define the overall mean solids velocity based on a median residence time estimated as 50% value of the cumulative solids RTD. Such a definition for median solids velocity was used by a few researchers (Rhodes *et al.*, 1991) when employing a dispersion model to describe the solids mixing. Note that the same problem of evaluating a mean solids velocity arises in the application of a dispersion model to the RTD data. Hence, it is deemed inaccurate to analyze the absolute values of overall solids holdup, even though the relative values or the ratios will qualitatively give an estimate of the proportion of the holdups.

Another way of measuring the overall solids holdup is by estimating the volume of the solids occupied in the riser. The volume can be measured by suddenly shutting down the motive inlet air and the solids feeding valve at the base of the down-comer, simultaneously. However, such measures of the solids volume are confounded by several errors, namely the error in measuring the collected solids volume, which requires assuming a solids packing fraction on 0.64. The error incurred due to the contribution of the solids from the standpipe (between the feeding valve and the riser) to the measured volume, which is not accounted in the overall riser volume. Finally, the human error involved in simultaneously closing the feeding valve and the motive air. Considering the above arguments, it was not surprising that we found at the operating condition of U_g^{riser} = 3.2 $m \cdot s^{-1}$ and G_s = 26.6 $kg \cdot m^{-2} \cdot s^{-1}$, an overall solids holdup of 8% with a standard deviation of 86%. Hence, it was concluded that obtaining an accurate estimate of the overall solids holdup in the riser is not possible. One can also calculate an estimate of the solids superficial velocity based on the overall solids mass flux and the overall solids holdup. However, such an estimate of the solids velocity is again subject to an error larger than 80%, despite neglecting the systematic error and hence measures of solids superficial velocity are deemed inaccurate.

To look at the overall flow patterns in these two regimes, moments of the PDFs of the RTD curves were evaluated. Referring to Figure 5-4, dimensionless variance of 1 was obtained for the operating condition in the FF regime, indicating that the solids flow in the riser (as far as the variance is concerned) is close to a single stirred tank. However, the dimensionless variance for the DPT regime is 6.2 (Figure 5-4b), indicating the existence of either stagnant zones or bypassing, or both.

In examining the solids RTDs (F-curves), smaller slopes are observed on the dimensionless time scale when an indication of a second peak is seen in the PDF curve. Absence of the second peak and rapid rise of the RTD (high slope) seem to be indicative of dilute transport, where the slip velocity between the gas and solids tends to be small and close to the terminal velocity of the particles. In contrast, solids flow pattern in Figures 5-4a is in the fast-fluidization regime. Similar results were observed at the other conditions which are discussed in the next section. Thus, the shape of the RTD seems to be indicative of the flow regime.

5.3.3 RTD, FPTD and Response Function of Conventional Injection–Detection

In this section, the results are presented to compare and contrast the different solids 'travel' time probability density functions (distributions are integrals of such PDFs) obtained as discussed in Section 5.2. Plots in Figure 5-6 show the histograms of the occurrences and the cumulative occurrences (proportional to F-curve) versus time for total residence time and first passage times. The means of the PDFs for the RTD and FPTD are quite different, with a difference of 41%, while there is only a 3% difference in the standard deviations. Lower mean of FPTD as compared to RTD is expected since the first passage time represents the time elapsed between the final entry at the inlet plane (with no return) to the first exit at the exit plane. However, the dimensionless variance for the FPTD, calculated to be 17, is much larger than that of the RTD (6.2), indicating either an enormous bypassing or stagnancy in the riser. The fact that the PDF of FPT has a long tail indicates that even some of the particles that get through the riser in a single pass still do exhibit prolonged stays in the riser due to backmixing (i.e. repeatedly falling back and rising again within the riser).

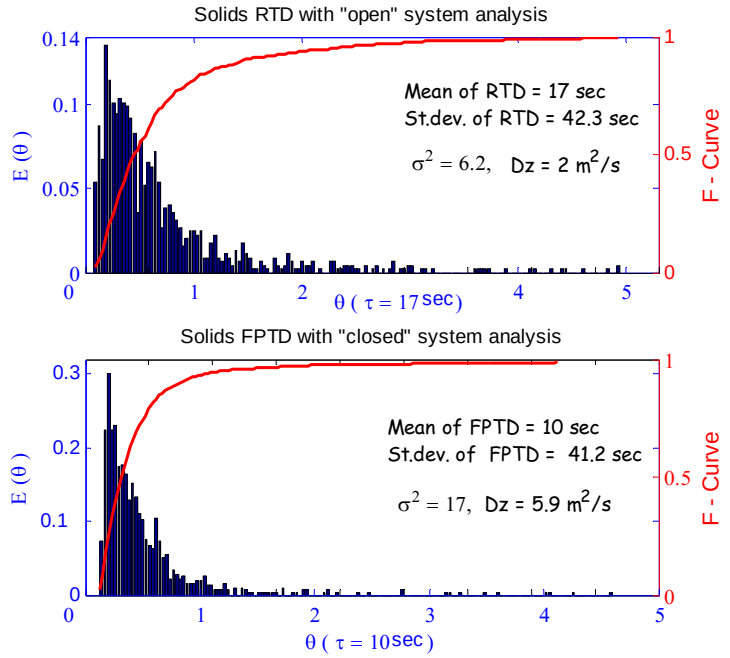

Figure 5-6: Comparison of the solids RTD and FPTD curves for the entire riser at U_g^{riser} = 3.9 m·s^{-1} and G_s = 33.7 kg·m^{-2}·s^{-1} obtained with "open" and "closed" system analysis, respectively.

From the ratio of the means of the RTD (17 sec) and the FPTD (10 sec), one concludes that 59% of the solids travel from inlet to exit in a single pass without re-exiting at the inlet Plane of the riser. However, even these solids exhibit a large dimensionless variance, which means that few solids go out fast and straight through the riser while the rest re-circulate internally in the riser by repeatedly slipping down and rising and slipping, etc. Hence, the data establishes that 41% of the solids in the riser at DPT conditions re-exit at the entry plane and keep re-entering. This value is of interest for modeling FCC risers. The dispersion coefficient calculated for the FPTD (Figure 5-6) was found to be 5.9 $m^2 \cdot s^{-1}$, which is 195% higher than the dispersion coefficient obtained for the RTD. The point is that neither is a good description of backmixing since the axial dispersion model does not apply in these situations. From the above we learn that an experiment with controlled boundaries ("closed-closed") will at best provide a FPTD, which provides an upper bound on the dispersion coefficients.

The percentage of solids recycle in the bottom section in the FF regime is 68%, which is higher than the percentage of solids recycle in the DPT regime (41%). Also, one can calculate the amount of solids in the recycle mode (at the bottom) given by the product of solids recycle percentage and the overall solids holdup ($\varepsilon_s^{overall}$). Hence, in the FF regime there are 4.1% of solids in the recycle mode as compared to 1.2% in the DPT regime. This high value of the solids in recycle mode provides the reason for occurrence of the dual peaks in the PDF of the RTD under FF regime, but not in the DPT regime. However, one can note that the dispersion coefficient is higher in the case of DPT regime even though the solids recirculation is higher in FF regime. Despite having uncertainties in the usage of an ADM model for riser flow, higher dispersion coefficient in the DPT regime conveys the message that the solids mixing in the riser is not only governed by the large scale solids recirculation, but some other phenomena too (discussed later).

Moreover, if a bundle of tracer particles were injected at the bottom of the riser and their concentration measured at the exit plane, the obtained response would not be either the shown RTD, or the FPTD, but a distribution of some other travel time of the solids. Hence, conventional tracer injection techniques would measure this travel time of the solids. Now, one can interpret the responses obtained from single tracer so as to

obtain the distribution of solids travel time that can be obtained in a conventional tracer injection-detection method. This is done by counting the time taken by the tracer since the first entry at the entrance plane to every visit at the cross section of the detector at the exit plane for each passage through the riser. Here a conventional tracer injection-detection method means that a bundle of the tracer particles (e.g. radioactive, fluorescent, phosphorescent) are injected so as to represent an impulse and its cross-sectional concentration is measured by a detector external to the riser, similar to the methods used by several researchers (Kojima *et al.*, 1989; Ambler *et al.*, 1990; Viitanen, 1993; Ran *et al.*, 2001).

The comparison of the distributions of residence time, first passage time and that of tracer response from a conventional tracer injection-detection methods are shown in Figure 5-7. Similar to the trends in the previous flow condition, FPTD has a mean value 66% lower than mean residence time, while the standard deviation is 44% lower. Also, the comparison shows that the tracer response from a conventional tracer injection-detection method overestimates the mean residence time by 64%. In addition, the dimensionless variance is underestimated by 31%. Such large differences in the measurements can lead to an adversely bad design of the riser systems. In addition, comparison of the dispersion coefficients is deemed inappropriate because an ADM model is applicable only under "closed-closed" boundaries.

One can note from Figure 5-6 and 5-7 that the dimensionless variance and the dispersion in a FPTD are relatively very high as compared to that of RTD and the tracer curve from conventional injection-detection method. This high dispersion can be explained by the heavy internal recirculation in the riser. Small scale backmixing at the entrance section of the riser and the large scale heavy internal recirculation throughout the riser results in the variance of the residence time distribution. Small scale backmixing at the entrance of the riser seems to effect the mean of the residence time more than its variance, while the large scale internal recirculation seems to effect the variance more than the mean. Hence, a FPTD, obtained by neglecting the backmixing at the entrance and exit sections, has a large effect (decrease) in its mean but relatively less effect on its variance. This results in having a high dispersion coefficient for FPTD. In fact, such large variances were observed at high fluxes too, which is discussed in the next section.

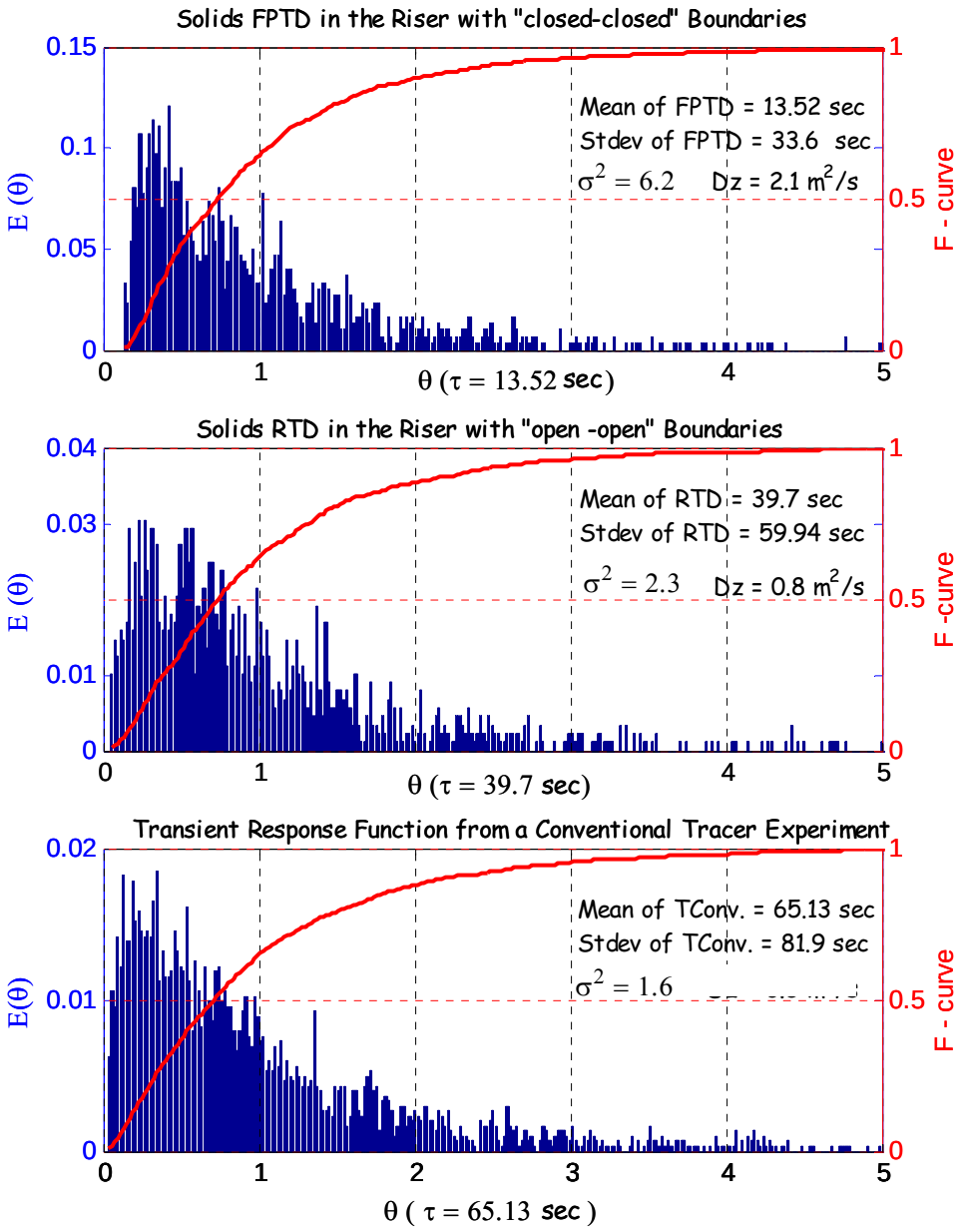

Figure 5-7: Comparison of the solids RTD, FPTD and the transient response curve from conventional tracer injection in the riser at $U_g^{riser} = 3.2$ m·s^{-1} and $G_s = 30.1$ kg·m^{-2}·s^{-1}.

5.3.4 RTDs at High and Low Fluxes

Two different CFBs were utilized to obtain the solids RTD data. One is with riser dimensions of 6 inch I.D. and 26 ft. tall and a down-comer of 2 inch I.D. installed at the Chemical Reaction Engineering Laboratory (CREL) to obtain data at low solids fluxes (< 40 $kg \cdot m^{-2} \cdot s^{-1}$). The second one is with riser dimensions of 5.5 inch I.D. and 15 ft. tall and a down-comer of 14 inch I.D. installed at Sandia National Laboratory (SNL) to obtain data at high fluxes (> 100 $kg \cdot m^{-2} \cdot s^{-1}$). Solids RTDs for the riser were acquired at different operating conditions by varying superficial gas velocities (U_g^{riser}) and by using different solids inventory and recirculation rates. The solids mass flux and the flow regime at these operating conditions are listed in Table 5-1. Operating flow regimes were obtained from the idealized flow regime map of Bi and Grace, 1997 (Chapter 4).

Table 5-1: Operating conditions and regimes for solids RTD measurements

U_g^{riser} ($m \cdot s^{-1}$)	3.2 CREL	3.9 CREL	4.5 CREL	5.49 SNL	5.56 SNL	7.71 SNL
G_s ($kg \cdot m^{-2} \cdot s^{-1}$) **Regime**	26.6 FF	30.1 DPT	32.1 DPT	102 FF	145 FF	119 DPT
G_s ($kg \cdot m^{-2} \cdot s^{-1}$) **Regime**	30.1 FF	33.7 DPT	36.8 DPT	-	-	-

FF – Fast Fluidization, DPT – Dilute Phase Transport.

Figure 5-8 presents the variation of the solids PDFs of residence times and their cumulative occurrence curves (F curve or RTD curves) under different operating conditions at low solids fluxes. Figures 5-8a and 5-8d indicate a second peak near their mean residence time (τ), while for all the other conditions, PDFs of RTD curves have a single peak, which occurs much before the mean residence time. In addition, a closer look at the cumulative occurrence plots (F curves) shows that curves in Figures 5-8a and 5-8d have smaller slopes as compared to the other curves. These effects can be explained by noticing that the flow pattern of the solids in Figures 5-8 b, c, e, f has approached the state of dilute-phase transport (refer to Table 5-1) where the slip velocity between the gas and solids tends to be small and close to the terminal velocity of the particles. Therefore,.

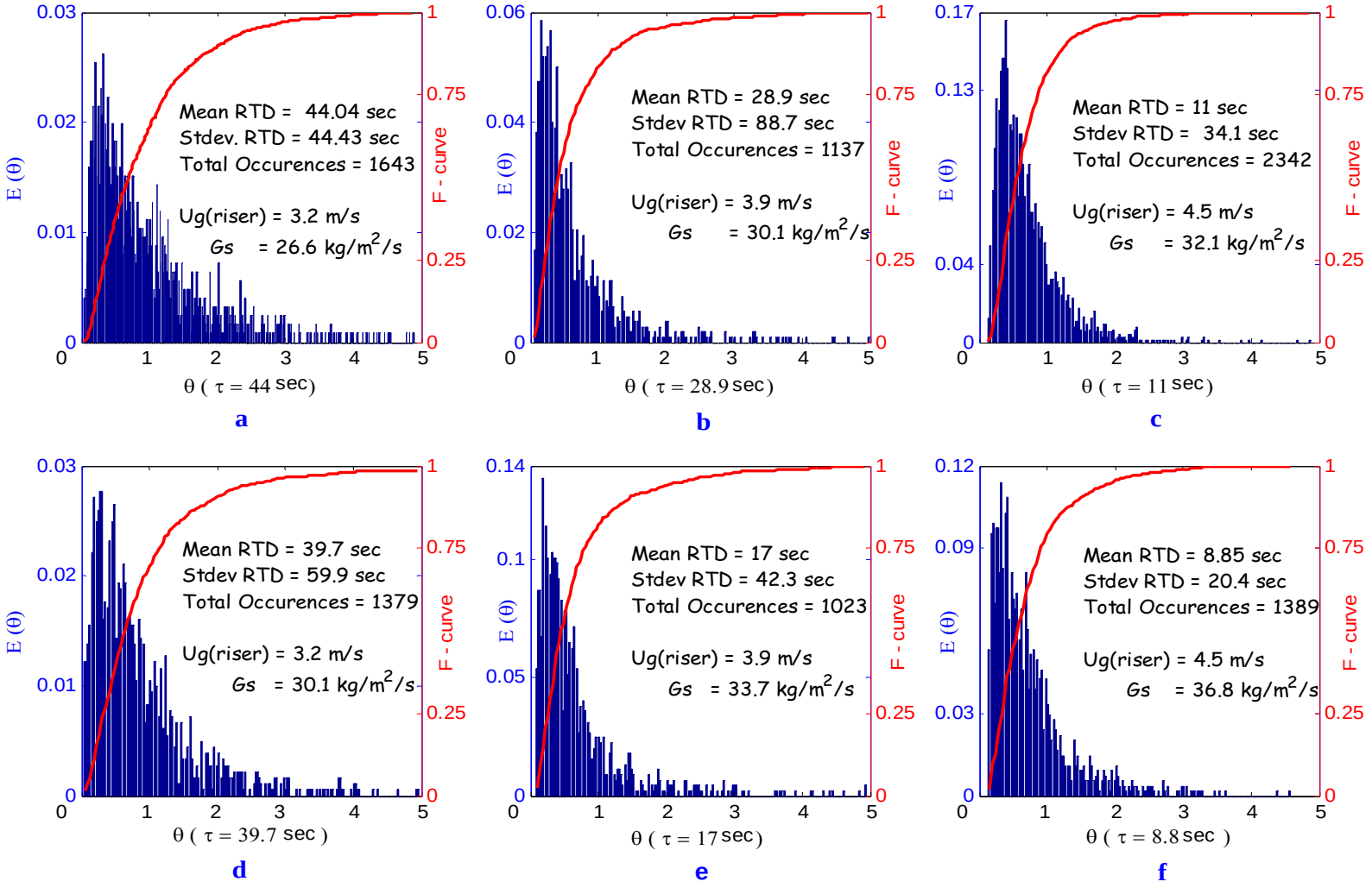

Figure 5-8: Solids RTD and its cumulative distributions at U_g^{riser} (m·s^{-1}) and G_s (kg·m^{-2}·s^{-1}) of: a) 3.2, 26.6, FF; b) 3.9, 30.1, DPT; c) 4.5, 32.1, DPT; d) 3.2, 30.1, FF; e) 3.9, 33.7, DPT; f) 4.5, 36.8, DPT respectively. Note that abscissas for each plot are different.

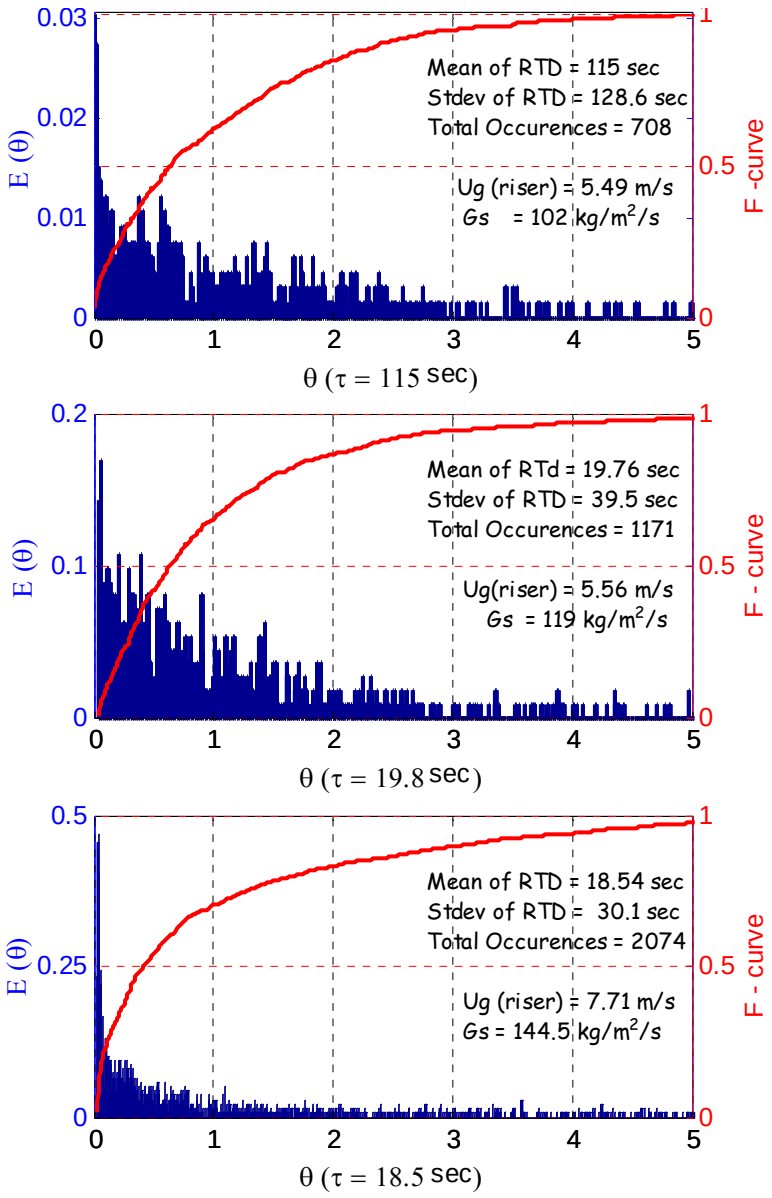

Figure 5-9: Solids RTD and its cumulative distributions at U_g^{riser} (m·s^{-1}) and G_s (kg·m^{-2}·s^{-1}) of: a) 5.49, 102, FF; b) 5.56, 145, FF; c) 7.71, 119, DPT respectively.

similar results can be observed in Figures 5-8 b, c, e and f with respect to the peak-emerging times and the shapes of RTD curves.

In analogy with the above low flux results, data for solids PDFs of RTDs at high flux conditions also exhibit a single peak occurring before the mean residence time in the DPT regime and multiple peaks in the FF regime, as shown in Figure 5-9. Examining the solids RTDs (F-curves), smaller slopes are observed on the dimensionless time scale when an indication of a second peak is seen in the PDF curve. Absence of the second peak and rapid rise of the RTD (high slope) seem to be indicative of dilute transport (refer to Table 5-1). In contrast, solids flow pattern in Figures 5-8 a, d and 5-9 a, b are in the fast fluidization regime. Thus, the shape of the RTD seems to be indicative of the flow regime.

It can also be observed from the plots in Figures 5-8 and 5-9 that for all the conditions the PDFs of the RTD curves are wide with long tails. These results indicate that the degree of mixing of solids is considerable and is caused most probably due to the internal solids circulation and exchange of solids between the dilute core and the dense annular region in the riser. Our tomography results, to be discussed later, do confirm such existence of solids holdup profile that favors the wall region with increased solids concentration. The large standard deviation of the RTD can indeed be observed from the raw data of the three detectors used for obtaining the RTD curve, as shown in Figure 5-10. Consider the tracer particle starting from the down-comer top at the first blue peak (in Figure 5-10). The tracer particle re-circulates at the riser bottom (red peaks) before it spends a long time of 248 sec in the riser and gets detected again at the riser bottom, before it finally leaves the riser (green peak detected at the riser top). While the total residence time during this passage was 248.52 sec, in the very previous passage the tracer particle had a residence time of 1.69 sec. Two orders of magnitude difference in the residence times explains the reason for the large apparent axial dispersion coefficient and the long tail in the RTD curve.

The mean and variance of the PDFs, and the mixing parameters and the axial dispersion coefficient are evaluated for all the flow conditions at low and high solids fluxes and are presented in Tables 5-2 a, b and c. As expected, the mean residence time decreases with increasing solids mass flux at constant gas superficial velocity for the flow

conditions in both FF and DPT regimes. The dimensionless variance increases with increased solids mass flux at constant gas superficial velocity in the FF regime, while it decreases with solids mass flux in the DPT regime. This result suggests that with the increasing solids mass flux in the FF regime, mixing increases and the flow deviates more and more from the plug flow. Conversely, in the DPT regime, mixing decreases and the flow approaches plug flow with increased solids flux. However, the change in parameters with the superficial gas velocity cannot be assessed with our data.

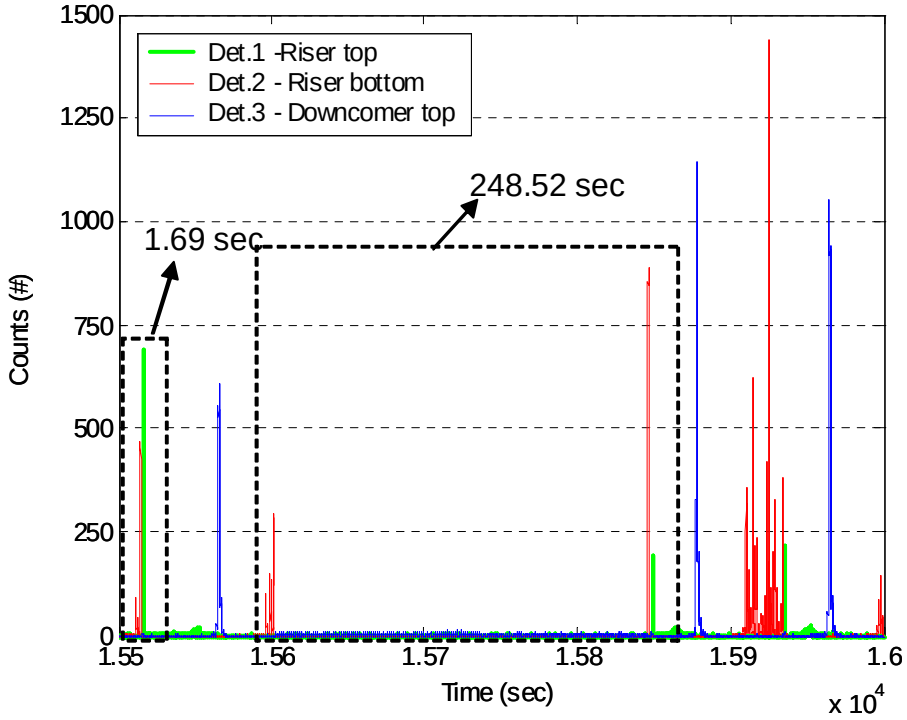

Figure 5-10: Part of the RTD raw data from the three detectors at $U_g^{riser} = 4.5$ m·s^{-1} and $G_s = 36.8$ kg·m^{-2}·s^{-1}.

The mean of the FPTDs are less than the corresponding means of RTDs, while those of the conventional impulse injection response method are higher. These trends were anticipated as discussed earlier in Section 5.2. The dimensionless variances are higher for the FPTDs and the reasons were discussed earlier. But, the dimensionless variances from a conventional impulse injection-response method are smaller since the mixing occurring near the boundaries (injection and detection) are not accounted.

Table 5-2a: Mixing parameters for the entire riser for low-flux flow conditions in DPT regime

U_g^{riser}, G_s	3.9, 30.1				3.9, 33.7				4.5, 32.1				4.5, 36.8			
	FPTD	RTD	TConv	Error	FPTD	RTD	TConv	Error	FPTD	RTD	TConv	Error	FPTD	RTD	TConv	Error
τ, sec	15	28.86	44.28	53	10	17	24	41	6.36	11	15.35	40	5.14	8.85	11.95	35
σ^2, -	27.8	9.4	5.7	-39	17.5	6.2	3.4	-45	28.2	9.6	5.5	-43	13.5	5.3	3.3	-38
$D_{z,ax}$, $m^2 \cdot s^{-1}$	4.3	1.4	1	-29	5.9	2	1.7	-15	7.9	1.9	1.7	-11	10.5	3.1	2.8	-10

Table 5-2b: Mixing parameters for the entire riser for low-flux flow conditions in FF regime

U_g^{riser}, G_s	3.2, 26.6				3.2, 30.1			
	FPTD	RTD	TConv	Error %	FPTD	RTD	TConv	Error %
τ, sec	14.3	44	75.44	71	13.52	39.7	65.13	64
σ^2, -	2	1	0.86	-14	6.2	2.3	1.6	-31
$D_{z,ax}$, $m^2 \cdot s^{-1}$	1.9	0.66	0.51	-23	2.1	0.8	0.5	-38

Table 5-2c: Mixing parameters for the entire riser for high-flux flow conditions in FF and DPT regimes

U_g^{riser}, G_s	5.49, 102 (FF)				5.56, 145 (FF)				7.71, 119 (DPT)			
	FPTD	RTD	TConv.	Error %	FPTD	RTD	TConv.	Error %	FPTD	RTD	TConv.	Error %
τ, sec	45.55	115	159.61	39	6.86	19.76	28.53	44	8.95	18.54	25.11	35
σ^2, -	1.8	1.3	1.4	5	1.2	4	3.9	-2.5	3.9	2.8	3.2	14
$D_{z,ax}$, $m^2 \cdot s^{-1}$	0.2	0.08	0.06	-33	2.6	0.73	0.54	-26	3.2	0.7	0.5	-29

Error referred to in the Tables 5-2 is the discrepancy in the values obtained from the of the residence time distribution curves and those obtained from conventional impulse injection-response method. It can be seen that the error in the means range from 35 to 71%, while in the dimensionless variance range from 2 to 45%. Error in the means in the FF regime seems to be higher than in the DPT regime. This can be expected as mixing is higher in the FF regime. Also, the magnitudes of error remain the same at high and low solids fluxes.

The percentage of the solids that get recycled through the bottom section (i.e. that cross the bottom inlet plane more than once), can be calculated from the ratio of the means of the FPTD and RTD. At low solids flux conditions, the solids recycle percentage seems to be varying between 42-48% in the DPT regime, while in the FF regime it is as high as 67%. At the high solids flux conditions, solids recycle percentage is between 61% and 65% in the FF regime, while in the DPT regime it is about 52%. Hence, the above patterns seem to suggest that solids recycle percentage at the bottom in the DPT regime is around 50%, while in the FF regime is around 65%. These values can be used in the mechanistic modeling of the solids flow in the riser.

To assess the variation of the solids residence time distributions with operating conditions, the trends in the mean solids velocity with superficial gas velocity and solids mass flux are considered. Here, the mean solids velocity is obtained from the mean residence times (τ). As expected, the mean solids velocity increases with increased solids mass flux at fixed superficial gas velocity. However, this result is in contradiction to the correlation reported by Smolders and Baeyens (2000). It should be noted that the injection and detection method used by Smolders and Baeyens (2000) was intrusive with sampling probes and the time resolution in obtaining the small mean residence times (3 – 11 sec) is also questionable. Variation of the solids mean velocity with the superficial gas velocity at fixed solids mass flux, as reported by several authors (Kojima *et al.*, 1989; Rhodes, 1990; Smolders and Baeyens, 2000), cannot be directly obtained from our data. We can also calculate the solids median velocities from the 50% value of the F-curves. The values of the RTD curve at large times have a significant influence on the mean residence times (τ) and the mean solids velocity, while they are of less importance for the

median residence times or the median solids velocities. Median solids velocities, hence, will exceed the mean solids velocities. Median solids velocity was also found to be increasing with solids mass flux and this is in contradiction to the correlations reported by Rhodes (1990) and by Smolders and Baeyens (2000). Rhodes (1990) reported that median solids velocity is independent of solids mass flux and the same doubts regarding the experimental time resolution can be raised regarding their data.

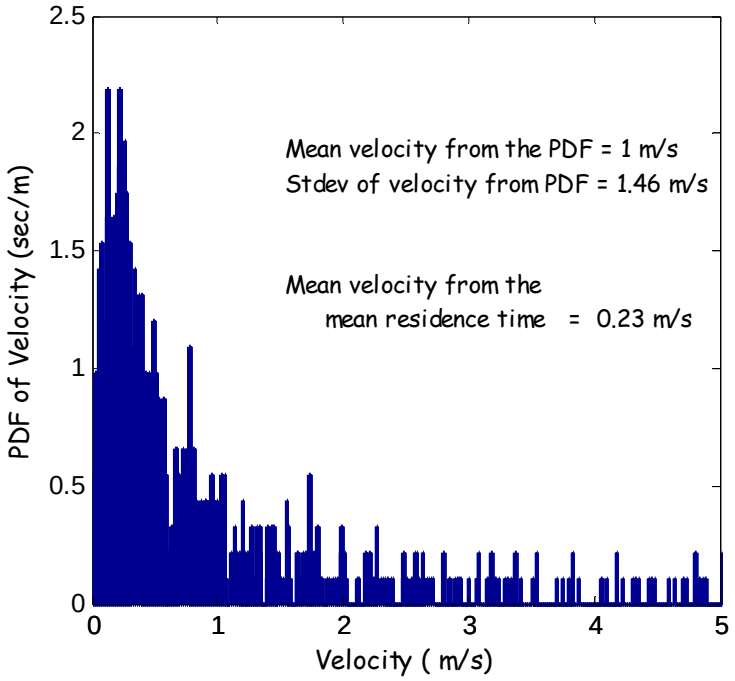

Figure 5-11: PDF of solids velocity in the riser derived from the residence time data in the FF regime at U_g^{riser} = 5.56 m·s^{-1} and G_s = 144.5 kg·m^{-2}·s^{-1}.

As discussed earlier, an alternate way to estimate the mean solids velocity is to construct a PDF of the solids velocity from the residence time data. Such a velocity PDF for one of the flow conditions is illustrated in Figure 5-11. A marked difference of 77% was found by comparing the mean velocities obtained from the first moment of the PDF and from the mean residence time. Also, one can observe a clear dual peak in the velocity PDF corresponding to the solids velocities in the core and core plus annulus. This result corroborates the core-annular flow structure with large internal recirculation in the FF

regime. Following the analysis presented in section 3.3.2, it can be proven that the mean velocity obtained from the velocity PDF is an upper bound for the 'mean' velocity obtained from the mean residence time. These values will be equal only in the pure plug flow condition and their ratio provides an estimate of the deviation from plug flow. But, the key message from Figure 5-11 is that mean velocity obtained from the PDF is a better representation of the mean solids velocity. However, in many studies employing a dispersion model to analyze the RTD data, mean solids velocity, V in the definition of the axial Peclet number ($Pe_z = VL/D_z$) is replaced by U_g^{riser} (Rhodes *et al.*, 1991; Wei *et al.*, 1998; Smolder and Baeyens, 2000). Hence to avoid confusion, we use the solids axial Peclet number as $Pe_{s,z} = V_pL/D_z$, where V_p is the mean solids velocity derived from the velocity PDF and the axial Peclet number $Pe_z = U_g^{riser}Pe_{s,z}/V_p$.

5.3.5 Axial Dispersion Coefficients

Table 5-3: Axial dispersion coefficients and Peclet numbers for all the flow conditions

U_g^{riser}, G_s ($m\cdot s^{-1}$,$kg\cdot m^{-2}\cdot s^{-1}$)	V_p from PDF ($m\cdot s^{-1}$)	V_p from τ ($m\cdot s^{-1}$)	$Pe_{s,z}$	Pe_z	$D_{z,ax}$ from PDF ($m^2\cdot s^{-1}$)	$D_{z,ax}$ from τ ($m^2\cdot s^{-1}$)
3.2, 26.6	0.38	0.18	2	16.7	1.4	0.66
3.2, 30.1	0.46	0.22	2.3	15.9	1.5	0.7
3.9, 30.1	0.81	0.41	2.1	10.3	2.8	1.4
3.9, 33.7	1.16	0.44	1.5	5	5.7	2.1
4.5, 32.1	1.35	0.95	3.6	12	2.8	1.9
4.5, 36.8	1.8	1.12	2.6	6.5	5.1	3.1
5.49, 102	0.44	0.04	2.4	30.1	0.84	0.08
5.56, 145	1	0.23	1.9	10.5	3.2	0.73
7.71, 119	2.2	0.33	2.2	7.7	4.6	0.7

Considering the fact that an ADM model can not sufficiently describe the solids mixing in risers, the discussion here is limited to predicting trends in solids mixing. Using the above definitions for the axial Peclet number and the solids axial Peclet number, axial dispersion coefficients were estimated. Again, two different dispersion coefficients can be evaluated from the two definitions of mean solids velocity (from velocity PDF and mean residence time). Table 5-3 provides the values of axial Peclet numbers and

dispersion coefficients for all the flow conditions investigated. Also, the mean solids velocity from the two different methods are provided, which differ by at least 30%. It can be observed that this difference is smaller for the conditions in the DPT regime than the conditions in the FF regime. The reason is that flow in the DPT regime is closer to plug flow than the flow in FF regime. Similarly, dispersion coefficients from two different calculations also differ. Note that dispersion coefficients reported earlier in Tables 5-2 were evaluated from the mean residence time. This method of calculation was deemed necessary in the earlier sections so as to compare the dispersion coefficients of RTD and from the conventional injection-detection method on equal basis.

The solids axial Peclet number can be seen from Table 5-3 to be an order of magnitude lower than axial Peclet number for most of the cases. Although, with the low Peclet numbers, the usage of such 1D dispersion model is highly questionable, the effect of operating conditions on the extent of solids mixing can be readily evaluated. It can be observed from Table 5-3 that the dispersion coefficient increases with solids mass flux both in the fast fluidization regime (U_g^{riser} = 3.2, 5.5 m·s^{-1}) and in the dilute-flow regime. However, this increase seems to be more pronounced at high solids flux conditions. Similar increasing trend of the dispersion coefficient was observed by Avidan (1980) and Kojima *et al.* (1989) in the dilute zone of the CFB riser. Patience *et al.* (1991) observed the same trend in a 0.083 m diameter riser and attributed this increase to the riser diameter. It should be noted, however, that the investigations of Avidan (1980), of the present work and of Kojima *et al.* (1989) were carried out in risers that differ in diameter by a factor of three. Hence, this increase of dispersion coefficient is in fact not a wall effect. In contrast, Rhodes *et al.* (1991) concluded from their experiments that solids dispersion decreased slightly with solids mass flux and proposed a supporting correlation. Rhodes *et al.* (1991) attributed this to the operation of the riser under similar profiles condition, where solids velocity and mixing are independent of solids mass flux. Nevertheless, it should be noted that Rhodes *et al.* (1991) obtained the exit concentration in their experiments from a sampling probe placed at different radial locations and this does not represent a true mixing cup concentration at the exit.

Considering the limited database, it is not easy to generalize. Axial Peclet number seem to be decreasing with the increasing solids mass flux, consistent with the finding

that the solids down-flow in the annulus increases with increasing solids circulation in the fast fluidization regime (Kim *et al.*, 2004). Also Bi (2004) collected the so far available data in the literature for both Group A and B particles and showed a similar trend in the FF regime. Similar decreasing trend in axial Peclet number can be seen from Table 5-3 in the dilute phase regime. One should note that we are operating in the dilute phase regime in the heterogeneous dilute flow or core-annulus dilute phase flow, according to the regime classification by Bi and Grace (1997). Heterogeneous dilute phase flow is typically characterized by particle streamers close to the riser wall leading to a core-annulus structure (Bi and Grace, 1997), which is the reason for increasing down-flow in the annulus with increasing solids mass flux in this regime. Also, Bi (2004) informs that Pe_z generally ranges from 1 to 10 for risers with abrupt exits and are higher in risers with smooth exits. Since the data reported here were obtained in risers with relatively smooth exits (axi-symmetric disengagement), Pe_z were consistently found to be larger than 5. Also, the numerical values of the dispersion coefficients reported in Table 5-3 are of the same order of magnitude as obtained by Rhodes *et al.* (1991), Smolders and Baeyens (2000) and Viitanen (1993), while those obtained by Avidan (1990), Wei *et al.* (1998) and Kojima *et al.* (1989) differ by orders of magnitude. This discrepancy might be due to different regions under investigation, and whether the RTD is obtained in the dilute zone or the complete riser.

5.3.6 Core-Annulus Interchange Model

Based on a core-annulus flow structure, several authors (Bolton and Davidson, 1988; Ambler *et al.*, 1990; Pugsley and Berruti, 1995; Harris *et al.*, 2002) presented models describing the axial solids mixing in the dilute zone. In their models, solids mixing is considered to be due to particle transfer between upward moving core and downward falling annulus phases. The mode of solids transfer between the two phases is modeled in different ways, such as due to interparticle collisions and turbulent diffusion, all of which were discussed in Table 2-1. One such core-annulus interchange model was developed and applied to describe the obtained data. Details of the model are provided in Appendix B.

5.4 Summary

Solids mixing in an "open" system such as the gas-solid riser was investigated by tracking a single radioactive tracer particle.

i. The assumption of ergodicity underlying the experiments was corroborated and true solids residence times, first passage times and total retention time were estimated.
ii. Dual peaks were seen in the PDF of the solids RTD for the experimental conditions in the fast-fluidization regime, but not in the dilute transport regime. The shape of the RTD seems to suggest the regime of operation.
iii. Absolute values of overall solids holdup estimated from the knowledge of solids mass flux and the RTD curve are deemed inaccurate, even though their relative values can qualitatively give an estimate of the proportion of the holdups.
iv. The solids recycle percentage at the bottom of the riser in the DPT regime is around 50%, while in the FF regime is around 65%.
v. Large discrepancies in the range of 35-71% are encountered in the means of conventional tracer injection-detection curves, while the error in dimensionless variances ranged from 2-45%.
vi. Dispersion coefficients obtained from FPTD overestimates and that from the conventional injection-detection curve underestimates the axial dispersion in risers.
vii. The dispersion model is not appropriate for use in modeling of solids flow in a gas-solid riser, although it can be used for studying the mixing trends with operating conditions.
viii. Dispersion coefficient increases with solids mass flux both in the fast fluidization and dilute-flow regimes.

It should be noted that the data obtained from single particle tracking is rich. One can precisely derive not only the distribution of total residence time in the system, but also other solids travel time distributions as illustrated in this chapter. Moreover, one can directly evaluate a macromixing index based on Trajectory Length Distribution (TLD)

and other mixing parameters such as return length and circulation time distribution, as proposed by Villermaux (1996). In addition, Cycle Time Distribution (CTD) can also be estimated from the data. CTD is defined as the time elapsed between consecutive passages of a certain fluid element past the cross section through which all the fluid passes (Mann and Crosby, 1973). Such mixing data is evaluated in a fully developed flow section of the riser and is discussed in the subsequent chapters. But, prior to discussing that, solids flow field and holdup measurements via CARPT and CT in a fully developed flow section are discussed in the next chapter.

Chapter 6

Solids Velocity Field and Holdup Measurements

6.0 Scope

The time-averaged mean and fluctuating solids velocity fields are quantified using the Computer Automated Radioactive Particle Tracking (CARPT) technique. Gamma ray Computed Tomography (CT) is used to measure the time averaged cross-sectional solids holdup distribution. Details of the experimental techniques, protocol of implementation and data analysis are discussed in this chapter. The challenges to implement CARPT on a pilot-plant scale riser are outlined. The experimental studies examine operating conditions in fast fluidization (FF) and dilute phase transport (DPT) regimes. Comparative and symbiotic analyses of the results obtained from CARPT and CT are used to develop a coherent picture of the solids flow field. This experimental data quantifies for the first time the solids velocity field, turbulent stresses, granular temperature, other flow characteristics available in the time series of Lagrangian tracer particle trajectories and solids holdup distribution. All of these can be used for the validation of CFD models. In addition, this work also demonstrates the power of CARPT and CT as flow mapping techniques in studying highly turbulent and opaque multiphase systems.

6.1 CARPT Technique

Computer Automated Radioactive Particle Tracking (CARPT) is an advanced non-invasive technique to measure the solids (in gas-solid, liquid-solid and gas-solid-liquid systems) or liquid (in gas-liquid systems) phase velocity field and turbulent parameters. This is based on the principle of tracking the motion of a single tracer particle as a marker of the solids phase, if the flow field of the solids phase needs to be measured (e.g. gas-solid riser), or of a neutrally buoyant particle if the flow field of the liquid phase needs to be measured (e.g. bubble column). This "tracer particle" (which represents the dispersed solid phase in the case of gas-solid system) contains a radioactive element emitting γ-rays. This radiation is received by an ensemble of specific detectors (NaI (Tl) scintillation crystals) placed "strategically" around the system being investigated. Since the intensity of the photon counts received by the detectors not only depends on the positions of the tracer and the detector, but also on the medium of attenuation in between them, the set-up needs to be calibrated in-situ i.e. on the system of interest at the operating conditions of interest. By utilizing the detectors' calibration, the particle position during the operation at the same operating condition used for calibration, can be reconstructed at each "instant" (discussed in Chapter 3). Then, after filtering the noise from the measured counts due to the statistical fluctuation of γ-rays using wavelet analysis (Degaleesan, 1997), the Lagrangian trajectory of the particle movement is determined and further processed to evaluate the instantaneous solids velocity along the particle trajectory. From this, many fluid dynamic quantities can be determined in a non-invasive manner such as time-averaged velocities (3-D solids flow field), turbulence parameters (kinetic energy, shear stress, turbulent eddy diffusivities).

The CARPT technique employed in this work has been successfully used previously in different laboratory scale systems. Examples include fluidized beds (Kondukov *et al.*, 1964; Lin *et al.*, 1985; Moslemian, 1987; Limtrakul, 1996), bubble column (Devanathan, 1991; Degaleesan, 1997; Ong, 2003; Rados, 2003), slurry bubble column (Rados, 2003), stirred tank (Rammohan *et al.*, 2001), liquid-solid riser (Roy, 2000), gas-solid riser (Godfroy *et al.*, 1999) and spouted bed (Larachi *et al.*, 1994). For

the gas-solid riser system investigated in this study, the challenge is to implement CARPT on a pilot-plant scale, which has been never accomplished before.

6.1.1 Challenges in Implementing CARPT on Gas-Solid Risers

The scale of the risers at CREL and SNL that we wanted to get data on, and the continuous nature of the solids flow through the riser and the whole CFB loop, as well as high solids velocities and possible attrition of the radioactive tracer particle, give rise to many CARPT implementation issues. These include:

a) selecting the proper radioactive particle,

b) devising a method for proper calibration, of detectors

c) selecting a data sampling time,

d) positioning the detectors,

e) selecting a safe procedure for introduction and recovery of the radioactive tracer parrticle,

f) post-processing method for the data.

Each of these issues is addressed below along with the steps taken to resolve them.

6.1.1a Selection of Radioactive Particle

To accurately track solids flow, the radioactive tracer particle used should have the same size, shape, and density as the solids material used. It should also have the same collisional properties. The duration of irradiation needed to get the desired level of the particle radioactivity (this depends on the size of the system, expected solids holdup and needed counts levels at the detectors) presents another practical consideration and constraint. The irradiation time depends on the particle density, cross sectional area, half-life of the radioisotope used in the particle, and the neutron flux of the nuclear reactor employed for the irradiation. Table 6-1 lists the possible radioisotopes which can be used as tracer, with their advantages and disadvantages. From the previous work of Larachi *et al.*, (1994), ^{198}Au (Gold) seems to be the best compromise (very easy to activate providing the possibility for using very small diameter tracers). However, due to its short half-life (about 2 days), it is not appropriate for use in our laboratory since there is no nuclear reactor near by.

Instead, we have chosen ^{46}Sc as the radioelement (half-life 83 days, density 3 g·cm^{-3}). The scandium particle is coated with a 7 μm thick polymer (Parylene N, density 1.1 g·cm^{-3}), which permits us to match the bulk density of the glass beads used as solids in the riser and to protect the scandium from possible attrition by abrasion (Rados, 2003). A schematic of such a composite particle is shown in Figure 6-1, along with a photograph of glass beads used. The bulk density and the mean diameter of the resulting tracer particle are 2.5 g·cm^{-3} and 150 μm, respectively. At this stage we did not have the facility to investigate the restitution coefficient of the tracer particle and compare it to the restitution coefficient of the soft glass beads used as solids,

Table 6-1: Principal Gamma-Emitter Isotopes for CARPT Experiments.

	^{60}Co	^{198}Au	^{46}Sc	^{59}Fe
Density (g·cm^{-3})	8.9	19.3	2.99	7.8
Half-life (days)	1927	2.69	83	44
Irradiation Time[(1)] (Metal diameter)	Fission Products (83 μm)	82 h (64 μm)	164 h (136 μm)	Impossible to activate at 120 μCi – An activity of 40 μCi requires 200 days of activation (89 μm)

[(1)] Theoretical irradiation time for a final activity of 120μCi in a nuclear reactor (neutron flux 5e13 n·cm^{-2}·s^{-1}) for a radioactive tracer coated with a polymer (density 1.1 g·cm^{-3}) whose bulk density is 2.55 g·cm^{-3} and overall diameter is 150 μm (actual radioelement diameter specified).

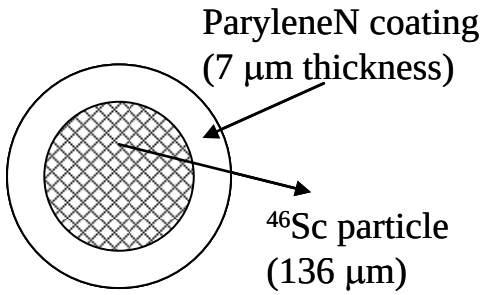

(a)

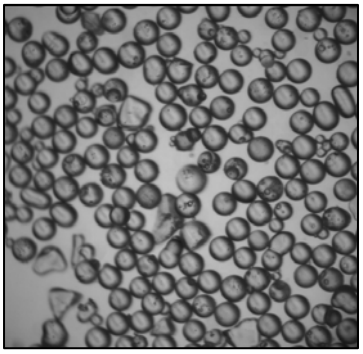

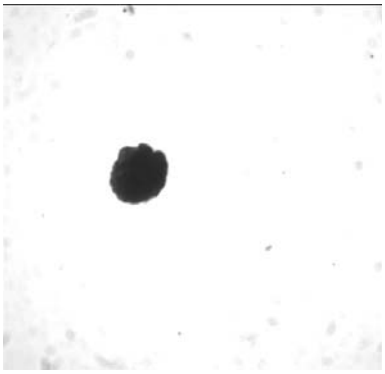

(b) (c)

Figure 6-1: a) Schematic of the composite radioactive tracer particle; b) Photograph of the glass beads used; c) Photograph of the Scandium tracer particle. Scales of the photographs are not the same.

6.1.1b Calibration of Detectors

Before performing the CARPT experiment, calibration of all detectors used must be performed in-situ, preferably at the same operating conditions as used in the actual experiment, to obtain the calibration curve (the relationship between intensity and the positions of the detector and the radioactive particle) for each detector. Different calibration methods have been evaluated:

a) "External" calibration using an automated device without solids flow: The advantage is the possibility of using a large number of calibration points (several hundreds). However, this method would require us to assume that the radiation absorption due to the solids inside the riser is negligible. Hence, this is not fully an 'in-situ' method.

b) "Internal" calibration (in-situ), using an intrusive rod for holding the radioactive tracer, at the actual solids flow: The advantage is that this method accounts for the attenuation due to the solids and includes the flow fluctuations in the calibration data. But, it provides only a few calibration points within reasonable time. This limitation would necessitate extrapolation to more calibrations points by the Monte-

Carlo based simulation developed in our laboratory by Yang (1997) and Gupta (2002). It is also necessary to manually repeat the calibration for each different experimental operating condition. A schematic showing the comparison of "external" and "internal" calibration setups is shown in Figure 6.2.

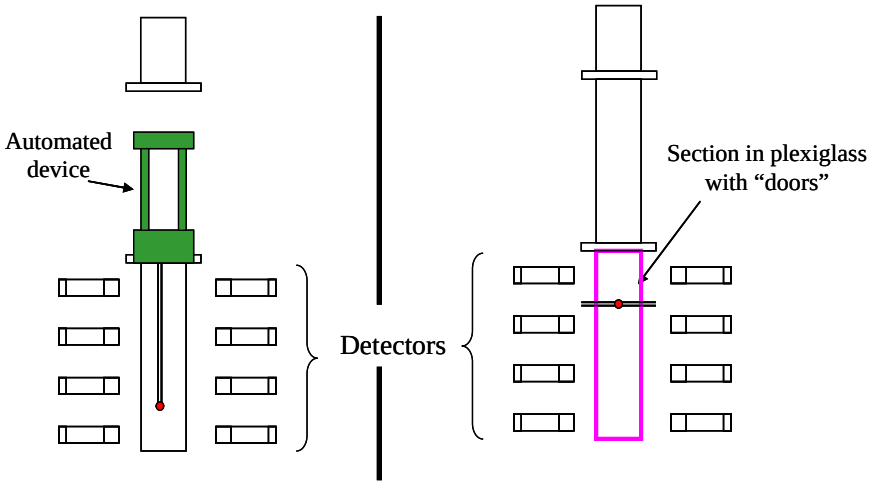

Figure 6-2: a) Schematic of the "external" calibration with an automated device; b) Schematic of the "internal" calibration through the walls.

A major issue is whether we can really assume that the γ-ray attenuation by the solids in the riser is negligible. Accordingly, an evaluation was performed to determine the effect due to the solids inside the riser. Beer-Lambert's Law and parameters obtained from the literature were used in the evaluation. Figure 6-3 shows the percentage differences between the γ-ray attenuation for air only and for air with solids (glass beads) over different distances. We can clearly see that even with 2% solids in the system, a value that is typical in the fully-developed region of a gas-solid riser, the attenuation due to the solids is *not* negligible. Indeed, it is about 10% at 30 cm distance between the radioactive tracer particle and the detector. Hence, we used the "in-situ" calibration method for all the operating conditions.

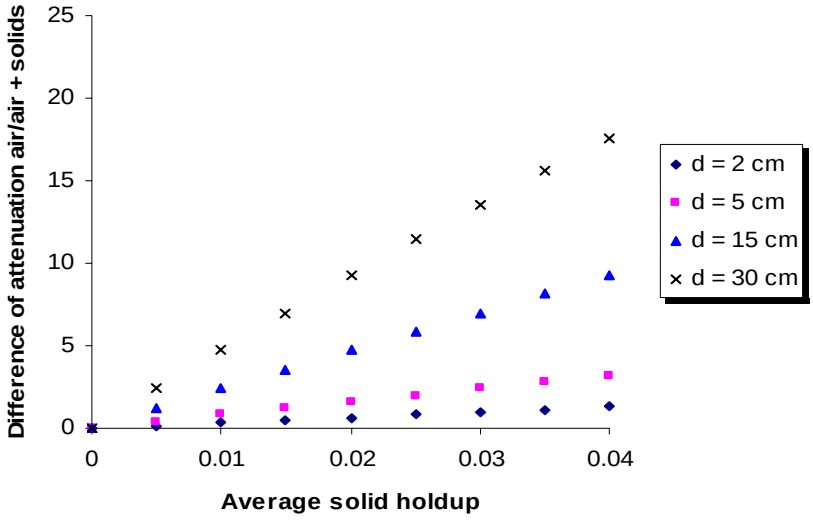

Figure 6-3: Difference in γ-ray attenuation of air only and of air with solids as a function of the solids holdup and the distance, where *d* = distance between the particle and the detector.

In the fully developed region of the riser, solids can reach high velocity (typically around 4–6 $m \cdot s^{-1}$ or higher, depending on the operating conditions). In such a case, the reconstruction of the trajectory of the radioactive tracer may be affected by what we call "dynamic" bias. In a previous study, Rammohan *et al*. (2001[a]) showed, for a circular tracer trajectory in a plane that this dynamic bias depends on the acquisition frequency of the counts. To study this effect, we designed an experiment that enables us to reproduce the range of high velocities of the radioactive tracer in the riser. We used a 6" diameter column, similar to our riser section, and with the same detectors' packing arrangement around it. The radioactive tracer particle was placed at the extremity of a small steel 'bullet' (1 cm length) and dropped from the top of the column. Due to gravity, the radioactive tracer is accelerated up to 4 $m \cdot s^{-1}$ (depending on the initial position) in free-fall. The trajectory of the tracer can be readily determined. Thus, by comparing the CARPT reconstructed trajectory with the actual calculated trajectory, the accuracy of the CARPT technique for this system was evaluated and the best sampling frequency for the CARPT experiment was chosen to be 200Hz.

6.1.1d Detector Positioning

The earlier study of Roy *et al.* (2002) proposed the implementation of CARPT in the gas-solid riser using 3 detectors per plane, placed 120 degrees apart, to get a desirable resolution. This arrangement is shown in Figure 6-4a. Based on this work, support for the detectors was designed as shown in Figure 6-4b and was used for both CARPT calibration and the experiment. It consists of two independent parts. Each part has two plates at each extremity that can hold 6 to 8 extruded aluminum bars. The advantages of this structure are portability and multi-functionality. We can use this system for different configurations of the detectors, such as 45 or 60^o angles between each detector.

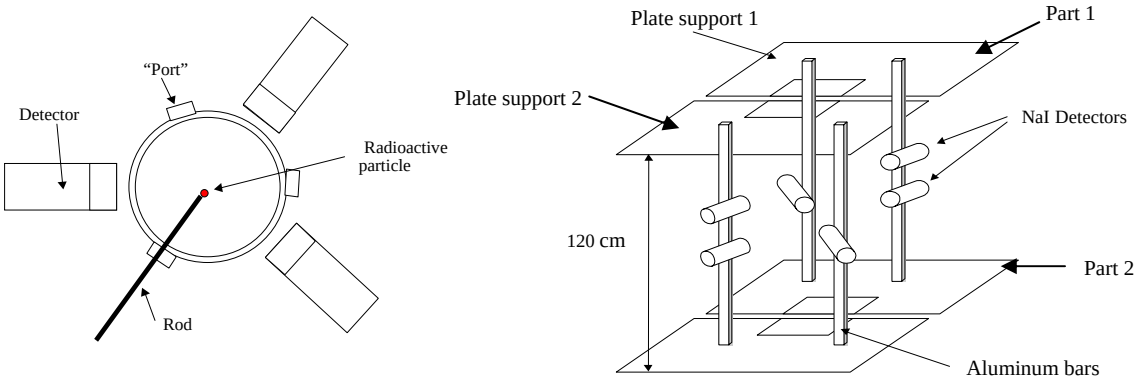

(a) **(b)**

Figure 6-4: a) Schematic view of the calibration procedure; b) Schematic diagram of the detectors support.

To accommodate both the "in-situ" calibration of detectors and the actual CAPRT experiments, a plexiglas section replaced the glass sections of the riser. This new section had three "ports" per plane placed at 120 degrees from each other (Figure 6-4a), with the "ports" in successive planes having a lag angle of 60 degrees. There were 7 planes of such "ports" with a spacing of 12 cm between them. Such a configuration allowed visualizing a total height of 72 cm for the CARPT experiment.

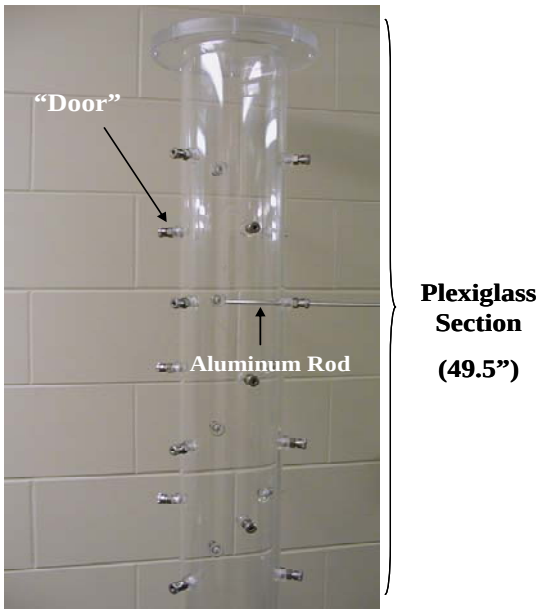

Figure 6-5: Photograph of the calibration section illustrating the calibration ports.

6.1.1e Procedure for Introduction and Recovery of Radioactive Tracer

Safety concerns for handling the single radioactive tracer particle in a pilot-plant scale system, like the CFB, are of prime importance. There are three key issues in this regard. One is the possibility of the single radioactive tracer to "leak out" into the environment during the riser operation. Second is the safe method for introduction and recovery of the radioactive tracer particle so as to reduce the radioactive dosage exposure for the personnel during these processes. Third is the possibility of the tracer contaminating all the solids in the system due to attrition, which was mentioned earlier. The first issue is resolved by checking repeatedly for possible air leaks through out the CFB system prior to the introduction of the tracer particle. An efficient procedure is to employ a pressure leak test. In such a test, the CFB system is initially pressurized and motive air is suddenly shut off. By looking at the pressure decay curves from the pressure transducers placed along the CFB loop, one can identify possible leaks. Indeed this method was employed for the leak test in the setup used at Sandia National Laboratory (SNL) (discussed later). Regarding the second issue, a protocol for introduction and recovery of the radioactive tracer particle was proposed and validated, as described

below. The final issue of possible solids contamination was resolved by tracer particle coating with Parylene. No attrition of scandium was detected and the Parylene layer remained intact.

First, the riser operated without the radioactive tracer particle for at least 2 hours to fill all the "dead zones" (e.g. top of the plate of the disengagement, connections, pipes) with the solids. All the connections of the riser loop were carefully inspected to detect any possible leakage.

The radioactive particle was pre-mixed with a small amount of glass beads (about 100 g) in a sealed container. Then, the solids plus the tracer were introduced carefully at the top of the down-comer (which was partially filled with solids) via an opening on the hopper. The tracer was always monitored with a Geiger-Muller counter to insure its position. Some solids were finally added to fill the down-comer to the required level.

The process was started by opening the air flow and by adjusting the air flow rate to the desired value with the rotameter, and then the solids valve from the down-comer was opened. The acquisition system was engaged to start recording the counts from the scintillation detectors. During the experiment, one Geiger-Muller (GM) counter was placed in front of the air-bag filter in case the radioactive particle leaves the loop, and two others at the bottom and top of the riser.

When the experiment was completed, the radioactive tracer was recovered from the bottom of the riser and placed in a sealed bag. The recovery of the single tracer was performed by repeatedly extracting a smaller sample of solids from a larger lot showing activity with GM counter and finally converging to a single particle. The recovered particle was checked for its activity at a fixed place before and after an experiment so as to assess any particle attrition. A more elaborate description of the procedure for safe handling of the radioactive tracer, approved by the radiation safety office, is available in our laboratory manuals.

6.1.1f Post processing of the data

Post processing of the time series data from the 18 detectors used requires the precise determination of the entry and exit time of the radioactive tracer in the CARPT

section of the riser. Hence, two sentry detectors are placed at the entrance and exit of the CARPT section and heavily shielded with lead sheets so that these detectors can "see" only the cross sectional plane along the axis of the detector as shown in Figure 6-6. Solids internal recirculation and backmixing in the riser necessitates precise determination of the residence time of the tracer in the section, which requires shielding of the sentry detectors shown in Figure 6-6. This is an improvement on the method used by Godfroy *et al.* (1999) and Roy (2000), where data was acquired only when the tracer was found to pass through the cross section of the sentry detector (without shielding). In the presence of high backmixing, such a process may lead to data being acquired when the tracer is outside the section of interest and may finally lead to an imaginary reconstructed position within the CARPT section.

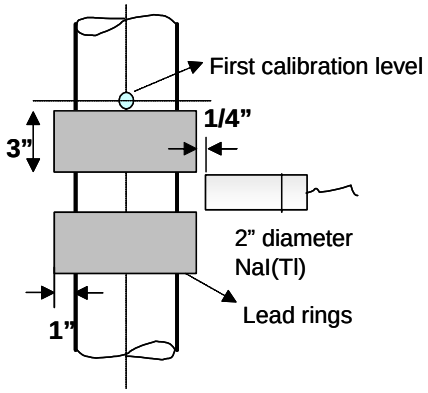

Figure 6-6: Schematic of the lead shielding provided for a sentry detector.

During every single passage of the tracer through the riser, the detector responses during the time that the tracer resided in the CARPT section was fragmented and then used for obtaining the Lagrangian velocity trace. Note that the trajectory of the tracer particle through the section of the riser is independent of any other previous trajectory and hence all such trajectories were 'added' to build the statistics for the velocity traces. Position rendition at every 'instant' was done as discussed in Chapter 3. The processing of the trajectory data to derive the velocity field and turbulence parameters was performed based on the work of Degaleesan (1997). It should be noted that the time during which useful data are collected (i.e. the time during which the tracer resides in the

CARPT section), is relatively very small compared to the time that the tracer takes to complete one cycle along the CFB loop. Hence, it was typically observed that for an experimental run of 50 hours, the time during which useful data was acquired is 2-3% of the total time of the experiment. Typically the total number of occurrences (instantaneous positions) of the tracer in the section investigated varied from 0.8 – 1.75 million. Note that the data was acquired at 200 Hz.

6.1.2 Experimental Setup

The CFB setup used for the experiments has been described in the Chapter 4. The CARPT experiments were performed in a section considered to be fully-developed (in a time-averaged sense) at an axial height varying from 4.6 – 5.85 m. This corresponds to a dimensionless axial height *z/D* varying from 30.5 – 38.5. The zone of investigation for CARPT is shown in Figure 6-7a. The detector support system along with the detectors is shown in the zoomed in photograph in Figure 6-7b.

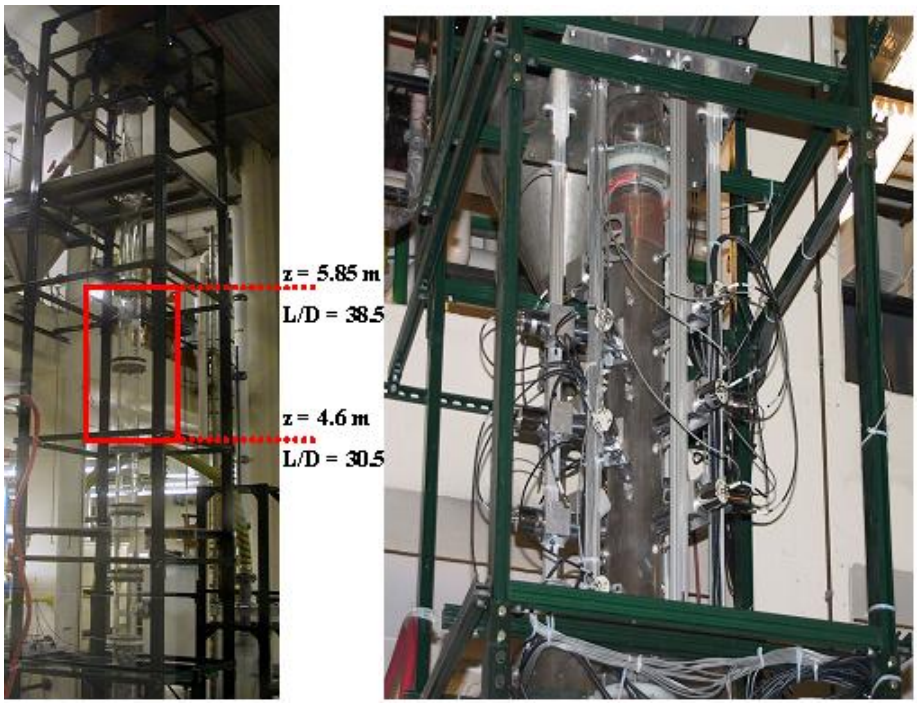

(a) (b)

Figure 6-7: Photographs showing the zone of investigation for CARPT

6.1.3 CARPT at Sandia National Laboratory

The CFB setup at Sandia National Laboratory (SNL) has different dimensions than that in our laboratory. Riser is a 5.5 inch I.D. and is 17 feet tall. The Plexiglas down-comer is 14 inch in diameter and is supplied with fluidizing air through several ports at the bottom and along the walls. Further details of the exact setup can be found in Trujillo *et al.* (2001). The large down-comer with the regulated fluidizing air through the standpipe and the down-comer provided a higher overall solids mass flux through the riser. The overall solids mass flux was determined using the method described in Chapter 4 and was found to be higher than that found for the flow conditions at CREL. The details of the operating conditions were shown earlier in Table 5-3. CARPT experiments on this setup were used to acquire solids velocity field data at high flux conditions. The zone of investigation for the CARPT experiments was at an axial height varying between 2.08 – 2.79 m with a dimensionless height (*Z/D*) range between 14.9 and 20. CARPT experiments were performed using the same procedure described earlier at three operating conditions.

6.2 CT Setup on Gas-Solid Riser

Gamma ray tomography experiments were performed on the CREL gas-solid riser facility at two different axial planes within the same zone of investigation as used for the CARPT experiments. The operating flow conditions for the CT experiments were maintained the same as those of the CARPT experiments. The experiments were performed at dimensionless axial heights (*Z/D*) of 33 and 36. Details of the CT setup employed can be found in Kumar *et al.* (1997) and in Roy *et al.* (2004). To perform tomography measurements on the CREL riser, the CT setup that was available had to be mounted on the gas-solid riser system. To have the CT setup, the radioactive source, detectors, lead shielding, stepper motors and the data acquisition system had to be dis-assembled from its present position and re-assembled back on the gas-solid riser setup. A photograph showing the tomography setup on the gas-solid riser is shown in Figure 6-8.

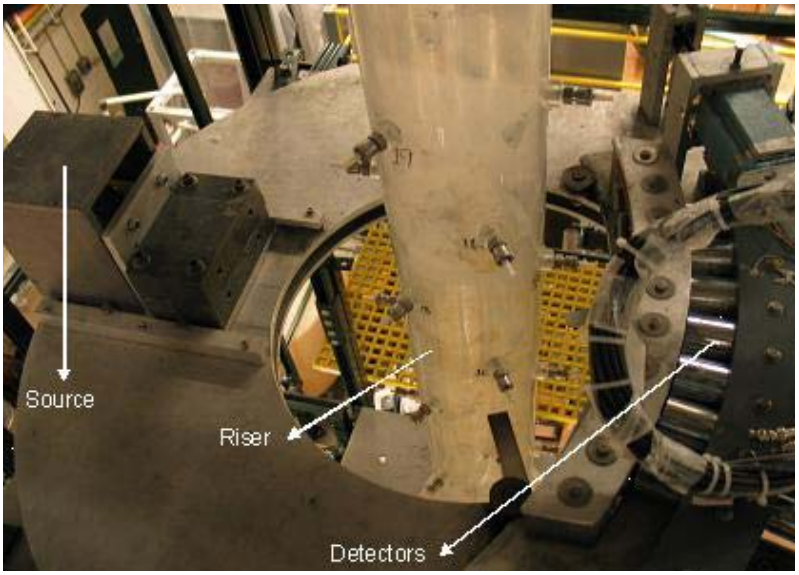

Figure 6-8: Photograph of the CT setup on gas-solid riser at CREL

In order to validate the CT setup on the riser, a phantom scan was performed after its re-assembly. The phantom scan was a beaker filled with water. An alternating-minimization (AM) algorithm described in Chapter 3 was used for the image reconstruction. The reconstructed image is shown in Figure 6-9 and is in good agreement with the true image (constant density inside the beaker).

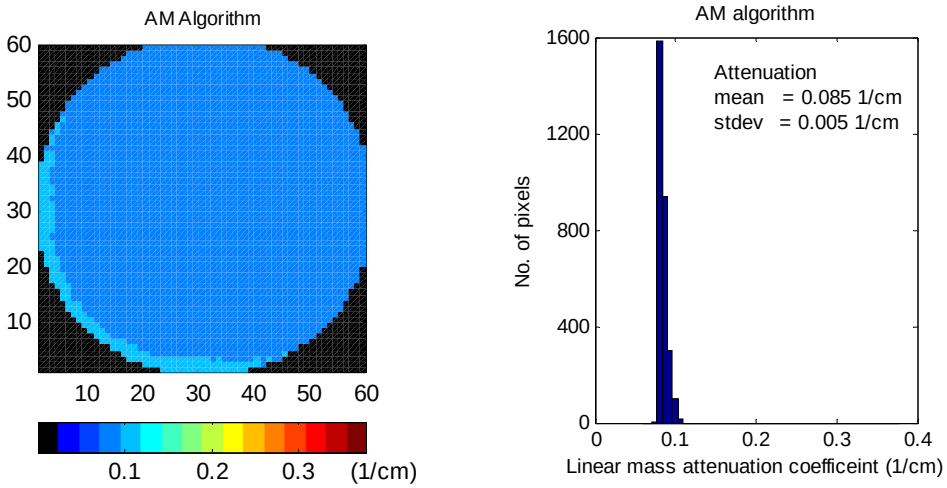

Figure 6-9: a) Reconstructed phantom scan of a beaker filled with water; b) Spread of attenuation in the domain.

6.2 Results and Discussion

In this section, the solids mean velocity field obtained from the CARPT experiments is discussed first and later the solids holdup from CT experiments. Comparative and symbiotic analysis of these two results are used to understand the complex solids flow structure in two different flow regimes- Fast Fluidization and Dilute Phase Transport.

6.3.1 Solids Velocity Field

6.3.1a Instantaneous Positions and Velocity Calculations

The knowledge of the tracer particle trajectory provides insights into the solids dispersion and mixing. Figure 6-10 shows the projection of the trace of the instantaneous particle positions sampled at 200Hz during a single passage through the riser visualized in three different planes – *x*-*z*, *y*-*z* and *x*-*y*. As the tracer particle moves around the CFB loop, it periodically resides in the zone of interrogation in the riser (Figure 6-7). During each passage through the riser, completely independent trajectories are obtained. Two such trajectories are depicted as examples in Figure 6-10. Clearly, in some instances the tracer particle passes through the section always moving upwards, while at other times it undergoes internal recirculation in the section. In both cases, the tracer particle takes a tortuous path undergoing acceleration at times and deceleration at other times.

The tracer positions at which its axial velocity is negative (Figure 6-10b) are indicated in red. This run was conducted at U_g^{riser} of 3.2 $m \cdot s^{-1}$ and G_s of 26.6 $kg \cdot m^{-2} \cdot s^{-1}$ under the fast fluidization regime. It can be observed that the tracer can acquire negative axial velocity starting near the center (core region) and often maintains such negative axial velocity as it moves towards the wall (annulus region). So during this episode the tracer particle falls both within the core as well as in the annular region. Analyzing many such trajectories shows that few times the tracer particle passed through the zone of interrogation straight with very little or no backmixing, while many more times it underwent internal recirculation with the tracer falling down. Also, it was observed that the span of the tracer residence time within the zone of interrogation varied widely

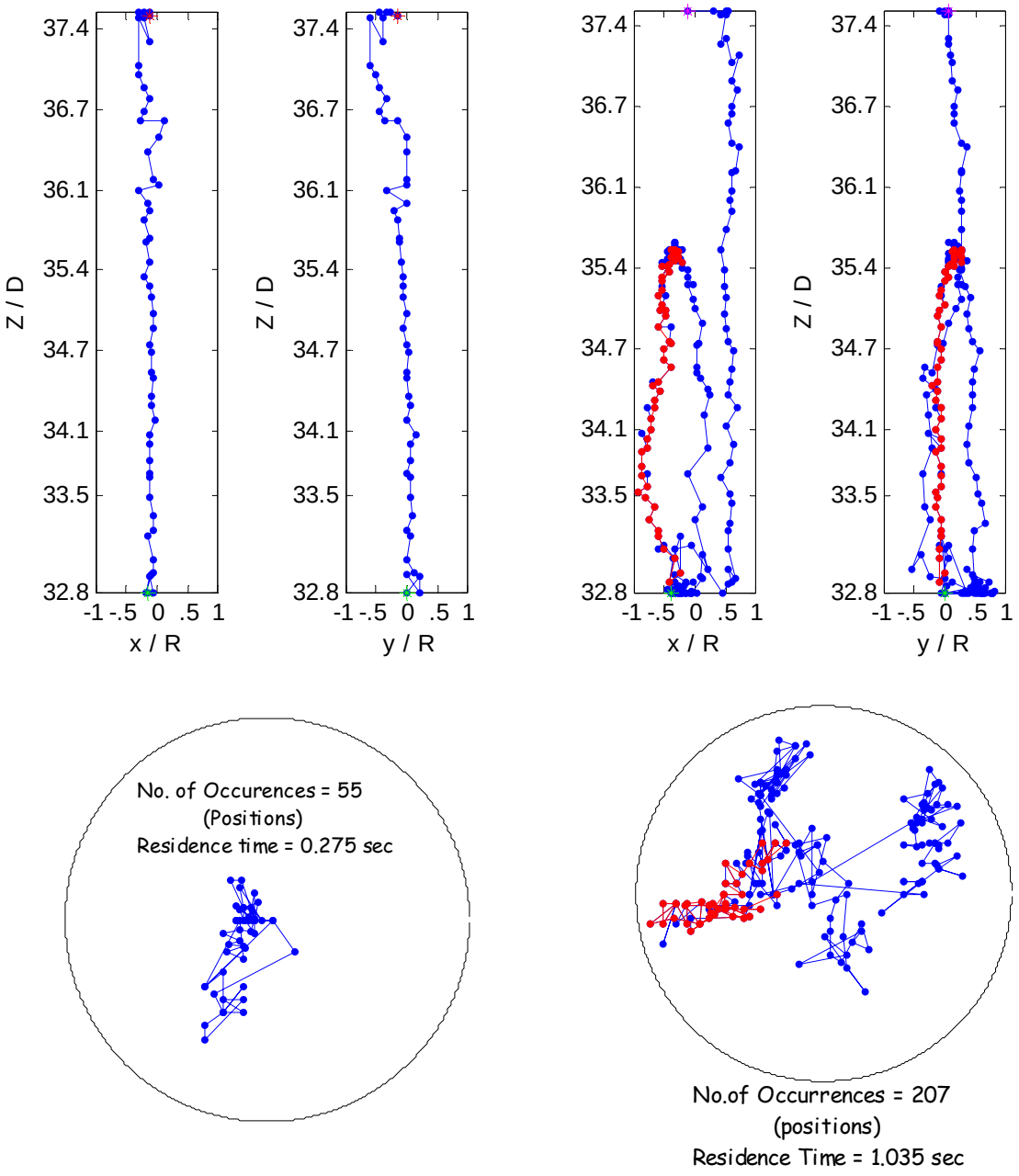

(a) (b)

Figure 6-10: Instantaneous position traces in *x*-*z*, *y*-*z*, *x*-*y* planes during two different passages through the CARPT section when the tracer: a) passed through the section straight; b) underwent internal recirculation inside the section. The operating conditions were – U_g^{riser} = 3.2 m·s^{-1} and G_s = 26.6 kg·m^{-2}·s^{-1} under the Fast Fluidization regime. Red points indicate downflow.

from 0.1 – 100 sec. That is three orders of magnitude variation of residence times in the section investigated. Such large residence time variation (without stagnation) explains why very large values of axial dispersion coefficients are often reported.

The accuracy of tracer position reconstruction is influenced by the way detectors are packed around the column (Larachi *et al.*, 1994; Roy *et al.*, 2001). Since near the lowest and highest axial levels in the CARPT section there will be a fewer number of detectors, the tracer position reconstruction near these axial levels is bound to be less accurate compared to the section in between. This can indeed be observed from the cluttering of the tracer positions (Figure 6-10) near the end axial planes of z/D = 32.8 and 37.4. Hence, to reduce the position error propagation to velocity calculations, the zone of interrogation was reduced to the section between the axial planes of z/D = 33.5 – 36.7. This translates to an interrogation zone of 48 cm between the axial heights of z = 5.1 – 5.6 m. All the subsequent CARPT results reported are within this zone of interrogation.

Figure 6-11 shows the evolution of the tracer axial and radial position, with time. Figure 6-11b shows the radial position time series, which indicates that the solids motion in the horizontal plane is principally random (dispersive). However, the actual mechanism of the lateral movement of the solids can be understood only once the radial mixing parameters are evaluated. It can also be noted from Figure 6-11b that the particle occurrences near the wall are more numerous than near the center or core region. The tracer particle axial position trace in time shown in Figure 6-11a indicates extensive internal recirculation. Also, the axial flow looks like a typical wall bounded flow, although there is no physical wall at the top of the riser in the axial direction. We are unsure whether the deflector placed at the exit of the riser causes such behavior. However, it is clear that in the axial direction the motion is ultimately directed upward with the particle tumbling up and down during a single passage through the riser section. Hence, both such large scale internal recirculation, superimposed with the fine scale particle fluctuations contribute to the solids axial backmixing.

To further understand the particle dispersion in risers, Hurst coefficients of the fluctuating velocity time series were evaluated following the method employed in Cassanello *et al.* (1995). For the operating conditions in the FF regime (U_g^{riser} = 3.2 m·s^{-1} and G_s = 30.2 kg·m^{-2}·s^{-1}), Hurst exponent in the axial direction was found to be 0.705,

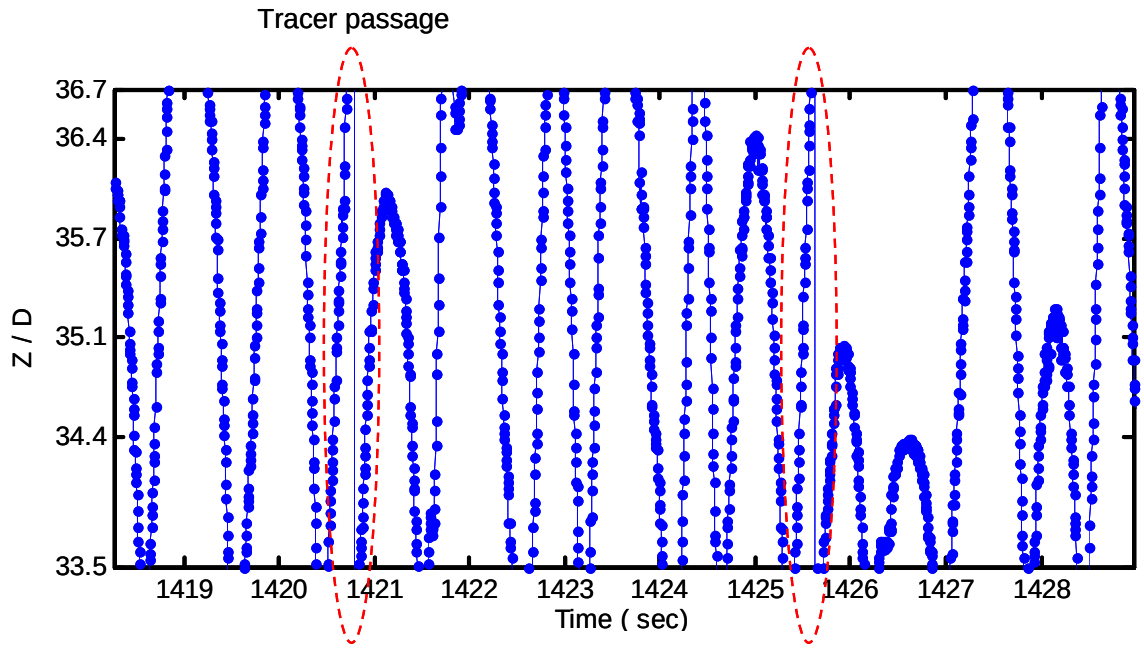

(a)

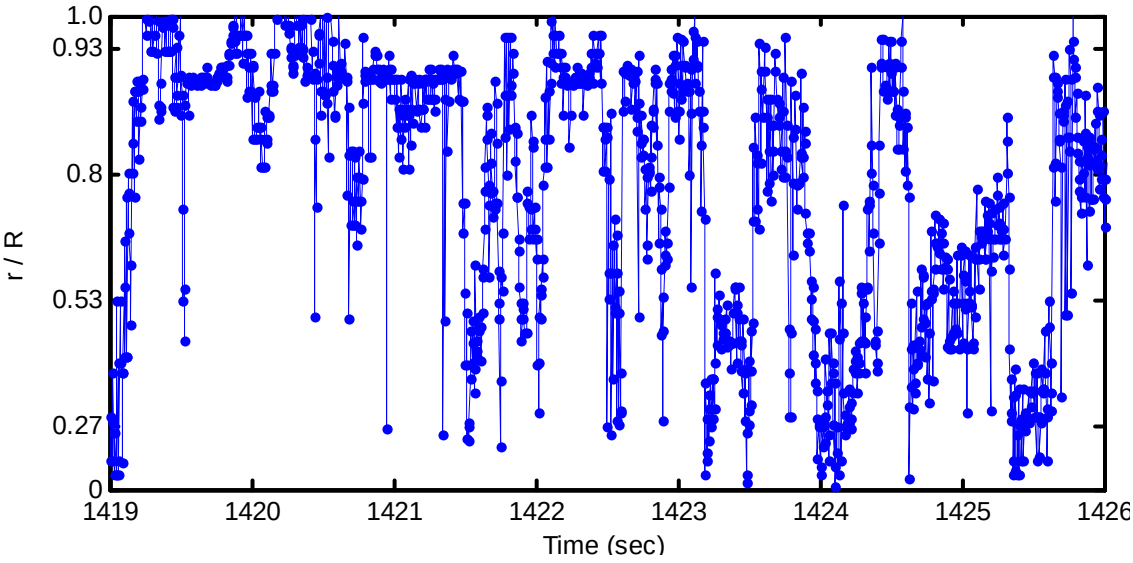

(b)

Figure 6-11: Variation of the tracer position with time visualized for a small period in the a) axial and b) radial directions. The operating conditions were – U_g^{riser} = 3.2 m·s^{-1} and G_s = 26.6 kg·m^{-2}·s^{-1} under the Fast Fluidization regime.

while for the coordinates in the transverse plane, they were found to be equal to a value of 0.429. Also, for a condition in the DPT regime (U_g^{riser} = 3.9 m·s^{-1} and G_s = 33.7 kg·m^{-2}·s^{-1}), axial component had a value of 0.607 and the radial and azimuthal components had values of 0.411 and 0.363 respectively. Hence, in the transverse plane the dispersion of particles is smaller than those moving in Brownian way and is probably imposed due to the particle interactions. However, high values, greater than 0.5, for the axial component indicates that the correlations of the fluctuations persist in time and is probably imposed due to intense axial mixing.

A time derivative of the tracer particle position yields the instantaneous Lagrangian velocity of the tracer. Now, by invoking *ergodicity*, we convert the velocity trace of the single tracer particle to the time-averaged Eulerian velocity field that is representative of the entire ensemble of particles. To perform this calculation, we assume an imaginary grid in the 3D space for the riser section. For any two successive tracer positions, the velocity is calculated by time-differencing the position data and assigned to all the compartments of the grid, where the velocity vector falls. Thus, one can build a histogram (i.e. probability density function (PDF)) of the instantaneous velocities in each compartment of the grid, given that the tracer particle visits these compartments a *sufficient* number of times. Hence, by claiming that the system is ergodic and stationary, one asserts that the moments of the histogram, calculated from the ensemble of observations for long enough time, are the same as those that would be obtained by analysis of time series of solids particle velocity at the given point (such as obtainable by a probe). Before discussing the velocity field results obtained from such assumptions, one needs to validate them, *post facto* as shown below.

6.3.1b *Post Facto* Validation

The *post facto* validation of the velocity field results included the following:

a) Checking for the ergodic and stationarity assumption – This was performed by checking for the velocity and turbulence quantities for occurrence independence.
b) Checking for mesh independence of the Eulerian quantities – This was performed by a trial and error procedure by varying the number of compartments for the column and using grids of different mesh sizes.

c) Checking for proper filtering procedure to remove the electronic and Poisson generated noise in the reconstructed positions – Noise was removed by following the wavelet filtering procedure proposed by Degaleesan *et al.* (2002). A trial and error procedure was performed to select the proper signal threshold for filtering.

The results for each of the above procedures are discussed below.

Wavelet Filtering

As discussed by Degaleesan *et al.* (2002), it is necessary to filter the instantaneous position data from a CARPT experiment to eliminate the contribution of spurious velocities to the measured instantaneous velocities. To achieve wavelet filtering, a signal threshold for the wavelet packet decomposition, *st*, needs to be selected such that the noise filtered from the data has the characteristics of white noise. In other words, the filtered signal should be random with zero mean and variance of one. The choice of *st* values depend on the extent of noise in *x(t)*, *y(t)* and *z(t)* series. As proposed by Degaleesan *et al.* (2002), the values for *st* are arrived at by looking at the filtered signal of the randomly selected data sets. However, it is not always possible to achieve the filtered signal to be white irrespective of different *st* values. Hence, a method proposed in the reviewer comments of Degaleesan *et al.* (2002) paper and as implemented by Ong (2003) was used to filter the data. By starting with the estimates of *st* values, the data was further processed to obtain the Lagrangian auto-correlation functions. These correlation function profiles are compared for the unfiltered data and the filtered data for different possibilities of *st* values. Except at the zero time lag, the correlation profile should converge to zero. However, this same behavior in the auto-correlation function was seen for all the different *st* values. Hence, as proposed by Ong (2003) the closest *st* value for which the correlation profiles match well with the averaged correlation profiles (averaged over the different *st* values) is chosen as the appropriate threshold value.

Figure 6-12 compares the axial and the radial Lagrangian auto-correlation profiles obtained from unfiltered and filtered data at different *st* values. It can be clearly observed that all the profiles of filtered and unfiltered fall on one another indicating little or no differences due to filtering. This result is unlike that from Ong (2003) where an artificial kink was observed in the profiles without filtering for bubble column flows. The reason

for the filtering to show no effect on autocorrelations in riser solids flow could be that the Poisson and electronic noise generated is very small compared to the actual solids flow fluctuations.

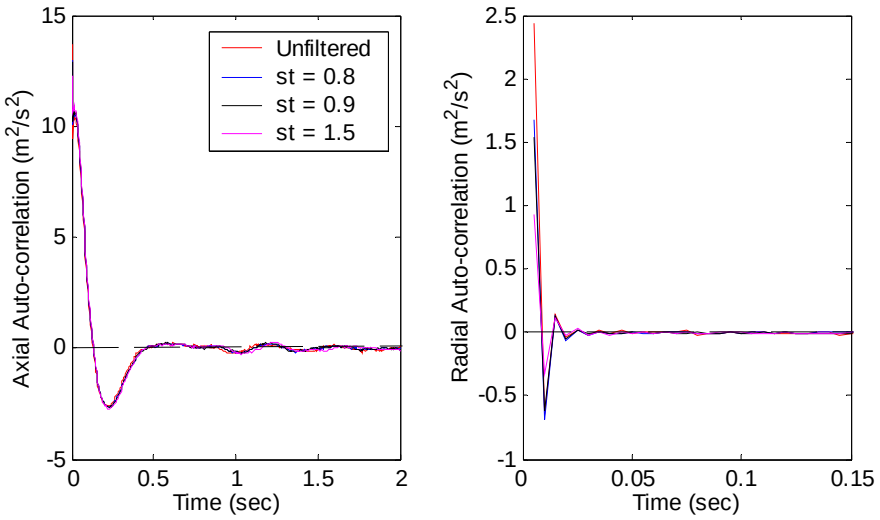

Figure 6-12: Spatially averaged Lagrangian auto-correlation function profiles in a) axial; b) radial directions (U_g^{riser} = 3.2 m·s^{-1}; G_s = 26.6 kg·m^{-2}·s^{-1}; FF regime).

The auto-correlation function seen in the Figure 6-12 is one of the two typical functional forms of the auto-correlation coefficient. This type shows negative loops, before finally converging to zero. The other type and the most common is the one which exhibits exponential decay with time. These types of correlation coefficients are commonly observed in homogeneous isotropic turbulence and represent a continuously increasing rate of dispersion (Snyder and Lumley, 1971). The former type of correlation functions have been commonly measured for heavy particles in turbulent gases (Mei *et al.*, 1991). Due to the inertial effects, heavy particle tend to fall out of correlated flows or eddies quickly, since the particle inertia prevents it from following the high frequency fluctuations of the fluid. The tracer particle, which is a part of an eddy structure moving upward, has the tendency to get caught in an adjacent down flowing structure, which causes the negative loops in the axial auto-correlation. The presence of the negative loops (axial auto-correlation) in Figure 6-12 can be explained based on the internal solids recirculation pattern. Similar negative loops can be observed in Figure 6-12 in the radial

auto-correlation function, but with much faster decay compared to axial. The presence of negative loops in the radial auto-correlation can be explained based on the lateral particle transfer or the particle exchange between core and annulus. Detailed discussion on the auto-correlation functions is done in the next chapter.

Further, we need to check if filtering affects the computed velocity field. Figure 6-13a shows the comparison of the unfiltered and filtered (with different *st* values) time-averaged velocity profiles for the operating conditions in the FF regime (U_g^{riser} = 3.2 m·s^{-1}; G_s = 26.6 kg·m^{-2}·s^{-1}). Also, Figure 6-13b shows the azimuthally and axially averaged radial profiles of the axial and radial Reynolds stresses and the shear stresses computed from filtered and unfiltered data. The message from the plots in Figure 6-13 is that there are little or no differences in the velocity and turbulent stress profiles before and after filtering. Similar conclusion was reached from the CARPT data for the operating conditions in the DPT regime (U_g^{riser} = 3.9 m·s^{-1}; G_s = 33.7 kg·m^{-2}·s^{-1}) as shown in Figure 6-14. However, one can see some differences in the turbulent kinetic energy profiles of the unfiltered and the filtered data with a very high threshold value of *st* =1.5. With such high threshold values, it was observed that the filtered noise is not white and shows trends of the flow fluctuations. Hence, as the threshold value increases, the data is 'over filtered' and thus affects the profiles of flow fluctuations. For this reason, such high threshold values (*st* > 1) were not considered for comparison. Thus, for the solids flow in the riser, flow fluctuations are relatively large so as to allow one to neglect the contributions due to the Poisson and electronic generated noise. Hence, for all the flow conditions reported, raw data was not filtered to compute the velocity field.

Ergodicity and Stationarity

Next, we need to check if the experiments reflect stationarity in the system, and whether the quantities computed from the raw data converge beyond a certain time window. In other words, it is necessary to ensure that statistically sufficient information has been collected so that the presented profiles of the velocity field are indeed representative of the solids flow field at a given operating condition. Figure 6-15a shows a typical result for the time-averaged velocity profiles computed from both the entire set of data collected and from 50% of the data. Also, Figure 6-15b shows a similar

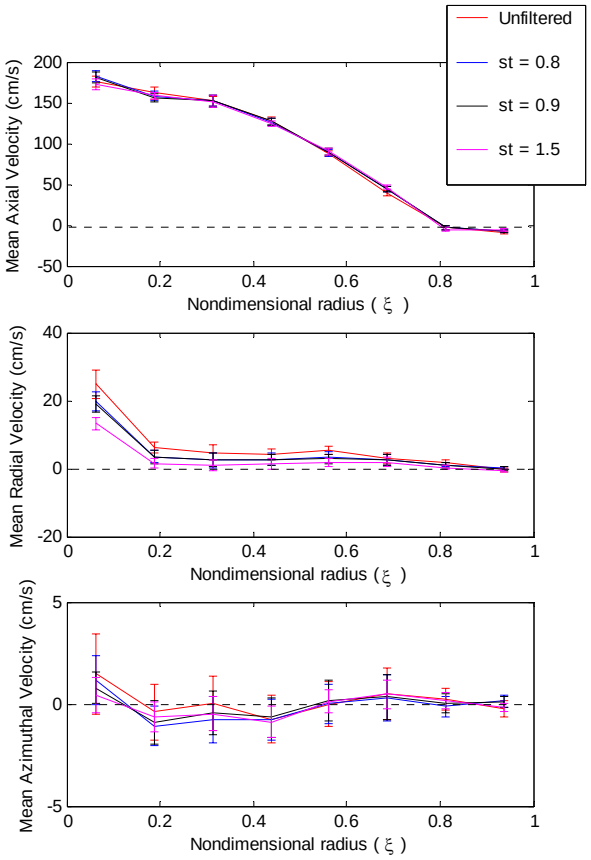

(a)

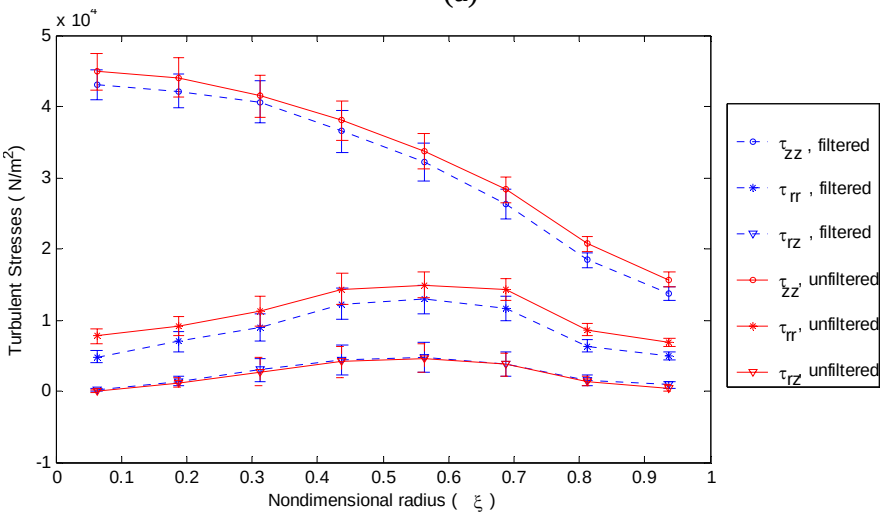

(b)

Figure 6-13: Azimuthally and axially averaged radial profiles of Eulerian quantities such as a) Time-averaged velocity components; b) Three components of turbulent stresses, comparing unfiltered and filtered data (U_g^{riser} = 3.2 m·s^{-1}; G_s = 26.6 kg·m^{-2}·s^{-1}).

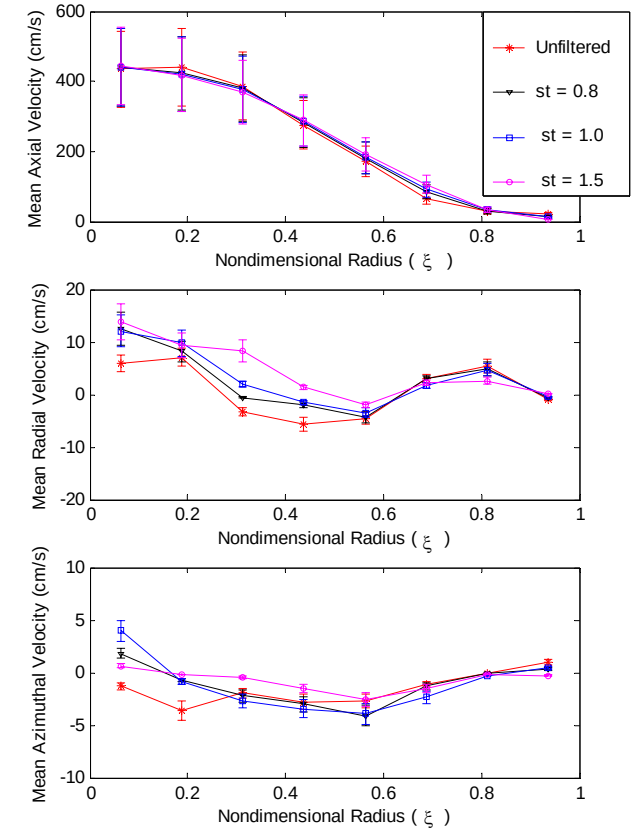

(a)

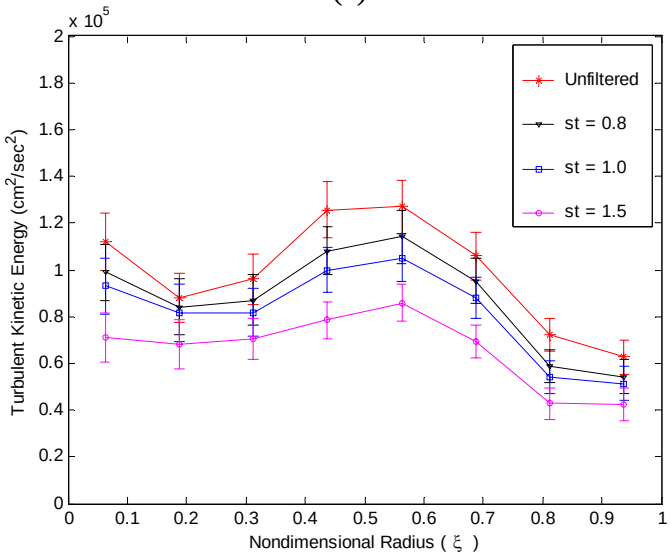

(b)

Figure 6-14: Azimuthally and axially averaged radial profiles of Eulerian quantities such as a) Time-averaged velocity components; b) Turbulent kinetic energy, comparing unfiltered and filtered data (U_g^{riser} = 3.9 m·s^{-1}; G_s = 33.7 kg·m^{-2}·s^{-1}).

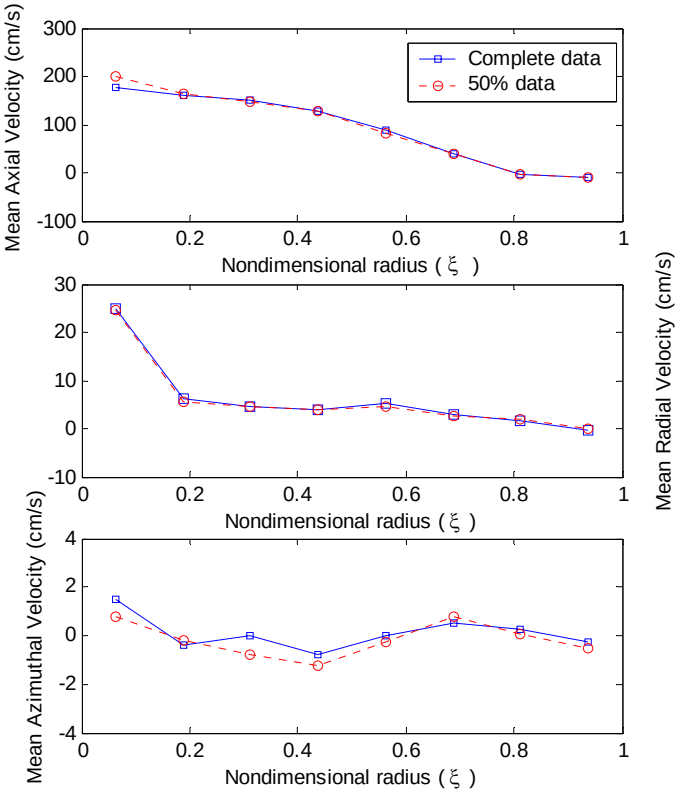

(a)

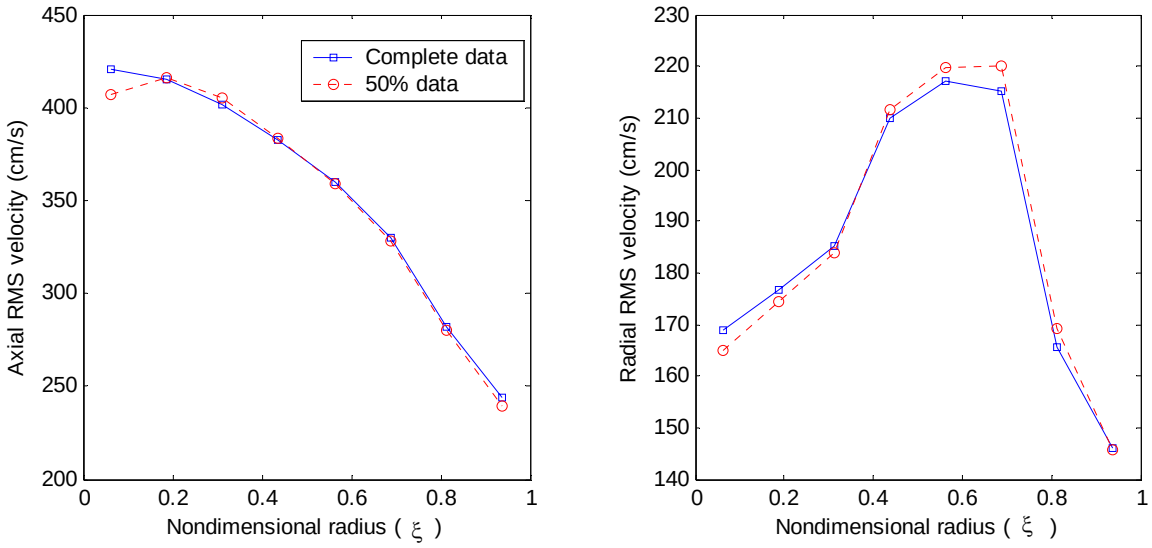

(b)

Figure 6-15: Azimuthally and axially averaged profiles, illustrating the effect of statistics of ensemble averaging at operating conditions of (U_g^{riser} = 3.2 m·s^{-1}; G_s = 26.6 kg·m^{-2}·s^{-1}) a) Velocity components; b) Axial and radial RMS fluctuating velocity.

comparison of the axial and radial root mean square (RMS) fluctuating velocities obtained from the entire data and from 50%of the data at the operating conditions in the FF regime at U_g^{riser} = 3.2 m·s^{-1} and G_s = 26.6 kg·m^{-2}·s^{-1}. It is apparent from these plots that computed profiles of the solids phase have converged and do not vary with increasing the length of the experiment. One should note that the convergence was found not only with respect to the time-averaged quantities, but also with the turbulent quantities too. Besides, one can also look at the radial profile of the particle occurrences (per unit volume) which is proportional to the solids holdup under 'well-perfusedness' assumption (discussed later). Figure 6-16 shows the comparison of the radial profile of the frequency of particle occurrences for the entire data set and for 50% of the data chosen randomly. This plot illustrates that the experiment has sufficient statistics to satisfy the ergodic assumption.

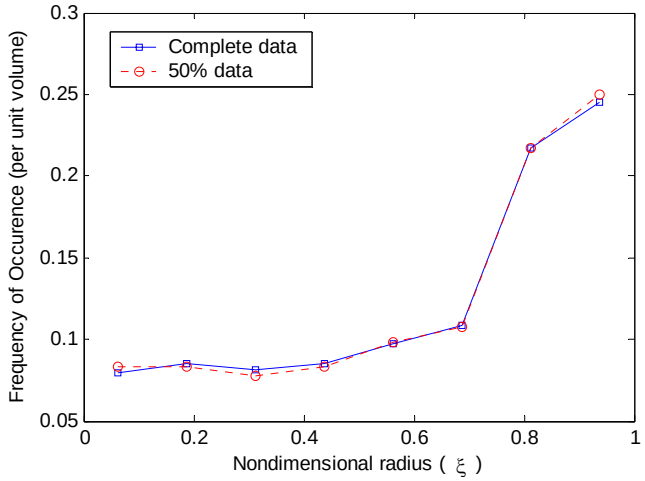

Figure 6-16: Comparison of the entire and 50% data for the radial profile of frequency of occurrences at operating conditions of U_g^{riser} = 3.2 m·s^{-1}; G_s = 26.6 kg·m^{-2}·s^{-1}.

The convergence of the ensemble averaged solids velocity profiles depends on having enough statistics so that the PDFs of the velocities do not change with further increase in the number of occurrences. This can indeed be observed by plotting the dependence of the mean velocity (e.g. axial component) with the total number of occurrences in each of the compartments of the imaginary grid. Figure 6-17 shows a typical plot of the mean (ensemble averaged) axial solids velocity with the total

occurrences (in a compartment) at three different radial locations at an axial height of *Z/D* = 35 in the riser. It can be observed that the profiles converge to 95% of the confidence intervals of its asymptotic value. This is a *post facto* evidence of a multiphase reactor being stationary and ergodic. Further, this also reflects reproducibility of the CARPT experiments, because each trajectory is independent and can be chosen in any sequence from a set of runs for a given operating condition.

Mesh Independence

The third issue for the post facto validation of the results is to establish mesh independence of the computed quantities. Three different compartment sizes as stated in Table 6-2 ranging from coarse to fine grid were evaluated. Figure 6-18 shows the mesh dependence of the radial profiles of the time-averaged velocity and the turbulent kinetic energy. It can be seen that there are small differences in the profiles from Mesh 3, while the profiles from Mesh 2 and 1 are approximately the same, indicating that the velocity and turbulent quantities from Mesh 1 are grid independent. Note that in Mesh 3 volume of the cells are three times those of cells in Mesh 1 and a similar proportional increase in the number of particle occurrences in each compartment. Hence, for all the experiments, Mesh 1 was employed where the nominal grid size was Δr = 0.95 cm, Δz = 2 cm, and $\Delta\theta$ was varied so that all the cells have equal volume of about 5.7 cm^3.

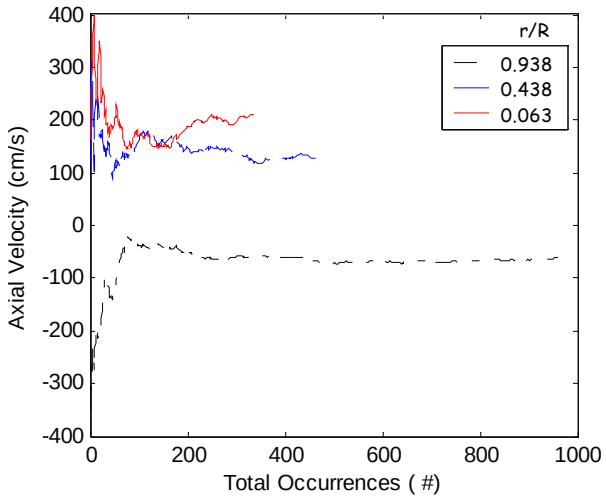

Figure 6-17: Typical plot illustrating the convergence of mean axial velocity with total occurrences in three of the compartments at an axial height of *Z/D* = 35.

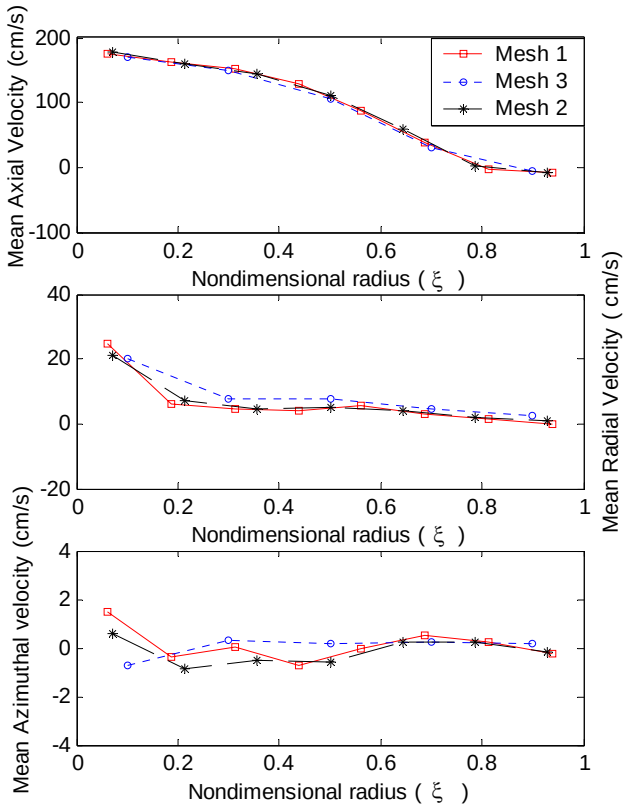

(a)

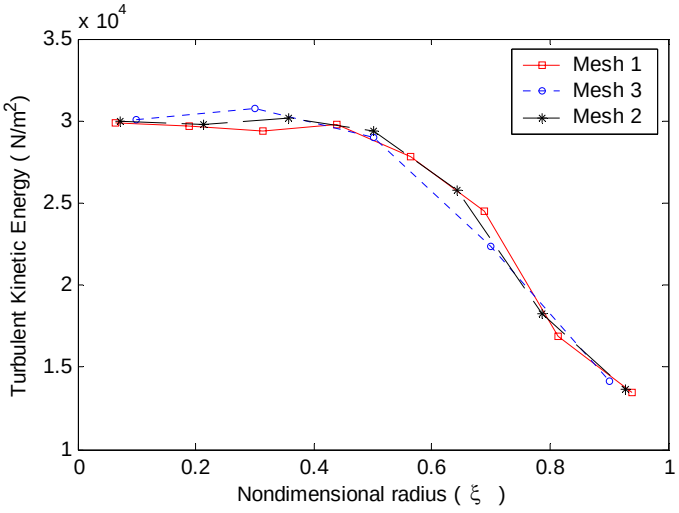

(b)

Figure 6-18: Azimuthally and axially averaged profiles illustrating the mesh convergence for the computed quantities of: a) Time-averaged velocity components; b) Turbulent kinetic energy per unit volume (U_g^{riser} = 3.2 m·s^{-1}; G_s = 26.6 kg·m^{-2}·s^{-1}).

Table 6-2: Details of the three different mesh evaluated to check for mesh independence

	N_r	N_θ (max)	N_z	Total grids	% of volume
Mesh 1	8	15	24	1536	0.065
Mesh 2	7	13	24	1176	0.085
Mesh 3	5	9	20	500	0.2

6.3.1c FF versus DPT Regimes

Earlier studies on riser flow established (e.g. Bader *et al.*, 1988; Miller and Gidaspow, 1992; Bi and Grace, 1995; Davidson, 2000; Parssinen and Zhu, 2001[b]) that in a time-averaged sense, solids flow upwards in the center or core region and downward near the wall, or annulus region, at conditions characteristic of the fast fluidized and heterogeneous dilute flow transport regimes. The typical characteristics of the solids flow in the fast fluidized and dilute phase regimes were summarized in Table 4-3 and discussed briefly in Chapter 4. However, there are only few studies (with intrusive techniques) that presented the velocity histograms (Fiedler *et al.*, 1997) or turbulent stresses (Tsuji et al., 1984; Van den Moortel et al., 1998; Tartan and Gidaspow, 2004). There are no studies presenting the full velocity field that show the components of turbulent stresses, turbulent kinetic energy, eddy diffusivities, solids residence time distribution and the solids holdup maps. In this section, velocity histograms (PDFs), time-averaged velocity vector plots and turbulent stress profiles at various locations in the riser are compared in the two operating regimes to quantify the solids flow structure.

Velocity PDFs

One acquires PDFs of the local velocity components in each of the compartments of the grid as discussed earlier. Figure 6-19 shows the PDFs of the axial solids velocity at three different radial positions (r/R = 0.063, 0.438, 0.938) and at three different axial planes (Z/D = 33.7, 35, 36; z = 5.12, 5.32, 5.47 m) at a particular angular position. The operating conditions for this experiment are in the FF regime with U_g^{riser} = 3.2 m·s^{-1} and

G_s = 26.6 kg·m^{-2}·s^{-1}. Also indicated in each of the PDF plots are the number of particle occurrences in the given compartment, and the mean and standard deviation of the axial velocity. Figure 6-19 leads to the following conclusions: a) large radial gradients in the ensemble averaged axial solids velocity; b) ensemble averaged axial slip velocity (assuming plug flow for gas phase) in the center or core region is much larger than the particle terminal velocity, while the ensemble average axial velocity near the wall is negative (downfall), which is an order of magnitude higher than the minimum fluidization velocity; c) very small axial variations within the zone of interrogation; d) two prominent axial velocities at the centerline – one negative and one positive, with the overall ensemble average being positive.

Similar conclusions were drawn from the solids axial velocity PDFs at another operating condition in the FF regime (U_g^{riser} = 3.2 m·s^{-1}; G_s = 30.2 kg·m^{-2}·s^{-1}). One possible explanation for the appearance of negative velocities at the centerline in the FF regime (Figure 6-19), which are absent in the DPT regime (Figure 6-20), could be due to the enhanced formation of clusters at higher solids holdups, which tend to fall down. Based on the same argument, the prominent negative solids velocity at the center can be associated with the cluster terminal velocity and an approximate cluster size can be estimated. Also, the prominent positive velocities at the centerline can be interpreted to be representative of the tracer particle which passed through the riser straight up with very little backflow. This bimodal PDF in the FF regime seems to gradually change to a uni-modal one as one moves towards the wall. Hence, the existence of clustering phenomenon, inferred from the negative axial velocities, seems to be prevalent throughout the riser cross section (more likely near the wall) in the FF regime.

In the DPT regime, with the operating conditions at U_g^{riser} = 4.5 m·s^{-1} and G_s = 36.8 kg·m^{-2}·s^{-1}, Figure 6-20 shows the spatial variation of the axial solids velocity PDFs at the same compartments. In contrast to the FF regime, PDFs at the centerline have a single peak with no negative velocities. Also, the ensemble-averaged solids velocity is positive near the wall even though one can note some negative instantaneous velocities. Hence, in the DPT regime no clustering occurs in the core. However, the radial particle exchange is still pronounced as suggested by the non-homogeneous particle segregation (interpreted from the number of occurrences) and the radial velocity PDFs (Figure 6-22).

Similar conclusions were drawn with regard to the absence of clustering in the central core from the axial velocity PDFs in the DPT regime at other operating conditions.

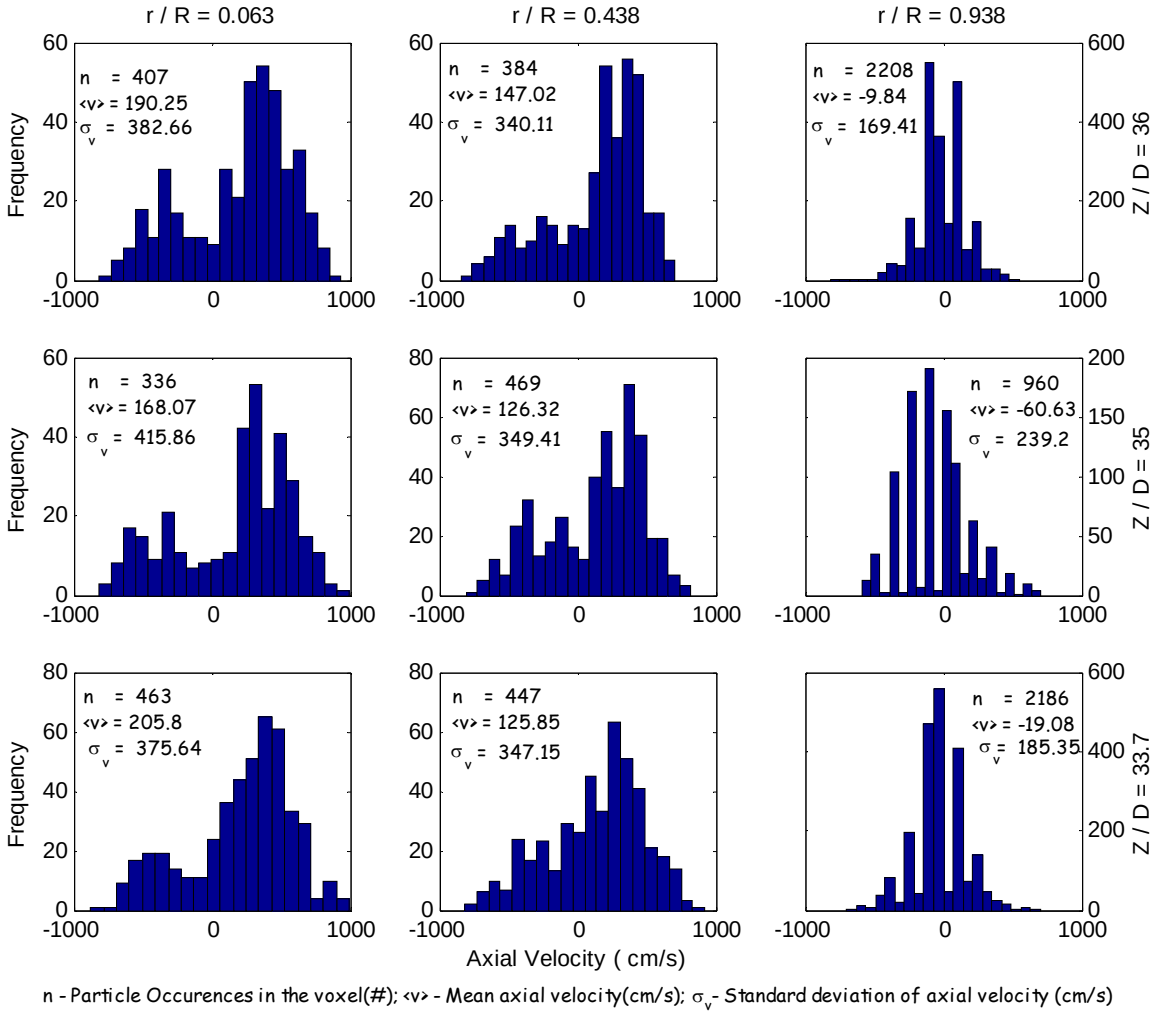

Figure 6-19: Spatial variation of the axial solids velocity PDFs with statistics illustrated at three different axial and radial locations and at a typical angular position in the FF regime at U_g = 3.2 m·s^{-1}; G_s = 26.6 kg·m^{-2}·s^{-1}.

The axial velocity PDFs shown in Figures 6-19 and 6-20 were obtained in a compartment at a particular angular location. Now one can also collect the statistics from every angular compartment at each radial location of interest to construct such axial

velocity PDFs. Such a velocity PDF would characterize the velocity variation along the perimeter at a particular radial position. Figure 6-21 displays such axial velocity PDFs at an axial location and at three different radial positions in the two regimes (FF and DPT). Comparing the PDFs in these two regimes with the corresponding ones from Figures 6-19 and 6-20, one can clearly notice that the functions do not change much with the increase in the statistics. The variation in the corresponding means and standard deviations is less than 7% except near the wall (r/R = 0.94), where the variation is large. Such small variation indeed reflects axi-symmetric flow.

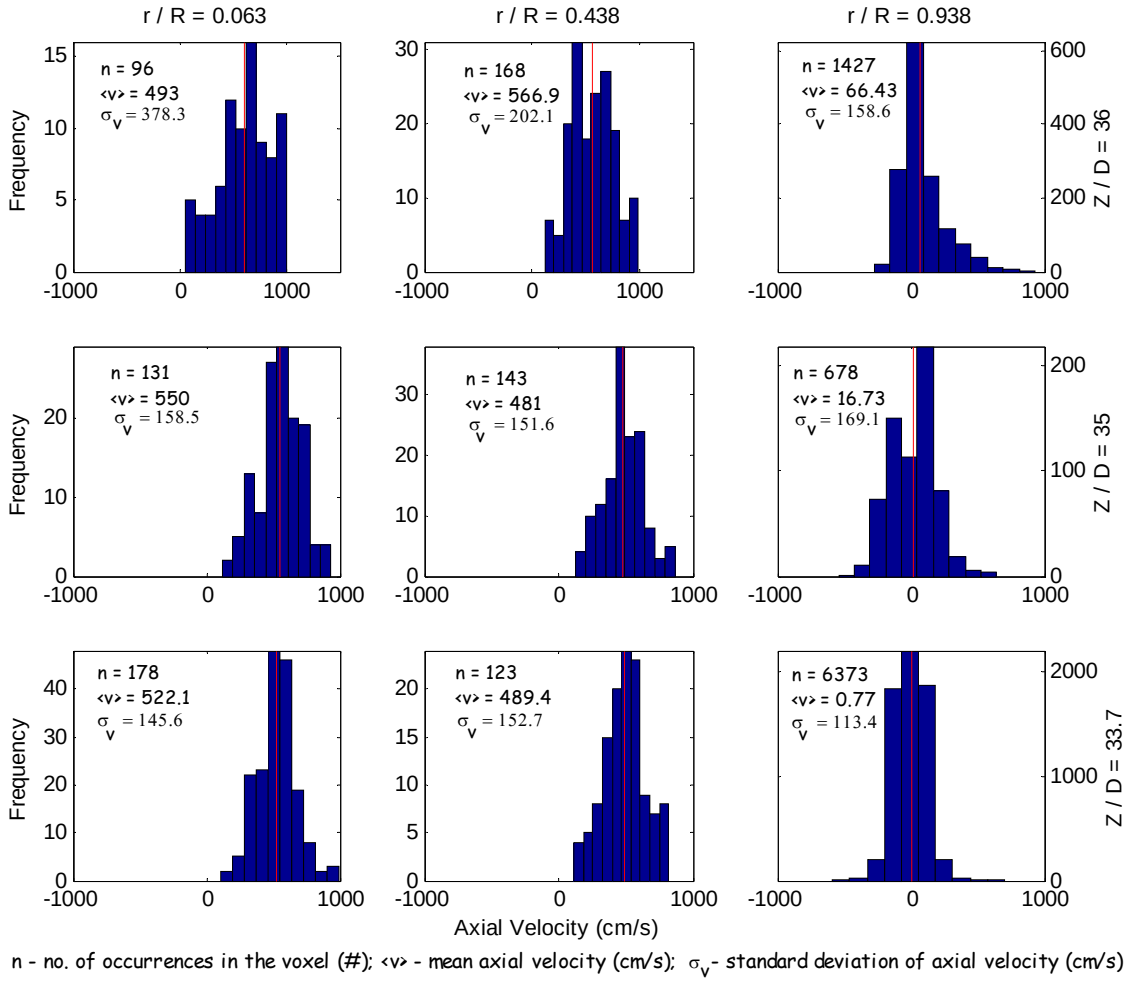

Figure 6-20: Spatial variation of axial velocity PDFs illustrated in three different axial and radial locations and at a typical angular position in the DPT regime at U_g = 4.5 m·s^{-1}; G_s = 36.8 kg·m^{-2}·s^{-1}.

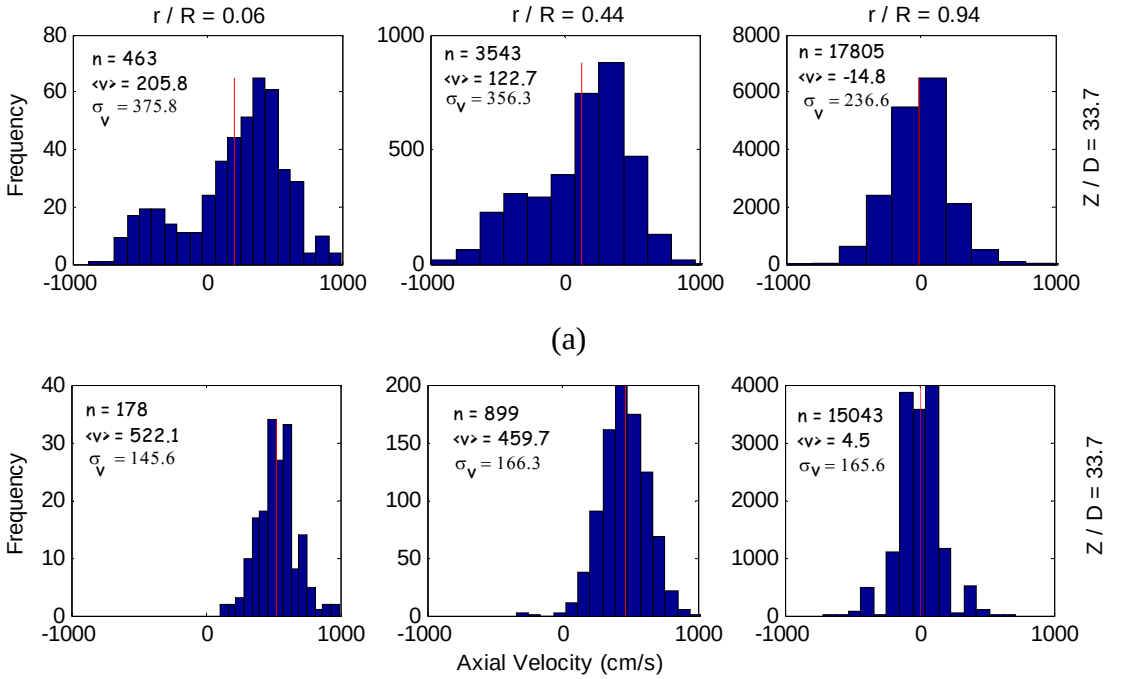

Figure 6-21: PDFs of the axial velocity with statistics from all the angular positions shown at three different radial locations and an axial height of *Z/D*=33.7 in: a) FF (U_g^{riser}=3.2 m·s^{-1}; G_s=26.6 kg·m^{-2}s^{-1}); b) DPT (U_g^{riser}= 4.5 m·s^{-1}; G_s=36.8 kg·m^{-2}s^{-1}).

Variation of radial velocity PDFs are shown in Figure 6-22 at the flow conditions in the FF regime at U_g^{riser} = 3.2 m·s^{-1} and G_s = 26.6 kg·m^{-2}·s^{-1}. Although the ensemble averaged values reveal that the velocity component is directed towards the wall, negative instantaneous radial velocities were observed. Also, the mean radial velocities are an order of magnitude smaller than the mean axial velocities. However, the standard deviation of the radial velocities was much higher (one order of magnitude) than their corresponding means. Similar result was established earlier using LDV measurements in a very dilute riser (Van den Moortel *et al.*, 1998). Similar variation of the radial velocity PDFs was seen for the conditions in DPT regime too.

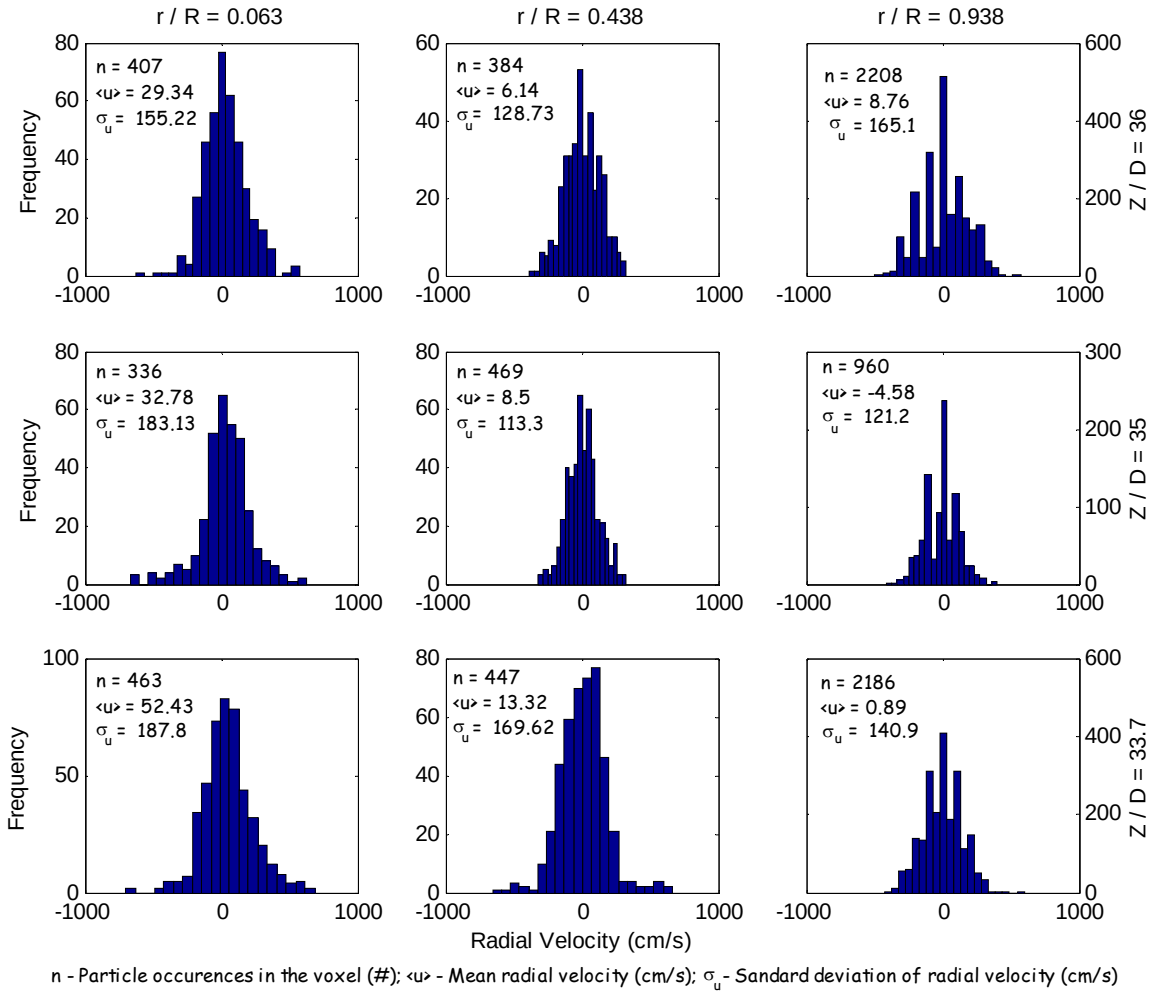

Figure 6-22: Spatial variation of radial velocity pdfs with statistics illustrated in three different axial and radial locations under FF regime at U_g = 3.2 m·s^{-1}; G_s = 26.6 kg·m^{-2}·s^{-1}.

FF versus DPT - Velocity Vector Plots

In this section, velocity vector plots representing the time-averaged solids velocities are presented to check for axi-symmetry in the solids flow pattern in the 3D risers in the two regimes- FF and DPT. Both the vertical and horizontal plane projections are given to interpret all the three components of the velocity vectors. The vertical planes are sliced through the center of the column at four different angles – 0-180^o, 45-225^o, 135-315^o, 90-270^o, while the horizontal cross-sectional views are obtained at two

different axial elevations. The display of the vector plots is accomplished using MATLAB.

Figure 6-23 displays the velocity vectors for the flow condition in the FF regime at U_g^{riser} = 3.2 m·s^{-1} and G_s = 26.6 kg·m^{-2}·s^{-1}. As evident from these figures, the flow pattern seems to be axi-symmetric. In addition, Figure 6-23a indicates that in the time averaged sense the solids flow upwards in the center and downwards near the wall in the FF regime, an observation frequently reported (e.g. Bader *et al.*, 1988; Miller and Gidaspow, 1992; Bi and Grace, 1995; Davidson, 2000; Parssinen and Zhu, 2001). However, in the DPT regime, the flow near the wall is also upwards (Figure 6-24). This difference in the flow pattern (compared to the FF regime) could be due to the decrease in the solids cross-sectional concentration, resulting in the decrease of the clustering effect. With the decreased cluster formation, the down-flow of solids is also reduced. Such upward flow near the wall was also observed by a few other researchers (Issangya *et al.*, 1998; Parssinen and Zhu, 2001), but under very high solids flux conditions, termed as dense phase suspension by Grace *et al.* (1999). Note that the flow conditions investigated in this work are quite different from the dense phase suspension regime.

The axial variation of the velocity is small (less than 11%) within the zone of interrogation in both flow regimes (as seen in Figures 6-23 and 6-24). The mean radial and azimuthal components of the velocity are very small compared to the axial component indicating that the time-averaged flow pattern is basically representative of a close to fully-developed flow within the zone. Similar observations were seen for other flow conditions investigated. However, one cannot argue in a strict sense that the flow of solids is fully developed based on Figures 6-23 and 6-24, since the mean radial velocities are only relatively small compared to the axial ones and are numerically not equal to zero.

The vector plots establish that even though the passage of individual solid particles through the zone of interrogation is tortuous (Figures 6-10 and 6-11), the time-averaged velocity field is structured with a clear pattern (Figures 6-23 and 6-24). Although the local variations (instantaneous velocities) can never be reproduced by any number of experiments (chaotic nature of the system), the time-averaged developed velocity profiles are reproducible.

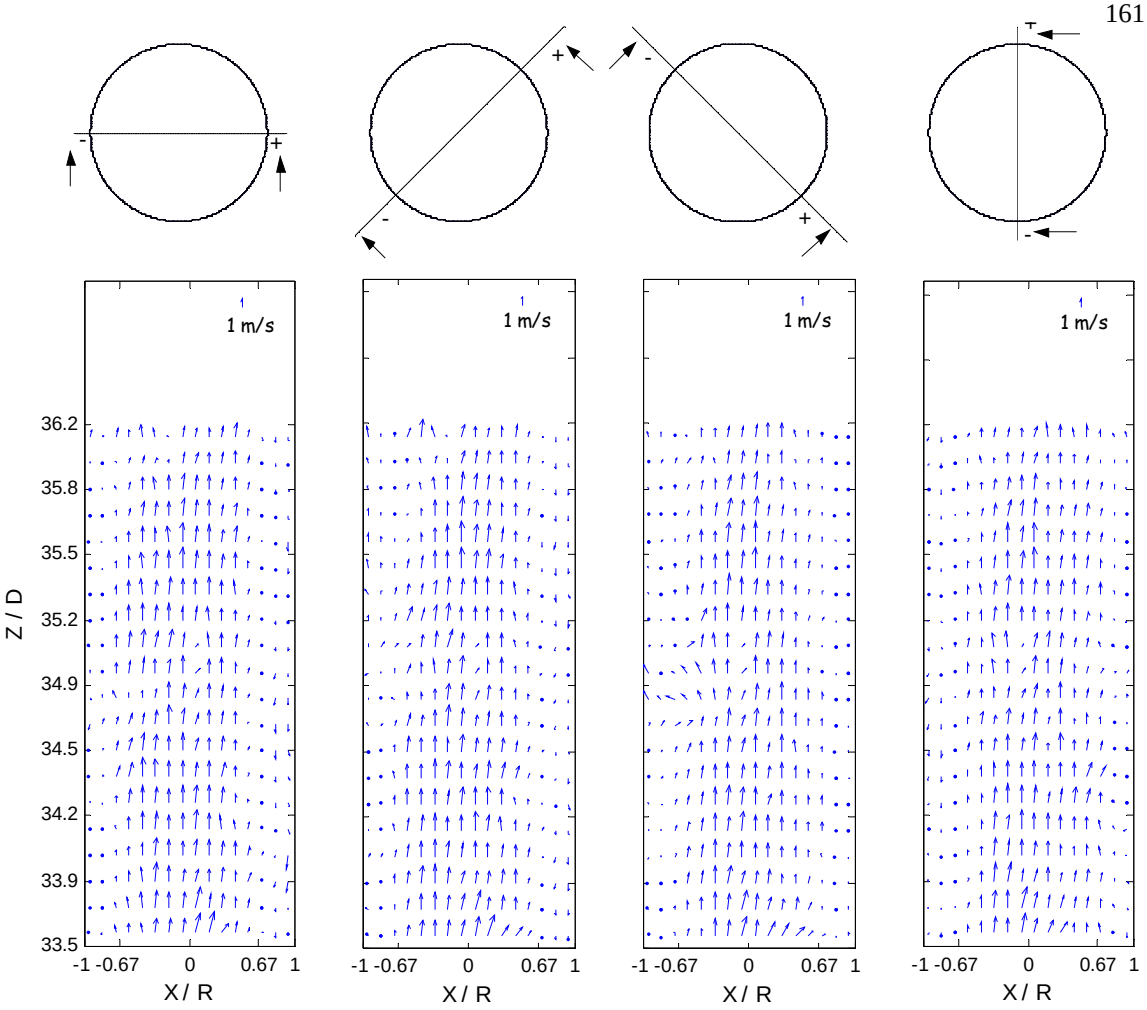

Figure 6-23: Visualization of the velocity vectors in the zone of interrogation in a) *r-z* plane at different angles; b) *r-θ* plane at different axial heights. The operating conditions are in FF regime at U_g = 3.2 m·s^{-1}; G_s = 26.6 kg·m^{-2}·s^{-1}.

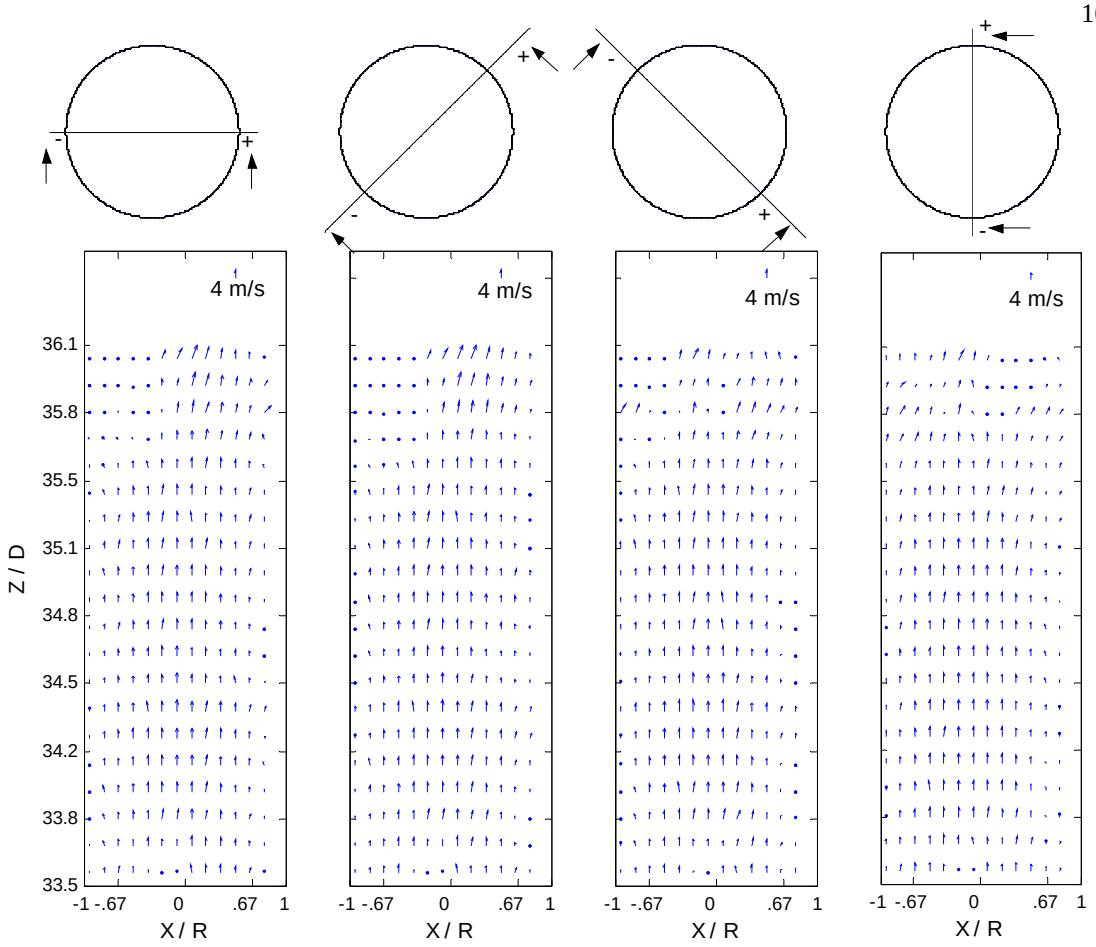

(a)

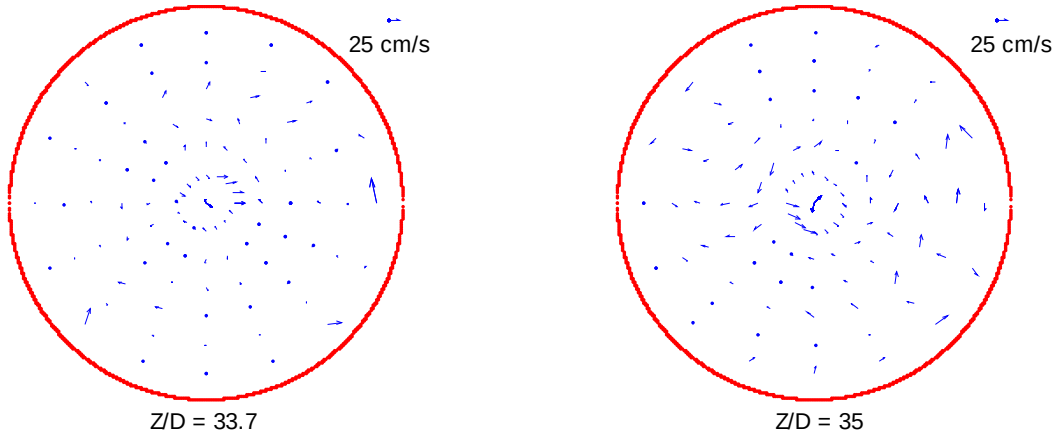

(b)

Figure 6-24: Visualization of the velocity vectors in the zone of interrogation in a) *r*-*z* plane at different angles; b) *r*-θ plane at different axial heights. The operating conditions are in DPT regime at U_g = 4.5 m·s^{-1}; G_s = 36.8 kg·m^{-2}·s^{-1}.

The time-averaged solids velocity components in the two flow regimes – FF and DPT are compared in Figure 6-25. In the plots of Figure 6-25, the velocities are circumferentially and axially averaged. In the FF regime, the axial solids velocity component exhibits negative values in an annulus at the wall, while in the DPT regime, such negative axial solids velocities are not observed. While there seem to be no annulus present in the DPT regime, the axial solids velocity profiles in both the regimes seem roughly parabolic. Within the spatial resolution of the velocity reconstruction, the inversion point of the axial velocity profile (corresponding to the annulus thickness) in all the cases in the FF regime is found to be in the same compartment (with r/R = 0.81). Hence, the down-flow of solids at the wall in the FF regime is expected to cause considerable backmixing of the solids phase.

It can be observed that both the solids axial and radial components of the time-averaged velocity in the DPT regime are higher in magnitude compared to the values in the FF regime, while azimuthal profiles in both seem to be negligible and close to zero. This result once again confirms axi-symmteric flow pattern of the solids in the riser. Values that deviate from zero in the central part may be caused by the poor statistics in the region with fewer particle occurrences.

The time-averaged radial velocity profile in both the regimes seems to be always positive (Figure 6-25). Thus, positive time-averaged radial velocities indicate that the flow is still not fully-developed (in a strict sense) and that the solids in the core have a tendency to move radially outward. The core seems to feed the solids to the annulus even at these elevations. However, the instantaneous radial velocities (from radial velocity PDFs) do exhibit negative velocities. Hence, the radial velocity profiles suggests that the movement of solids from core to annulus seems to be governed by the gradients in the time-averaged velocity profiles, while the movement of solids from annulus to core (if prevalent) is governed by the fluctuating velocity profiles in the fully-developed zone.

FF versus DPT - Turbulent Stresses and Kinetic Energy

CARPT technique provides turbulent stresses and kinetic energy in the entire three dimensional flow field (Moslemian, 1987; Devanathan *et al.*, 1990). The expressions for calculating the turbulent stresses, turbulent kinetic energy and Lagrangian

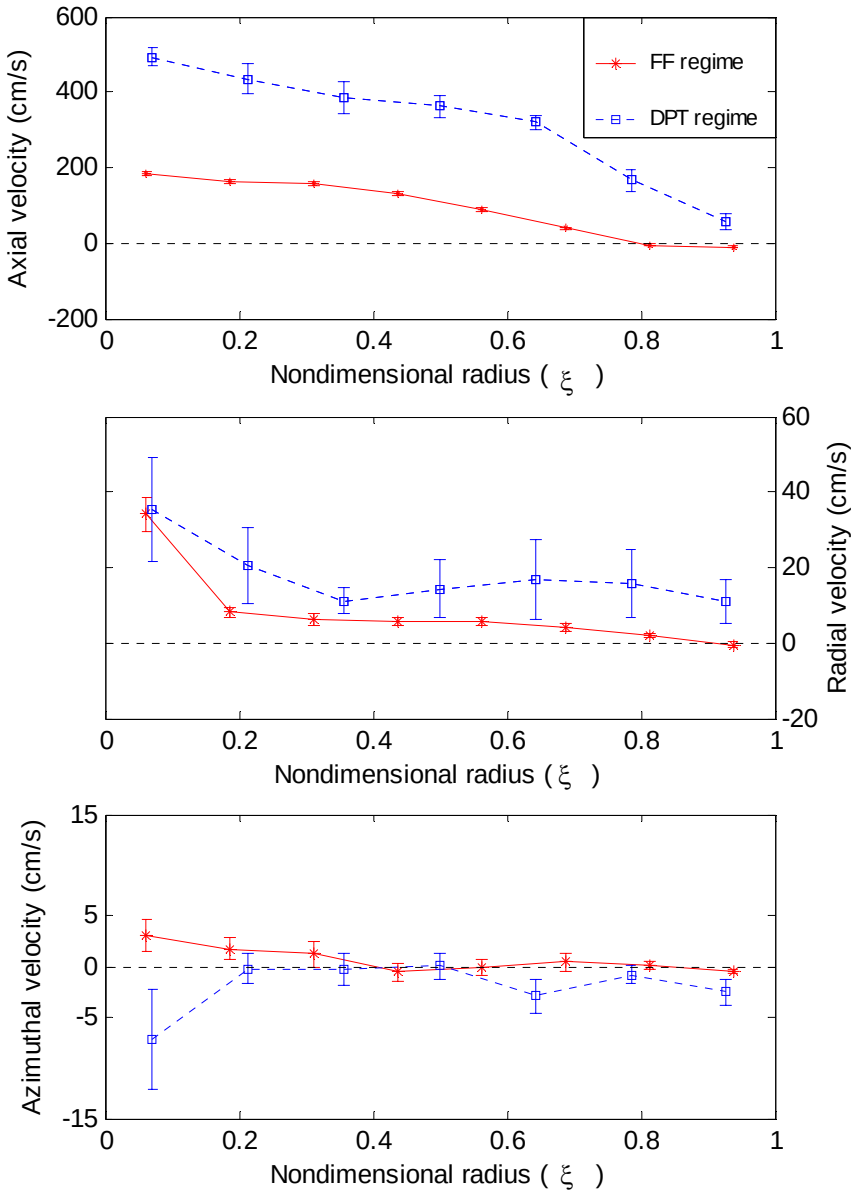

Figure 6-25: Circumferentially and axially averaged time-averaged velocity components compared at two different regimes – FF (U_g^{riser} = 3.2 m·s^{-1}; G_s = 26.6 kg·m^{-2}·s^{-1}) and DPT (U_g^{riser} = 4.5 m·s^{-1}; G_s = 36.8 kg·m^{-2}·s^{-1}).

auto-correlations are dealt extensively by Moslemian (1987), Degaleesan (1997), Roy (2000) and are not presented here. It is known that turbulence is characterized by random fluctuations and statistical characterization of the flow parameters leads to important information about the flow (Monin and Yaglom 1971; Wilcox, 1994). The instantaneous flow information is usually obtained from higher order correlations of the fluctuation quantities that represent the turbulent interactions. Turbulent stress is one such interaction which represents the transport of momentum due to the turbulent velocity fluctuations. The main diagonal terms in a turbulent stress tensor contribute to the pressure at a point in the flow, while the non-diagonal terms are the tangential or shear stress components. The energy associated with the fluctuating quantities, called the turbulent kinetic energy, is the sum of the three normal stress components. Turbulence kinetic energy (per unit bulk density) in granular flows is also called granular temperature. Sinclair and Jackson (1989) were the first to analyze fully developed riser flow using the kinetic theory of granular flow. Several kinetic theory based models to describe the granular flow are available (Gidaspow *et al.*, 1994; Pita and Sundaresan, 1993; Dasgupta *et al.*, 1994).

The primary aim in this section is to present the detailed experimental study of the turbulent quantities required for the CFD model verification. Experimental data for turbulent quantities is very limited and is available only for dilute, low flux riser flows. This data is usually obtained by imaging techniques such as PIV or LDV and/or by invasive probes. Imaging techniques, as discussed earlier (Chapter 2), have limitations that the CARPT technique can overcome.

Contour plots for turbulent Reynolds stresses and kinetic energy were obtained using MATLAB at four different vertical planes at the following angles – 0-180^o, 45-225^o, 135-315^o, 90-270^o within the zone of interrogation (Z/D = 33.7-36.7). Figure 6-26 compares the contour plots of the axial normal Reynolds stress (per unit bulk density, $\varepsilon_s\rho_s$) for the operating conditions in the FF (U_g^{riser} = 3.2 m·s^{-1}; G_s = 30.2 kg·m^{-2}·s^{-1}) and the DPT (U_g^{riser} = 3.9 m·s^{-1}; G_s = 33.7 kg·m^{-2}·s^{-1}) regimes. For the case in the FF regime, a clear core with smaller axial normal stress and an annulus with higher stress can be seen. However, such clear demarcation was absent in the case of the DPT regime. A more uniform radial variation can be observed in the DPT regime. The other normal stresses

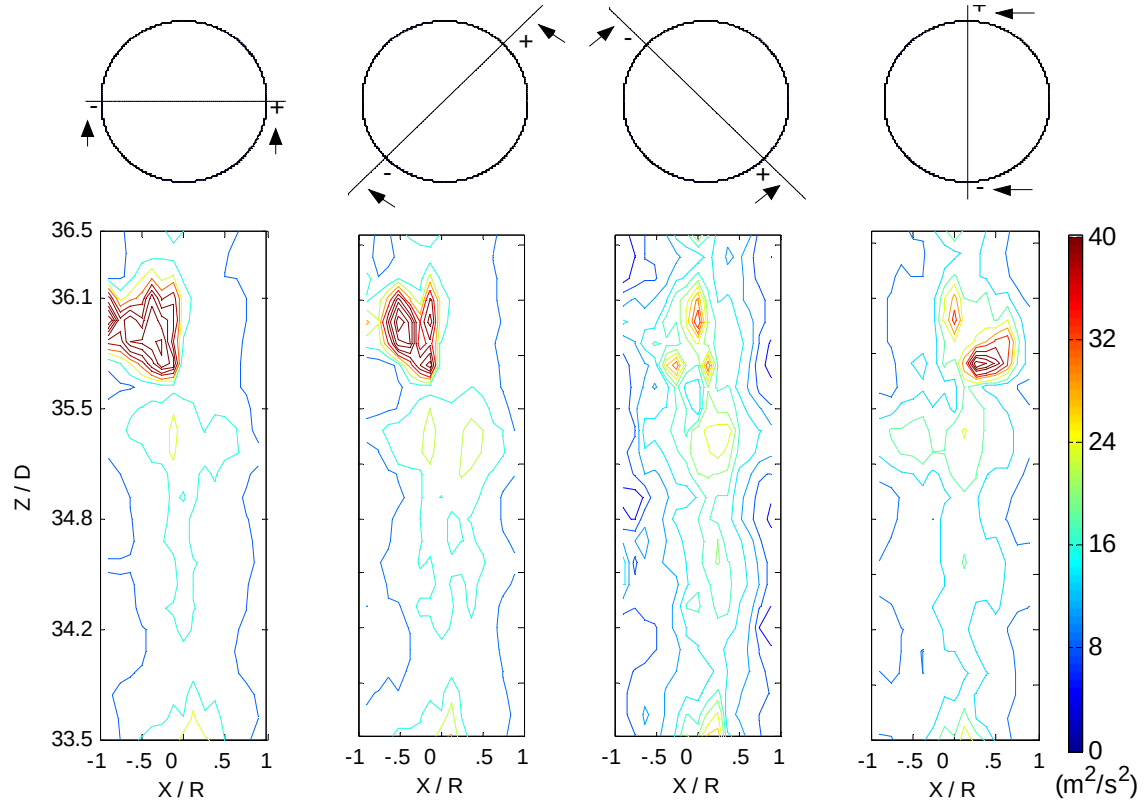

Figure 6-26: Comparison of the contour plots visualized at different longitudinal views of the axial normal Reynolds stress per unit bulk density in a) FF regime (U_g^{riser} = 3.2 m·s^{-1}; G_s = 30.2 kg·m^{-2}·s^{-1}) and, b) DPT (U_g^{riser} = 3.9 m·s^{-1}; G_s = 33.7 kg·m^{-2}·s^{-1}).

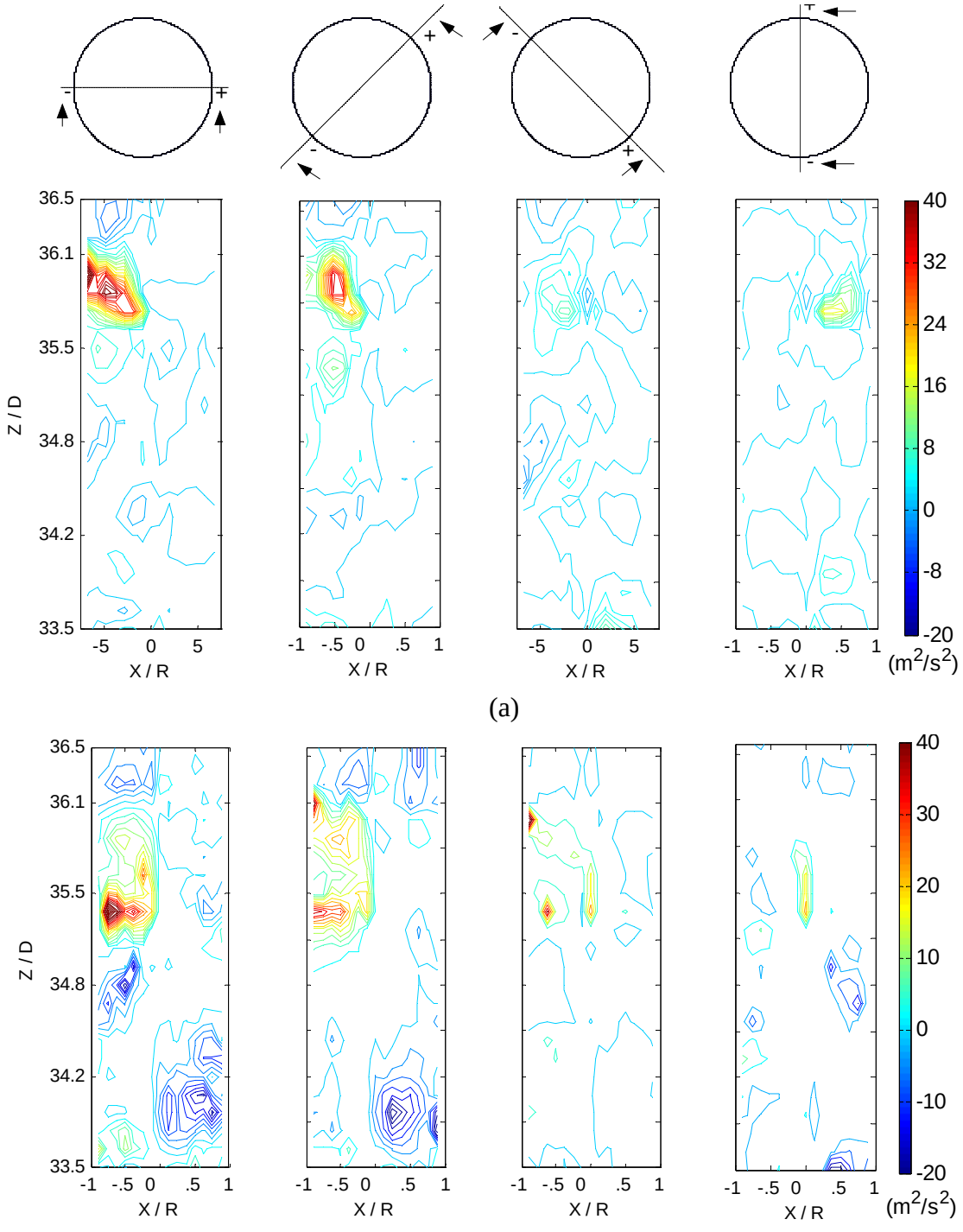

Figure 6-27: Comparison of the contour plots visualized at different longitudinal views of the axial and radial shear stress per unit bulk density in a) FF regime (U_g^{riser} = 3.2 m·s^{-1}; G_s = 30.2 kg·m^{-2}·s^{-1}) and, b) DPT (U_g^{riser} = 3.9 m·s^{-1}; G_s = 33.7 kg·m^{-2}·s^{-1}).

(radial and tangential) were relatively much smaller in magnitude than the axial and also did not show any trend except being uniform in both FF and DPT regimes. Hence, these contour plots are not shown for brevity. In addition, these plots show that the flow in the riser is anisotropic ($\tau_{zz} \neq \tau_{rr} \neq \tau_{\theta\theta}$) which is in agreement with the results for riser flow of FCC particles (Gidaspow and Huilin, 1996). Figure 6-27 similarly compares the contour plots of the shear stresses, τ_{rz} in the FF and DPT regimes. As expected from theory, the shear stress is zero in the center and increases radially (very small increase) and then decreases near the wall. Significant negative shear stress (τ_{rz}) can be observed in the case of the DPT regime suggesting that the radial gradient of the axial mean velocity is also negative (turbulent viscosity is a positive number). Similar trends were seen for the other shear stress ($\tau_{z\theta}$ and $\tau_{r\theta}$) profiles. In general, it was observed that although the mean velocity profiles (Figure 6-24) show higher magnitudes in the DPT regime (higher superficial gas velocity and overall solids mass flux), the turbulent Reynolds stresses seem to be lower than in the FF regime.

Figure 6-28 shows the comparison of the turbulent kinetic energy per unit bulk density in the two regimes. The turbulent kinetic energy can be scaled with a constant to obtain the granular temperature. A clear demarcation between the core and the annulus in the turbulence energies was observed in the FF regime (Figure 6-28a). However, in the DPT regime, the turbulent kinetic energy was more uniform (Figure 6-28b) in the radial direction, although it decreased near the wall. Very small axial variation of the turbulent kinetic energy was seen in both regimes.

Figure 6-29 shows the contours of the particle occurrences per unit volume in the FF and DPT regimes. With an assumption of 'well-perfusedness', or no stagnation in the zone of interrogation, one can interpret the solids volume fraction to be proportional to the ratio of the particle occurrences (in a compartment) to the total number of occurrences. Similar interpretation of the particle occurrences was used in other multiphase systems (Moslemian, 1987; Dudukovic *et al.*, 1991; Godfroy *et al.*, 1999; Stellema, 1998). In other words, the contours shown in Figure 6-29 are those of the solids volume fraction, whose magnitude needs to be scaled appropriately.

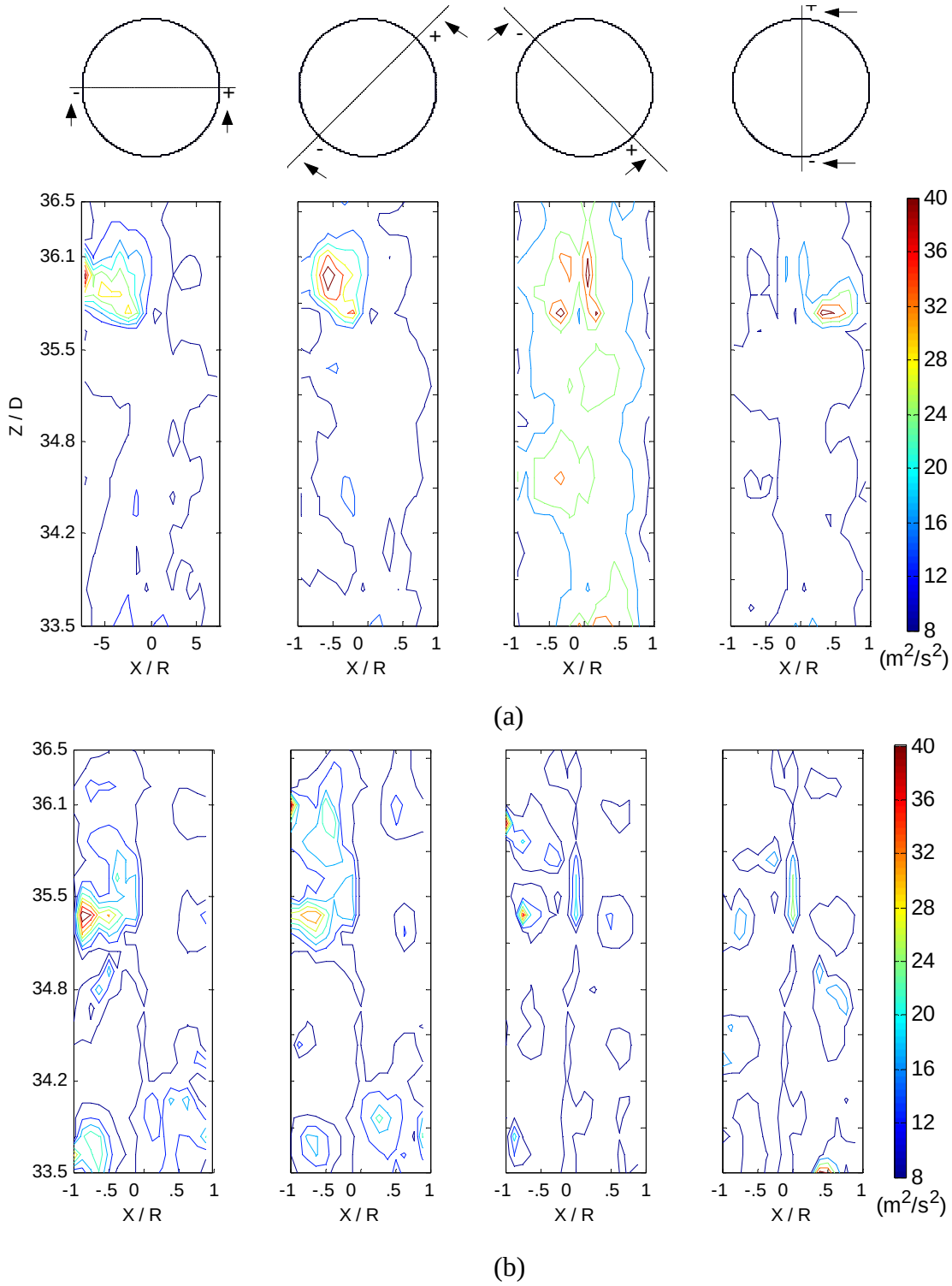

Figure 6-28: Comparison of the contour plots visualized at different longitudinal views of the turbulent kinetic energy per unit bulk density in a) FF regime (U_g^{riser} = 3.2 m·s^{-1}; G_s = 30.2 kg·m^{-2}·s^{-1}) and, b) DPT (U_g^{riser} = 3.9 m·s^{-1}; G_s = 33.7 kg·m^{-2}·s^{-1}).

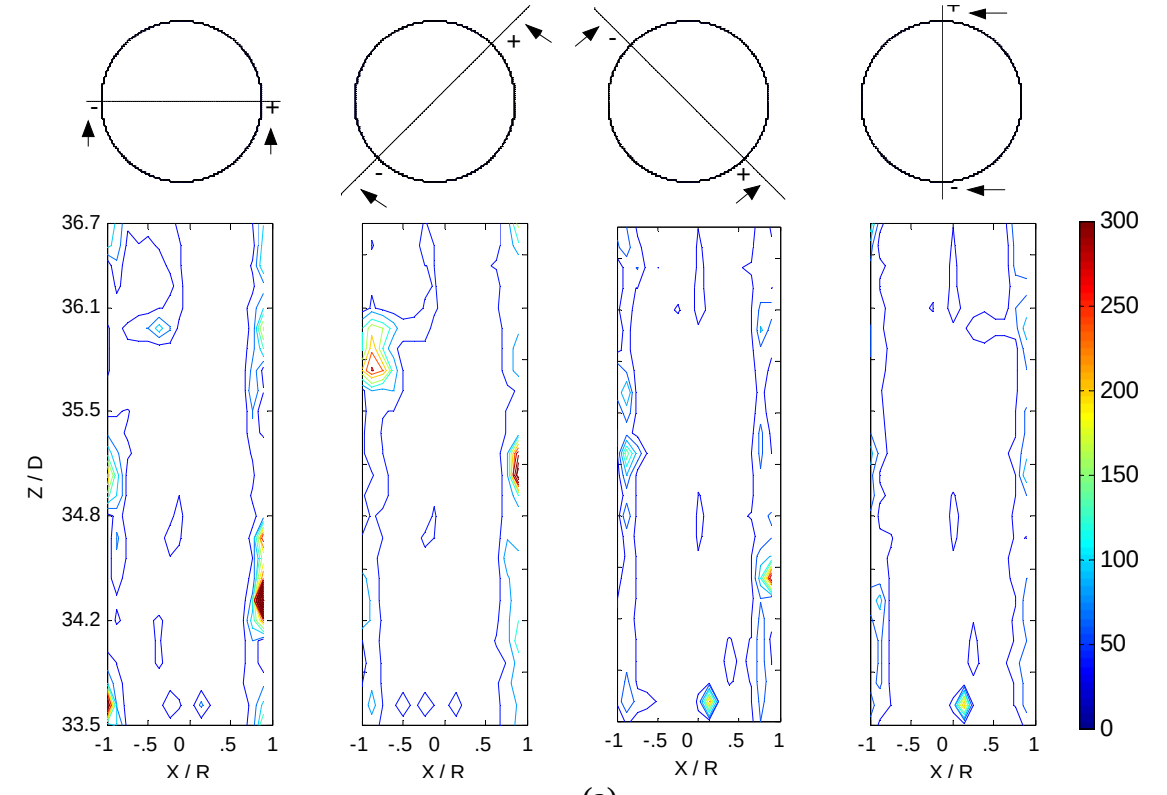

(a)

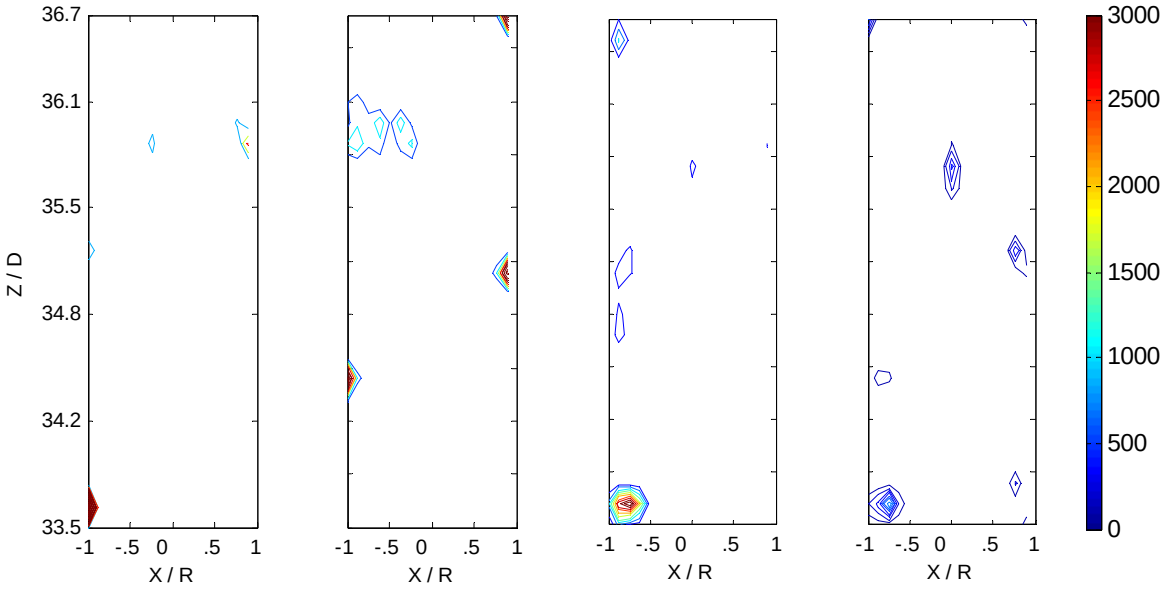

(b)

Figure 6-29: Comparison of the contour plots visualized at different longitudinal views of the particle occurrences per unit volume in a) FF regime (U_g^{riser} = 3.2 m·s^{-1}; G_s = 30.2 kg·m^{-2}·s^{-1}) and, b) DPT (U_g^{riser} = 3.9 m·s^{-1}; G_s = 33.7 kg·m^{-2}·s^{-1}).

To do the scaling one needs an independent measurement (like tomography) of the solids concentration. Such analysis is done later while discussing the results from tomography. The solids concentration in Figure 6-29a (FF regime) clearly shows a concentrated annulus layer near the wall and a dilute core in the center. One can interpret the annulus wall layer thickness based on these contours. This is another way of obtaining the annulus thickness, methods reported in the literature are based on the axial velocity and flux profile's 'cross-over' points (Bi *et al.*, 1996). It can also be observed from Figure 6-29 that there are some concentrated pockets of solids near the wall and a few in the core region. These concentrated pockets cannot be directly interpreted as 'clusters' considering that the lifetime of the clusters is very small and that these contours are derived from several particle trajectories observed over hours of experiment. If one makes an ergodic assumption (validated earlier) that observing several independent single particle trajectories is equivalent to observing all the trajectories of the ensemble of particles in the system, then the concentrated pockets can be interpreted as 'clusters'. Hence, the message is that there is a definite probability of the 'cluster' formation in these regions of concentrated pockets.

Thus, Figures 6-29a and 6-29b convey the message that the clustering phenomenon in the FF regime is significant near the wall region and can also occur in the core of the riser. In contrast, in the DPT regime, the solids concentration is more uniform (both radially and axially) and the intensity of clustering much less compared to that in the FF regime. Notably, the contours in both regimes seem to be nearly axi-symmetric. Based on the symmetry in most of these observations, the 3D velocity data were azimuthally and axially averaged to obtain the one-dimensional variation of the velocity and turbulent fields along the radial direction.

FF versus DPT – Radial variation of velocity and turbulent fields

Further analysis is restricted to the discussion of the azimuthally, axially and ensemble-averaged quantities of the velocity and turbulence profiles. All the quantities were axially averaged from Z/D = 33.5-36.7 (z = 5.1–5.6 m) and the error bars on each profile represent the range of values encountered for all z levels. In order to show

generality in the comparison of FF and DPT regimes, the flow conditions presented in the radial profile plots are different from those in the contour plots (Figures 6-26 to 6-29).

The variation of radial profiles of the time-averaged velocity was discussed earlier with reference to Figure 6-25. A substantial increase in the mean axial velocity was observed in the center of the flow when superficial gas velocity and mass flux were increased from the FF to DPT regime (Figure 6-25). Also, the mean radial velocity showed the same trend. A significant velocity variation was indicated between the central core and annulus zone near the wall. Near to the transition between these two zones, the axial and radial components of the mean velocity are of the same order, revealing a particle motion principally directed toward the riser walls. However, axial and radial velocity fluctuation profiles in Figure 6-30 show an opposite trend (to that of mean profiles) for comparison between FF and DPT regimes. The axial velocity fluctuations are of the same order of magnitude as the mean values. On the other hand, the radial velocity fluctuations are significant and are always greater than the measured mean values. This observation is in agreement with the earlier experimental studies by Van den Moortel *et al.* (1998) and Godfroy *et al.* (1999).

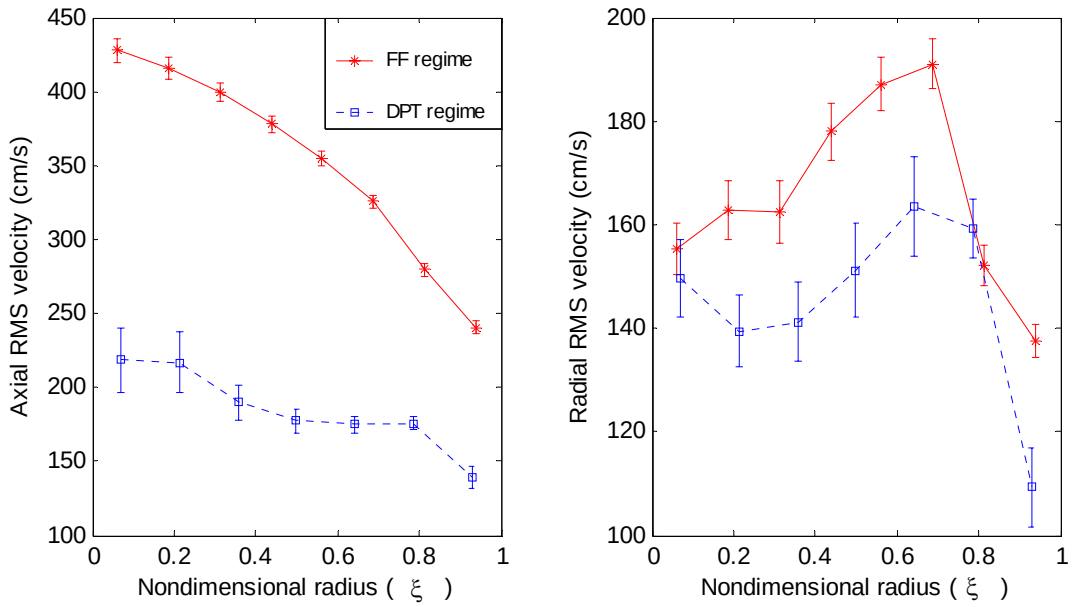

Figure 6-30: Comparison of the azimuthally and axially averaged radial profiles of the RMS fluctuating velocity components in a) axial and , b) radial in the FF regime (U_g^{riser} = 3.2 m·s^{-1}; G_s = 26.6 kg·m^{-2}·s^{-1}) and, b) DPT (U_g^{riser} = 4.5 m·s^{-1}; G_s = 36.8 kg·m^{-2}·s^{-1}).

Figure 6-30 suggests that with the increase in solids concentration, particle fluctuating velocities also increase. Note that the flow condition in the FF regime (U_g^{riser} = 3.2 m·s^{-1}; G_s = 26.6 kg·m^{-2}·s^{-1}) has a higher solids holdup compared to the DPT condition (U_g^{riser} = 4.5 m·s^{-1}; G_s = 36.8 kg·m^{-2}·s^{-1}) as observed from the particle occurrence plots and the tomography results (discussed later). However, this is contrary to the commonly reported simulation results (Dasgupta *et al.*, 1994; Ranade, 1999) and experimental data (Van den Moortel *et al.*, 1998; Godfroy *et al.*, 1999). These authors argue that with the increased solids concentration, the mean free path of the solids is reduced, resulting in the reduction of velocity fluctuations. However, there is a competing mechanism for increasing the particle velocity fluctuations due to the increase in particle collision frequency. As reported by Gidaspow and Huilin (1996), collision frequency increases with particle concentration, which increases the velocity fluctuations with solids holdup under 'dilute conditions' (solids holdup less than 5-10%). Note that 'dilute conditions' need not imply the DPT regime of operation. All the flow conditions investigated on the CREL riser had a solids holdup less than 10% (tomography results). Hence, the above argument leads to the conclusion that although the mean velocity increases, the velocity fluctuations decrease with the increase in the superficial gas velocity in the 'dilute conditions'.

A similar increasing trend in the solids velocity fluctuations with the increase in solids holdup was observed by Benyahia *et al.* (1998) under 'dilute conditions'. This finding also substantiates our comparison between the FF and DPT regimes. Note that increasing the solids mass flux at constant gas superficial velocity, or decreasing the gas superficial velocity at constant mass flux, increases the solids holdup (tomography results). Figure 6-30 shows a decay of axial velocity fluctuations radially in both the FF and DPT regimes following the same trend as the mean values (minimum reached at the wall). The low variations of the axial solids velocity (fluctuation velocity being very close to the mean values) reveal the great agitation of the solids along the flow direction. The radial solids velocity fluctuation profile in both the FF and DPT regimes interestingly show a peak near r/R = 0.7 (Figure 6-30). This radial position, according to the radial particle occurrence profile, corresponds to the transition from a flat solids holdup profile to a drastically increasing one. Hence, the peak in the radial solids velocity

fluctuation profile corresponds to the transition from a lean core with nearly constant solids concentration to a dense zone with increasing solids concentration. Hence, the relative magnitudes of fluctuation velocities with their means show the significance of the fluctuations over the mean particle motions with regards to the particle transport.

In Figure 6-31 the ratio of the axial to the radial solids velocity fluctuation profiles in the FF and DPT regimes are presented. As it can be seen, the axial solids velocity fluctuations are always greater than the radial ones but not by much. In the FF regime, the anisotropy is significant decaying slightly from 2.5 near the center to 1.5 near the annulus, while in the DPT regime the anisotropy is nearly uniform around 1.2. Thus, the dilute risers in the DPT regime tend towards isotropic turbulence. Note the clear distinction in the ratio values across the flow regimes. Hence, the conclusion is that fluctuating motion is principally directed along the main axis of the solids flow.

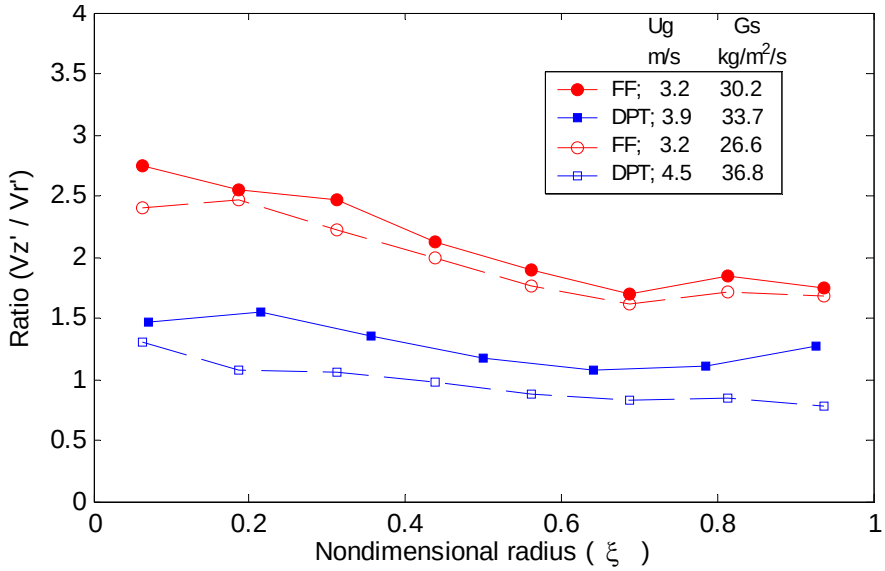

Figure 6-31: Ratio of the axial to radial RMS fluctuating velocity profiles

There is experimental evidence that the particle turbulence in risers is not isotropic for both Group A and B particles (Tsuji *et al.*, 1984; Miller and Gidaspow, 1992; Van den Moortel *et al.*, 1998; Tartan and Gidaspow, 2004). The normal stresses in the axial direction are much larger than in the radial and angular directions. Figure 6-32

compares the radial profiles of the spatially averaged turbulent Reynolds stresses (per unit bulk density) in the FF and DPT regimes.

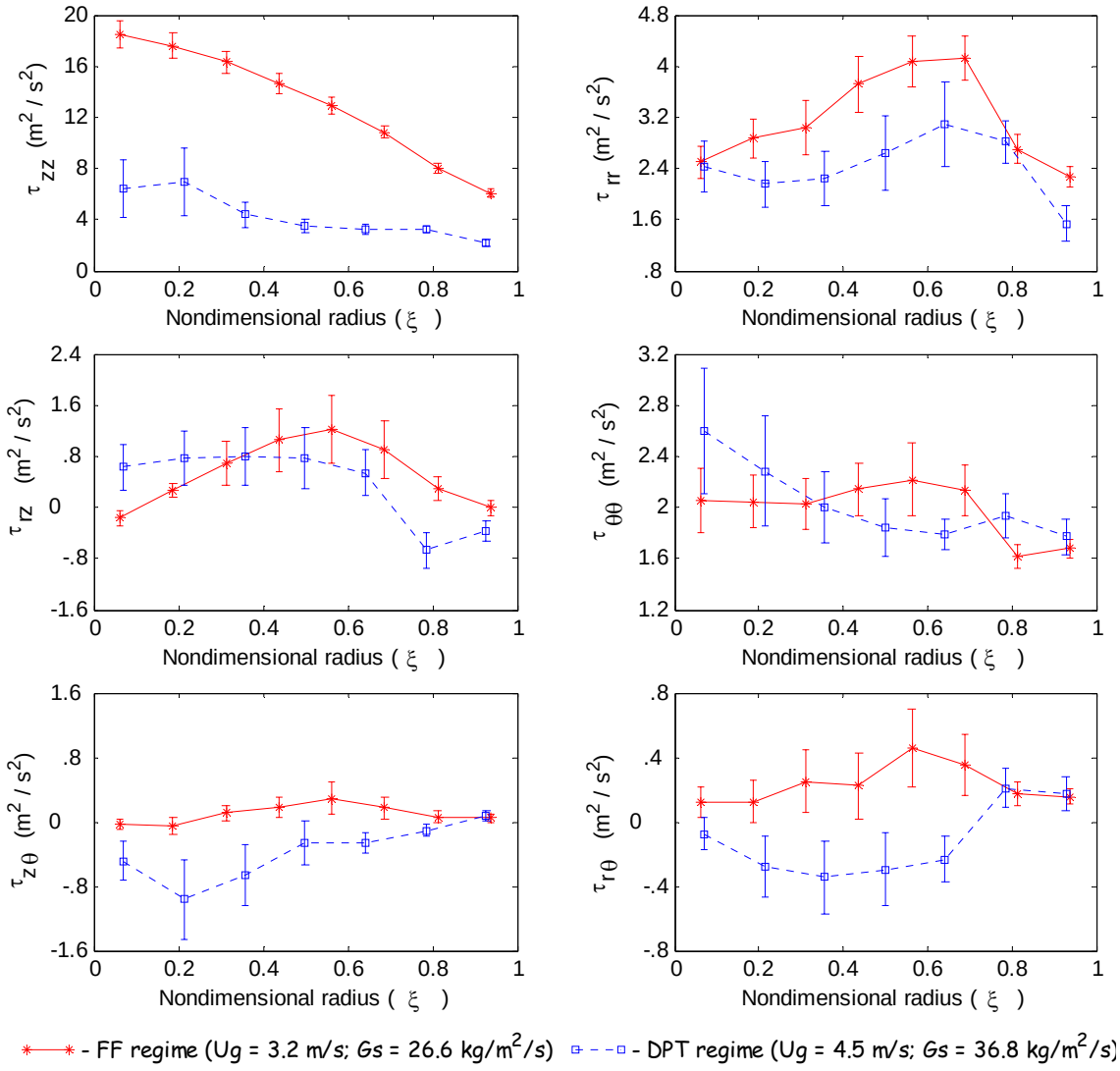

Figure 6-32: Comparison of the azimuthally and axially averaged radial profiles of the turbulent Reynolds stress components in the FF and DPT regimes.

It can be clearly observed that the axial normal stresses are about 3 to 5 times higher than the radial and azimuthal normal stresses. This is due to the high gradient in the axial solids velocity in the radial direction. In addition, the radial and tangential solids

velocities are quite small and, hence, their gradients are also small. The Reynolds shear stress, τ_{rz}, is much lower than the radial and angular normal stresses (about 1/2 to 1/3), while the shear stresses involving the angular fluctuating velocities, $\tau_{z\theta}$ and $\tau_{r\theta}$, are negligible and can be considered to be zero. Similar to the RMS velocity fluctuation profiles, the axial and radial solids normal stresses are found to be higher in the FF regime than in the DPT regime (Figure 6-32). The reason could be due to the higher solids concentration in the FF regime, leading to significantly higher number of particle collisions. Hence, particle collisions are the controlling mechanism for momentum transfer due to the fluctuating velocities or are the turbulent Reynolds stresses. However, one can note that the shear stresses were comparable in magnitude in both regimes, indicating that the changes in solids turbulent viscosity (as given by Equation (6-1)) are mainly governed by the gradients in the mean velocities. Since the solids phase turbulence was found to increase with solids holdup, the data and trends are consistent with those of Tartan and Gidaspow (2004).

Although the angular and radial normal stresses are about the same order of magnitude, the radial normal stress was always higher than the angular normal stress. A distinct feature for conditions in the DPT regime is that angular normal stress peaks at the center of the column. This suggests that the vertical structures spiraling up the column have a tendency to cross over the axis, especially at high superficial gas velocities. This behaviour of vortex structures rules out the possibility of performing a transient simulation using 2D axi-symmetric conditions. Imposing a zero gradient at the centerline, as done in axi-symmetric conditions, would contradict the measured flow structure.

The relationship between the shear stress, τ_{rz}, and the gradient of the mean axial velocity can be obtained using Bossinesq's hypothesis as shown by Equation (6-1).

$$\mu_s^{turbulent} = \frac{\varepsilon_s \rho_s \overline{v_r' v_z'}}{\partial v_z / \partial r} \tag{6-1}$$

The validity of the Boussinesq's theory is questionable since the hypothesis was originally proposed for single phase flows with isotropic turbulence. However, such

closure is often used in the two-fluid modeling of granular flows (Dasgupta *et al.*, 1994) due to lack of a proper anisotropic closure. Also, the same hypothesis was employed to calculate the turbulent shear viscosity of liquid in bubble column flows (Degaleesan, 1997; Ong, 2003). Hence, Equation (6-1) was employed to obtain the solids phase viscosity profiles.

Figure 6-33 shows the radial variation of the solids viscosity calculated from Boussinesq's hypothesis for flow conditions in FF and DPT regimes. The solids holdup values required for the calculations were estimated from the radial profiles of the particle occurrences (per unit volume). The ratio of the particle occurrences in a compartment to the total occurrences was taken to be proportional to the solids volume fraction. The proportionality constant was estimated for each flow condition by comparing the cross-sectional average holdup to that obtained from tomography. The turbulent viscosity profiles calculated by equation (6-1) and shown in Figure 6-33 do not make any physical sense. The two peaks in the FF regime, one in the core near the center and one near the wall can not be realized with any physical flow structure. Also, for the flow conditions in the DPT regime, negative solids viscosities were calculated near the wall. Hence, the only explanation is that the Boussinesq's hypothesis does not hold for solids flow in a riser and yields physically unrealizable turbulent viscosity values.

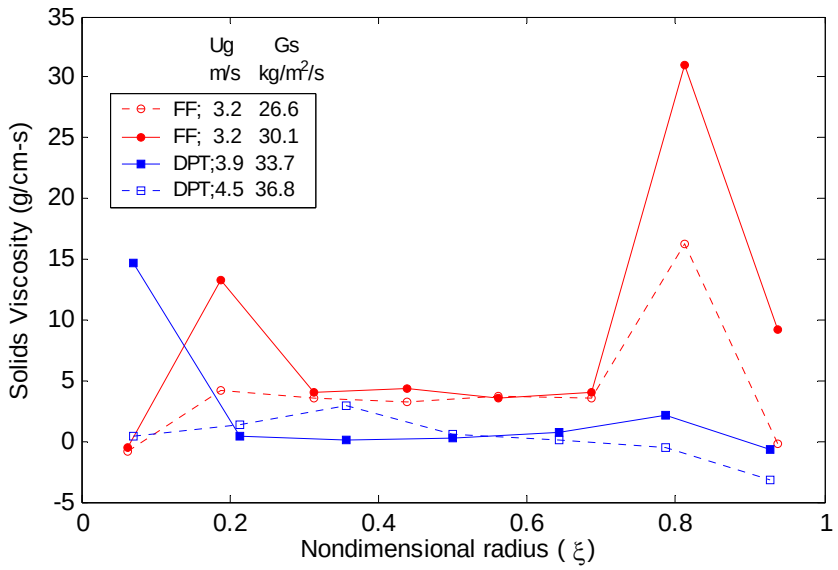

Figure 6-33: Radial variation of solids turbulent viscosity calculated from Boussinesq's hypothesis.

Based on the kinetic theory of granular flows (isotropic), a constitutive relation for the solids viscosity was derived relating it to the granular temperature (turbulence kinetic energy) and solids holdup (Chapman and Cowling, 1961; Ding and Gidaspow, 1990; Benyahia *et al.*, 1998). The following expressions describe the closure relations that are typically used in a kinetic theory based model.

Solid phase shear viscosity (μ_s) is given by:

$$\mu_s = \frac{2\mu_{s,dil}}{(1+e)g_0}\left[1+\frac{4}{5}g_0\varepsilon_s(1+e)\right]^2 + \frac{4}{5}\varepsilon_s\rho_s d_p(1+e)g_0\sqrt{\frac{\Theta_s}{\pi}} \tag{6-2}$$

where Θ_s is the granular temperature, d_p is the sauter mean size of the solids distribution, ρ_s is the density of the solids (glass beads), ε_s is the local solids holdup and the solids phase dilute viscosity ($\mu_{s,dil}$) is given by:

$$\mu_{s,dil} = \frac{5\rho_s d_p\sqrt{\Theta_s\pi}}{96} \tag{6-3}$$

g_0 is the radial distribution function which becomes very large as the solids holdup approaches the maximum packing ($\varepsilon_{s,max}$ = 0.64 for the glass beads used) and is given by:

$$g_0 = \frac{3}{5}\left[1-\left(\frac{\varepsilon_s}{\varepsilon_{s,\max}}\right)^{\frac{1}{3}}\right]^{-1} \tag{6-4}$$

e is the restitution coefficient, taken to be 0.89 based on the reported measured values by Forester *et al.* (1994) and recommendation by Tartan and Gidaspow (2004).

The above expressions were used, along with the measured granular temperatures (turbulence kinetic energy per unit bulk density), and the solids holdup profiles derived from the CARPT data to calculate the viscosity profiles. Figure 6-34 presents the solids viscosity profiles for different flow conditions in the FF and DPT regimes. In contrast to the Boussinesq's calculations (Figure 6-33), it can be seen that the viscosity values and trends do make physical sense. The solids viscosity was found to be decaying monotonically in the radial direction in the FF regime, but in the DPT regime it shows a hump around *r/R* = 0.7. The reason for such a hump can be explained based on the solids holdup profile (cross-sectional view). At the radial position (*r/R* = 0.7) the solids

concentration starts to increase rapidly (particle occurrence profiles) and represents the approximate interface between the lean core and a dense phase annulus. Thus, the particle exchange at this interface is frequent and vigorous, thereby decreasing the easy movement of the solids phase, which increases the solids viscosity. Although the same argument holds in the case of the FF regime, the axial fluctuations of the particles dominate (compared to radial), resulting in a higher turbulent transport of particles axially. Thus, in the FF regime, the decrease in the axial fluctuations (radially) dominates the peak in radial fluctuations, resulting in a smooth gradient of solids viscosity.

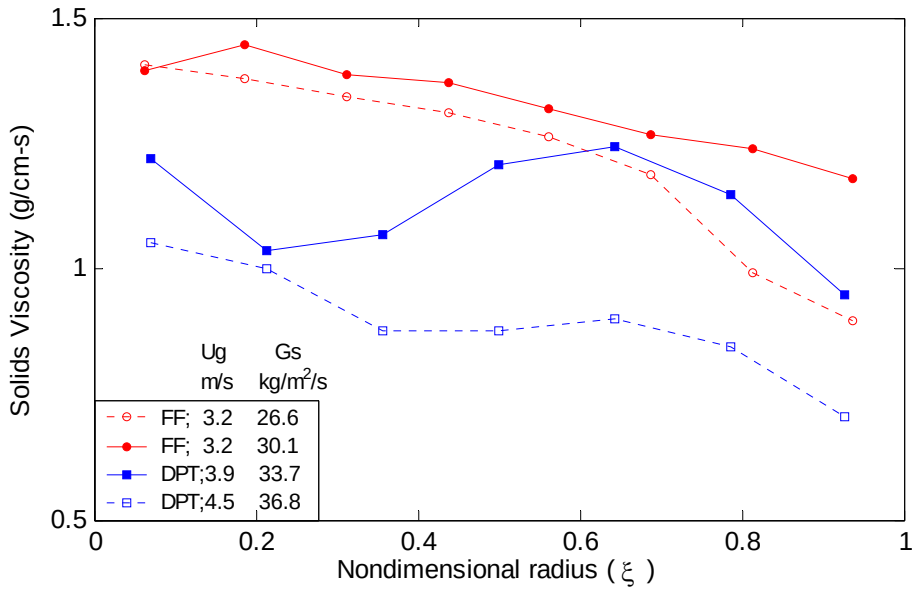

Figure 6-34: Radial profiles of the solids viscosity calculated from kinetic theory based expressions

The solids viscosity in each of the flow conditions exhibit similar radial trends as that of the granular temperature, indicating that the viscosity is almost independent of the solids holdup in the range of the measurements studied. This result is in agreement to that of Tartan and Gidaspow (2004), who estimated solids viscosities in relatively dilute 3" diameter riser using 'PIV with probe' technique. With the same Group B particles and a larger mean particle diameter (3.5 times) Tartan and Gidaspow (2004) found nearly constant viscosities in the core (for all the flow conditions investigated). The viscosity values reported by them were lower, possibly due to the lower solids holdup, resulting in

lower velocity fluctuations (under ‘dilute conditions’). Besides, the use of an intrusive imaging technique with a 0.5 cm diameter probe to measure the velocity fluctuations is questionable. Hrenya and Sinclair (1997) in their simulations reported higher viscosities for FCC particles compared to Gidaspow and Huilin (1996), who employed the same ‘PIV with probe’ technique.

The solids viscosity from Figure 6-34 can be noted to be increasing with the solids concentration (from DPT to FF regime). This can be explained with the following interpretation of Equation (6-2) of Gidaspow (1994).

kinematic viscosity = mean free path x random oscillating velocity

The mean free path decreases with increasing solids concentration, while the velocity fluctuations increase due to the increase in the collision frequency under ‘dilute conditions’. Hence in dilute risers ($\varepsilon_s < 0.05$-0.1), the increase in the collision frequency dominates the decrease in the mean free path, while it is vice-versa in dense risers. Also, Gidaspow and Huilin (1996), based on experimental data, showed that for different particles, the dimensionless viscosity calculated based on Equation (6-2) shows a minimum at solids holdup of 0.057 and increases beyond that.

It can also be observed from Figure 6-34 that with the decrease in the solids concentration, tending towards more dilute flow conditions, the viscosity profile tends to become flat. This is due to the fact that the granular temperature and the solids holdup profiles tend to be nearly flat in a dilute riser. Both of these profiles are presented subsequently. An unusual hump in the viscosity profile can be noted for the flow condition of U_g^{riser} = 3.9 $m \cdot s^{-1}$ and G_s = 33.7 $kg \cdot m^{-2} \cdot s^{-1}$ compared to the other three profiles. This is possibly because the flow condition is close to the regime transition boundary between FF and DPT (type A choking velocity) as shown in Chapter 4.

Figure 6-35 compares the radial profiles of the granular temperature in the FF and DPT regimes. Based on the earlier discussion, the velocity fluctuations and hence the granular temperature increases with the solids holdup for ‘dilute conditions’ and decreases for higher solids holdups. The relative dominance of the increase in the collision frequency over the decrease in the mean free path (with solids holdup) enforces the above trend for the granular temperature. With the solids holdup increasing from the

DPT to the FF regime, the increase in the collision frequency seems to be dominant compared to the decrease in the mean free path. However, with the solids holdup increasing radially in each of the regimes, the decrease in the mean free path becomes dominant (at different magnitude for each of the regimes) compared to the increase in the collision frequency. This effect is less pronounced in the DPT regime (compared to FF) as suggested by a relatively flat radial profile of the granular temperature. The observations from Figure 6-35 suggest that the granular temperature is strongly correlated to the solids holdup. Also, the above arguments suggest that the peak in the granular temperature may occur around a solids holdup value of 1-6%, in contrast to that reported by Gidaspow and Huilin (1996) of 5-10%. Considering the fact that Gidaspow and Huilin (1996) and Tartan and Gidaspow (2004) employed imaging techniques like PIV or 'PIV with probe', the reliability of the velocity measurements away from the walls is questionable. Also, in their granular temperature calculations, the angular velocity fluctuations were assumed equal to the radial component. In addition, the densitometry technique employed had a coarse resolution (> 1.27cm) and yields only line-averaged solids holdups. In view of the above uncertainities, the position of the peak in the granular temperature reported by Gidaspow's group at 5-10% solids holdup is uncertain.

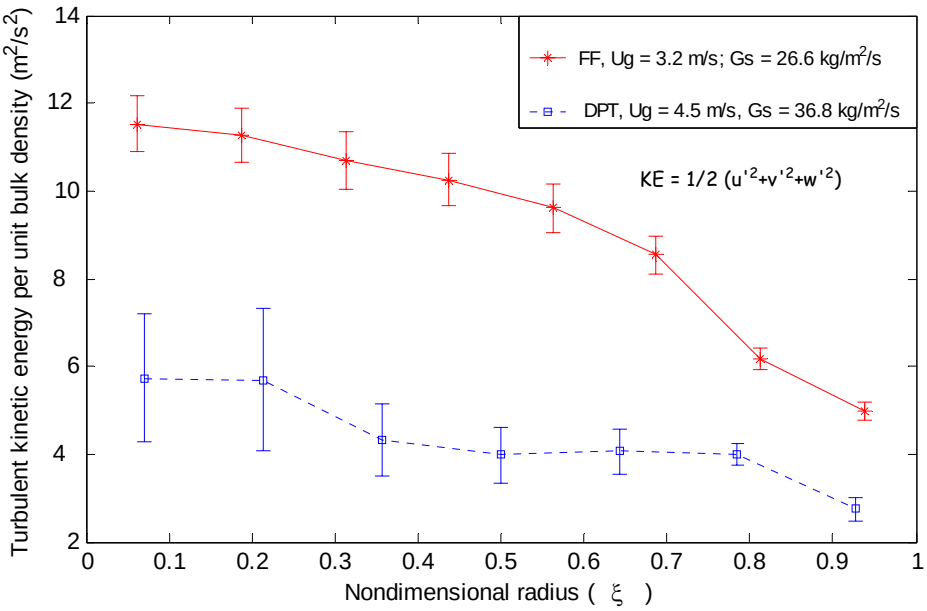

Figure 6-35: Radial profiles of the turbulent kinetic energy (per unit bulk density) in the FF and the DPT regimes.

It is noted here that due to the data acquisition frequency of 200 Hz for CARPT experiments, the maximum range of frequencies tracked by the tracer particle are up to 100 Hz. Therefore, the present measurements represent only scales up to 100 Hz of the turbulent structures. However, since the large scales contain the most energy, it is expected that what remains due to small scales is not very significant in magnitude. There are several studies reporting the dominant frequencies of oscillation of particles in the dense and dilute zones for a wide variety of operating conditions (Gidaspow, 1994; Bai *et al*., 1999; Marzocchella *et al*., 1997; Osseo and Donsi, 1999; Benhayia *et al*., 1998; Malcus *et al*., 2000). Typical macroscopic frequency range reported was up to 4 Hz.

6.3.2 Solids Holdup Measurements

Significant experimental evidence is available which show radial segregation of the solids in gas-solid risers (Saxton and Worley, 1970; Schuurmans, 1980; Hartge *et al*., 1986; Berker and Tulig, 1986; Horio *et al*., 1988; Azzi *et al*., 1991; Zhang *et al.*, 1991; Rhodes *et al.*, 1998; Grassler and Wirth, 1999; Issangya *et al*., 2000; Parssinen and Zhu, 2001[a]). According to Sinclair and Jackson (1989), the central problem in constructing a satisfactory model for riser systems is to understand the mechanism that gives rise to lateral particle segregation. The intent in this section is to study the solids holdup distribution to complement the CARPT data in providing valuable insight into the physics of the complex hydrodynamics. To achieve these objectives, accurate estimation of solids holdup is required. Hence, the accuracy of estimating the solids holdup via γ-ray tomography is discussed before presenting the riser holdup profiles.

Improvements in the image reconstruction by implementing an Alternating–Minimization (AM) algorithm were discussed in Chapter 3. The AM algorithm was found to improve the image quality near the high attenuation (high holdups) regions. The CT scanner setup was validated with a phantom scan of a beaker filled with water. The reconstructed image showed that the flat distribution of the single phase (water) was reconstructed with the mean total attenuation coefficient of 0.085 cm^{-1}. The discrepancy with the theoretical mass attenuation value of water at the photo peak of Cs-137 (660 keV) was found to be less than 2.3%. The phantom scans that illustrated the improvements obtained by the AM algorithm and the validation of the CT scanner setup

were stationary. Hence, the dynamic bias in these phantom scans arises only from the stochastic nature of the emissions from a γ-ray source. However, during the actual riser scan, solids holdup fluctuations also contribute to the bias. If the sampling time is small enough, then the variation of the holdup within the time interval is small allowing one to assume an approximately static holdup. Hence, the sampling frequency should be at least twice the macroscopic oscillation frequencies of the solids in order to assume a static holdup within each pixel (imaginary grid assumed for image reconstruction). There is a vast experimental and modeling evidence of the dominant frequency range for riser flow to be up to 4 Hz (for example Malcus *et al.*, 2000). Another constraint in selecting a high sampling frequency is the need to obtain adequate statistics in the photon counting process. For the CT scanner in our laboratory, a sampling frequency of 20 Hz is low enough for statistical counting errors to be small. In fact, EM reconstruction algorithm models the photon emission and detection to be a Poisson distribution, yielding good image estimates even at low counts (Lange and Carson, 1984). Also, note that the scan is not intended to capture the small time scale fluctuations in the flow. An inherent approximation involved is that these small time scale fluctuations lead to solids movement within the spatial resolution. Therefore a sampling frequency of 10 Hz was considered to be sufficiently high for assuming a static holdup approximation.

The CT setup in our laboratory is a III generation scanner with a rotating fan beam geometry where the collimated radioactive source and the fan like array of collimated detectors rotate around the column to produce many projections. Hence, all the projections are not obtained in a snapshot (within the sampling time). Therefore for each view (with set of projections) to be independent (with respect to time), one needs to obtain several samples at each view. The number of samples should be high enough (longer time) so as to capture the smallest dominant frequency of the flow. Also, by considering an average of a series of samples as a single measurement, statistical noise in the images is reduced. Thus, this second averaging (ensemble) correspond to the time-averaging of the holdup.

To estimate the length of time (number of samples) required for averaging, the following procedure was followed. The riser was scanned at the operating condition

corresponding to the lowest superficial gas velocity and flux for a large number of samples. The data at each projection was split into subsets with different number of samples. Based on the means of the corresponding subsets, images were reconstructed and compared. Figure 6-36 compares the azimuthally averaged radial profiles of the solids holdup obtained by averaging for different lengths of time. Among the four different cases investigated, it can be observed that for the lowest length of time (20 Hz, 114 samples), the solids holdup was underestimated mainly near the walls compared to the other three cases. The profiles for the other three lengths of time fall on one another and the discrepancy in their mean holdups is less than 2%. The discrepancy of the lowest time length case (Δt = 5.7 sec) with the other three cases was more than 21%. The reason for the discrepancy could be that the large scale oscillations of the flow were not captured during averaging with the smaller time length. Similar issue of the length of averaging arises typically in the CFD modeling of the flow. As pointed by Benyahia *et al*. (2002), due to the oscillatory nature of the riser flow, the selection of averaging time plays an important role in the prediction of the proper time-averaged values. Another possible reason could be due to the decrease in the density resolution of the scanner with the increase in the sampling frequency. Hence, all the tomography experiments were performed with 10 Hz sampling frequency for 114 samples.

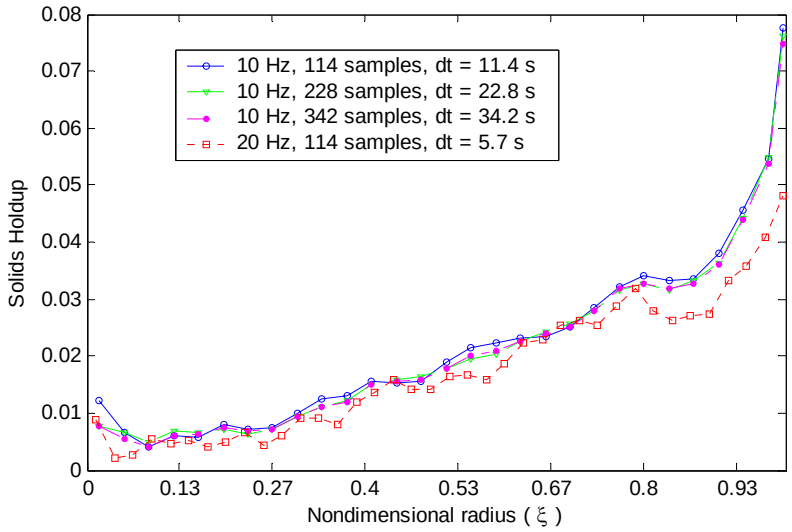

Figure 6-36: Circumferentially averaged radial profiles of the solids holdup as a function of the length of time-averaging (U_g^{riser} = 3.2 m·s^{-1}; G_s = 30.1 kg·m^{-2}·s^{-1}).

The main factors that determine the imaging capabilities of a CT scanner are its achievable spatial, temporal and density resolutions (Kumar *et al.*, 1997). A measure of the spatial resolution is the point spread function which is the extent to which an image of a point object will be blurred. The effective detector aperture width is taken to be the spatial resolution of the scanner and the expression to calculate it was derived by Yester and Barnes (1977). The spatial resolution for the CT scanner in our laboratory was found to be 1.7-mm at the center of the column. The resolution employed for reconstructing the solids holdup tomograms in the riser was 2.7-mm. The single important factor that determines the density resolution is the random fluctuations in the photon counts. De Vuono *et al.* (1980) derived an expression for the density resolution obtainable from all the measurements in an entire scan as follows:

$$\frac{\sigma_p}{\rho} = \frac{n}{2\mu_w \rho_w d_i \sqrt{mM_d}} \tag{6-5}$$

where n is the number of beams in each view, m is the number of views, M_d is the average number of photon detected per beam, μ_w is the mass attenuation of water, ρ_w is the density of water and d_i is the inside diameter of the column. The density resolution for the designed CT scanner in our laboratory for a 6" column was found to be 8.1 x10^{-3} g·cm^{-3}. Hence, the holdup resolution with glass beads in the riser is 3.2x10^{-3}.

Figure 6-37 shows the tomograms of the riser at the operating conditions of investigation (Table 5-3). Qualitatively all the scans reveal increased solids holdup near the walls and with nearly the same relative increase from their means. The distributions seem to disclose nearly axi-symmetric flow as predicted from the velocity distributions (Figures 6-24). In the FF regime, solids holdup seems to exhibit a three layer stratification with gradual gradient, while in the DPT regime there seems to be a smooth gradient, which is less than that in the FF regime. Also, there is an overall reduction in the solids volume fraction in the DPT regime with the corresponding increase seen in the velocity PDFs (Figures 6-19 to 6-22). Albeit, there seems to be large radial solids segregation towards the wall in both cases. Radial migration of solids is a complex phenomenon and is not properly understood (Fan and Zhu, 1998).

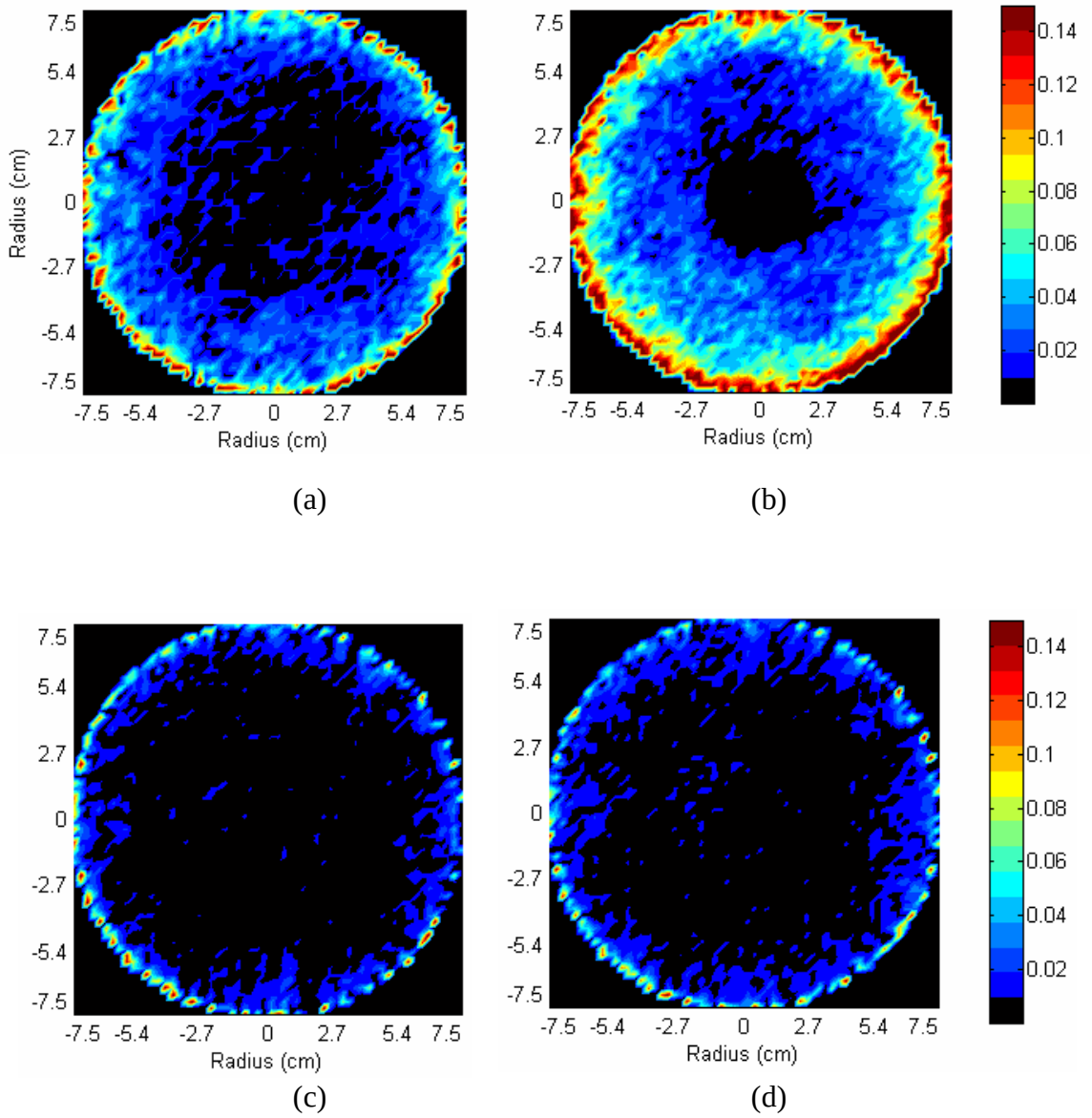

Figure 6-37: Contour plots of the solids holdup at Z/D = 33 (z = 5 m) in the riser under the operating conditions: a) U_g^{riser}=3.2 m·s^{-1}; G_s=26.6 kg·m^{-2}·s^{-1}; b) U_g^{riser}=3.2 m·s^{-1}; G_s=30.1 kg·m^{-2}·s^{-1}; c) U_g^{riser}=3.9 m·s^{-1}; G_s=33.7 kg·m^{-2}·s^{-1}; d) U_g^{riser}=4.5 m·s^{-1}; G_s=36.8 kg·m^{-2}·s^{-1}.

The effect of increasing the solids mass flux at constant gas superficial velocity is an increase in the solids holdup (Figure 6-37). This increase arises because more solids are fed into the riser section for the same gas superficial velocity and hence for the same energy input to the system. The effect of increasing the gas superficial velocity at constant solids mass flux can be understood by viewing it as a decrease in the solids holdup due to the increase in the solids velocity. Since the gas injected is the only source of energy that drives the solids circulation, constant solids mass flux with higher gas flow drives more solids out of the riser. Consequently, solids holdup decreases. Such a trend can be verified directly in our experiments only by comparing one pair of conditions (U_g^{riser}=3.2 and 3.9 m·s^{-1}; G_s=30.1 kg·m^{-2}·s^{-1}).

The qualitative findings presented above can be quantitatively verified by circumferentially averaging the solids holdup distributions. Figure 6-38 shows such a plot of the radial profiles for all the operating conditions investigated. The two profiles in the FF regime show distinctly higher holdups (relatively) and also higher radial gradients. Clearly, three distinct slopes in the profiles can be identified (FF regime) illustrating a three layer stratification observed in the tomograms (Figure 6-37). The solids concentration was nearly zero in the center (up to r/R = 0.27 and 0.5 for high and low fluxes, respectively), increases linearly up to r/R = 0.8 and 0.85 for high and low fluxes, respectively, and later increases linearly with a higher slope. However, in the DPT regime, the solids holdup profiles seem to be relatively flat and show very little variation (within 20%) among the different operating conditions. Nevertheless, the relative (with respect to mean) radial increase of the solids holdup seems to be high and is comparable to that in the FF regime. To compare the relative increase in the radial solids concentration, radial profiles of the reduced holdup, defined as $\frac{\varepsilon(r)-\varepsilon(0)}{\bar{\varepsilon}-\varepsilon(0)}$ are plotted in Figure 6-39. Also such reduced holdup profiles were correlated with the radial position in the literature.

Reduced holdup profiles in Figure 6-39 show a similarity in shape and magnitude for all the flow conditions investigated. Although the velocity and holdup profiles were quite different in the FF and DPT regimes, the reduced holdup seem to show similar profiles. This indicates that the relative increase of the holdup profiles (with respect to

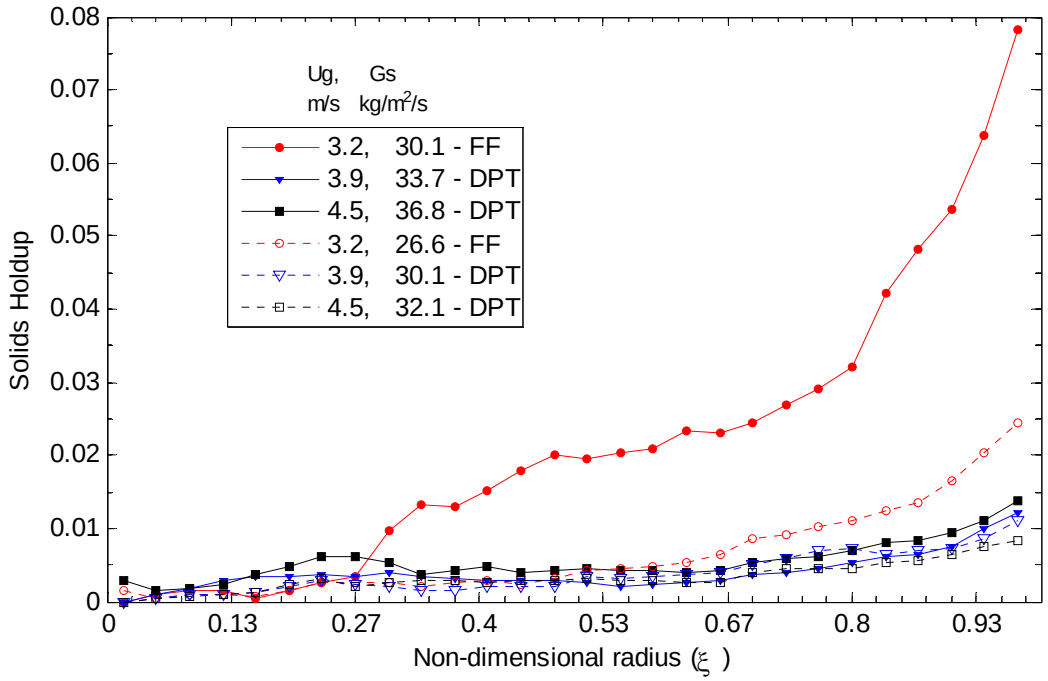

Figure 6-38: Azimuthally averaged radial profiles of the solids holdup

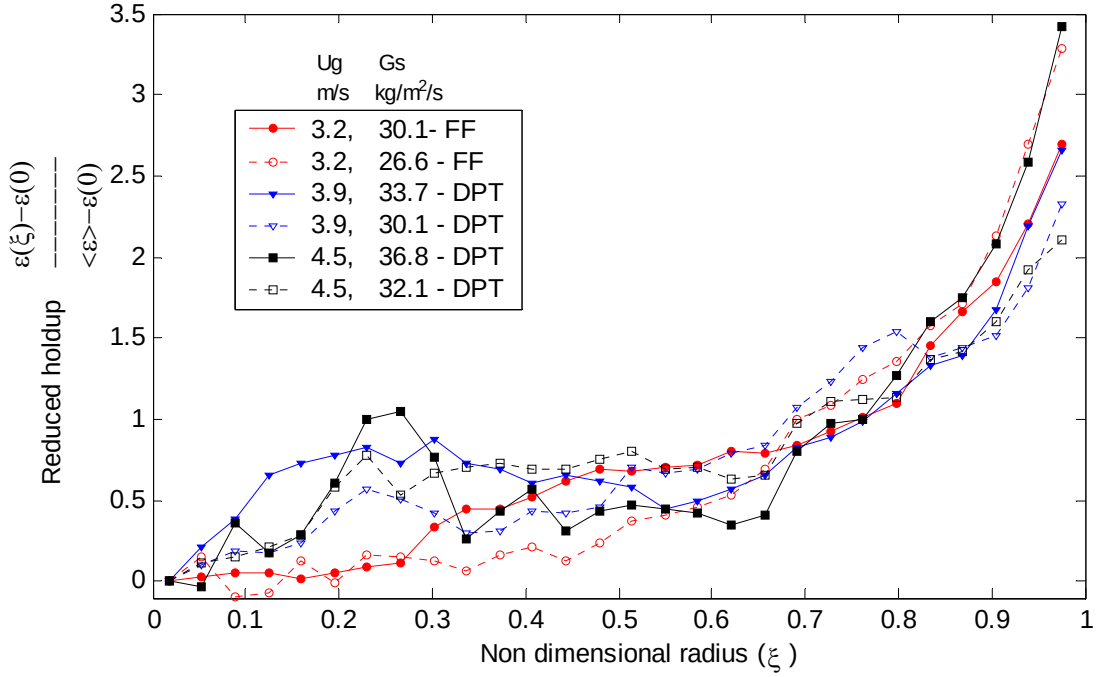

Figure 6-39: Azimuthally averaged radial profiles of the reduced holdup.

corresponding mean) radially is the same in both the regimes. However, a close look at Figure 6-39 indicates that for the conditions in FF regime, the reduced holdup is smaller than those in the DPT regime in the core region, while the trend is opposite near the walls. One can observe very small negative values of the reduced holdup profiles in the core region. These errors can be attributed to measuring very low holdups (mainly in the core) because of which the holdup reduced with the centerline holdup were negative.

The reduced holdup profiles are typically correlated with the radial position to be incorporated in a phenomenological flow model. Patience and Chaouki (1992) and Schlichthaerle and Werther (1999) employed the following form of correlation:

$$\frac{\varepsilon_s(r)-\varepsilon_s(0)}{\langle\varepsilon_s\rangle-\varepsilon_s(0)}=\frac{m+2}{2}\left(\frac{r}{R}\right)^m \tag{6-6}$$

A more general form of Equation (6-6) was employed to model the radial profiles of gas holdup in bubble columns (Kumar, 1994; Chen *et al*., 1998; Ong, 2003).

$$\varepsilon_s=\langle\varepsilon_s\rangle\frac{m+2}{m+2+2c}\left[1+c\left(\frac{r}{R}\right)^m\right] \tag{6-7}$$

In the above equations, $\langle\varepsilon_s\rangle$ is the cross-sectional average solids holdup, constant *m* is related to the steepness of the profile, and constant *c* is related to the extent of solids present in the local wall region. Equation (6-7) was employed to correlate the solids holdup data. Table 6-3 provides the results of fitting the above functional form to the solids holdup profiles. It is clear from the available data (Table 6-3) that the cross-sectional average solids holdup shows trends with both the superficial gas velocity and solids mass flux. However, the effect on the curvature parameters *m* and *c* is not so evident. To facilitate such understanding, Figure 6-40 shows the relative holdup profiles for all the flow conditions from the fitted parameters. Parameter *c* seems to be very high in the FF regime (greater than 10) and decreases with the change of regime to DPT (less than 5). In contrast, exponent *m* was found to be lower in the FF regime as compared to that in DPT regime, indicating a steeper profile in the FF regime. However, for the

operating condition with U_g^{riser}= 3.9 m·s^{-1} and G_s=33.7 kg·m^{-2}·s^{-1}, which is close to the regime transition, a *c* value of 9.5 is found intermediate between FF and DPT regimes. Also, the *m* value was found to be low (4), indicating abnormalities near the regime transition conditions. It can be observed from Equation (6-7) that the exponent *m* alone is not representative of the gradient of the solids holdup. The radial steepness of the solids holdup profile can be assessed with a parameter *F* given by:

$$F = \left(\frac{d\varepsilon_s}{d\xi}\right)_{average} = \left(2\int_0^1 \xi \frac{d\varepsilon_s}{d\xi}\cdot d\xi\right)_{average} = \frac{2\langle\varepsilon_s\rangle cm(m+2)}{(m+1)(m+2+2c)} \tag{6-8}$$

Table 6-3 lists the values of the steepness factor *F* for the each of the operating conditions. It can be observed that *F* increases with the solids mass flux at constant superficial gas velocity both in the FF and DPT regimes. Although not conclusive enough, comparing the *F* values at operating conditions with the constant mass flux G_s = 30.1 kg·m^{-2}·s^{-1}, shows that *F* decreases with increase in superficial gas velocity. Both trends are inline with those reported by Zhang *et al.* (1991).

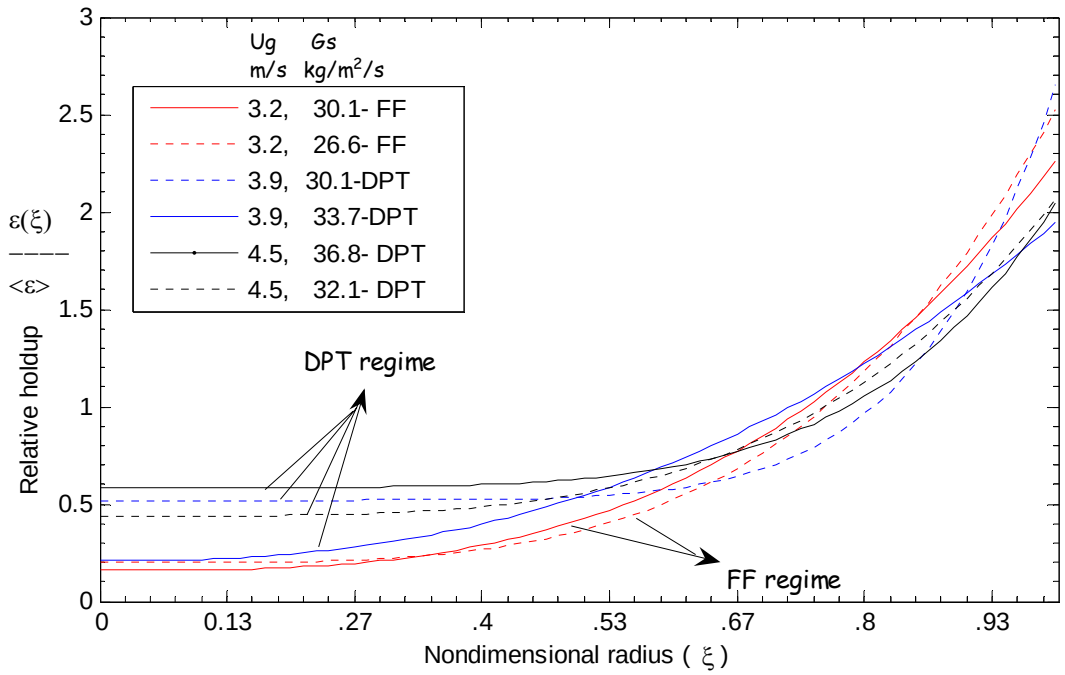

Figure 6-40: Relative holdup profiles obtained from the holdup correlation.

Table 6-3: Correlation fits for the radial holdup profiles.

Operating Conditions	**Mean from CT**	$\varepsilon_s = \langle\varepsilon_s\rangle \frac{m+2}{m+2+2c}\left[1+c\left(\frac{r}{R}\right)^m\right]$					Rhodes *et al.* (1992)			Patience and Chaouki (1995)			Wang *et al.* (1998)	
U_g^{riser} (m·s^{-1}) G_s (kg·m^{-2}·s^{-1})	$\langle\varepsilon_s\rangle_{CT}$ %	$\langle\varepsilon_s\rangle$ %	m	c	D %	F	$\langle\varepsilon_s\rangle$	β	D %	$\langle\varepsilon_s\rangle$	k	D %	$\langle\varepsilon_s\rangle$	D %
3.2, 30.1	2.9	3.24	3	13.5	12	0.1	3.23	1.98	11	3.1	1.32	7	2.65	-9
3.2, 26.6	0.85	0.97	3.9	12	14	0.037	0.98	2.1	15	0.94	1.26	10	0.73	-14
3.9, 33.7	0.48	0.53	4	9.5	11	0.019	0.53	1.7	10	0.5	1.15	4	0.41	-15
3.9, 30.1	0.45	0.51	7	4.2	12	0.019	0.51	1.36	12	0.51	1.13	14	0.44	-2
4.5, 36.8	0.61	0.67	5.1	2.5	10	0.017	0.67	1.14	10	0.67	1.1	10	0.59	-3
4.5, 32.1	0.4	0.43	3.9	3.8	8	0.011	0.44	1.44	10	0.42	1.12	5	0.36	-10

Discrepancy, $D = \frac{\langle\varepsilon_s\rangle - \langle\varepsilon_s\rangle_{CT}}{\langle\varepsilon_s\rangle_{CT}} \times 100$

F – Steepness factor

m, c, β, k – Regressed constants

Rhodes *et al.*(1992) - $\varepsilon_s = \langle\varepsilon_s\rangle\left[1-\beta/2+\beta\left(\frac{r}{R}\right)^2\right]$; Patience and Chaouki (1995) - $\frac{\varepsilon_s - \langle\varepsilon_s\rangle^k}{\langle\varepsilon_s\rangle - \langle\varepsilon_s\rangle^k} = 4\left(\frac{r}{R}\right)^6$;

Wang *et al.* (1998) - $\frac{\varepsilon_s}{\langle\varepsilon_s\rangle} = 0.82 + 48\left(1-\frac{r}{R}\right)\cdot\exp\left[-22\left(1-\frac{r}{R}\right)\right]$ for 1.5% < $\langle\varepsilon_s\rangle$ < 5%; $\frac{\varepsilon_s}{\langle\varepsilon_s\rangle} = 0.905 + \left(\frac{r}{R}\right)^{19}$ for $\langle\varepsilon_s\rangle$ < 1%

Table 6-3 also lists the various available correlations for the radial profiles of solids holdup. The regressed constants and the mean holdup values are indicated for each of the correlations. The correlation by Patience and Chaouki (1992) seems to give the least discrepancy of 8% (averaged for all the operating conditions).

Relative holdup profiles in Figure 6-40 reveal distinctive flow behavior in the FF and DPT regimes. In the central core region, the relative holdup is distinctively lower in the FF regime compared to DPT, although both are flat. The uniformly flat region in the FF regime seems to extend until r/R = 0.27 (approximately), while in DPT it extends until r/R = 0.45 (approximately). Beyond that, the relative holdup increases with close to similar slopes in the FF and DPT regimes. While in the DPT regime, such radial gradients prevail until the wall, in the FF regime higher radial gradients are indicated starting from r/R = 0.8 (approximately). Hence, the above trends reveal three different characteristic layers in the FF regime, while the DPT regime has two characteristic layers. Similar stratification can be observed in the tomograms (Figure 6-37). Note that for the flow condition at U_g^{riser}= 3.9 m·s^{-1} and G_s=33.7 kg·m^{-2}·s^{-1}, close to regime transition, a mixed behavior with FF characteristics near the core transiting slowly to DPT characteristics near the wall is observed.

Although it is difficult to generalize the findings with the limited experimental data available, one can observe from Figure 6-40 that in the FF regime the solids concentration in the core is insensitive to the average holdup $\langle \varepsilon_s \rangle$. On the other hand in the DPT regime, average holdup influences the core solids concentration and is insensitive to the wall concentration. Similar trend with two distinctive variational regions in the radial profiles was reported by Xu *et al.* (1999) for FCC particles. However, none of the studies (within the literature reviewed in Chapter 2) reported the three characteristic layers in the FF regime conditions. Most of the studies, covering a wide range of operating conditions (including DPT and FF) reported only a two layer structure with a nearly constant core in the center transiting to a steep increasing holdup near the wall (Hartge *et al.,* 1986; Martin *et al.,* 1992; Rhodes *et al.,* 1998; Xu *et al.,* 1999; Issangya *et al.*, 2000; Malcus *et al.,* 2000). The reason could be that the employed techniques in the studies have a poor spatial resolution (only 5-10 solids holdup data

across the riser radius). Also, the wall effects influence most of the sensing techniques employed. The results with X-ray tomography from Wirth's group (Wirth *et al.*, 1991; Grassler and Wirth, 1999), with a spatial resolution as good as 6 mm also could not capture such three layer stratification. As a matter of fact, such three layer stratification could not be captured in the velocity fields from CARPT results (Figures 6-23 to 6-29) for the same reason that the spatial resolution (for Eulerian averaging) is relatively poor.

The radial profiles of the granular temperature (Figure 6-35) seem to have a similar shape as that of the gas holdup ($1-\varepsilon_s$) profiles. In order to understand their relationship and to obtain a functional form for the granular temperature, Θ_s, the reduced profiles of the two measured quantities were plotted in Figure 6-41. Considering the fact that the granular temperature was obtained from CARPT data with relatively low spatial resolution, there seems to be a fair comparison of the reduced profiles in both the regimes. Hence one can assume an approximate functional relation given by:

$$\frac{\Theta_s(r)-\Theta_s(0)}{\langle\Theta_s\rangle-\Theta_s(0)} \approx \frac{\varepsilon_s(r)-\varepsilon_s(0)}{\langle\varepsilon_s\rangle-\varepsilon_s(0)} \qquad \Rightarrow \Theta_s(r) \approx a\varepsilon_s(r)+b \tag{6-9}$$

Such a functional form can be employed to derive the dependence of solids viscosity (Equation 6-2) variation with solids holdup, which can be used as an input in a two-fluid approach of a CFD model. One should note that the relationship given in Equation (6-9) is limited to dilute conditions in risers. The riser was investigated only under 'dilute conditions' where solids fluctuations increase with the solids holdup, while it is known that beyond certain holdup limit (1-6%) fluctuations decrease with further increase in the solids holdup.

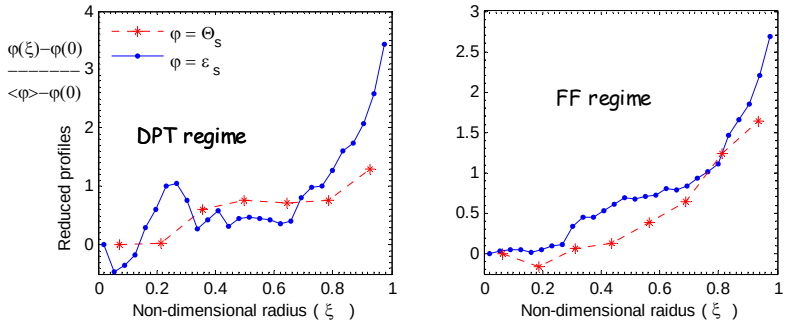

Figure 6-41: Reduced profiles of the granular temperature, Θ_s and the solids holdup, ε_s in: a) DPT (U_g^{riser}=4.5 m·s^{-1}; G_s=36.8 kg·m^{-2}·s^{-1}); b) FF (U_g^{riser}=3.2 m·s^{-1}; G_s=30.1 kg·m^{-2}·s^{-1})

Axial Variation of Solids Holdup

It was established in the earlier section that the axial variation of solids velocity within the zone of investigation was negligible. To check whether solids flow is indeed fully developed in the zone of investigation the radial profiles of the solids holdup at two different axial planes are shown in Figure 6-42 for all the operating conditions under investigation. Although there are slight variations in the holdup profiles at the two different axial planes, the differences are within the density resolution of the scanner. Hence, the axial gradients of the solids holdup are negligible in the zone of investigation.

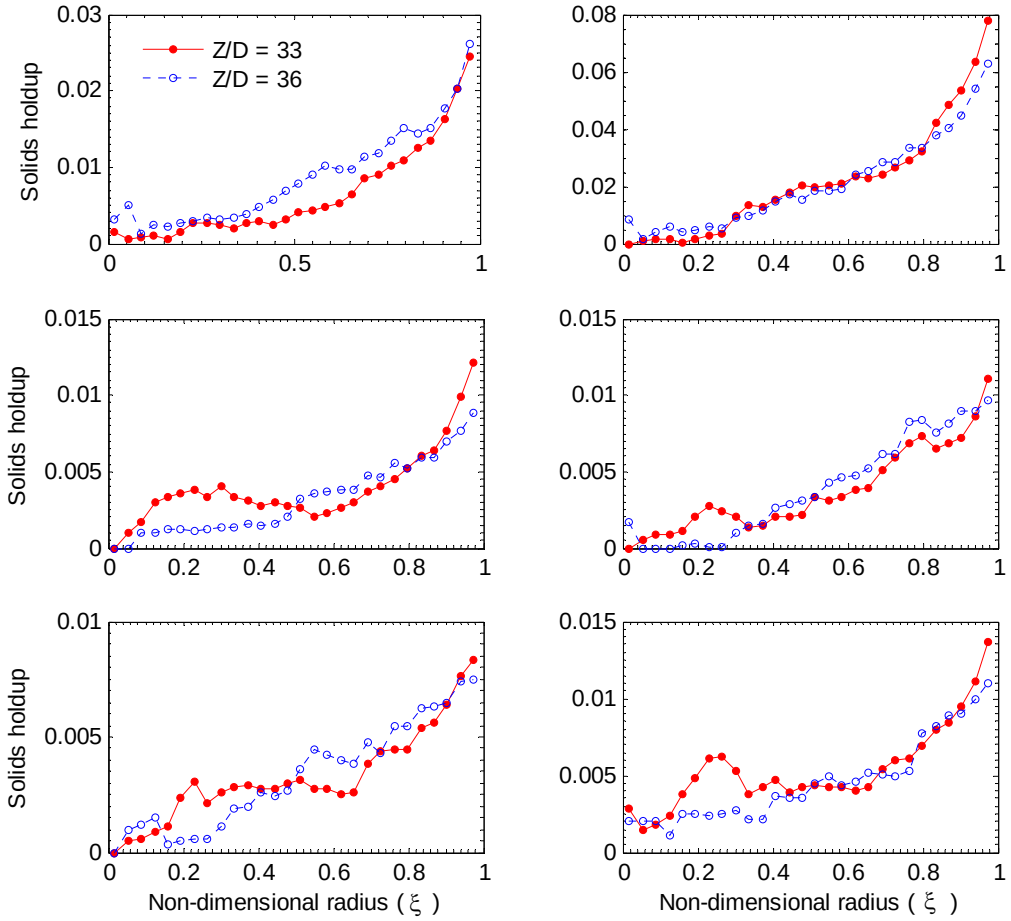

Figure 6-42: Radial solids holdup profiles in the riser under the operating conditions: a) U_g^{riser}=3.2 m·s^{-1}; G_s=26.6 kg·m^{-2}·s^{-1}; b) U_g^{riser}=3.2 m·s^{-1}; G_s=30.1 kg·m^{-2}·s^{-1}; c) U_g^{riser}=3.9 m·s^{-1}; G_s=30.1 kg·m^{-2}·s^{-1}; d) U_g^{riser}=3.9 m·s^{-1}; G_s=33.7 kg·m^{-2}·s^{-1}; e) U_g^{riser}=4.5 m·s^{-1}; G_s=32.7 kg·m^{-2}·s^{-1}; f) U_g^{riser}=4.5 m·s^{-1}; G_s=36.8 kg·m^{-2}·s^{-1}.

6.3.3 Comparison of CT versus CARPT Derived Holdup Profiles

By assuming 'well-perfusedness' (Moslemian, 1989; Dudukovic *et al.*, 1991; Godfroy *et al.*, 1999; Stellema, 1998), particle occurrences per unit volume obtained from CARPT data can be related to solids holdup as follows:

$$\left(\frac{Occurrences(per \cdot unit \cdot volume)}{Total \cdot Occurrences}\right)_{CS} \propto \varepsilon_s \qquad (6\text{-}10)$$

Figure 6-43 presents the typical comparison of the reduced holdup profiles derived from CARPT and that obtained from CT. Comparison in both FF and DPT regimes seems to be fair with the CARPT derived profiles overpredicting the averaged reduced holdups in the wall region. Similar trends were observed for all the operating conditions under investigation. Again the reason for such overprediction of wall holdup by CARPT could be due to the low spatial resolution for Eulerian averaging in the CARPT technique or to insufficient statistics in the wall region. Considering the fact that the profiles were derived from two independent experimental techniques, this comparison serves as a validation of results for both the techniques.

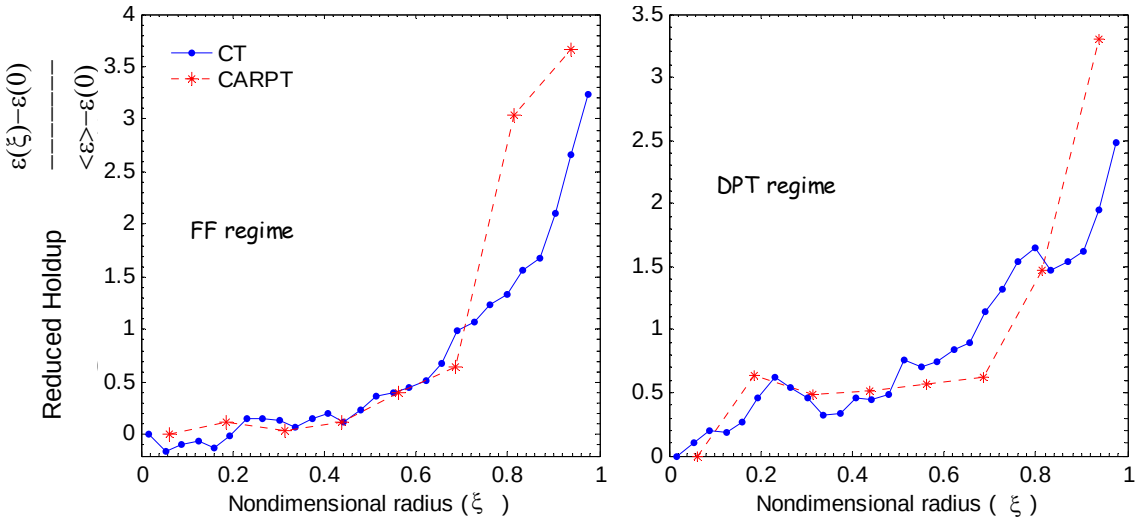

Figure 6-43: Comparison of the reduced holdup profiles derived from CARPT and CT at: a) FF (U_g^{riser}=3.2 m·s^{-1}; G_s=26.6 kg·m^{-2}·s^{-1}); b) DPT (U_g^{riser}=3.9 m·s^{-1}; G_s=33.7 kg·m^{-2}·s^{-1})

6.4 Summary

Single radioactive particle tracking in the gas-solid riser yielded a wealth of solids instantaneous and time-averaged flow information. Added to it the γ-ray tomography provided detailed time-averaged volume fraction profiles of the two phase riser flow enabling some new insights into these complex multiphase flow phenomena. Following are the key findings from this chapter with regards to the solids flow in risers:

i. CARPT technique was implemented on a pilot-scale gas-solid riser and the challenges in implementing were overcome.

ii. Instantaneous particle traces reveal occasional downflow in the core region (near center) only under the FF regime. Both large scale internal recirculation superimposed by fine scale fluctuations contribute to axial backmixing, while in the horizontal plane solids mixing is principally dispersive.

iii. *Post Facto* validation of CARPT derived quantities showed the system is *ergodic*, and the results are mesh independent. Velocity fluctuations are large enough to neglect Poisson and electronic generated noise in the data.

iv. Solids axial velocity, interpreted from the PDFs, showed large radial gradients with negative at the wall in the FF regime. In DPT regime, negative axial velocities were not observed in the center, while near the wall showed negative velocities with its ensemble average being positive.

v. Solids flow is nearly axi-symmteric and is close to fully-developed (within the zone of interrogation) revealed by both the velocity and holdup profiles.

vi. The movement of solids from core to annulus seems to be governed by the gradients in the time-averaged velocity profiles, while the movement of solids from annulus to core (if prevalent) is governed by the gradients in the fluctuating velocity profiles in the fully-developed zone.

vii. Contour plots of turbulent kinetic energy and particle occurrences reveal a clear core-annular flow structure within the FF regime, while the profiles are uniform in the DPT regime.

viii. Clustering phenomena seem to exist throughout the riser cross section (more likely near the wall) along with the particle exchange between core and annulus.

ix. Although the ensemble average solids velocity increases, the solids velocity fluctuations decrease with the increase in the solids mass flux and/or superficial gas velocity under ‘dilute conditions’.

x. Flow in the riser is anisotropic with the fluctuating motion principally directed along the main axis of flow.

xi. Boussinesq’s hypothesis does not hold for solids flow in a riser and yields physically unrealizable viscosity values.

xii. The relative dominance of the increase in the collision frequency over the decrease in the mean free path (with solids holdup) dictates the trends for the granular temperature and solids viscosity. These two mechanisms result in granular temperature to increase with the increasing solids holdup under low flux conditions investigated in the CREL riser.

xiii. Selection of the proper length of time-averaging (during each projection) affects the holdup profile obtained from in a CT experiment. For the riser flow, the length of time-averaging using a sampling frequency of 10 Hz and 114 samples (per projection) was found to be sufficient.

xiv. Tomograms reveal three different characteristic layers in the FF regime, while the DPT regime has two characteristic layers.

xv. Steepness in the radial profiles of solids holdup increases with the solids mass flux at constant superficial gas velocity both in the FF and DPT regimes.

xvi. Reduced holdup profiles derived from CARPT and CT match fairly well.

Besides solids flow dynamics, CARPT can also provide solids local mixing information. The effect of operating conditions on the solids flow structure, circulation patterns and local mixing are discussed in the next chapter.

Chapter 7

Further Analysis of Solids Flow and Mixing: Effect of Operating Conditions

7.0 Scope

CFBs exhibit very complex flow dynamics caused by interactions between the gas and solids phases. As discussed in the previous chapter the motion of solids is driven by many mechanisms that are difficult to identify and to quantify. From an engineering viewpoint, the operating conditions determine the solids flow and mixing which in turn influence the performance of the CFB. On to continue building the understanding of solids flow and mixing, in this chapter, the effect of operating conditions is studied. Further, CARPT experiments provide rich Lagrangian data, using which solids residence time distributions, eddy diffusivities, and other ways of characterizing the local solids transient flow field can be obtained and these are discussed in this chapter. Finally, the problem of satisfying the overall continuity with CARPT and CT data is discussed.

7.1 Introduction

Academic researchers in the last decades acquired a lot of knowledge about local solids dynamics in CFB units close to walls at low solids fluxes where these systems are observed by optical techniques. On the other hand people in industry have gained a lot of practical experience in FCC units as well as in CFB combustors. Furthermore, the modeling effort, starting with the model of Sinclair and Jackson (1989), revealed a remarkably rich variety of behavior for gas-solid flow in a vertical pipe over the range of possible flow conditions. However, there is still considerable uncertainty and disagreement with regard to the dependence of fine scale solids flow structures on the operating conditions. Moreover, the effect of operating conditions on the extent and mechanism of solids backmixing and dispersion needs to be quantified. This dependency is very important in scale-up, design and optimization. An attempt is made, in this chapter, to ascertain the effect of operating conditions on the solids flow field parameters such as velocity, turbulent stresses, granular temperature and on mixing parameters such as residence times, circulation times, and local dispersion coefficients.

7.2 Effect of Operating Conditions

7.2.1 Solids Velocity Fields

Before proceeding to the effect of operating conditions on the solids velocity field, a brief discussion is in order on the flow structure characteristics of high solids flux conditions (>100 $kg \cdot m^{-2} \cdot s^{-1}$) in the SNL's riser. Checks for *Post Facto* validation with regards to the ergodicity of the system, mesh independence and filtering procedure were performed similar to that described in Chapter 6. Results are not shown graphically for the sake of brevity. The flow parameters displayed occurrence independence (beyond 70% data) for the three operating conditions investigated in the SNL's riser. By computing the Eulerian quantities with different mesh sizes given in Table 6-2, a mesh size given by 'Mesh 1' resulted in mesh independent profiles. Wavelet filtering (Degaleesan, 1997) of the position data showed no differences in the velocity auto-correlation profiles, indicating

that flow fluctuations are high enough to allow one to neglect the Poisson and electronic generated noise. The mean velocity fields, when visualized in *r*-*z* and *r*-θ planes (Figure 7-1) revealed an almost axi-symmetric flow structure of the solids for the three flow conditions (Table 5-3) investigated in the SNL's riser.

Figure 7-1 also reveals relatively small ensemble-averaged radial and azimuthal velocity components (compared to axial) as expected in fully-developed flow. The axial variation of the ensemble-averaged velocity vectors is less than 13% indicating a close to fully-developed flow in a time-averaged sense. However, the solids flow inferred from Figure 7-1 can not be taken to be fully developed in a strict sense, since the radial velocities are only relatively small and are numerically not equal to zero. The radial variation of the velocity vectors in Figure 7-1 indicates the solids flowing upwards in the central core and the solids moving downwards in an outer annulus. This represents the core (up) and annulus (down) flow structure often postulated in the literature. Such strong radial variation can indeed be seen from the ensemble averages of the solids axial velocity probability density functions (PDFs) shown in Figure 7-2. The axial velocity PDFs in both the regimes display significant negative velocities near the wall transitioning to no negative velocities at the center. This solids flow pattern is in contrast to that in the low flux flow conditions (Figures 6-19 to 6-21), where velocity PDFs reveal a bimodal axial velocity PDF with negative velocities near the center. The negative axial velocities at the center were interpreted to be due to clusters falling down (Chapter 6). Hence, in contrast to the low flux conditions, clustering phenomenon does not seem to occur in the central core at high flux conditions in the FF regime.

In the DPT regime (Figure 7-2b), the ensemble-averaged solids axial velocities near the wall are negative, which was not the case at the low solids flux conditions in the DPT regime. This is probably due to the increase in the solids concentration at high solids flux, resulting in increased tendency for clustering near the wall which in turn increases the solids down-flow. Thus, the velocity PDFs from FF and DPT regimes suggest that the clustering phenomenon is localized near the walls at high solids fluxes, while it is common throughout the riser cross-section (FF regime) at low solids fluxes.

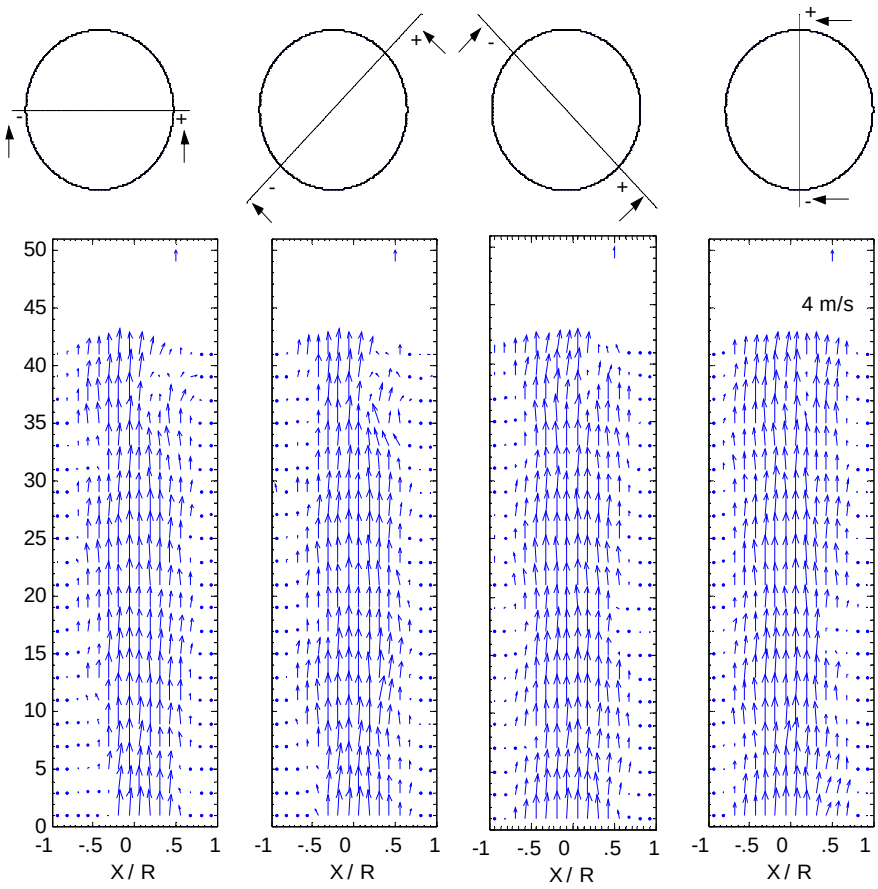

(a)

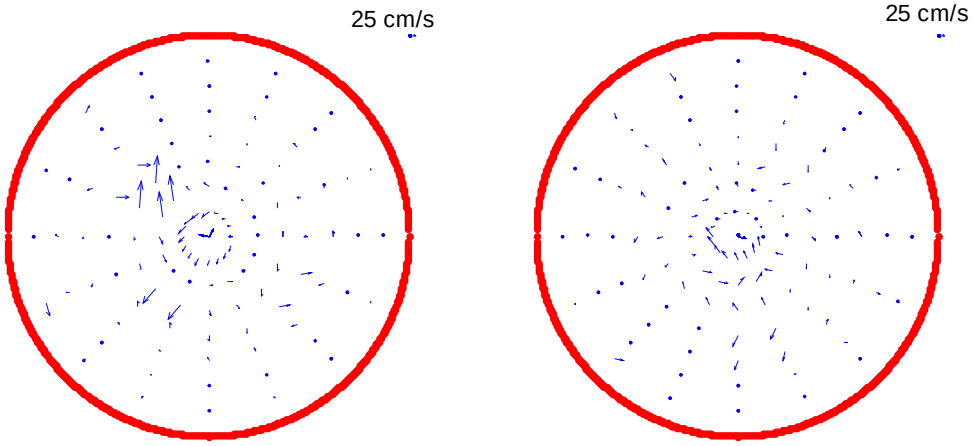

(b)

Figure 7-1: Visualization of the velocity vectors in the zone of interrogation in a) *r*-*z* plane at different angles; b) *r*-θ plane at different axial heights (*z*/*D* = 16.3, 18.5). The operating conditions are in FF regime at U_g = 5.56 m·s^{-1}; G_s = 144.5 kg·m^{-2}·s^{-1}.

Each of the axial velocity PDFs shown in Figure 7-2 was obtained based on the statistics from a single compartment at a particular angular position. Now one can also collect the statistics from every angular compartment at each radial location to construct axial velocity PDFs. Such a velocity PDF characterizes the velocity variation along the perimeter at a particular radial position. Comparing the velocity PDFs from a single compartment to that obtained from the perimeter (similar to the results from low flux conditions), we noticed that the functions do not change much with the increase in the statistics. The variation in the corresponding means and standard deviations was found to be less than 7% except near the wall (r/R = 0.94), where the variation is large. Such small variation indeed reflects axisymmetric flow.

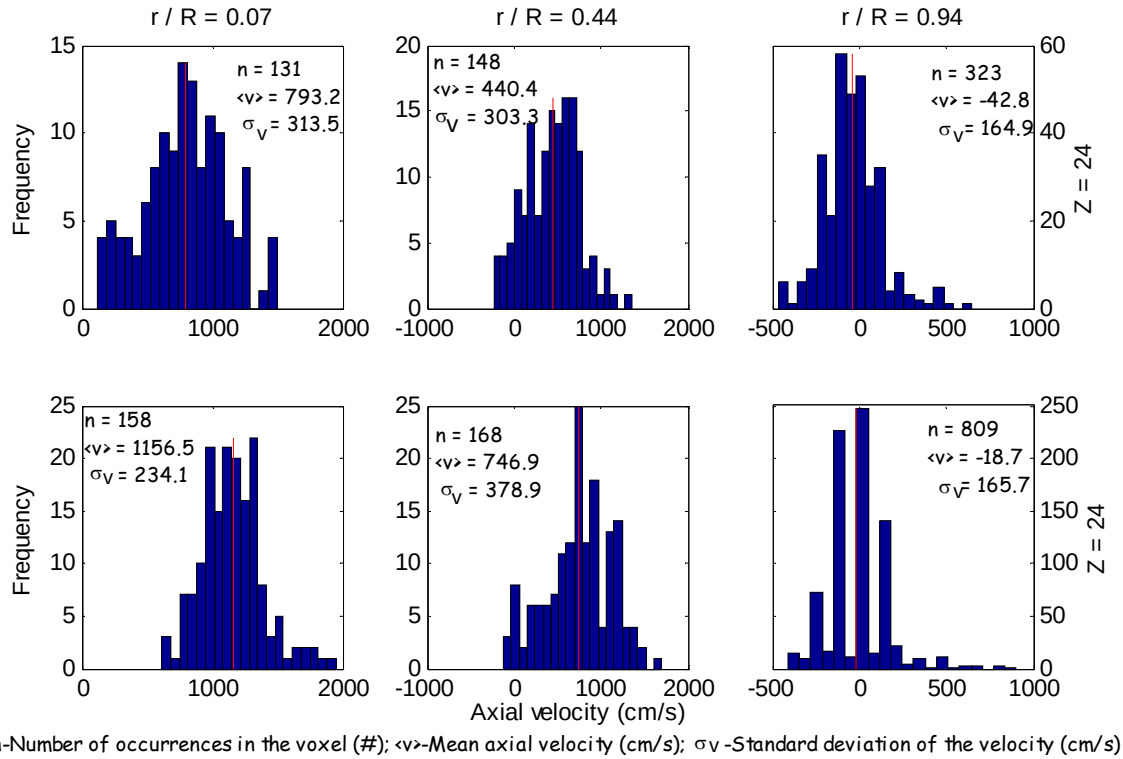

Figure 7-2: Probability density functions of the axial velocity at three radial locations in a) FF (U_g=5.5 m·s^{-1}; G_s=144 kg·m^{-2}s^{-1}); b) DPT (U_g= 7.7 m·s^{-1}; G_s=119 kg·m^{-2}s^{-1}).

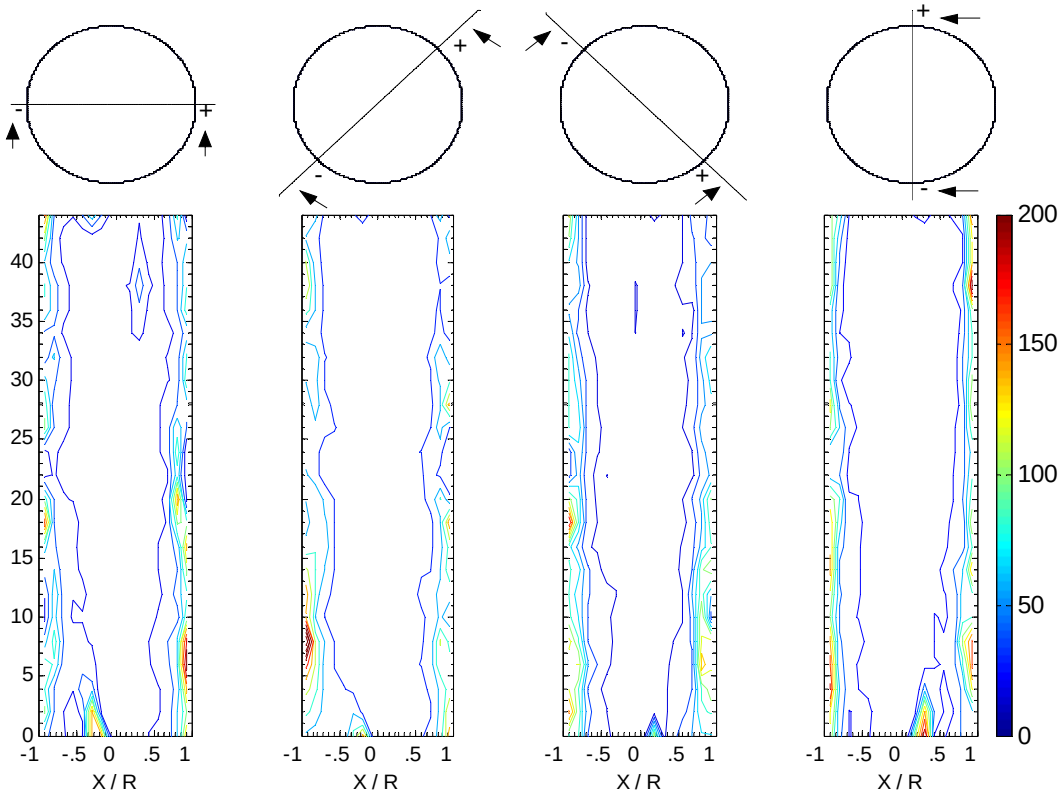

(a)

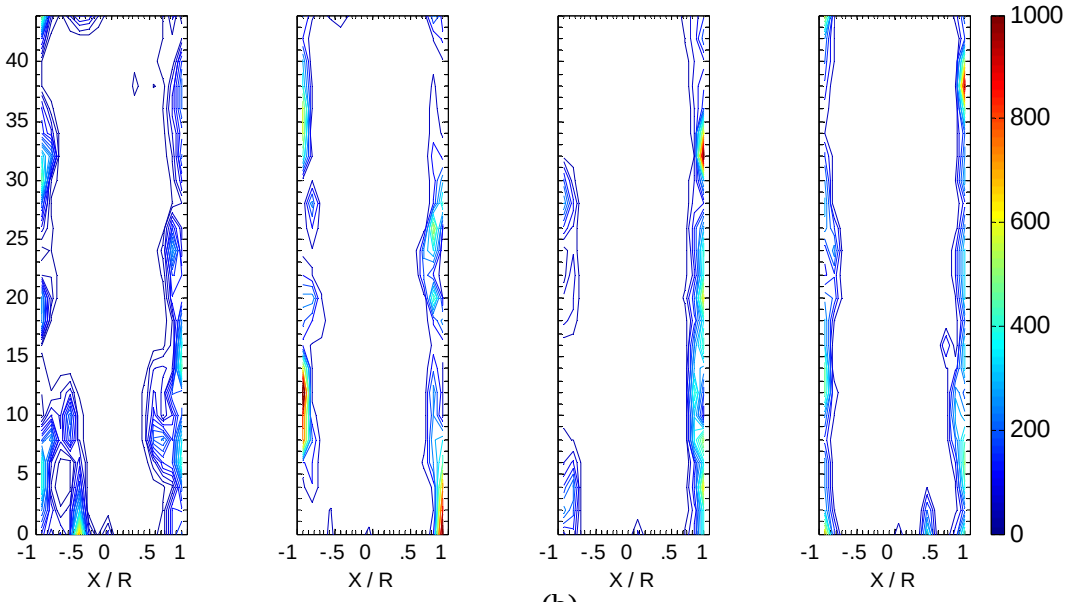

(b)

Figure 7-3: Contour plots visualized at different longitudinal views of the particle occurrences per unit volume (#/cm^3) in a) FF regime (U_g^{riser} = 5.56 m·s^{-1}; G_s = 144.5 kg·m^{-2}·s^{-1}) and, b) DPT (U_g^{riser} = 7.71 m·s^{-1}; G_s = 119 kg·m^{-2}·s^{-1}).

Tracer particle occurrence profiles, when visualized in different *r-z* planes as shown in Figure 7-3, also convey the same message. Radial segregation seems to be intense in both FF and DPT regimes at high solids fluxes. Annulus thickness indicated by the contours in Figure 7-3 was found to be higher in the FF regime as compared to that in the DPT regime. The annulus thickness increases with the increasing solids flux at constant gas superficial velocity (U_g^{riser} = 5.5 m·s^{-1}; G_s = 102, 144.5 kg·m^{-2}·s^{-1}). In contrast to no annulus found at low solids flux conditions (Figure 6-28), the DPT regime at high solids flux conditions exhibits a dense film of solids moving downwards (Figure 7-3b). Although the total number of particle occurrences was different in each of the flow conditions in Figures 7-3a and 7-3b, the magnitudes of the values in the contours suggest that the annulus is denser and thinner in the DPT regime, while it is less concentrated and thicker in the FF regime. This result indicates that radial segregation is more severe in the DPT regime at high solids fluxes (beyond a certain solids volume fraction limit). At low solids fluxes, as reported in Chapter 6, negligible radial segregation was observed in the DPT regime. Absence of any contour lines in the central core region, both in the FF and DPT regimes, indicate presence of a relatively very small and uniform solids concentration in the core region. Thus, solids aggregation tendency or cluster formation is negligible in the core region at high solids fluxes which supports the conclusion from the velocity PDFs.

Contour plots of turbulent kinetic energy per unit bulk density, shown in Figure 7-4 suggest an approximately axi-symmetric turbulent field in both the FF and DPT regimes. Comparing Figures 7-3 and 7-4, profiles of turbulent kinetic energy seem to correlate well with those of the particle occurrences in the FF regime (similarity with the gas holdup). However, in the DPT regime such similarity is not observed. This is in contrast to the low flux results where both FF and DPT profiles seem to correlate well.

7.2.2 Mean Radial Velocity Profiles

Contour plots in the previous section displayed an axi-symmteric flow structure inside risers. Also, the axial variation in the flow parameters was negligible, indicating the flow to be fully-developed in the zone of investigation. Hence, all the profiles were

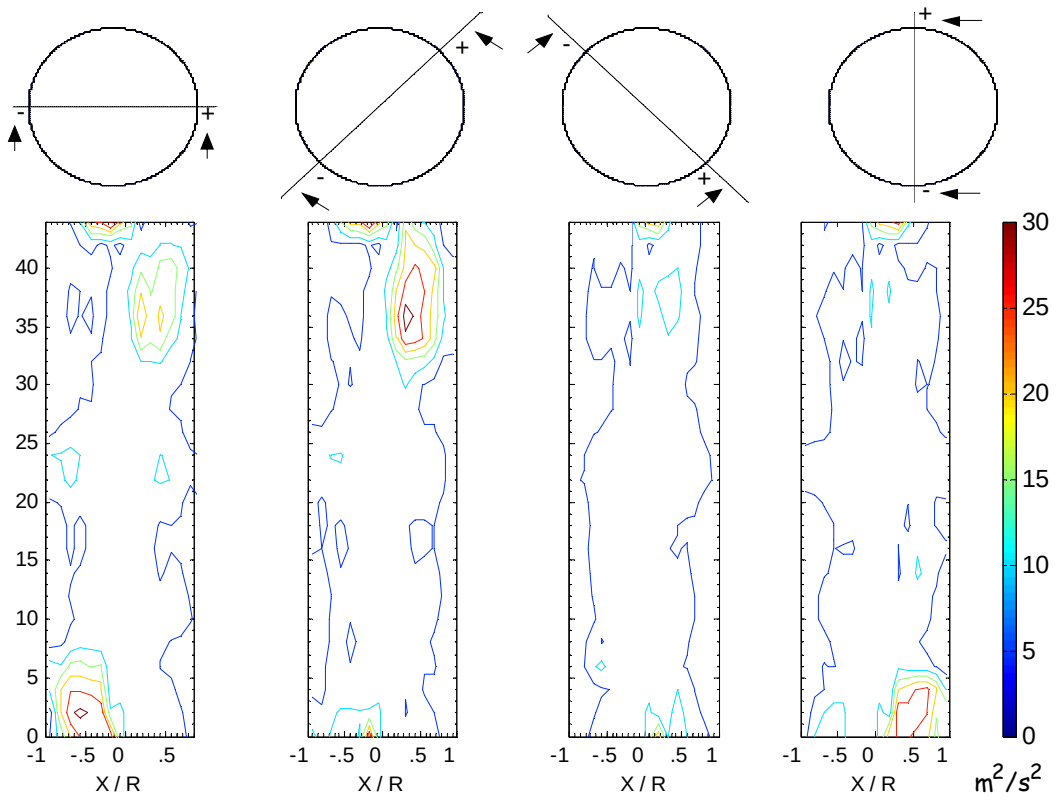

(a)

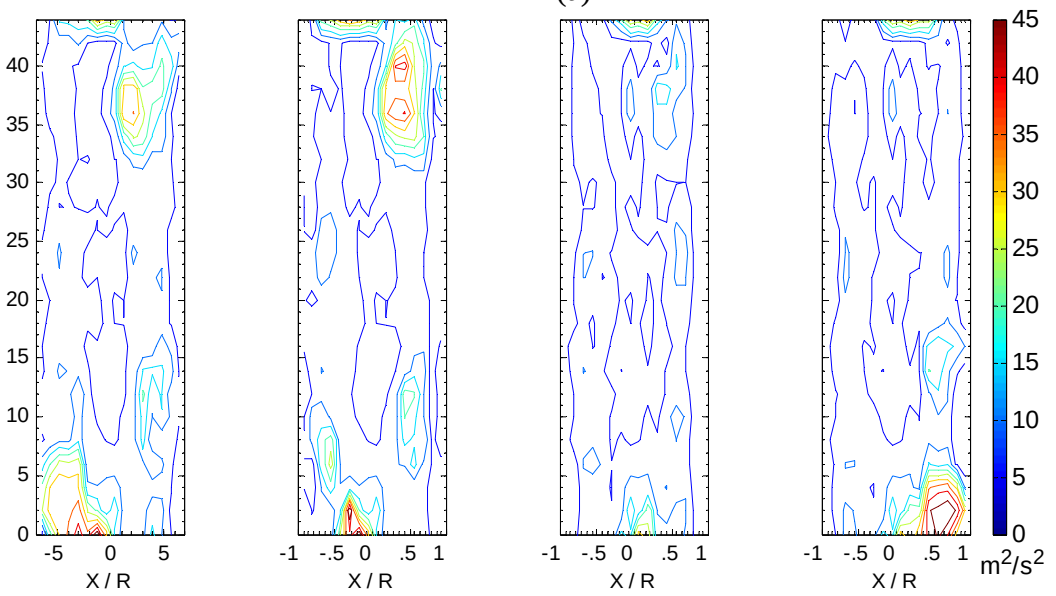

(b)

Figure 7-4: Contour plots visualized at different longitudinal views of the turbulent kinetic energy per unit bulk density in a) FF regime (U_g^{riser} = 5.56 m·s^{-1}; G_s = 144.5 kg·m^{-2}·s^{-1}) and, b) DPT (U_g^{riser} = 7.71 m·s^{-1}; G_s = 119 kg·m^{-2}·s^{-1}).

azimuthally and axially averaged so as to investigate the effect of operating conditions on the one dimensional flow structure in risers.

Figure 7-5 displays the radial profiles of the ensemble-averaged and spatially averaged solids axial velocity for all the operating conditions investigated. To assess the similarity in the mean axial velocity profiles, the velocities were normalized in Figure 7-5a with the corresponding cross-sectional averaged values, reported in the legends. Figure 7-5a suggests that the shapes of the mean solids axial velocity profiles are similar in both risers at low and high solids fluxes. This result is in agreement with the "similar profiles" concept of Monceaux *et al*. (1986) and Rhodes *et al.* (1992), where both studies showed that at a given gas velocity, radial profiles of relative solids mass flux changed very little with the changes in the mean solids flux in the riser. The relative solids holdup profiles also varied very little with the operating conditions as reported in Chapter 6. Hence, both the time-averaged relative axial velocity and holdup profiles for a range of operating conditions investigated can be described with a single functional form for each. Berruti *et al.* (1995) speculated that such "similar profiles of mass flux" may be valid over a very limited range of operating conditions. Although the total solids mass flux can not be determined accurately from the time-averaged solids axial velocity and holdup profiles (due to the lack of the cross-correlation values of the fluctuating solids axial velocity and solids holdup), our results seem to be in near agreement with the concept of Monceaux *et al*. (1986) and Rhodes *et al.* (1992).

The flow condition at U_g^{riser} = 5.5 m·s^{-1} and G_s = 102 kg·m^{-2}·s^{-1}, however, exhibits a slightly different functional form near the center of the column (Figure 7-5a). This deviation is probably due to the flow being close to the regime transition, resulting in the oscillating flow of the suspension, moving in slugs.

The mean axial velocity, as seen in Figure 7-5b, increases with the increase in solids mass flux at constant gas velocity, which agrees with most of the reported studies (e.g. Berruti *et al*., 1995). A substantial increase in the mean solids axial velocity is observed in the center of the column when superficial gas velocity and solids mass flux are increased from the FF to the DPT regime (Figure 7-5b). Within the spatial resolution of the velocity reconstruction, the inversion point of the axial solids velocity profile

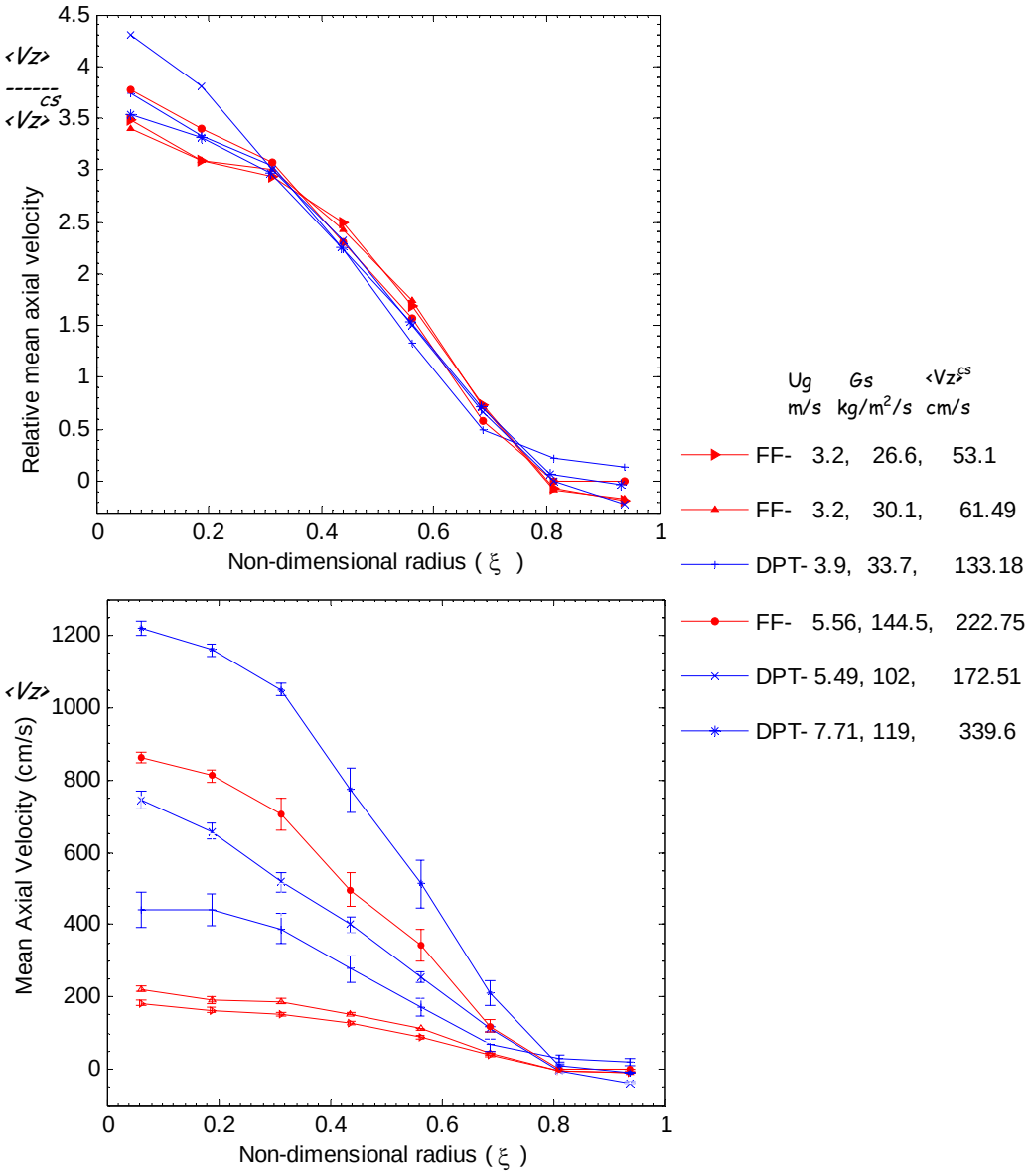

Figure 7-5: Circumferentially and axially averaged time-averaged radial profiles of a) relative axial velocity; b) axial velocity for all the flow conditions investigated. (Note that the data was obtained from two different risers, at low solids fluxes in the CREL riser and at high solids fluxes in SNL's riser).

(corresponding to annulus thickness) was found to be located in the same compartment (with r/R = 0.81). Hence, the down-flow of solids at the wall is expected to cause considerable backmixing in the solids phase. It can also be observed from Figure 7-5b that the error bars indicated on the velocities are relatively small (within 15%), supporting the earlier conclusion of the solids flow being close to fully-developed.

In the profiles shown in Figure 7-5b, the error bars represent the range of the values encountered while circumferentially and axially averaging the data. The same is true for all the subsequent plots of the radial variation of the turbulent parameters.

7.2.3 Radial Profiles of Turbulent Parameters

The radial profiles of relative axial and radial normal solids stresses are shown in Figure 7-6. The axial normal solids Reynolds stress seems to decay in the radial direction monotonically in the FF regime, while in the DPT regime, it peaks at an intermediate radial position and then decays. The above trend seems to persist at both the low and high solids fluxes. The cross-sectional average of the solids axial normal stress increases with the increase in the solids flux at constant gas velocity. Note that the operating condition at U_g^{riser} = 5.49 m·s^{-1} and G_s = 102 kg·m^{-2}·s^{-1} is indicated as DPT, while it is very close to the regime transition (Figure 4-14). Interestingly, the radial normal stress for all the flow conditions shows a peak close to the radial position of r/R = 0.7. The reason, as discussed in Chapter 6, could be that this radial position is the interface at which the flat and low solids holdup profile, prevalent in the core region starts to increase drastically with radius towards the wall. Hence, the radial particle exchange between the dilute core and dense wall region is extensive at this interface. It can be noticed that the cross-sectional average of the solids radial normal stress increases with solids flux at low solids flux conditions, while it decreases with solids flux at high solids flux conditions. The reasons for such trend in solids Reynolds stresses are discussed later along with the trends for granular temperature.

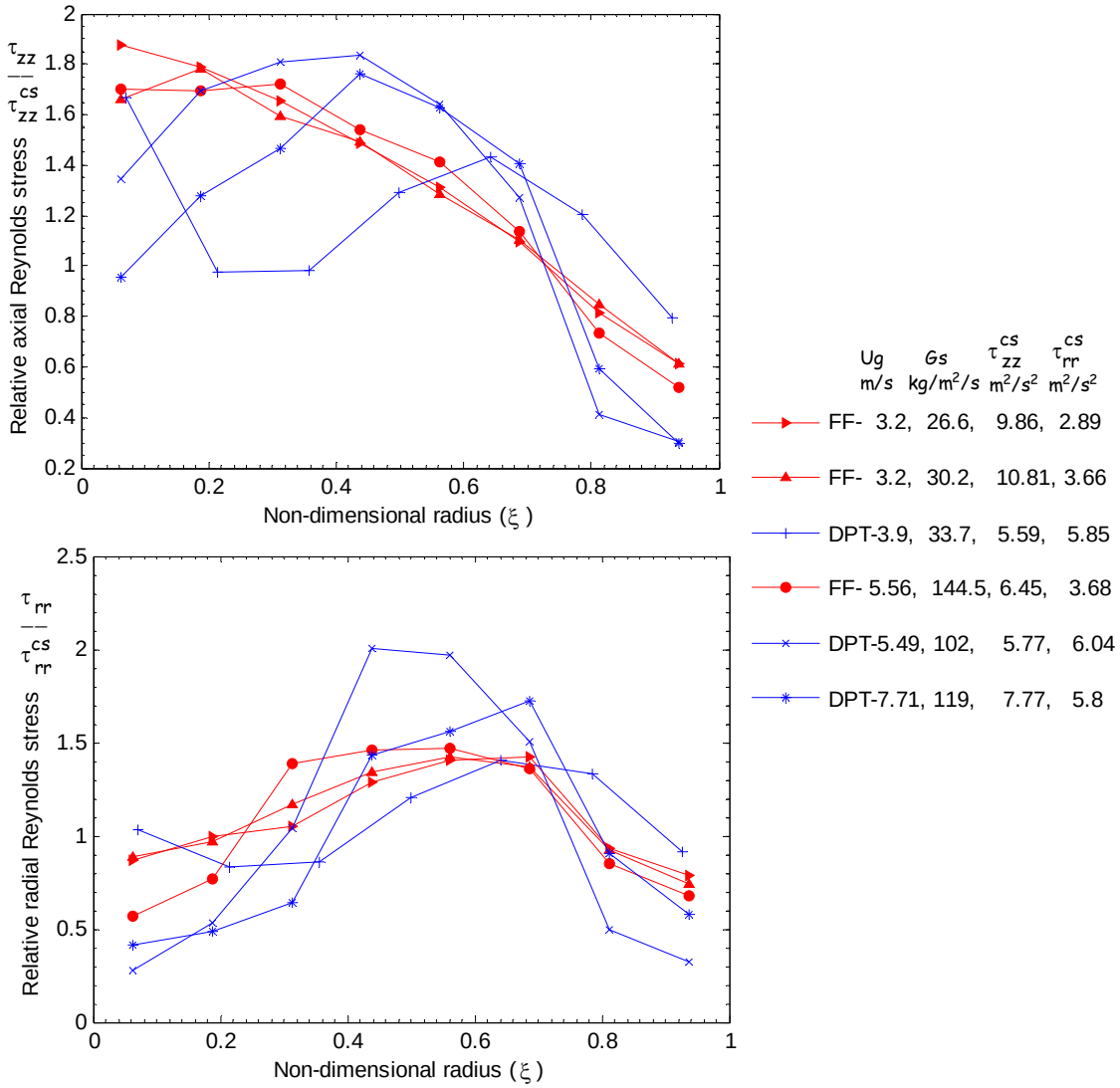

Figure 7-6: Circumferentially and axially averaged radial profiles of the relative Reynolds normal stresses in a) axial and, b) radial directions for all the flow conditions investigated. (Note that the data was obtained from two different risers, at low solids fluxes in the CREL riser and high solids fluxes in the SNL's riser).

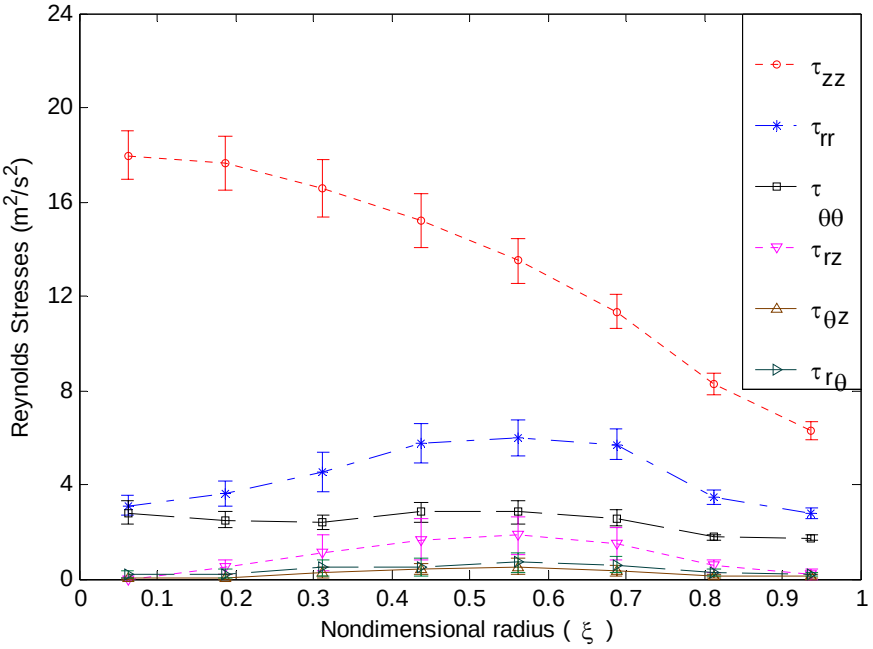

(a)

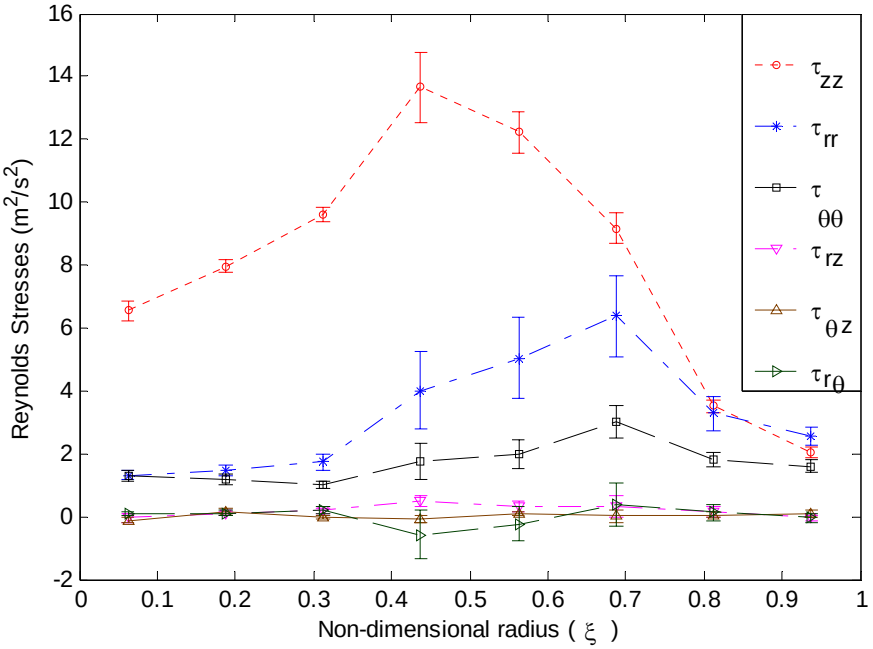

(b)

Figure 7-7: Circumferentially and axially averaged radial profiles of the Reynolds stresses in a) FF regime (U_g^{riser} = 3.2 m·s^{-1}; G_s = 26.6 kg·m^{-2}·s^{-1}) and, b) DPT (U_g^{riser} = 7.71 m·s^{-1}; G_s = 119 kg·m^{-2}·s^{-1}).

Spatially-averaged radial profiles of the six components of the Reynolds stress tensor are plotted in Figure 7-7. Clearly, turbulence in both the FF and DPT regimes (Figures 7-7a and 7-7b, respectively) is anisotropic. The solids azimuthal normal stress is much smaller than the axial and radial normal components in both regimes and their profiles look relatively flat. The shear stress, τ_{rz}, is one order of magnitude smaller than the normal stresses. The radial profiles of the solids shear stress, as noticed in Figure 7-7, show a peak near the radial position r/R = 0.5 and tend to zero near the center and the walls. Similar trend was observed for all the operating conditions from both the risers (CREL and SNL). These results for solids shear stress are in agreement with the data and simulations reported by Tartan and Gidaspow (2004). The solids shear stress is found to increase with the increasing solids flux at both the low and high solids fluxes. The angular components of the shear stress, $\tau_{\theta r}$ and $\tau_{z\theta}$, can be observed from Figure 7-7 to be negligible and are considered zero.

The granular temperature in kinetic theory of granular flows, when scaled by a constant, represents the turbulent kinetic energy of solids. The radial profiles of the turbulent kinetic energy (per unit bulk density) for all the operating conditions are displayed in Figure 7-8. The contribution from azimuthal component is much smaller than the axial and radial, indicating strong anisotropic nature of turbulence.

The contribution of the axial fluctuations dominates and hence, the granular temperature profiles are similar to the respective axial normal stress profiles. The granular temperature in the FF regime decreases monotonically with radial position, while it shows a peak in the DPT regime. Such a trend can be observed both at low and high solids flux conditions. The granular temperature increases with the increasing solids flux at constant gas velocity at low solids flux conditions, while it decreases with the increasing solids flux at high flux conditions. It was argued in Chapter 6 that the relative dominance of the increase in particle collision frequency over the decrease of the mean free path with increasing solids concentration dictates the trends in granular temperature. A decrease in the gas velocity, or an increase in the solids flux, increases the solids concentration. The results shown in Figure 7-8 support the hypothesis that particle fluctuations increase with solids concentration in the ‘dilute conditions’

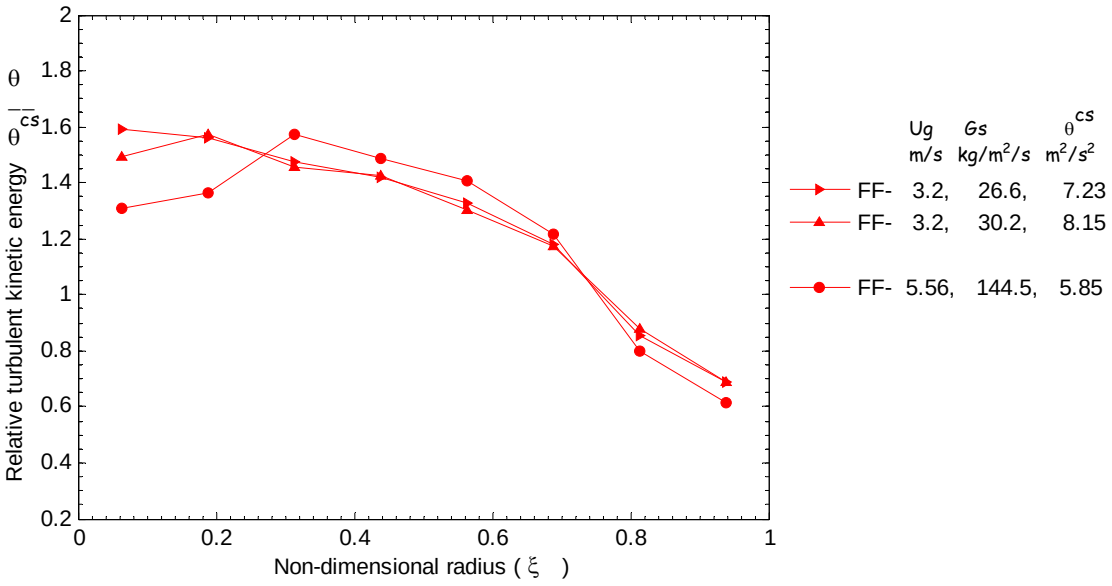

(a)

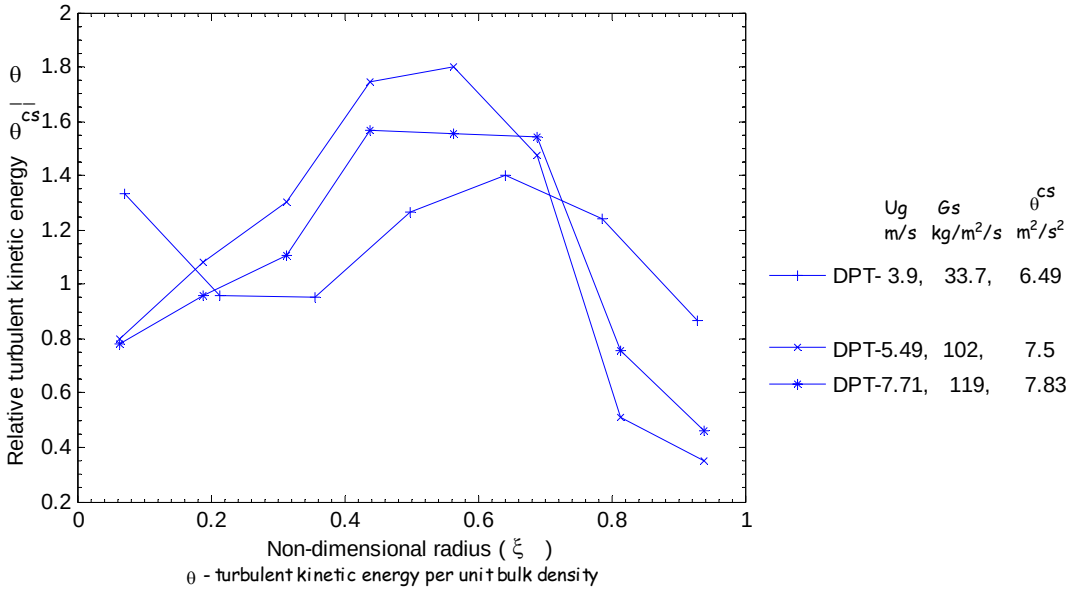

(b)

Figure 7-8: Circumferentially and axially averaged radial profiles of the relative turbulent kinetic energy per unit bulk density for the flow conditions in a) FF regime; b) DPT regime. (Note that the data was obtained from two different risers, under low solids fluxes in the CREL riser and at high solids fluxes in the SNL's riser).

(ε_s < 0.01 - 0.06) and decrease beyond some solids holdup limit. Tartan and Gidaspow (2004) reported that in dilute conditions the granular temperature peaks at an intermediate radial location. The trends in Figure 7-8 suggest that despite the solids concentration being higher, such a peak in the granular temperature occurs in the DPT regime.

7.3 Solids Backmixing

It is clear from Chapter 6 that the solids motion can be considered as a mean convective flow field superimposed by eddy diffusion. The overall mixing in the riser was characterized by the solids residence time distribution in Chapter 5. With regard to elementary reactor design, the information on mean convective flow field and overall mixing is often sufficient. However, for the purpose of understanding the mixing mechanisms and incorporating it into a reactor model, which can be predictive at different flow regimes, it is necessary to study the local solids mixing. In this section, CARPT data is analyzed as Lagrangian tracks to characterize the local backmixing which includes the effects of convection, local circulation and particle dispersion.

7.3.1 Residence Time Distributions

Monitoring the distribution of residence times of a single tracer particle during its multiple visits to the riser generates the residence time distribution of the entire solids phase. This idea was employed to obtain RTDs for the entire riser as described in Chapter 5. The zone of investigation in a CARPT experiment is a section with “open-open” boundaries, resulting in the particle movement across these boundaries. Situations described by Nauman and Buffham (1983) in determining the actual residence time distribution from impulse-response tracer experiments do not arise here with single particle tracking. With the knowledge of the 3D position of the tracer, determining the precise residence times of the tracer in the local section of the riser becomes possible. Hence, obtaining RTDs using single particle tracking, as opposed to the conventional tracer impulse response methods, has the advantages that residence time in the section of interest can be determined precisely and that during particle visits the flow oscillations with both small and large time scales are effectively sampled.

The limited number of detectors below at the inlet plane and above the exit plane of the CARPT section results in poor position reconstruction near these regions (refer to Chapter 3). Hence, for reasons of accuracy, two planes were selected in each of the risers (CREL and SNL) as the inlet and exit planes. In the CREL riser, a zone with an axial height of 48 cm between Z/D = 33.5 (z = 5.1 m) and Z/D = 36.7 (z = 5.6 m) and for the SNL riser, a zone with an axial height of 42 cm between Z/D = 16.3 (z = 2.28 m) and Z/D = 19.33 (z = 2.7 m) are used as the system. The histograms of residence time distributions of the tracer particle, along with the corresponding trajectory lengths (distance traversed by the tracer), in these zones are shown in Figures 7-9 and 7-10.

In the FF regime, as shown in Figure 7-9, the PDFs suggest a possible multi-modal characteristic at both low and high solids fluxes. Such RTDs were observed for the entire riser system (Chapter 5) and were interpreted to be occurring due to the core-annulus flow structure and the extensive solids backmixing in the bottom entry zone. However, a PDF that exhibits multi-mode characteristics even in the upper dilute zone of risers (Z/D = 33.5, 16.3) indicates that solids backmixing in risers is mainly due to the internal recirculation of solids in the riser itself. In contrast, PDFs of RTDs in the DPT regime (Figure 7-10) are unimodal, despite the negative axial velocities near the wall (Figure 7-4) and a considerable annulus thickness (Figure 7-3) observed at high fluxes. Also, it can be observed that all the PDFs of the solids RTDs exhibit long extended tails, especially in the DPT regime, due to the long internal recirculation of solids. One should note that such long residence times in risers were never reported in the literature due to inherent disadvantage with the conventional injection-detection methods in their ability to capture the large time scale flow oscillations. Also, the issue raised by Shinnar *et al.* (1972) for recirculating systems regarding the inability of the classical impulse –response tracer techniques to distinguish between dispersed and recirculated tracer now can be overcome since we know precisely the time spent in the riser by the tracer particle that travels straight through and the time spent in the riser by the particles that recirculate in the riser. Hence, the core-annulus flow structure in the riser results in a PDF of the solids RTD which is unimodal with an early peak followed by an extended tail in the DPT.

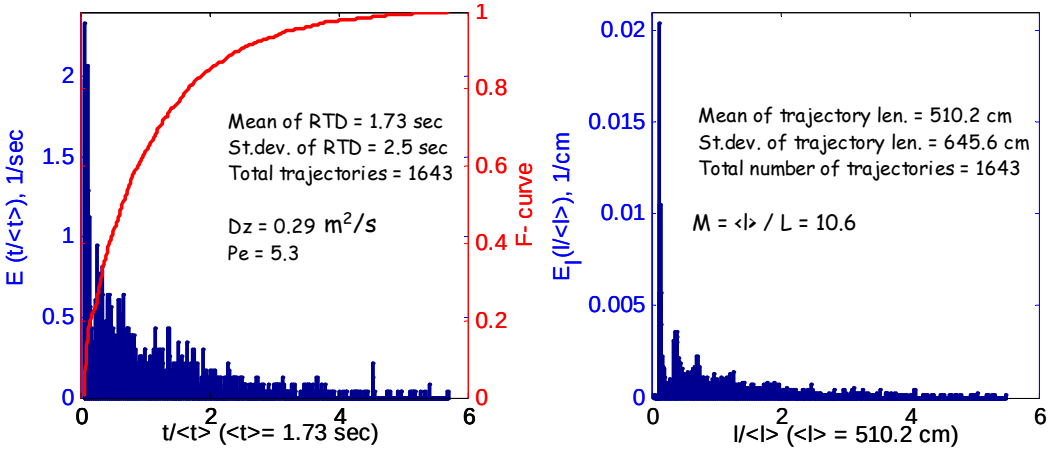

(a)

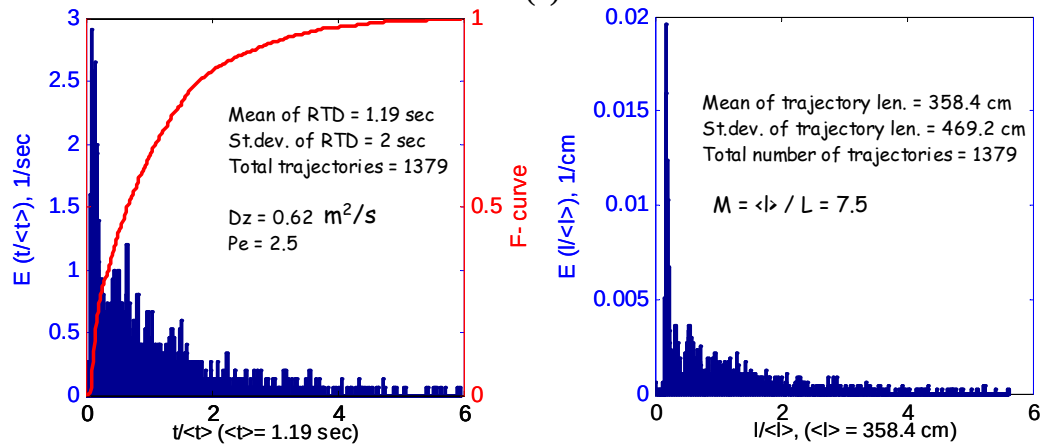

(b)

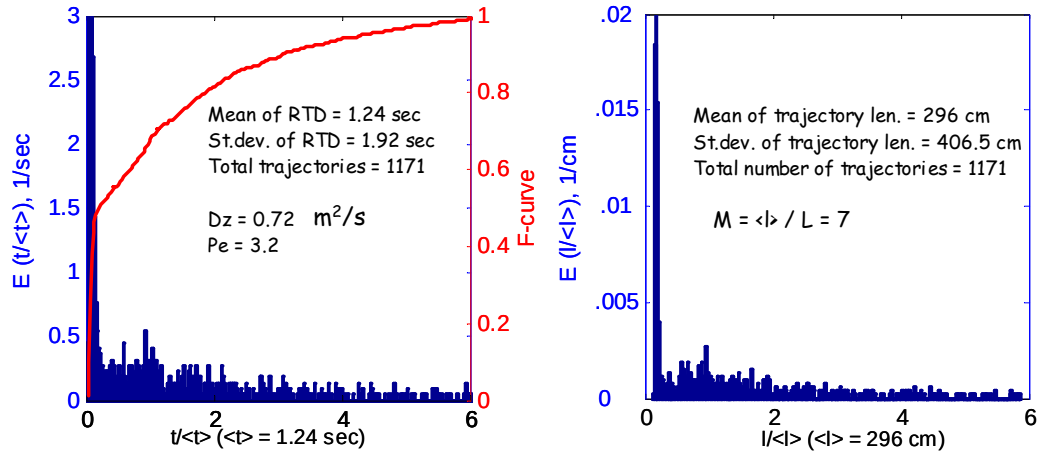

(c)

Figure 7-9: PDFs of residence time and trajectory length for the operating conditions in the FF regime with U_g^{riser} (m·s^{-1}), G_s (kg·m^{-2}·s^{-1}) values of: a) 3.2, 26.6; b) 3.2, 30.1; c) 5.56, 144.5. Note that the abscissas of each plot are different.

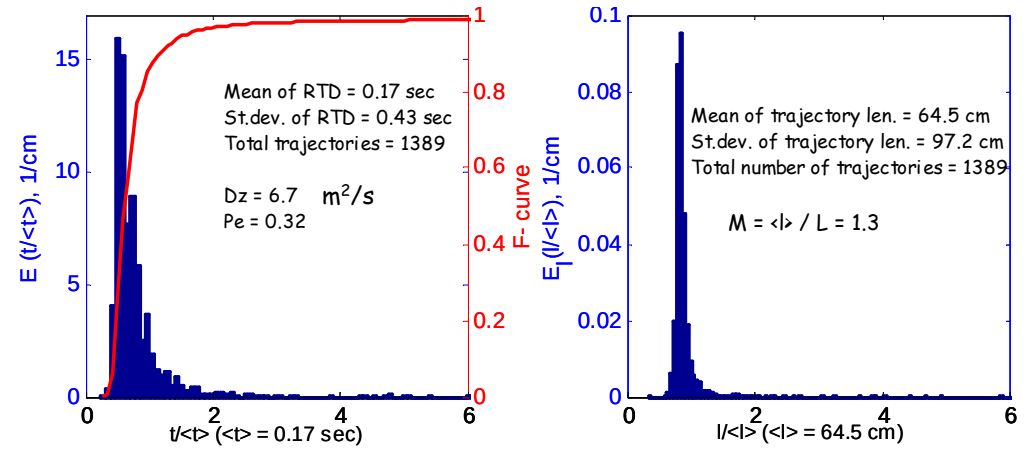

(a)

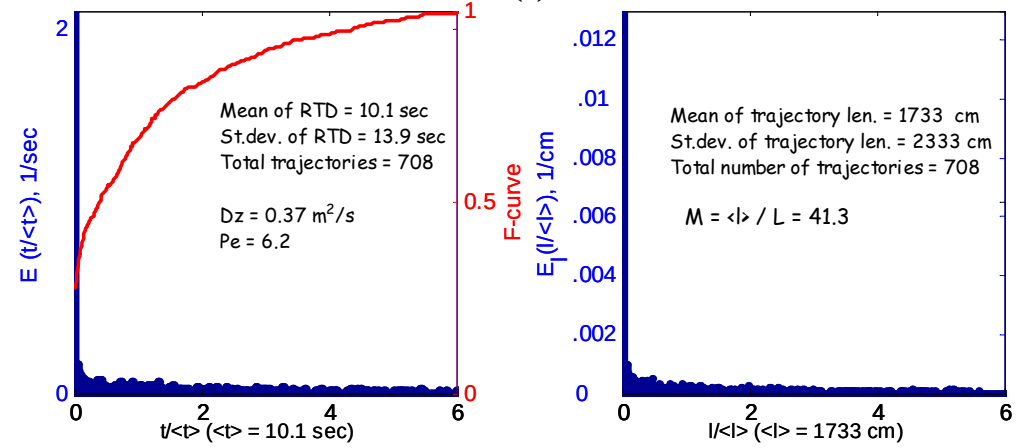

(b)

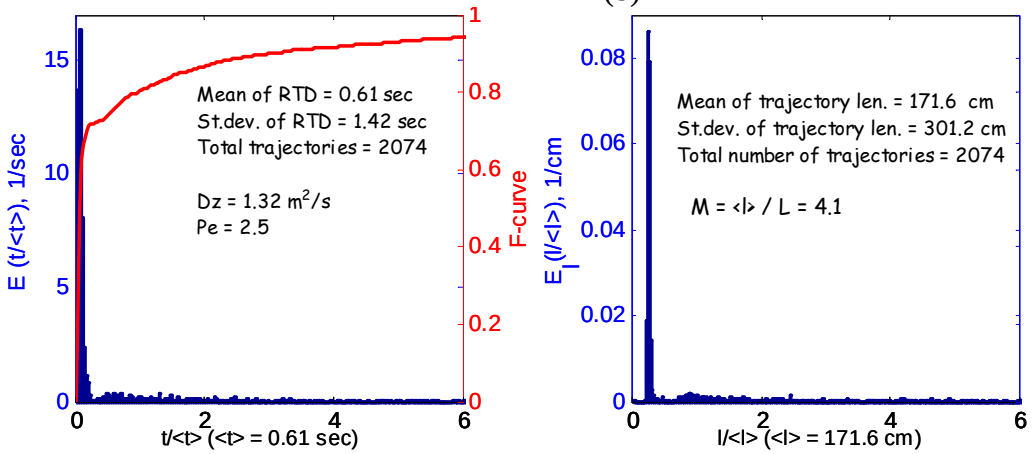

(c)

Figure 7-10: PDFs of residence time and trajectory length for the operating conditions in the DPT regime with U_g^{riser} (m·s^{-1}), G_s (kg·m^{-2}·s^{-1}) values of: a) 4.5, 36.8; b) 5.49, 102; c) 7.71, 119. Note that the abscissas of each plot are different.

regime. In the FF regime the PDF of the solids RTD exhibits almost multi-modal characteristic along with the very extended tail

The solids dispersion in the risers is grossly characterized by a one-dimensional axial dispersion model (ADM). The solids axial Peclet number and the axial dispersion coefficient found by fitting the ADM model in time domain to the E-curve are indicated in the plots (Figures 7-9 and 7-10) and in Table 7-1. It can be observed that the solids axial dispersion coefficient increases with increased solids flux both in the FF and DPT regimes. Indeed, such result was also observed from the RTD for the entire riser (Figure 5-12) and was attributed to the increase in the solids down-flow in the annulus with the increased solids flux. An abnormally high solids mean residence time (10.1 sec) was observed for the operating condition at U_g^{riser} = 5.49 m·s^{-1} and G_s = 102 kg·m^{-2}·s^{-1}. The reason could be that this flow was near the regime transition, close to the choking velocity (V_{CA}), resulting in the suspension oscillating up and down in slugs. This results in the tracer particle either being transported quickly through the riser (early peak in the PDF of the solids RTD) or oscillating up and down in slugs, consequently having high residence times.

Indeed, such high residence times at the same operating conditions were also reported for the entire riser in Chapter 5. One should note that residence times for the entire riser were obtained from a different set of detector signals (and different data interpretation methods) as compared to the local residence times obtained in the CARPT section. Thus, two independent results validate the unusual behavior at the operating conditions close to flow regime transition. This gives yet another confirmation that an ADM model does not fit well the observed PDFs with long tails and is not a good measure of the solids backmixing in risers.

A high dimensionless variance is characteristic of the residence time distribution in the DPT regime for which PDFs are shown in Figure 7-10. At constant gas superficial velocity, a decrease in solids mass flux decreases the down-flow of solids in the annulus (see mean solids velocity profiles shown in Figure 7-5), resulting in longer solids residence times (compared to that in the FF regime). Although the first peaks of the PDFs appear at almost the same times in the FF and DPT regimes, increased span of solids

residence times increases the axial dispersion coefficients in the DPT regime. Indeed, it can be observed from Figure 7-10c that at the highest gas flow condition (U_g^{riser} = 7.71 m·s^{-1}), the F-curve does not reach one even after six residence times.

Another way of quantifying the extent of mixing is by employing the trajectory length distributions which are also shown in Figures 7-9 and 7-10. This concept was introduced by Villermaux (1996) and was effectively used in the mixing studies of Kiared *et al.* (1997) and Roy (2000). Villermaux defines a 'macromixing index', *M*, to be the ratio of the mean trajectory length to a characteristic length scale of the system (length of the CARPT section here). The values of macromixing index, *M*, and the dimensionless variance of the trajectory lengths are given in Table 7-1 for all the operating conditions. It can be observed that the macromixing index is higher in the FF regime as compared to that in the DPT regime, barring the flow condition near to the regime transition. This can be explained based on the decrease in residence times with the increase in gas velocity and/or solids mass flux. Although residence time plots indicate an increase in solids mixing (axial dispersion coefficient and dimensionless variance), the 'macromixing index' seems to decrease with increasing solids flux (at constant gas velocity) and suggest less solids backmixing in the DPT regime. However, given the fact that the macromixing index was obtained directly from the particle trajectory data, while the axial dispersion coefficient was obtained by fitting an approximate model to the RTD, macromixing index seems to a better characteristic of the solids mixing in risers.

7.3.2 Circulation Time Distributions

To study internal circulation patterns in a reactor, Villermaux (1996) introduced the return length distributions. The return length is the distance that the particle travels after crossing a specific surface until it comes back and crosses the same surface again. The time taken to do so can be termed as circulation time. Figures 7-11 and 7-12 show typical histograms of circulation times and number of returns per trajectory at axial planes of *Z/D* = 35.3 (*z* = 5.37 m) at low solids fluxes and *Z/D* = 17.7 (*z* = 2.48 m) at high solids fluxes. Since the axial variation of the flow parameters was found to be negligible within the zone of interrogation, it is assumed that the internal circulation patterns also

Table 7-1: Local mixing parameters

Operating Conditions	**Residence Time and Trajectory length Distributions**							**Number of Returns and Circulation Time Distributions**		
U_g^{riser} ($m \cdot s^{-1}$) G_s ($kg \cdot m^{-2} \cdot s^{-1}$)	$\langle t \rangle_{res}$ (sec)	$(\sigma/\langle t \rangle)^2_{res}$	$D_{z,ax}$ ($m^2 \cdot s^{-1}$)	$Pe_{s,z}$	$\langle l \rangle$ (cm)	$(\sigma/\langle l \rangle)^2$	$\langle l \rangle/L$	$\langle t_c \rangle_{cir}$ (sec)	$(\sigma/\langle t_c \rangle)^2_{cir}$	$M_{returns}$
3.2, 26.6, FF	1.73	2.04	0.3	5.3	510.2	1.6	10.6	4.6	2.5	7.5
3.2, 30.1, FF	1.2	2.9	0.6	2.5	358.4	1.7	7.5	4	2.7	5.4
5.56, 144.5, FF	1.24	2.4	0.7	3.2	296	1.9	7	2.17	1.9	6.2
3.9, 33.7, DPT	0.34	5.9	3.8	0.38	120.7	8.6	2.5	1.48	5.6	5.1
4.5, 36.8, DPT	0.17	6.2	6.7	0.32	64.5	2.3	1.3	0.07	14.6	2.5
5.49, 102, DPT	10.1	1.9	0.4	6.2	1733	1.8	41.3	2.73	7.5	9.6
7.71, 119, DPT	0.61	2.3	1.3	2.5	171.6	3.1	4.1	2.72	4.1	8.2

$\langle t \rangle_{res}$ – mean residence time; $(\sigma/\langle t \rangle)^2_{res}$ – dimensionless variance of RTD; $D_{z,ax}$ – axial dispersion coefficient (ADM); $Pe_{s,z}$ – axial solids Peclet number; $\langle l \rangle$ - mean trajectory length; $(\sigma/\langle l \rangle)^2$ – dimensionless variance of trajectory length distribution; $\langle l \rangle/L$ – macromixing index; $\langle t_c \rangle_{cir}$ – mean circulation time; $(\sigma/\langle t_c \rangle)^2_{cir}$ – dimensionless variance of circulation time distribution; $M_{returns}$ – mean number of returns per trajectory.

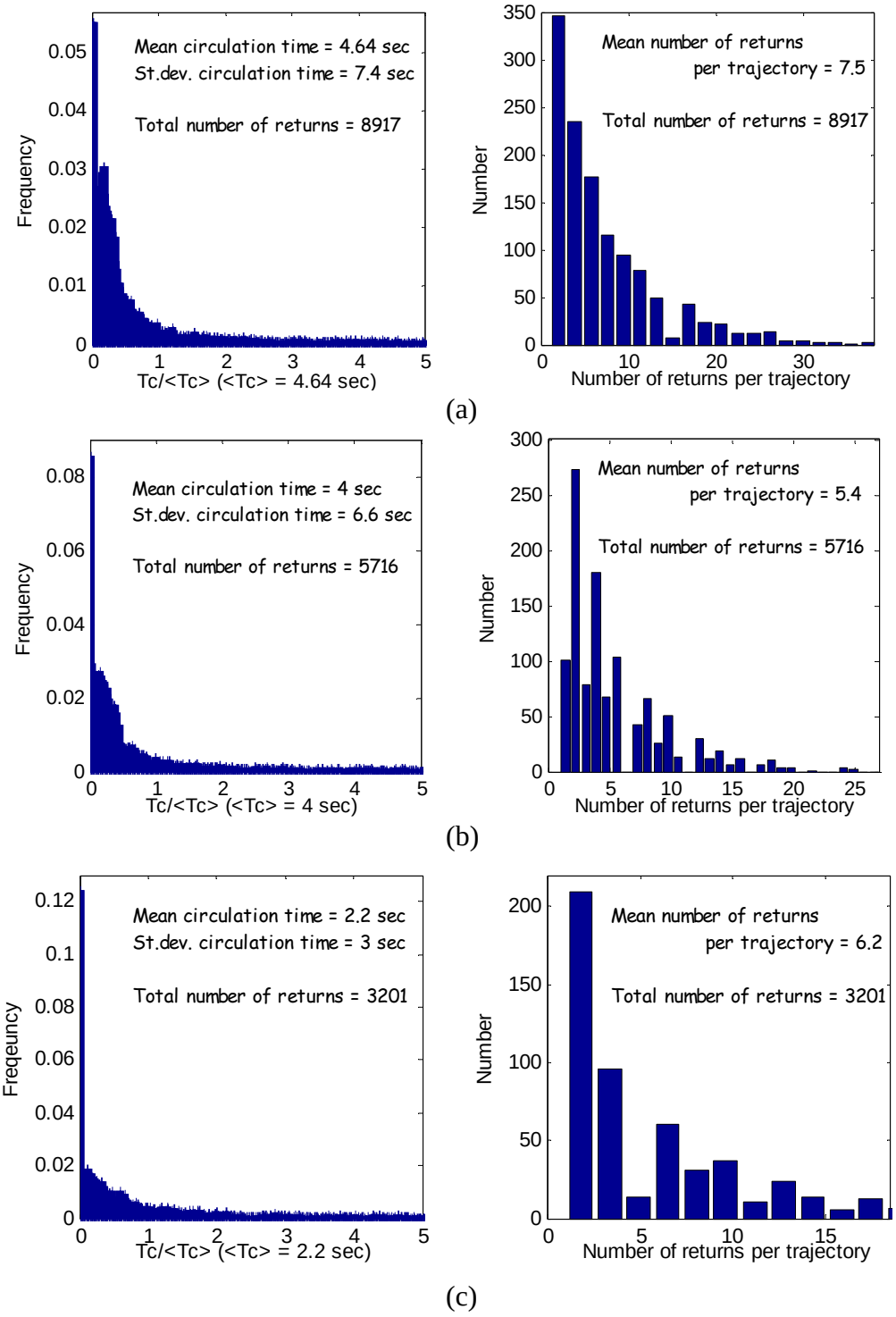

Figure 7-11: PDFs of circulation time and number of returns per trajectory for the operating conditions in the FF regime with U_g^{riser} (m·s^{-1}), G_s (kg·m^{-2}·s^{-1}) values of: a) 3.2, 26.6; b) 3.2, 30.1; c) 5.56, 144.5.

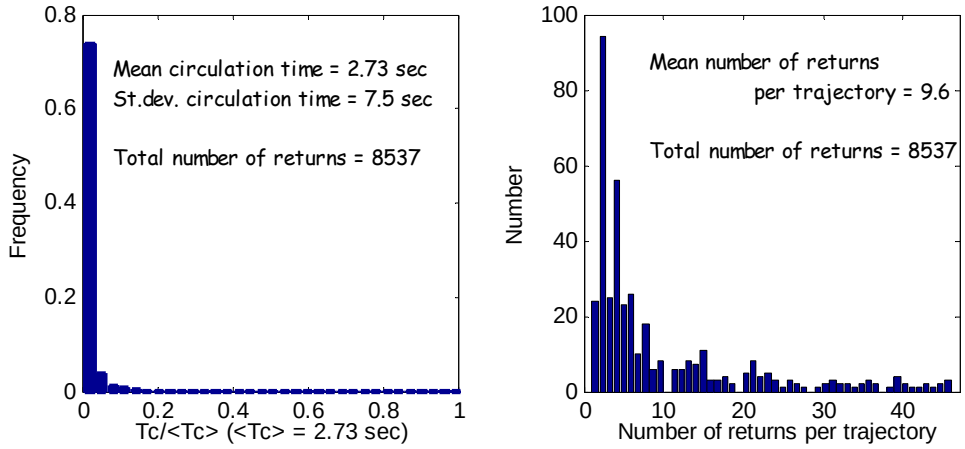

(a)

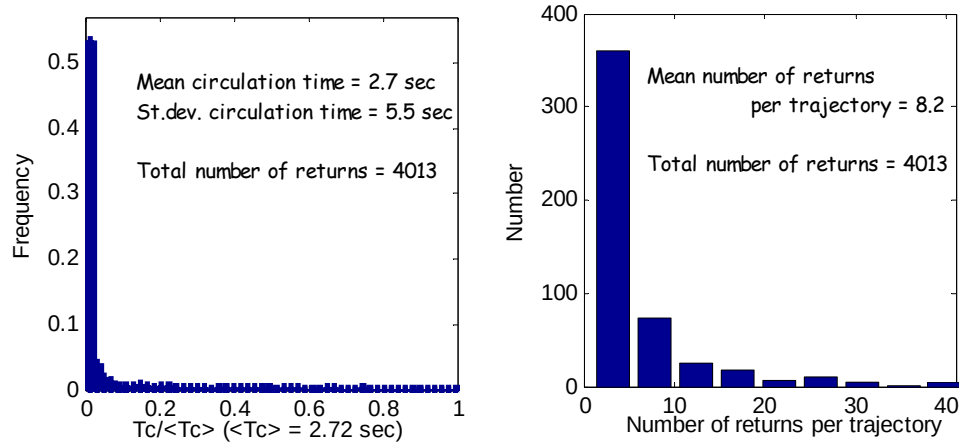

(b)

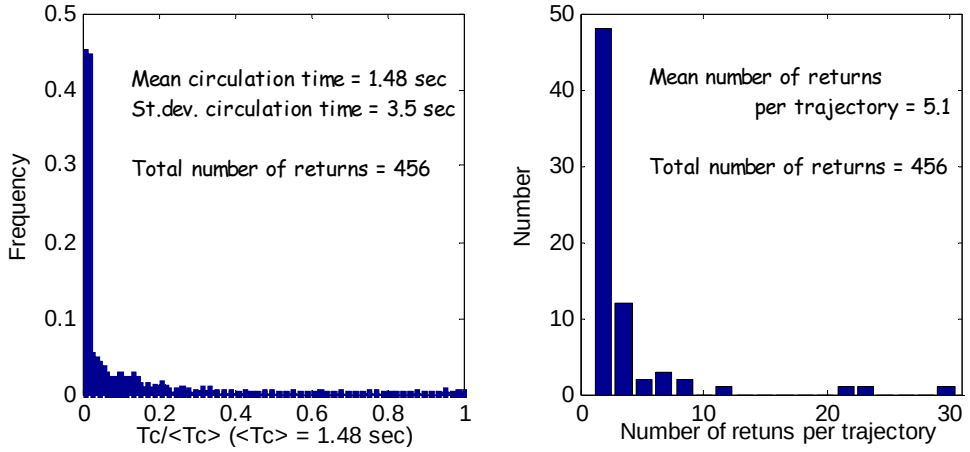

(c)

Figure 7-12: PDFs of circulation time and number of returns per trajectory for the operating conditions in the DPT regime with U_g^{riser} (m·s^{-1}), G_s (kg·m^{-2}·s^{-1}) values of: a) 5.49, 102; b) 7.71, 119; c) 3.9, 33.7; d) 4.5, 36.8.

show negligible changes in the zone. Hence, the circulation time distributions are analyzed only at one axial plane. Note that due to the limited zone of interrogation with "open-open" boundaries, return length distributions cannot be constructed but internal circulation times are known precisely.

One can note from the distributions of the number of returns that the tracer particle crosses the plane of interest multiple times and eventually flows out of the riser. The PDFs of the circulation time distributions, shown in Figures 7-11 and 7-12, indicate that solids circulate through the planes in small loops over small times. This is indicated by the peak in the PDFs of circulation time distributions at very small times for all the flow conditions. Also, one can observe that the PDFs of the circulation time distribution decays progressively to zero and the rate of decay increases with the solids mass flux and/or gas superficial velocity. Similar to the PDFs of the RTDs, the PDFs of circulation times also display long extended tails corresponding to the long residence times.

Solids internal axial recirculation in the riser is enhanced with the increase in the number of returns per trajectory, which shows a decreasing trend with solids mass flux at constant gas superficial velocity. This decrease in the recirculation is due to the increase in the solids convection with solids mass flux. However, note that the axial dispersion increases with solids mass flux (Figure 7-9 and 7-10). The mean of the circulation times was also found to decrease with the increase in the solids mass flux at constant gas velocity. Illustrating an increase in axial recirculation in the DPT regime, mean returns per trajectory were found to be generally higher than in the FF regime. Such increase in the returns was found to be due to the increase in the longer circulation loops which can be inferred from the extended tails in the PDFs of the circulation time distributions. Thus, an increase in the dimensionless variance in the RTDs in the DPT regime is due to the increase in the axial recirculation. One should note that the total number of returns indicated in each of the plots does not represent the extent of recirculation because the length of the experiment for each of the conditions was different. It is provided only to indicate that the PDFs were reconstructed from a sufficiently high number of samples.

7.3.3 Evaluation of Eddy Diffusivities

One can also construct PDFs of radial circulation patterns (if prevalent) with respect to a radial plane (z-θ) at different radial locations. Such characterization enables one to quantify radial dispersion of solids which includes the effect of local solids dispersion as well as effects of convective flow of solids. In addition to the global axial and radial mixing, the local mixing also contributes to reactor performance, especially for fast reactions. This section discusses the dispersion at local scales characterized by solids diffusivities. Such solids diffusivities can later be used in a convection-diffusion model.

Physically, turbulence is composed of motions having a wide range of length and time scales. Qualitatively, turbulence is described as the interaction of eddies of various sizes, where an eddy is defined as a structure in which the fluctuating velocity components are correlated. This internal structure of the turbulent flow fields is partly captured by the correlation functions. Second order Lagrangian correlation functions are typically used to describe the diffusive power of turbulence (e.g. Batchelor, 1953). Calculation of Lagrangian correlation functions from CARPT data has been adequately discussed by Moslemian (1987), Degaleesan (1997) and Roy (2000).

Lagrangian auto-correlation functions (f_{zz} and f_{rr}) are displayed in Figure 7-13 and 7-14. The figures represent the data that has been axially and azimuthally averaged, since only small variation was observed along the axial and azimuthal directions. The auto-correlation coefficients were scaled with their corresponding values at the zero lag, $\overline{v'^2}$, and are shown at various radial positions in Figure 7-13. Note that for enhanced legibility of the figure an offset on the ordinate of 0.25 is allowed for each condition. With increasing time lag, auto-correlation functions typically tend to zero, indicating a loss of memory of the past. The statistics required for calculating the auto-correlation functions are stricter than those required for calculating the mean and turbulent quantities. Hence, the calculations were made with a relatively coarser mesh (Mesh 2 in Table 6-2).

The zero lag of the axial auto-correlation function decreases with radial position, while the radial correlation function shows a peak between the center and the wall. These trends can be observed from the cross-sectional averaged values provided in the legends

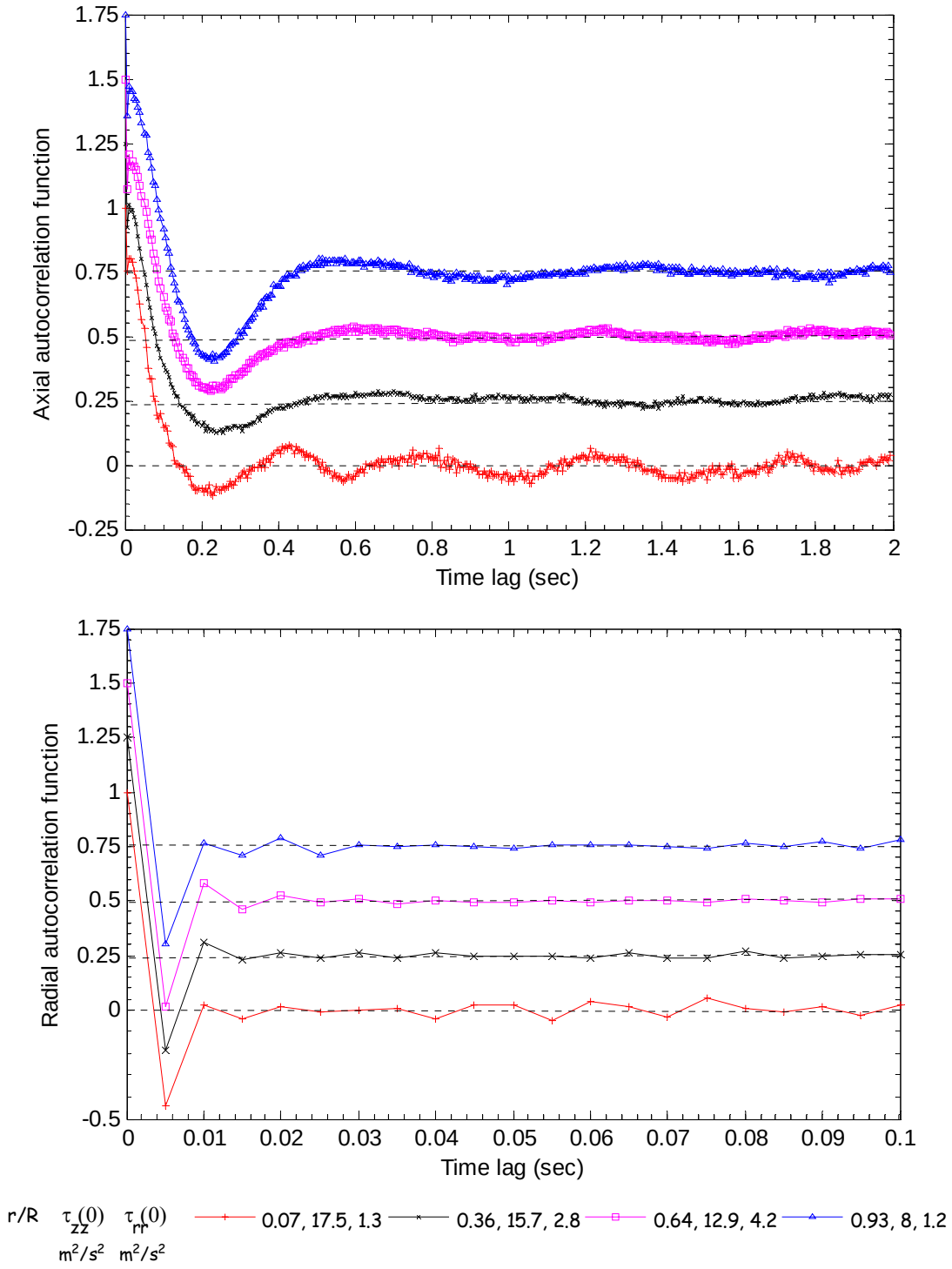

Figure 7-13: Autocorrelation functions for a typical case in the FF regime at U_g^{riser} = 3.2 m·s^{-1} and G_s = 30.1 kg·m^{-2}·s^{-1} in a) axial, and b) radial. Each of the profiles in both the plots is scaled by separating with a constant of 0.25 for the sake of clarity.

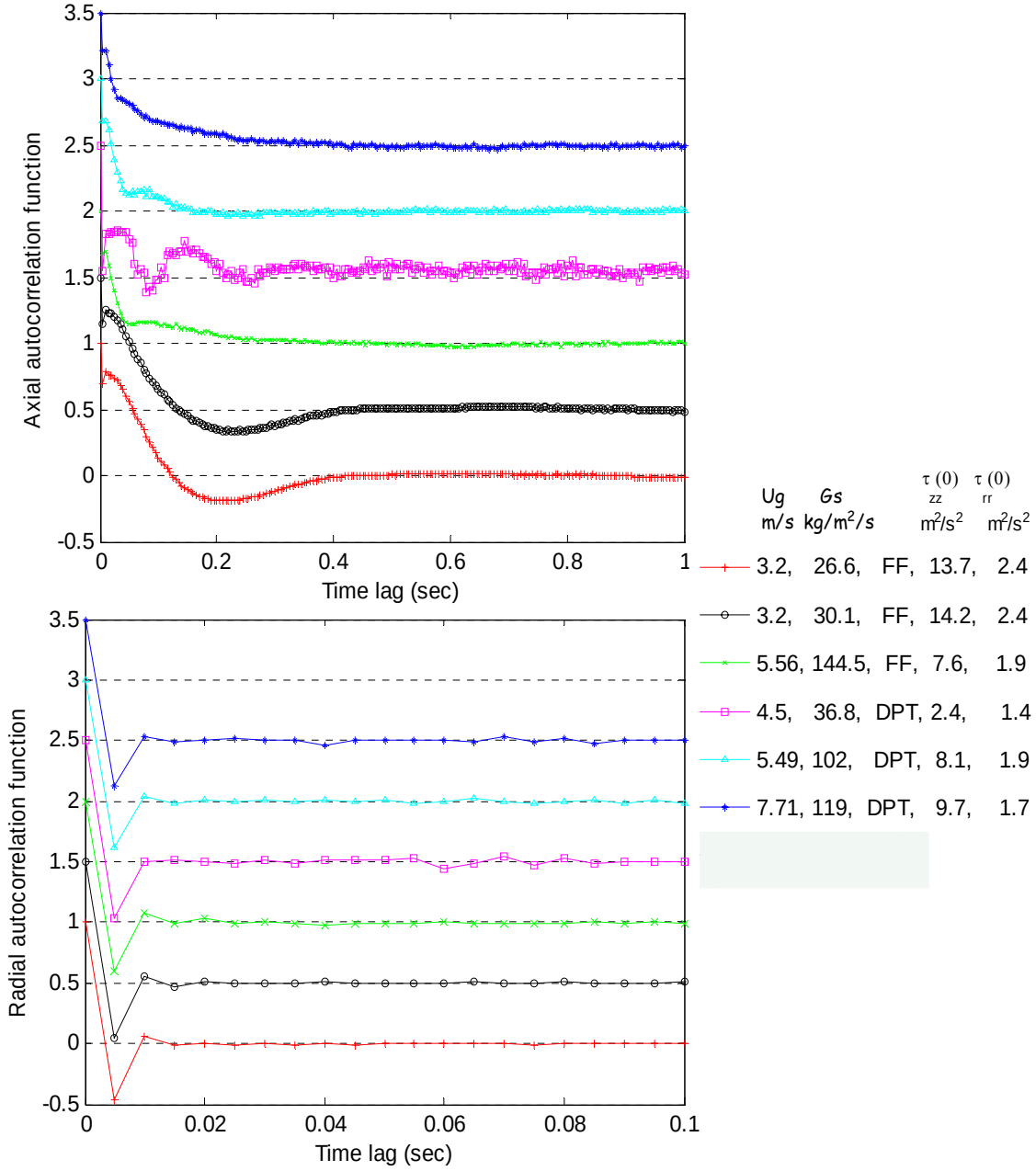

Figure 7-14: Spatially averaged autocorrelation functions for all the operating conditions in a) axial, and b) radial. Each of the profiles in both the plots is scaled by separating with a constant of 0.5 for the sake of clarity.

of Figure 7-13. The above trends are similar to those of the corresponding normal stresses, since the Lagrangian correlation function for a large number of samples (or particles) approach the Eulerian velocity correlations. Also, $\overline{v_z'^2}$ is much larger than $\overline{v_r'^2}$. Figure 7-13 shows large radial variation of the auto-correlation functions, indicating different characteristic mixing times at the center and at the wall. Further, one can also observe that the axial auto-correlation function display negative loops with the frequency of the loops decreasing with radius. As discussed in Chapter 6, such negative loop correlation functions are typical in wall bounded flows and for heavy particles in turbulent gases. Thus, such oscillatory loops occur in the axial correlation function due to high internal recirculation, while in the radial autocorrelation function it is due to the physical walls of the cylindrical column. In addition, the time scale associated with the correlation functions can be seen to be relatively smaller in the radial direction. Due to this small time scale, we are not sure if the radial auto-autocorrelation function is fully captured with the employed sampling frequency of 200 Hz. To verify, one has to acquire the data at higher sampling frequency and compare the auto-correlation functions, which unfortunately was not attempted in this study.

The zeroth order moment of the autocorrelation function, $f_{\alpha\alpha}(t)$, is defined as the Lagrangian integral time scale and is given as follows:

$$\tau_{L\alpha} = \int_0^\infty f_{\alpha\alpha}(t) \cdot dt \tag{7-1}$$

Thus Lagrangian integral time is the time during which the particle remains in a region within which velocities are correlated *i.e.* within an eddy. It has much smaller values in the radial than in the axial direction. The smaller the integral time scale, the sooner the particle loses memory of its past, which reduces the extent of dispersion in the medium (Degaleesan, 1997). Hence, the dispersion in the radial direction has to be much smaller than in the axial. Equation (7-1) was evaluated for all the operating conditions by integrating the autocorrelation from $\tau = 0$ to $\tau_{5\%}$ where the auto-correlation function reaches its asymptotic value within 5%. The cross-sectional averaged values of the integral times are reported in Table 7-2. It can be observed that axial and radial integral

times follow exactly the opposite trends as that of the turbulent kinetic energy. As was discussed in Chapter 6, the relative dominance of the increase in particle collision frequency and the decrease of the mean free path with increased solids concentration determine the trends in turbulent solids kinetic energy. The increase in particle fluctuations (turbulent kinetic energy) results in a particle leaving the correlated region or an eddy sooner and, hence, the integral time scales exhibit opposite trend as that of turbulent kinetic energy.

7.4 Solids Eddy Diffusivities

An accurate and robust model for the turbulent transport and values of the stress tensor, $\overline{u_i' u_j'}$, can lead to predictions of turbulent flow characteristics. Typically, in a Euler-Euler type CFD model, turbulence closure is achieved by a model such as k-ε or its modified versions, and one invokes the Boussinesq-like gradient transport hypothesis. This introduces the problem of closure for turbulent or eddy diffusivity. Since one of the objectives of this work was to provide the benchmark data for the validation of CFD models and closures, this section discusses the quantification of eddy solids diffusivities. Turbulent diffusivities can be evaluated from the Lagrangian auto-correlation functions. Since most of the experimental techniques employed for the study of riser solids dynamics do not provide Lagrangian data, estimation of turbulent diffusivities is unique to CARPT. Moreover components of the eddy diffusivity tensor are needed since it was shown earlier that Boussinesq approximation based on isotropic assumption does not conform to the data collected by CARPT.

An open question arises in evaluating the turbulent eddy diffusivities from CARPT data. Generally, turbulent diffusivity is modeled with the isotropic assumption due to its simplicity as, $D_{ij} = C_k \frac{k^2}{\varepsilon}$. However, Durbin and Reif (2001) noted the shortcomings of scalar diffusivity models in predicting the scalar flux vector (misalignment between the scalar flux and the mean scalar gradient). This was corrected by replacing the scalar diffusivity by tensor diffusivity, also referred to as dispersion

tensor (Durbin and Reif, 2001). Several non-isotropic closures, such as those given in Equation (7-2), are typically employed (Sureshkumar, 2001).

$$D_{ij} = \begin{cases} \dfrac{k}{\varepsilon}\left(\overline{u_i' u_l'} + \overline{u_j' u_l'}\right) \\ \dfrac{k}{\varepsilon} \cdot \overline{u_i' u_j'} \\ \dfrac{k}{\varepsilon} \cdot \overline{u_l'^2} \end{cases} \tag{7-2}$$

Slaughter *et al.* (1993) and Godfroy *et al.* (1999) employed the second formulation to estimate the solids axial dispersion coefficients, where the time scale term k/ε was replaced with the axial Lagrangian integral time. Indeed, this relation results in the classic relation of eddy diffusivity being proportional to the product of characteristic velocity (RMS velocity) and characteristic time (integral time scale). However, the rate of production of turbulent fluxes depends on the mean velocity gradients, if the gradients are present. Based on the studies of Corssin (1953) and Lee and Duckler (1976), Degalessan (1997) derived the expressions for axial diffusivities to include the effect of mean velocity gradients. Durbin and Reif (2001) noted that in the presence of velocity gradients, diffusivity will be an asymmetric tensor, which was not considered by Degalessan (1997). Durbin and Reif (2001) showed that the dispersion tensor is given by:

$$D_{ij} = C_c \frac{k}{\varepsilon}\left(\overline{u_i' u_j'} - D_{lj}\frac{\partial U_i}{\partial x_l}\right) \tag{7-3}$$

Clearly, Equation (7-3) shows asymmetry in the diffusivity tensor with the presence of velocity gradients. The formulation of Degalessan (1997) for the axial diffusivity fits into Equation (7-3), in that correlation coefficients are integral sums (integrated in time) instead of multiplying with a suitable time scale such as k/ε, as is done by Durbin and Reif (2001). It can also be noted that in the formulation of Degalessan (1997), the term with the velocity gradient has the opposite sign to that of Equation (7-3). Apparently, for reasons not clear at present, Degalessan's formulation yields negative axial diffusivities near the wall. Hence, Equation (7-3) was employed to evaluate the solids diffusivities in risers.

Expressions for the components of the diffusivity tensor evaluated from Equation (7-3) can be found in Ong (2003), where the *z-r* component of the tensor was used to check the continuity (mass balance) of CARPT and tomography data in bubble columns. One notes that the usage of Equation (7-3) requires data for the dissipation rate, ε, and an estimated constant C_c. However, models available for dissipation rate assume isotropicity, which turns out to be a grossly incorrect assumption for solids flow in risers. Durbin and Reif (2001) state that the rate of production of turbulent fluxes (the term inside the bracket in Equation (7-3)) has to be multiplied by a suitable time scale, k/ε, on dimensional grounds. Hence, an alternate way is to replace $C_c k/\varepsilon$ with the corresponding integral time scale, τ_{Lij}. The integral time scales (τ_{Lz}, τ_{Lr}, τ_{Lrz}) required to estimate the axial and radial diffusivities are directly evaluated from Lagrangian correlation functions using Equation (7-1).

Substituting the corresponding integral time scales into Equation (7-3), axial and radial solids diffusivities are estimated and are shown in Figures 7-15 and 7-16. The profiles are scaled with their respective cross-sectional averaged diffusivities to better visualize the similarity. Axial solids diffusivities exhibit decay in the radial direction in the FF regime, while at DPT conditions they show a slight increase with the radial location. The random solids fluctuations decrease with the increasing particle concentration resulting in decreased diffusivity as seen in the FF regime. However, in the 'dilute conditions' ($\varepsilon_s < 0.06$) the particle fluctuations increase with the solids concentration resulting in the increase in axial diffusivity near the center of the column in the DPT regime. Besides, axial recirculation is found to be relatively higher in DPT (see PDFs of circulation time distributions) which increases the effective diffusivity, resulting in the increase of axial diffusivities in the radial direction. Hence, in the FF regime, the effect of large scale solids axial recirculation is smaller compared to the small scale fluctuations on the solids axial dispersion, while the opposite occurs in the DPT regime.

Radial diffusivity profiles shown in Figures 7-15 and 7-16 indicate a decreasing trend as the radial position increases towards the wall. However, a hump occurs (an

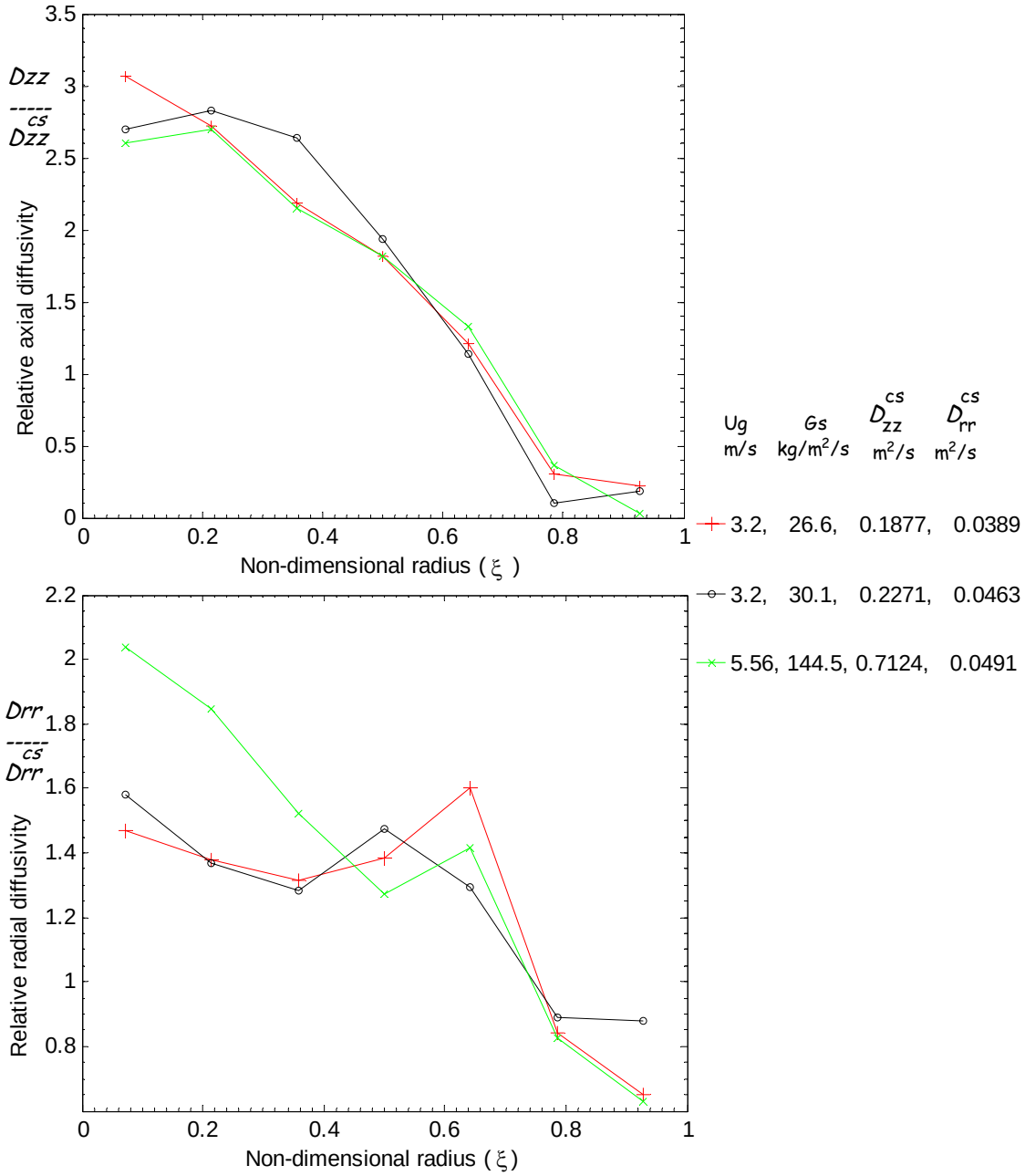

7-15: Radial profiles of relative (scaled by cross-sectional average) solids diffusivities for the flow conditions under FF regime in a) axial, and b) radial.

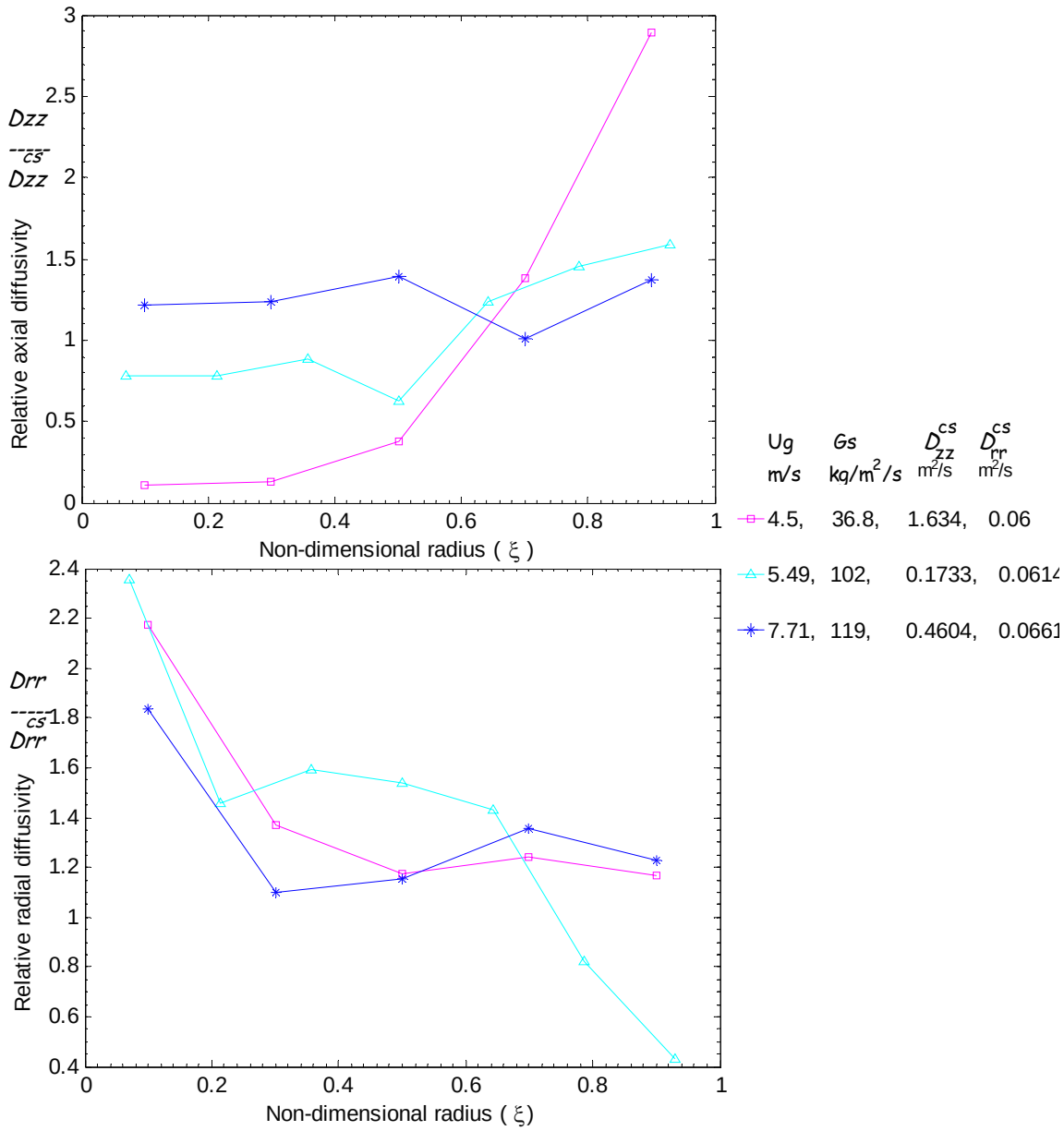

7-16: Radial profiles of relative (scaled by cross-sectional average) solids diffusivities for the flow conditions under DPT regime in a) axial, and b) radial.

Table 7-2: Parameters characterizing local solids dispersion

Operating Conditions U_g^{riser} ($m \cdot s^{-1}$) G_s ($kg \cdot m^{-2} \cdot s^{-1}$)	$R_{zz}(0)$ ($m^2 \cdot s^{-2}$)	$R_{rr}(0)$ ($m^2 \cdot s^{-2}$)	τ_{Lz} (milli sec)	τ_{Lr} (milli sec)	D_{zz}^{cs} ($cm^2 \cdot s^{-1}$)	D_{rr}^{cs} ($cm^2 \cdot s^{-1}$)	Axial Dispersion Coefficient from RTD ($cm^2 \cdot s^{-1}$)
3.2, 26.6, FF	13.7	2.44	98	11.2	1876.9	389	2920
3.2, 30.2, FF	14.17	2.43	92.5	13.5	2270.9	463.3	6200
5.56, 144.5, FF	7.59	1.94	60.5	16.8	7124	491.2	7240
4.5, 36.8, DPT	2.39	1.38	114	30.7	16337.4	596.8	67000
5.49, 102, DPT	8.09	1.9	45.8	21.8	1732.5	614.3	3700
7.71, 119, DPT	9.68	1.65	70.9	29.2	4604.4	661.4	13200

$R_{zz}(0)$ - Axial auto-correlation Coefficient; $R_{rr}(0)$ - Radial auto-correlation Coefficient ; τ_{Lz} - Axial integral time; τ_{Lr} - Radial integral time; D_{zz}^{cs} – Cross-sectional average of axial solids diffusivity; D_{rr}^{cs} - Cross-sectional average of radial solids diffusivity.

increase and then a decrease) near $r/R = 0.7$ in the FF regime. The occurrence of such a peak could be due to the opposite effects of recirculation and radial fluctuations on the particle diffusivities. The recirculation can be expected to be more pronounced in the center, increasing the diffusivity, while near the wall the decrease in random fluctuations is large, effectively decreasing the diffusivity. The radial dependence of the random fluctuations can be verified from the radial normal stress profiles (Figure 7-6), but the recirculation patterns cannot be predicted. This is because a typical surface at constant radius (a cylinder) needed to characterize the effect of circulation patterns in the radial direction has to cover the entire riser, while the zone of interrogation in CARPT experiments ranges only over a small portion of the riser.

The cross-sectional averaged values of the solids diffusivities are summarized in Table 7-2. The variation in the cross-sectional averaged radial diffusivities with the operating conditions is small. The radial diffusivities are an order of magnitude smaller than the respective axial diffusivity values. Axial diffusivities can be seen to increase with the solids mass flux at constant gas velocity. The reason for this increase is due to the increase in both the small scale axial fluctuations (Figure 7-6) and the large scale axial recirculation (Table 7-1). When compared to axial dispersion coefficients that were obtained from RTDs (Figure 7-9 and 7-10), axial diffusivities are smaller. This is expected since the axial dispersion coefficients from RTDs include the overall effect of the axial, radial and azimuthal diffusivities as well as the convective backflow.

The solids diffusivities are actually functions of time and they reach an asymptotic value for large times. Hence, for the purposes of design or input to a mechanistic reaction engineering model, one need to choose the diffusivity values appropriate for the characteristic time scale of the process.

In summary, the solids backmixing characterized by several mixing parameters aided in understanding the solids mixing mechanisms and the effect of operating conditions on them. This understanding can be directly used in the design, scale-up and in improving the models. Kinetic theory would greatly benefit from clarifying the questions of what assumptions must be abandoned or what ingredients must be added to improve and extend to anisotropic and realistic description of CFB flow phenomena. To close the

thesis aptly, the last section is devoted to cross check the data from CARPT and CT for the overall mass balance.

7.5 Overall Continuity Problem

It is possible to estimate the solids local mass flux, given the local velocities from CARPT and local holdups from CT. However, any such possibility would tacitly set the covariance of ε_s and V_s or the average of fluctuating mass flow $\langle \varepsilon_s' V_s' \rangle$ to zero. Availability of fluctuating velocity field does not help much. One would require a measurement technique to estimate the solids phase velocity and holdup time series simultaneously to estimate the covariance term. Similar problem was confronted when estimating the overall mass flux, described in Chapter 4. For the solids flow in the standpipe (down-comer) being close to plug flow, which was *post facto* validated, the covariance term was found to be negligible. However, such is not the case for the solids flow in risers.

In this section, an effort is made to quantify the discrepancy between the estimated local solids mass fluxes and the overall mass flux obtained in Chapter 4. Note that solids velocity and holdup, obtained from two independent measurements (CARPT and CT) are used to estimate the mass flux and compare with another independent measurement of overall mass flux. The problem can be simply expressed as follows:

$$G_s(r) = \rho_s \left[\langle \varepsilon_s(r) \rangle \langle V_s(r) \rangle + \langle \varepsilon_s'(r) \cdot V_s'(r) \rangle \right] \tag{7-4}$$

$$G_s^{overall} = 2\rho_s \left[\int_0^1 \xi \langle \varepsilon_s(\xi) \rangle \langle V_s(\xi) \rangle \cdot d\xi + \int_0^1 \xi \langle \varepsilon_s'(\xi) \cdot V_s'(\xi) \rangle \cdot d\xi \right] = \langle G_s \rangle^{overall} + G_s'^{overall} \tag{7-5}$$

Certainly, based on the close correlation found for the profiles of the granular temperature and gas holdup (1-ε_s), shown in Chapter 6, the covariance term is not negligible and neither are fluctuating solids velocities (RMS velocities in Figure 6-29). Alternate way is to model the covariance term by invoking the turbulent transport

hypothesis, as was done by Ong (2003). It follows from Hinze (1975) and Durbin and Reif (2001) that the cross-correlation of the velocity fluctuations with passive scalar concentration, *c*, is given by:

$$\left\langle u_i' c' \right\rangle = -D_{ij} \frac{\partial \langle c \rangle}{\partial x_j} \tag{7-6}$$

Here, *c* is the solids holdup, which affects the velocity field and hence is not a passive scalar. Thus the negative sign before the diffusivity is not required. Since only the radial gradient of the solids holdup is prevalent, the tensor notation in Equation (7-6), when expanded results in only one term with the diffusivity D_{zr}. The *z*-*r* component of the dispersion tensor can be obtained from the expression (Equation (7-3)) given by Durbin and Reif (2001) as follows:

$$D_{zr} = C_c \frac{k}{\varepsilon} \left(\overline{u_z' u_r'} - C_c \frac{k}{\varepsilon} \overline{u_r' u_r'} \frac{\partial U_z}{\partial r} \right) \tag{7-7}$$

Combining Equations (7-6) and (7-7), the fluctuating component of the solids mass flux, $G_s^{\,\prime\, overall}$, can be estimated. In order to calculate the overall mass fluxes from CARPT and CT data (area averaging), it was necessary to extrapolate both the holdup and axial velocity plots near the center as well as near the walls of the column. The solids holdup and its radial derivative profiles were extrapolated using the functional form derived in Chapter 6 (Equation 6-7), while a spline fit was employed for the solids velocity and diffusivity D_{zr} profiles.

Table 7-3: Overall continuity checks

Operating Conditions U_g^{riser} (m·s^{-1})	G_s (kg·m^{-2}·s^{-1}) (TOF-Densitometry)	$\langle G_s \rangle^{overall}$ (kg·m^{-2}·s^{-1})	$G_s^{\,\prime\, overall}$ (kg·m^{-2}·s^{-1})	Discrepancy %
3.2, FF	26.6 ± 1.1	13.7	9.7	-12
3.2, FF	30.2 ± 1.4	15.2	11.6	-11
3.9, DPT	33.7 ± 1.2	18.3	12.5	-9
4.5, DPT	36.9 ± 0.9	30.8	9.6	9.4

Typical results for the overall continuity checks are summarized in Table 7-3. It can be seen that the discrepancies are less than 12%, within engineering accuracy. Considering the fact that for each of the operating conditions, data was obtained from three independent experimental techniques, comparison within engineering limits is remarkable. It can be observed that the overall average mass flows are always greater than the product of averages ($<G_s>$), showing that the covariance term is always positive. This result is non-intuitive and the reasons for such positive contribution of the fluctuating mass flow are not clearly understood. More research is required in this direction.

One can observe that the percentage contribution of the fluctuating component to the overall mass flux varies from 26-37%. Hence, neglecting the covariance term in experimental techniques such as isokinetic sampling leads to systematic errors. Such high contribution of the fluctuating components also establishes the importance of understanding the mechanism and quantification of turbulent solids transport. This enhances the importance of the experimental results reported throughout this work.

7.6 Summary

The uniqueness of CARPT data lies in providing rich Lagrangian information along with the ensemble-averaged Eulerian flow field. The effect of operating conditions on the local solids backmixing, required for the design and scale-up, and for the quantification of solids diffusivities, required for CFD closures are addressed in this Chapter. Following are the key observations with regard to the solids flow and mixing in gas-solid risers operated in the FF and DPT regimes:

i. CARPT data from SNL's riser displayed occurrence independence and the Eulerian flow parameters were mesh independent. Solids flow within the zone of interrogation was fully-developed and axi-symmteric.

ii. The clustering phenomenon (if present) is localized near the walls at high solids fluxes, while it is common throughout the riser cross-section (FF regime) at low solids fluxes.

iii. Radial solids segregation is more severe in the DPT regime at high solids fluxes (beyond a certain solids volume fraction limit). Solids aggregation tendency or cluster formation is negligible in the core region at high solids fluxes in this regime.

iv. The shapes of the mean solids axial velocity profiles are similar for both risers at low and high solids fluxes, in agreement with the "similar profiles" concept of Monceaux *et al*. (1986) and Rhodes *et al.* (1992).

v. The cross-sectional average of the solids axial velocity was found to increase with the increase in the solids mass flux at constant gas velocity.

vi. Granular temperature was found to increase with solids concentration at 'dilute conditions' ($\varepsilon_s < 0.01$-0.06) and decrease beyond certain solids holdup.

vii. The core-annulus flow structure in the riser results in a PDF of the RTD with an early peak followed by an extended tail in the DPT regime, while in the FF regime it exhibits the appearance of possible multiple (two) peaks along with the extended tail.

viii. The solids dispersion as characterized by an axial dispersion coefficient increases with solids mass flux both in the FF and DPT regimes. In contrast, the 'macromixing index', *M*, decreases with the increasing solids flux at constant gas velocity. The macromixing index M is a better measure of the trends in solids backmixing. With regard to solids backmixing, a riser system does not behave as between plug flow and stirred tank and hence the axial dispersion model does not capture the physics of backmixing, does not fit the observed PDFs well and should not be used.

ix. Rate of decay of PDFs of the circulation time distributions increases with the solids mass flux and/or gas superficial velocity. Solids axial recirculation, also characterized by number of returns per trajectory, decreases with solids mass flux at constant gas superficial velocity.

x. The axial auto-correlation function displays negative loops with the frequency of the loops decreasing with increased radial position in the riser. With the regime transition from FF to DPT, the negative loops transits to an exponential decay.

Axial and radial integral time scales show opposite trends to granular temperature changes.

xi. The asymmetric dispersion tensor given by Durbin and Reif (2001) based on gradient diffusion hypothesis resulted in meaningful diffusivities profiles.

xii. In the FF regime, the effect of large scale axial solids recirculation on the solids axial dispersion is smaller compared to the small scale fluctuations, while it is the other way around in the DPT regime. The radial dispersion was found to be governed by radial recirculation at the center, while it was governed by small scale fluctuations near the wall.

xiii. The contribution of the cross-correlation of the fluctuating solids holdup with fluctuating solids velocity to the overall mass flux was found to be high and the assumption of negligible covariance term for solids flow in risers can lead to errors in mass balance well in excess of 25%.

xiv. Overall continuity for solids flow using CARPT and CT data in the riser was satisfied within engineering accuracy.

Chapter 8

Summary, Conclusions and Recommendations

8.0 Summary and Conclusions

The focus of this work was to provide more insights into the solids dynamics in the riser section of the circulating fluidized bed, employing non-invasive flow monitoring techniques, CARPT and CT. Reliable data was obtained on solids trajectories, velocities – averaged and instantaneous, solids holdup distribution and solids fluxes in the riser as a function of the operating conditions. Besides providing imminent information on solids dynamics for the first time, the work provides a database for local solids dynamics in a pilot-plant scale CFB, which can be used to validate/develop phenomenological models for the riser. This study also provides benchmark data for validation of CFD codes and their current closures. In accomplishing the above work, advances in the reconstructive algorithms for the CARPT and CT techniques were also achieved. The summary of the key findings from the work are listed below:

i. Chapter 3 discusses the improvements in the reconstruction algorithms for the non-invasive flow monitoring techniques – CARPT and CT. A new approach for tracer position rendition was developed by coupling a cross-correlation based search algorithm, for identifying the unknown tracer particle position, and a semi-empirical model for relating the counts received to the particle position. The developed algorithm for identification of CARPT particle position was validated by reconstructing particle positions from both the time-averaged and instantaneous calibration counts for known particle positions not used in the calibration. The uncertainty in the position reconstruction was evaluated to be within 5 mm. An alternating minimization (AM) algorithm for transmission tomography, developed by O'Sullivan and Benac (2001), was implemented with a suitable model for the CT image reconstruction and was found to provide marginal improvements in the image quality. The improvement is better near the walls of the column, which is the region of interest in this study, and in systems with stainless steel internals.

ii. An accurate measurement of the overall solids mass flux in a gas-solid CFB was obtained with the use of single radioactive particle tracking and densitometry, both of which are non-invasive and in-situ techniques. A calibration curve for overall solids mass flux as a function of the superficial gas velocity in the riser was established. Quantitative and qualitative improvements in densitometry, and "time of flight" experiments, as well as in data processing, were recommended and applied. It was also confirmed that the flow in the down-comer (2" column) is predominantly plug flow. Using a simple timing and weighing method, solids flux values were underestimated and compared to values obtained from the "time of flight" and densitometry method. The overall solids mass flux data reported was proved to be reproducible and tracer particle occurrence independent. Flow conditions under investigation were identified to be in fast-fluidization (FF) and in core-annular dilute phase transport (DPT) regimes.

iii. Solids mixing in an "open-open" system such as the gas-solid riser was investigated by tracking a single radioactive tracer particle to obtain an accurate estimate of solids residence times. The assumption of ergodicity underlying the experiments was corroborated and true solids residence times, first passage times and retention times

were estimated. Dual peaks were seen in the PDF of the solids RTD for the experimental conditions in the fast-fluidization regime, but not in the dilute transport regime. The shape of the RTD seems to suggest the regime of operation. Absolute values of overall solids holdup estimated from the knowledge of solids mass flux and the RTD curve are deemed inaccurate, even though their relative values can qualitatively give an estimate of the proportion of the holdups. The solids recycle percentage at the bottom of the riser in the DPT regime is around 50%, while in the FF regime is around 65%. Large discrepancies in the range of 35-71% are encountered in the means of conventional tracer injection-detection curves, while the error in dimensionless variances ranged from 2-45%. Dispersion coefficients obtained from FPTD overestimates and that from the conventional injection-detection curve underestimates the axial dispersion in risers. The dispersion model is not appropriate for use in modeling of solids flow in a gas-solid riser, although it can be used for studying the mixing trends with operating conditions. Dispersion coefficient increases with solids mass flux both in the fast fluidization and dilute-flow regimes.

iv. Single radioactive particle tracking, in the designated section of the riser, yielded a wealth of solids instantaneous and time-averaged flow information. Added to it the γ-ray tomography provided detailed time-averaged volume fraction profiles of the two phase riser flow enabling some insights into the complex phenomena that occur in the riser. Large scale internal recirculation superimposed by fine scale fluctuations both contribute to axial backmixing, while in the horizontal direction, solids mixing is principally dispersive. Solids axial velocity, interpreted from the PDFs, showed large radial gradients with negative at the wall in the FF regime. In DPT regime, negative axial velocities were not observed in the center, while near the wall showed negative velocities with its ensemble average being positive. Solids flow is nearly axi-symmteric and is close to fully-developed (within the zone of interrogation) revealed by both the velocity and holdup profiles. The movement of solids from core to annulus seems to be governed by the gradients in the time-averaged velocity profiles, while the movement of solids from annulus to core (if prevalent) is governed by the gradients in the fluctuating velocity profiles in the fully-developed zone. Contour

plots of turbulent kinetic energy and particle occurrences reveal a clear core-annular flow structure within the FF regime, while the profiles are uniform in the DPT regime. Clustering phenomena seem to exist throughout the riser cross section (more likely near the wall) along with the particle exchange between core and annulus. Although the ensemble average solids velocity increases, the solids velocity fluctuations decrease with the increase in the solids mass flux and/or superficial gas velocity under 'dilute conditions'. Flow in the riser is anisotropic with the fluctuating motion principally directed along the main axis of flow. The relative dominance of the increase in the collision frequency over the decrease in the mean free path (with solids holdup) dictates the trends for the granular temperature and solids viscosity. These two mechanisms result in granular temperature to increase with the increasing solids holdup under low flux conditions investigated in the CREL riser. Selection of the proper length of time-averaging (during each projection) affects the holdup profile obtained from in a CT experiment. For the riser flow, the length of time-averaging using a sampling frequency of 10 Hz and 114 samples (per projection) was found to be sufficient. Tomograms reveal three different characteristic layers in the FF regime, while the DPT regime has two characteristic layers. Steepness in the radial profiles of solids holdup increases with the solids mass flux at constant superficial gas velocity both in the FF and DPT regimes. Reduced holdup profiles derived from CARPT and CT match fairly well.

v. The uniqueness of CARPT data lies in providing rich Lagrangian information along with the time-averaged Eulerian flow field. Effect of operating conditions on the local solids backmixing required for the design and scale-up and for the quantification of solids diffusivities required for CFD closures were addressed in Chapter 7. At high solids fluxes, the clustering phenomenon (if present) was localized near the walls, while it is common throughout the riser cross-section (FF regime) at low solids fluxes. Radial solids segregation is more severe in the DPT regime at high solids fluxes (beyond a certain solids volume fraction limit). The shapes of the mean solids axial velocity profiles are similar for both risers at low and high solids fluxes, in agreement with the "similar profiles" concept of Monceaux *et al*. (1986) and Rhodes *et al.* (1992). Granular temperature was found to increase with solids concentration at

'dilute conditions' (ε_s < 0.01-0.06) and decrease beyond certain solids holdup. The core-annulus flow structure in the riser results in a PDF of the RTD with an early peak followed by an extended tail in the DPT regime, while in the FF regime it exhibits the appearance of possible multiple (two) peaks along with the extended tail. The solids dispersion as characterized by an axial dispersion coefficient increases with solids mass flux both in the FF and DPT regimes. In contrast, the 'macromixing index', *M*, decreases with the increasing solids flux at constant gas velocity. The macromixing index M is a better measure of the trends in solids backmixing. With regard to solids backmixing, a riser system does not behave as between plug flow and stirred tank and hence the axial dispersion model does not capture the physics of backmixing, does not fit the observed PDFs well and should not be used. Rate of decay of PDFs of the circulation time distributions increases with the solids mass flux and/or gas superficial velocity. Solids axial recirculation, also characterized by number of returns per trajectory, decreases with solids mass flux at constant gas superficial velocity. The axial auto-correlation function displays negative loops with the frequency of the loops decreasing with increased radial position in the riser. With the regime transition from FF to DPT, the negative loops transits to an exponential decay. In the FF regime, the effect of large scale axial solids recirculation on the solids axial dispersion is smaller compared to the small scale fluctuations, while it is the other way around in the DPT regime. The radial dispersion was found to be governed by radial recirculation at the center, while it was governed by small scale fluctuations near the wall.

vi. The contribution of the cross-correlation of the fluctuating solids holdup and fluctuating solids velocity to the overall solids mass flux was found to be high and the assumption of negligible covariance term for solids flow in the risers is invalid. Overall continuity for solids flow using CARPT and CT data in riser was satisfied within engineering accuracy.

It should be noted that the data obtained from single particle tracking is rich. Besides, the above derived results, one can interpret the data to obtain further insights of the chaotic

solids flow in the risers. Such possible extensions of this work are discussed in the next section.

8.1 Recommendations for Future Research

The accomplishments attained provide the foundation for future investigations. Suggestions for extending the work conducted in different parts of this study are listed below:

i. For the operating conditions investigated on the CREL and SNL risers, mean axial pressure drop profiles along the riser height will complement the CARPT data, required for the validation of CFD codes/models. With the present experimental techniques obtaining pressure fluctuations is difficult and often not possible because the signal is masked either by the purged air or protective mesh to avoid particle clogging. Novel ways of obtaining pressure time series will aid in the validation and improvement of the CFD models/codes.

ii. Typical flow characteristics in the FF and DPT regimes were described in Chapters 5, 6 and 7. For delineating the flow regimes, one can obtain Hurst exponents from the radial and axial velocity time series. For the same purpose one can use symbolic dynamics on the tracer position data. With the symbol-sequences of the location of tracer particle entrance into the zone of investigation, one can analyze how the histograms evolve from the symbols frequencies to the symbol-sequence frequencies. Using such histograms, one can calculate Shannon and Renyi-q entropies and compare with results obtained from maps, which can serve as a differentiating pointer of the flow regime. Furthermore, one can quantify the chaotic nature of the solids flow by estimating the information loss rate by following the fate (time divergence) of two very close initial states. In order to do that, return maps can be constructed by plotting I_{i+1} versus I_i, where I is the series of intervals between successive appearances of the tracer in the scanned region.

iii. Characterizing ‘cluster’ properties, such as the cluster velocity, cluster residence times, its typical sizes, its contribution to the holdup in the annulus, etc. is necessary

for proper understanding of the non-homogeneous distribution of solids in the riser. This requires new and innovative ways of studying clustering phenomenon. One possible suggestion is to glue the present single tracer particle with glass beads in different proportions and study the circulation and dynamics of such composite larger tracer cluster in risers.

iv. Characterize the solids RTDs and other mixing parameters along the height of the riser, i.e. study solids RTDs with the single particle tracking along the riser height to study different zones – bottom, acceleration, top (fully-developed). Mixing parameters estimated can assist in modeling different zones of the riser and unifying into a phenomenological based model for solids mixing in the riser.

v. One can develop/validate closure models for the Reynolds stresses and for the exchange terms using the obtained CARPT data. Besides the obtained information in the work, another requirement for the closure models is to quantify the local solids mass flux accurately. This can give a handle on estimating the velocity and holdup cross-correlation term and the method for modeling such term. Right now, only intrusive methods are available to characterize 'first-hand' data on local solids flux. One alternate way is to obtain solids velocity and holdup time series simultaneously. Appropriate technique(s) are not available and research in this direction is warranted.

vi. Characterize the solids dynamics and circulation patterns at the entrance region of the riser. To do this, one can perform CARPT and CT experiments at the entrance (bottom) region. Also, study the effects of different configurations of solids and gas entrances (side injection, bottom injection, multiple, etc.). Furthermore, one can characterize with CARPT and CT techniques, the acceleration zone or the middle zone between the bottom and the fully-developed zones. Validate the results obtained from such experimentation and the information from the work with the CFD models. More importantly, assess the turbulent parameters such as diffusivities, granular temperature, Reynolds stresses. Comparison of chaotic, heterogeneous, non-equilibrium, unsteady instantaneous phenomena is extremely difficult but is necessary as comparison only with the averaged values can be misleading.

vii. The method for the position rendition from the CARPT data can be improved by developing a stochastic based model for relating the counts detected with the position of the tracer particle. Such a stochastic based model can be coupled with the present cross-correlation based search for the best tracer position.

viii. A phenomenological model for the solids flow and mixing initiated in Appendix B can be improved. One can employ a 1D hydrodynamic model for core and annulus separately incorporating the velocity and holdup profiles from CARPT and CT results and derive a value for interchange coefficient from the radial diffusivities obtained from CARPT.

ix. Estimating collisional properties (restitution and friction coefficients) of the employed solid particles and the composite radioactive tracer particle will aid in modeling CREL and SNL riser flows, specifically for the discrete element simulations. Accurate technique and an elaborate apparatus are required for measuring such collisional properties. The two biggest challenges in such experiments are to bring the two spheres to collide without initial spin and to measure precise projections of the impulse on the normal and tangential directions with sufficient accuracy. One such experimental study was done by Foerster *et al.* (1994) for ballotini glass beads for large size particles and a similar procedure can be applied for the particles employed in this study. For impact properties on a flat plate, one can melt a bunch of employed glass beads to form a flat plate with sufficient thickness and utilize a similar apparatus as that of Foerster *et al.* (1994) to drop and visualize the particle impact. However, one should be wary that such measurements can yield only an approximate estimate of the coefficient of restitution, while recent work from Brillinatov's group (Ramirez *et al.*, 1999; Brillinatov and Poschel, 2000) showed that coefficient of restitution depends on the normal component of impact velocity. One should probably use functional form given by Brillinatov and fit the constants involved with the experimental results.

Apart from the possible extensions of this work, as discussed above, there are several areas of research related to the flow of gas-solids mixture in risers that are of

interest. Few of these ideas that can possibly be studied with the present tools at CREL are listed below:

i. Fines are required for smooth circulation in standpipes. However, the influence of fines on the hydrodynamics of riser flow is not properly understood. Studies on the effect of the percentage of fines used in the solids distribution on the riser hydrodynamics can be performed.

ii. Highly exothermic reactions may require internals for heat removal to maintain temperature uniformity. Research is required on the influence of internals on the riser hydrodynamics and catalyst attrition.

iii. Demarcation of the regime transition of the fast fluidized regime is often debated (Rhodes, 2003). One can possibly use a densitometry technique to obtain the power spectrum of the line-averaged solids concentration at different axial heights to differentiate the typical characteristics of the fast fluidized regime.

iv. Very few studies characterize the gas-phase turbulence in risers. Gas-phase velocities and RTDs are difficult to obtain and reliable techniques are not available to characterize them. Research on the novel experimental techniques to describe the gas-phase hydrodynamics can help in modeling the two phase flow in risers.

v. Often it is desired to minimize solids backmixing and approach plug flow of solids. The use of internals in risers may be able to approach this goal. CARPT–CT should be used to characterize it. Or a downer configuration should be used with the particles and gas moving co-currently downwards either with solids in free fall or in a moving bed configuration.

vi. In a few years, once the computational capabilities reach the point so as to perform a discrete element simulation (DES) of all the particles in the riser, one can compare the statistics of particle trajectories derived from CARPT experiments with such simulations. Availability of the CARPT data from this work is valuable for the validation and development of such discrete element methods.

APPENDIX A

Flowchart of the Cross-Correlation Based Search for Position Rendition from CARPT Data

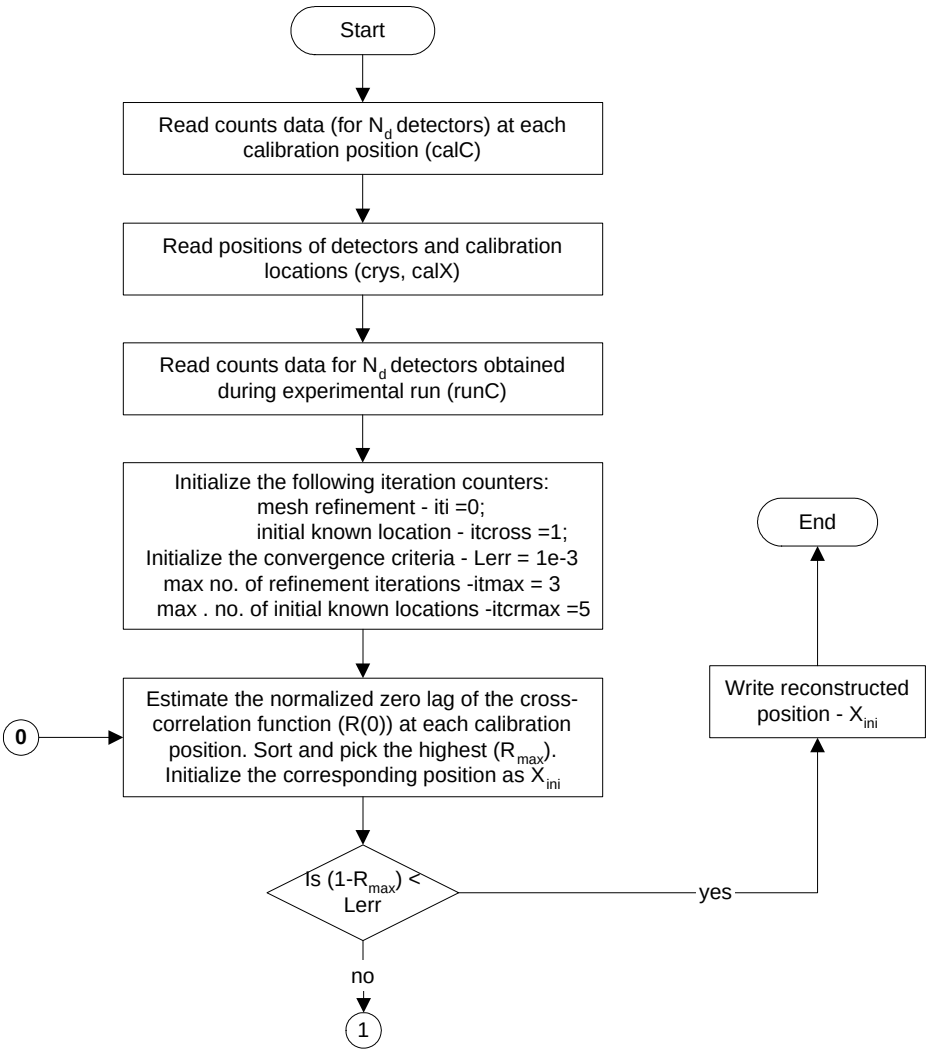

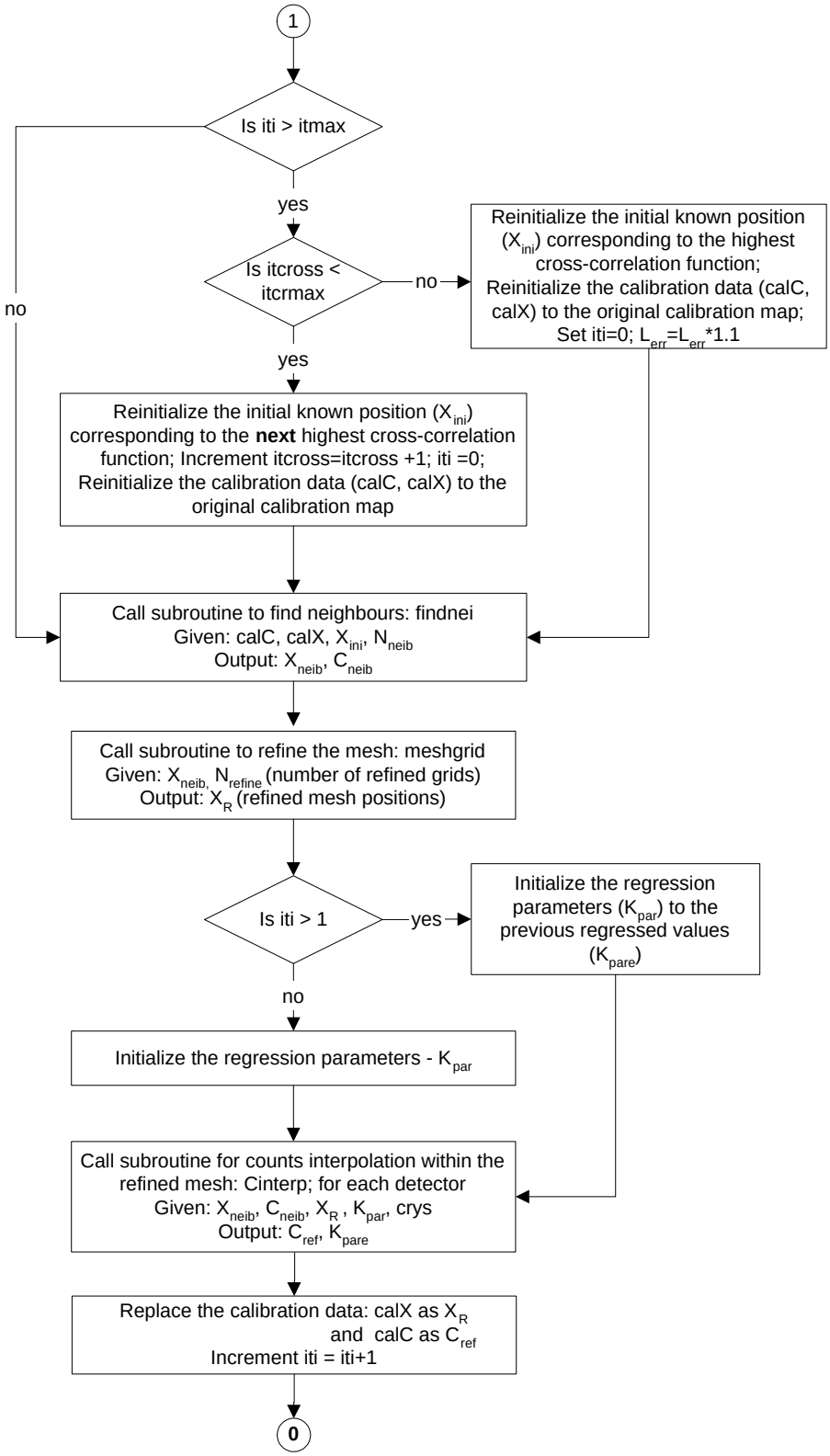
1
Is iti > itmax
yes
no
Is itcross < itcrmax
no
yes
Reinitialize the initial known position (X_{ini}) corresponding to the highest cross-correlation function; Reinitialize the calibration data (calC, calX) to the original calibration map; Set iti=0; L_{err}=L_{err}*1.1
Reinitialize the initial known position (X_{ini}) corresponding to the **next** highest cross-correlation function; Increment itcross=itcross +1; iti =0; Reinitialize the calibration data (calC, calX) to the original calibration map
Call subroutine to find neighbours: findnei
Given: calC, calX, X_{ini}, N_{neib}
Output: X_{neib}, C_{neib}
Call subroutine to refine the mesh: meshgrid
Given: X_{neib}, N_{refine} (number of refined grids)
Output: X_R (refined mesh positions)
Is iti > 1
yes
Initialize the regression parameters (K_{par}) to the previous regressed values (K_{pare})
no
Initialize the regression parameters - K_{par}
Call subroutine for counts interpolation within the refined mesh: Cinterp; for each detector
Given: X_{neib}, C_{neib}, X_R , K_{par}, crys
Output: C_{ref}, K_{pare}
Replace the calibration data: calX as X_R and calC as C_{ref}
Increment iti = iti+1
0

APPENDIX B

Phenomenological Modeling of Solids RTD in Risers

This section initiates a method for using the information derived from the experimental data in developing an improved phenomenological model for solids flow and RTD in risers.

The aim here is to evaluate models that provide reasonable representation of the solids flow and their non-uniform distribution in risers. A mechanistic model based on the core-annulus structure was employed, with the goal of giving physical significance to the model parameters, and minimizing number of such parameters.

As discussed earlier, the axial density profile varies along the height of the riser, typically exhibiting an initial rapid decay in the lower section (Yerushalmi *et al.*, 1976; Kwauk *et al.*, 1991; Kunii and Levenspiel, 1991). In this developing flow region, particles experience both a large upward drag force and vigorous collisions with other particles and 'clusters' of particles. Hence, this developing flow section was modeled as a stirred tank with the height of stirred tank obtained from the model/method of Kunii and Levenspiel (1991). In the remaining developed flow region of the riser, a two zone core-annulus model with varying annulus thickness was used. In this developed zone, changes in core and annulus solids vertical velocities with height are likely to be small (Senior and Brereton, 1992). Hence, radial profile of solids time averaged axial velocity, derived from CARPT and radial profile of solids density derived from CT were used in this

developed section. However, due to significant decay of the axial density profile, there must be a net transfer of solids from core to annulus. Conversely, if riser exit effects are significant, axial density profile will be different (Pugsley *et al*., 1997) forcing a net solids transfer towards the core. Hence, both modes of solids transfer, core to annulus and annulus to core must be present. Different mechanisms of solids transfer were discussed in Chapter 2.

Preliminary estimations were performed based on a similar flow dynamic model found in the open literature. The model presented by Berruti and Kalogerakis (1989) was employed. A system of six non-linear algebraic equations were solved to characterize the steady state flow structure. The cross-sectional average voidage (ε_{avg}) along the riser height needs to be determined beforehand. For this purpose, the method described by Kunii and Levenspiel (1990) was employed.

To simulate the solids RTD, a model for the tracer flow inside the riser was developed. There are several studies reporting such tracer balances coupled with different hydrodynamic models to simulate solids RTD (Avidan, 1980; Ambler *et al.*, 1990; Corleen et al., 1990; Smolders and Bayens, 2000; and many others). In this work, tracer model is formulated so as to be consistent with the solids flow dynamic model.

The tracer injection is described by the unsteady state tracer balances for the upward flowing core and the downward moving annulus zone. Plug flow without dispersion is assumed for both zones, and backmixing is caused by the exchange of particles between the core and the annulus, represented by two interchange coefficients I_{ac} and I_{ca} (refer to Figure B-1). Tracer balances in the core and annulus on a differential element give rise to a set of linear coupled hyperbolic equations.

$$\frac{\partial(E_c f_c)}{\partial z} + \{I_{ca} f_c - I_{ac} f_a\} = -\frac{E_c}{U_{sc}}\left(\frac{\partial f_c}{\partial t}\right) \tag{B-1}$$

$$\frac{\partial(W f_a)}{\partial z} + \{-I_{ca} f_c + I_{ac} f_a\} = \frac{W}{U_t}\left(\frac{\partial f_a}{\partial t}\right) \tag{B-2}$$

where f_a , f_c are the mass fractions of tracer in the core and annulus, (dimensionless)

I_{ca}, I_{ac} are the interchange coefficients (core-annulus), ($kg.m^{-3}.s^{-1}$)

m^* is the rate of tracer mass injection, ($kg.s^{-1}$)

E_c, W are the solids mass flux in the core and annulus respectively, (kg.m^{-2}.s^{-1})

U_{sc}, U_t are the solids velocity in the core and annulus respectively, (m.s^{-1}).

The above coupled equations require two boundary conditions:

1) $$m^*(t) + f_a(0,t).W = f_c(0,t).E_c \qquad \text{(B-3)}$$

where, m*(t) = $m_{inj}/\delta t$, for $t \le \delta t$

= 0, else

2) $$f_a(L,t) = 0, \qquad \text{(B-4)}$$

The second boundary condition is based on the experimental observation of no annulus at the exit in the present gas-solid riser setup. The initial condition is given by: $f_a(z,0) = f_c(z,0) = 0$.

A mass balance around the differential volume along the riser gives the net solids flow rate from core to annulus at any height given by:

$$I_{ca} - I_{ac} = -\frac{dE_c}{dz} \qquad \text{(B-5)}$$

To account for the mixing occurring at the bottom of the riser, the bottom portion of the riser was modeled as a continuous stirred tank. The height of the tank was taken to be the height up to which the average voidage is constant, obtained from hydrodynamic model. A tracer mass balance across the CSTR results in a dimensionless ODE given by (refer to Figure B-1):

$$\frac{\rho_P H}{G_s \tau} \cdot \frac{df_B}{d\bar{t}} = \frac{f_{in}(\bar{t})}{\pi R^2 G_s} + \left(\overline{W} f_a\right)\Big|_{x=H} - K f_B \qquad \text{(B-6)}$$

Along with an initial condition

$$\text{at } \bar{t} = 0,\ f_B = 0 \qquad \text{(B-7)}$$

The entrance boundary condition for Equation (8) is given by

$$K f_B = \overline{E}_c f_c\Big|_{x=H} \qquad \text{(B-8)}$$

where K is obtained by the overall solids mass balance:

$$K = G_s - W\big|_{x=H} = \overline{E}_c\Big|_{x=H} \qquad \text{(B-9)}$$

The coupled set of equations (B-1) and (B-2) are hyperbolic, since the eigenvalues of the set of equations are $\overline{U}_{sc}\left(\bar{z}\right)$ and $-\overline{U}_t$, which are real and distinct. It is known in this case that an explicit scheme is unconditionally unstable. Hence, Lax finite difference scheme was employed to obtain the solution. The truncation error for this explicit scheme is $O\left(\Delta\bar{t}, \frac{\Delta\bar{z}^2}{\Delta\bar{t}}\right)$. The numerical stability for the Lax differencing scheme is analysed by Fourier analysis, which shows that differencing scheme is conditionally stable for the Courant number $\nu \le \frac{1}{\left(\overline{U}_{sc} + \overline{U}_t\right)_{\max}}$.

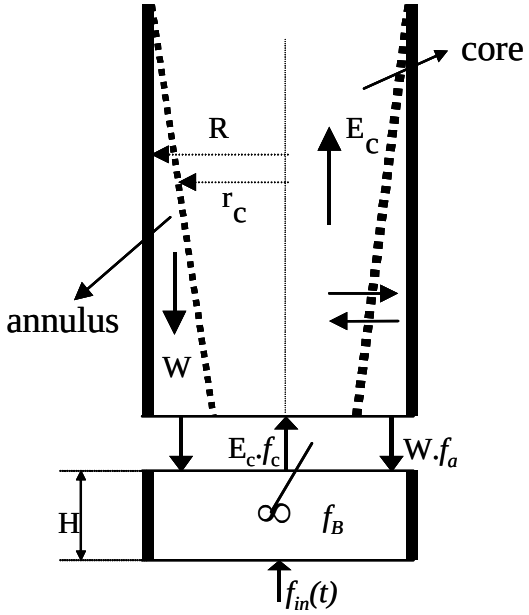

Figure B-1. Schematic of the core-annulus model with the CSTR at the bottom.

B.1 Results and Discussion

Equations described above were solved using the finite difference scheme and the results of the RTD curves are plotted in Figures B-2. The model does not capture the second peak in the RTD curve for the condition at which the superficial gas velocity is 3.2 $m.s^{-1}$. However, the peak height and the position of the first peak are in fair

comparison with the experimental data. It was found that the percentage difference in the mean residence times predicted by the model and indicated by data is around 21% and 40% for the superficial gas velocities of 3.2 and 3.9 m.s^{-1}, respectively. The reason for the difference in the results might be due to the discrepancy in values predicted by the hydrodynamic model – holdup and solids velocities. The mass balance for both the simulated results was satisfied within 5%. In the core-annulus model, more research on the parameter analysis is necessary to obtain better results. Work is in progress to develop a 1D hydrodynamic model for core and annulus separately incorporating the velocity and holdup profiles from CARPT and CT results and to derive a value for interchange coefficient from the radial diffusivities obtained from CARPT.

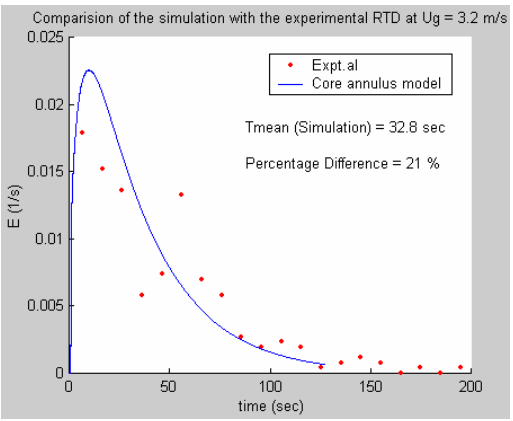

(a)

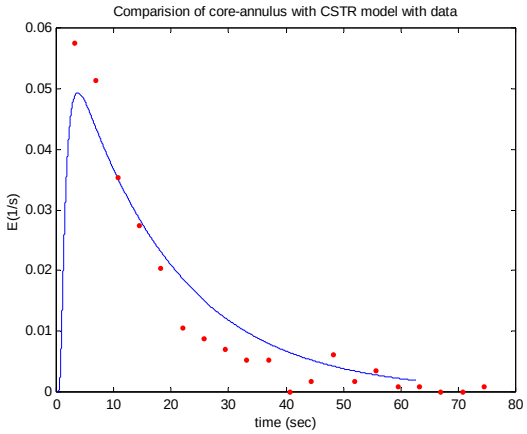

(b)

Figure B-2: Comparison of the core-annulus model simulation with the experimental solids RTD at U_g^{riser} and G_s of: a) 3.2 m.s^{-1} and 26.7 kg.m^{-2}.s^{-1}; b) 3.9 m.s^{-1} and 33.7 kg.m^{-2}.s^{-1}.

APPENDIX C

Time-Averaged Axial Differential Pressure Profiles

Starting from the pioneering work of Yerushalmi *et al.* (1976), axial flow structure in risers is typically characterized by pressure drop measurements. Time series of the pressure drop can provide some insights into the flow structure (Kwauk *et al.*, 1986; Bai *et al.*, 1992), particularly the axial solids distribution. Under some assumptions, discussed in detail by Horio??? (1997) and O'Hern *et al.* (2003), the axial pressure gradients can be related to the time-averaged solids holdup. Also, pressure fluctuations, if measured accurately, can be used as a pointer for regime transition and for deriving the typical flow frequencies. In addition, such axial pressure drop profiles can complement the CARPT data for the validation of CFD codes/models.

In this work, an attempt is made to obtain the time-averaged axial pressure drop profiles in the Sandia's riser for the operating conditions at which CARPT experiments were performed. The differential pressure measurements were obtained simultaneously during the CARPT experiments. Details of the instrumentation and measurement procedure are outlined elsewhere (Trujillo *et al.*, 2001; O'Hern *et al.*, 2003). Reference (gage) pressure is obtained at the top of the riser. Sintered metal discs (10-micron nominal pore size, Swagelok Co.) were placed as in-line filters to protect from solids contamination. The presence of these in-line filters severely reduces the frequency response of the pressure transducers. Frequency response roll-off begins near the 1 Hz driving frequency. Data was sampled continuously through the riser operation at a rate of about 2.5 Hz.

The time-averaged axial differential pressure profiles for the three operating conditions performed on Sandia's riser are shown in Figure C-1. The flow condition in the dilute phase regime (U_g = 7.71 m·s^{-1} and G_s = 119 kg·m^{-2}·s^{-1}) and the one close to the regime transition (U_g = 5.49 m·s^{-1} and G_s = 102 kg·m^{-2}·s^{-1}) exhibit a similar pressure gradient profile close to the "S"-shaped profile. Also, the flow conditions at U_g = 5.56 m·s^{-1} and G_s = 144.5 kg·m^{-2}·s^{-1}exhibit a more pronounced "S"-shaped pressure gradient profile characteristic of the fast fluidized (FF) regime. Hence, the key conclusion is that "S"-shaped pressure gradient profile need not represent the flow condition to be in the FF regime, although the converse could be true.

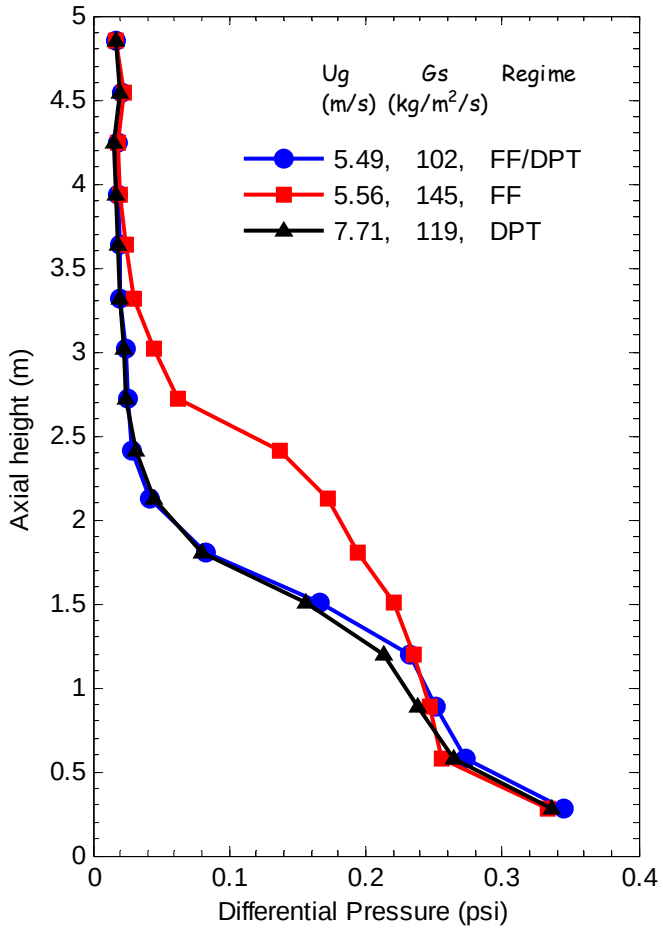

Figure C-1: Axial profiles of the differential pressure obtained in SNL riser.

References

Adewumi, M.A. and Arastoopour, H., 1986, "Two-dimensional steady state hydrodynamic analysis of gas-solids flow in vertical pneumatic conveying systems", *Powder Tech.*, 48, 67-74.

Ambler, P.A., Milne, B.J., Berruti, F., Scott, D.S., 1990, "Residence time distribution of solids in a circulating fluidized bed: experimental and modeling studies", *Chemical Engg. Sci.*, (45) 8, 2179-2188.

Arena, U., Malandrino, A., Marzocchella, A. and Massimilla, L., 1991, "Flow structures in the risers of laboratory and pilot CFB units", *Circulating Fluidized Bed Technology III*, P.Basu, M.Horio and M.Hasatani, Eds., Pergamon Press, New York, 137-144.

Avidan, A.A., 1980, "*Bed expansion and solids mixing in high velocity fluidized beds*", Ph.D Dissertation, The City College, New York.

Avidan, A.A., Edwards, E. and Owen, H., 1990, "Innovative improvements highlight FCC"s past and future", *Oil and Gas J.,* Jan. 33-58.

Azzi, M., Turlier, P., Large, J.F., Bernard, J.R., 1991, "Use of a momentum probe and gamma densitometry to study local properties of fast fluidized beds", *Circulating Fluidized Bed Technology III*, P.Basu, M.Horio and M.Hasatani, Eds., Pergamon Press, New York, 189-194.

Bader, R., Findlay, J. and Knowlton, T.M., 1988, "Gas/Solid flow patterns in a 30.5 cm diameter circulating fluidized bed riser", *Circulating Fluidized Bed Technology II*, P.Basu and J.F. Large, Eds., Pergamon Press, New York, 123-137.

Bai, D.R., Jin, Y., Yu, Z.Q. and Zhu, J.X., 1992[a], "The axial distribution of the cross sectionally averaged voidage in fast fluidization beds", *Powder Technol.*, 71, 51-58.

Bai, D., Yi, J., Jin, Y. and Yu, Z., 1992[b], "Residence time distributions of gas and solids in a CFB", *Fluidization VII*, O.E.Potter and D.J.Nicklin, Eds., Engineering Foundation, New York, 195-202.

Bai, D., Zhu, J.X., and Jin, Y., and Yu, Z., 1995, "Internal recirculation flow structure in vertical upflow gas-solids suspensions: Part I- A core-annulus model", *Powder Tech.*, 85, 171-77.

Bai, D., Issangya, A.S. and Grace, J.R., 1999, "Characteristics of gas-fluidized beds in different flow regimes", *Ind. & Eng. Chem. Res.*, 38, 803-811.

Batchelor, G.K., 1953, "The theory of homogeneous turbulence", Cambridge University Press, Cambridge.

Benyahia, S., Arastoopour, H., Knowlton, T.M., 1998, "Prediction of solid and gas flow behaviour in a riser using a computational multiphase flow approach", *Fluidization IX*, L.S. Fan and T.M. Knowlton, Eds., Engineering Foundation, New York, 493-500.

Benyahia, S., Arastoopour, H. and Knowlton, T.M., 2002, "Two-dimensional transient numerical simulation of solids and gas flow in the riser section of a circulating fluidized bed", *Chem. Eng. Comm.*189-4, 510-527.

Berruti, F., Chaouki, J., Godfroy, L., Puglsey, T.S., and Patience, G.S., 1995, "Hydrodynamics of circulating bed risers: a review ", *The Canadian Journal of Chemical Engineering*, 73, 579-601.

Berruti, F. and Kalogerakis, N., 1989, "Modelling the internal flow structure of circulating fluidized beds", *The Canadian Journal of Chemical Engineering*, 67, 10-14.

Berker, A. and Tulig, T.J., 1986, "Hydrodynamics of gas-solid flow in a catalytic cracker riser: Implications of reactor selectivity performance", *Chem. Eng. Sci.*, 41, 821-827.

Beuther, H., Innes, R.A. and Swift, H.E., 1978, "Process for preparing Acrylonitrile", U.S. Patent 4,102,914 assigned to Gulf research and Development Co., July 25.

Bi, H.T. and Fan, L.-S., 1991, "Regime transitions in gas-solid circulating fluidized beds", *AIChE Annual Meeting*, Los Angeles.

Bi, H.T., Grace, J.R. and Zhu, J-X, 1994, "On types of choking in vertical pneumatic systems", *Int. J. Multiphase Flow*, 19, 1077-1092.

Bi, H.T. and Grace, J.R., 1995, "Flow regime diagrams for gas-solid fluidization and upward transport", *Int. J. of Multiphase Flows*, 21, 1229-1236.

Bi, H.T., Zhou, J., Qin, S-Z., Grace, J.R., 1996, "Annular wall layer thickness in circulating fluidized bed risers", *The Canadian J. of Chem. Eng.*, 74, 11-14.

Bi, H.T. and Grace, J.R., 1999, "Flow patterns in high-velocity fluidized beds and pneumatic conveying", *The Canadian J. of Chem. Eng.*, 77, 223-230.

Bi, H.T., 2004, "Gas and solids mixing in high-density CFB risers", *Int. J. of Chem. Reactor Engg.*, 2, 1-12.

Bodelin, P., Molodtsof, Y. and Delebarre, A., 1994, "Flow structure investigations in a CFB", *Circulating Fluidized Bed Technology IV*, A. A. Avidan, Ed., American Institute of Chemical Engineers, New York, 118-122.

Bolio, E.J., Yasuna, J.A. and Sinclair, J.L., 1995, "Dilute turbulent gas-solid flow with particle-particle interactions", *AIChE J.*, 41, 1375-1388.

Bolton, L. and Davidson, J., 1988, "Recirculation of particles in fast fluidized risers", in *Circulating Fluidized Bed Technology II* (Eds. P.Basu and J.F.Large), Pergamon Press, Oxford, 139-146.

Brillinatov, N. and Poschel, T., 2000, "Self-diffusion in granular gases", *Physical Review E*, 16-2, 1716-1721.

Brereton, C.M.H. and Grace, J.R., 1993, "Microstructural aspects of the behaviour of circulating fluidized beds", *Chem. Eng. Sci.*, 48, 2565-2572.

Burkell, J. J., Grace, J. R., Zhao, J., and. Lim., C. J., 1988, "Measurement of solids circulation rates in circulating fluidized beds.", *Circulating Fluidized Bed Technology, vol. II*, Pergamon Press, Oxford, 501-509.

Chapman, S. and Cowling, T.J., 1961, "The mathematical theory of non-uniform gases", Cambridge University Press, London.

Chang, D.P.Y., Sorbo, N.W., Murchison, G.S., Adrian, R.C. and Simeroth, D.C., 1987, "Evaluation of circulating fluidized bed combustor as a potential hazardous waste incinerator", *J. Air Pollution Control Assoc.*, 37, 266-274.

Chaouki, J., Larachi, F., and Dudukovic, M.P., 1997, "Non-invasive monitoring of multiphase flows", Elsevier, New York.

Chen, J., P., Gupta, S., Degaleesan, M. H., Al-Dahhan, M. P., Dudukovic and B. A., Toseland, 1998, "Gas holdup distributions in large-diameter bubble columns measured by computed tomography", *Flow Measurement and Instrumentation*, 9(2), 91-101.

Cheremisinoff, N.P., 1986, "Review of experimental methods for studying the hydrodynamics of gas-solid fluidized beds", *Ind. Eng. Chem. Process Des. Dev.*, 25, 329-351.

Cody, G.D., Bellows, R.J., Goldfarb, D.J., Wolf, H.A. and Storch Jr., G.V., 2000, "A novel non-intrusive probe of particle motion and gas generation in the feed injection zone of the feed riser of a fluidized bed catalytic cracking unit", *Powder Tech.*, 110, 128-142.

Contractor, R.M., 1988, "Butane oxidation to maleic anhydride in circulating solids riser reactor", *Circulating Fluidized Bed Technology II*, Eds. P.Basu and J.F. Large, Pergamon Press, Toronto, 467-477.

Corleen, D.C., Klinzing, G.E., Shah, Y.T. and Dassori, C.G., 1990, "Hydrodynamics and mixing of solids in a recirculation fluidized bed", *Ind. Eng. Chem., Res.*, 29, 1785-1792.

Coronella, C. J., Deng, J., 1998, "A novel method for isokinetic measurement of particle flux within the riser of a circulating fluidized bed", *Powder Technology*, 99(3), 211-219.

Corssin, S., "An account of some features of the phenomenon in fully turbulent regions", *Proc. of Iowa Thermodynamics Symposium,* (1953), 5-29.

Csiszár, I., 1991, "Why least squares and maximum entropy? An axiomatic approach to inference for linear inverse problems", *The Annals of Statistics*, 19, 4, 2032-2066.

Dasgupta, S., Jackson, R. and Sundaresan, S., 1994, "Turbulent gas-particle flow in vertical risers", *AIChE J.,* 40-2, 215-228.

Davidson, J.F., 2000, "Circulating fluidized bed hydrodynamics", *Powder Tech.*, 113(3), 249-60.

Degaleesan, S., S. Roy, S. B. Kumar and M. P. Dudukovic", 1996, "Liquid backmixing based on convection and turbulent dispersion in bubble columns", *Chem. Eng. Sci.*, 51, 1967-1976.

Degaleesan, S., 1997, *Fluid dynamic measurements and modeling of liquid mixing in bubble columns*, D.Sc. Thesis, Washington University, Saint Louis, Missouri.

Degaleesan, S., Dudukovic, M. P., Pan, Y., 2002, "Application of wavelet filtering to the radioactive particle tracking technique", *Flow Measurement and Instrumentation*, 3(1-2), 31-43.

Dempster, A.P., Laird, N.M. and Rubin, D.B., 1977, "Maximum likelihood for incomplete data via the EM algorithm", *J. R Stat Soc Series B*, 39, 1-38.

Deng, X.J., 1993, "CFPC process", *CFB-IV*, Ed. A.A.Avidan, AIChE, New York, 472-477.

Devanathan, N., D. Moslemian and M. P. Dudukovic, 1990, "Flow mapping in bubble columns using CARPT", *Chem. Engng. Sci.,* 45, 2285-2291.

Devanathan, N., 1991, "*Investigation of liquid hydrodynamics in bubble columns via a computer automated radioactive particle tracking (CARPT) Facility"*, D.Sc. Thesis, Washington University, Saint Louis, Missouri.

De Vuono, A. C.; Schlosser, P. A.; Kulacki, F. A.; Munshi, P., 1980, "Design of an isotopic CT scanner for two phase flow measurements", *IEEE Transactions on Nuclear Science,* NS27-1, 814-20.

Ding, J. and Gidaspow, D., 1990, "A bubbling fluidization model using kinetic theory of granular flow", *AIChE J.*, 36, 523-538.

Dry, M.E., 1982, "The Sasol route to fuels", *CHEMTECH 12*, 744-750.

Donsi, G. and Osseo, L.S., 1993, "Gas solid flow pattern in a circulating fluid bed operated at high gas velocity", *Circulating fluidized bed technology IV*, A.A.Avidan, Ed., American Institute of Chemical Engineers, New York, 577-581.

Du, B. and Wei, F., 2002, "Lateral solids mixing behavior of different particles in a riser with FCC particles as fluidized material", *Chemical Engineering and Processing*, 41, 329-335.

Dudukovic, M.P., Devanathan, N., Holub, R., 1991, "Multiphase reactors: models and experimental verification", *Rev. Inst. Frac. Petr.,* 46, 439-464.

Dudukovic, M.P., 2002, "Opaque multiphase flows: experiments and modeling", *Experimental Thermal and Fluid Science,* 26, 6-7, 747-761.

Durbin, P.A. and Reif, P. B.A., 2001, "Statistical theory and modeling for turbulent flows", John Wiley & Sons.

Elmas, M., 1973, "Fluidised bed powder coating", Powder Technology Publication Series No.5, Ch. 1.

Fan, L.S., and Zhu, C., 1998, "Principles of gas-solid flows", Cambridge University Press.

Fiedler, O., Werther, J., Labahn, N., Kumpart, J. and Christofori, K., 1997, "Measurement of local particle velocities and velocity distributions in gas-solid flows by means of spatial filter method", *Powder Tech.*, 94, 51-57.

Foerster, S.F., Louge, M.Y., Chang, H. and Allia, K., 1994, "Measurements of the collision properties of small spheres", *Phys. Fluids*, 6-3, 1108-1115.

Geldart, D., 1986, "Gas fluidization technology", John Wiley & Sons, Ch. 3.

Gidaspow, D., 1994, "Multiphase flow and fluidization: continuum and kinetic theory descriptions", Academic Press Inc.: Boston.

Gidaspow, D. and Huilin, L., 1996, "Collisional viscosity of FCC particles in a CFB", *AIChE J.*, 42-9, 2503-2510.

Godfroy, L., Larachi, F., and Chaouki, J., 1999, "Position and velocity of a large particle in a gas/solid riser using the radioactive particle tracking technique", *The Canadian J. of Chem. Engg.,* 77.

Godfroy, L., Larachi, F., Kennedy, G., Grandjean, B.P.A., and Chaouki, J., 1997, "On-line flow visualization in multiphase reactors using neural networks", *Appl. Radiat. Isotop.,* 48(2), 225-235.

Grace, J.R., and Bi, H., 1997, "Introduction to circulating fluidized beds", In J.R. Grace, A.A. Avidan, and T.M.Knowlton, *Circulating Fluidized Beds*, Ch.1.

Grace, J.R., Issangya, A.S., Bai, D., Bi, H-T. and Zhu, J.-X., 1999, "Situating the high-density circulating fluidized bed", *AIChE J.*,45, 2108.

Graf, R., 1986, "First operating experience with a dry flue gas desulphurization process using a circulating fluidized bed", *Circulating Fluidized Bed Technology*, Ed. P. Basu, Pergamon Press, Oxford, 317-328.

Grassler, T. and Wirth, K. E. 1999, "Radial and axial profiles of solids concentration in a high-loaded riser reactor", *Circulating Fluidized Bed VI*, Ed. J. Werther, DECHEMA, Frankfurt, 65-70.

Gupta, P., 2002, "*Churn-turbulent bubble columns: experiments and modeling"*, D. Sc. Thesis, Washington University, St.Louis, Missouri.

Gupta, S.K., Pugsley, T. and Berruti, F., 1999, "A process simulator for circulating fluidized bed reactors", *CFB VI*, Ed. J. Werther, DECHEMA, Frankfurt, 443-448.

Hallstrom, C. and Karlsson, R., 1991, "Waste incineration in circulating fluidized bed boilers: test results and operating experiences", *CFB III*, Ed. P.Basu, Pergamon Press, New York, 417-422.

Harris, B. and Davidson, J., 1994, "A core-annulus deposition model for circulating fluidisezed beds" in *Circulating Fluidized Bed Technology IV, E*d. A.Avidan, AIChE, New York, 32-39.

Harris, B.J., Davidson, J.F. and Xue, Y., 1994, "Axial and radial variation of flow in circulating fluidized bed risers", *Circulating Fluidized Bed Technology IV*, A.A.Avidan, Ed., American Institute of Chemical Engineers, New York, 103-110.

Harris, A., Thorpe, R. and Davidson, J.F., 2002[a], "The measurement of particle residence time distributions in circulating fluidized beds", *CFB VII,* Edited by Grace, J.R., Zhu, J. and Lasa, H.D., Ontario.

Harris, A. T., Davidson, J. F. and Thorpe, R. B., 2002[b], "A novel method for measuring the residence time distribution in short time scale particulate systems", *Chemical Engineering Journal* (Amsterdam, Netherlands), 89(1-3), 127-142.

Hartge, E.U., Li, Y., and Werther, J., 1986, "Analysis of the local structure of the two-phase flow in a fast fluidized bed", *Circulating Fluidized Bed Technology*, P.Basu Ed., Pergamon Press, New York, 153- 160.

Hartge, E. U., Rensner, D., and Werther, J., 1988, "Solids concentration and velocity patterns in circulating fluidized beds", *Circulating Fluidized Bed Technology II*, Pergamon Press, Oxford, 165-180.

Helmrich, H.K., Schurgerl, K., and Janssen, K., 1986, "Decomposition of $NaHCO_3$ in laboratory and bench scale circulating fluidized bed reactors", in: Basu, P. (Ed.), *Circulating Fluidized Bed Technology*, Pergamon Press, New York, 161-166.

Herb, B., Dou, S., Tuzla, K.,and. Chen, J. C, 1992, "Solid mass fluxes in circulating fluidized beds", *Powder Technology*, 70, 197-205.

Herbert, P., Reh, L., Nicolai, R., 1999, "The ETH experience: experimental database and results from past eight years", AIChE symposium series, 321 95, 61-66.

Hinze, J. O., 1975, "Turbulence", (2nd Ed.) McGraw-Hill, New York.

Hirsch, M., Janssen, K. and Serbet, H., 1986, "The circulating fluidized bed as reactor for chemical and metallurgical processes", *Circulating Fluidized Bed Technology*, Ed. P. Basu, Pergamon Press, Oxford, 329-340.

Horio, M., Morishita, K., Tachibana, O. and Murata, M., 1988, "Solids distribution and movement in circulating fluidized beds", *Circulating fluidized bed technology II*, Eds. P.Basu and J.F. Large, Pergamon Press, Toronto, 147-154.

Horio, M. and Takei, Y., 1991, "Macroscopic structure of recirculating flow of gas and solids in circulating fluidized beds", *Circulating Fluidized Bed Technology III*, Eds. P. Basu, M. Horio and M. Hasatani, Pergamon Press, New York, 207-212.

Horio, M. and Clift, R., 1992, "A note on terminology: 'cluster' and 'agglomerates", *Powder Technology,* 70, 196.

Howard, J. R., 1989, "Fluidized bed technology: principles and applications", Adam Hilger, Bristol and New York.

Hrenya, C.M. and Sinclair, J.L., 1997, "Effects of particle-phase turbulence in gas-solid flows", *AIChE J.*, 43, 853.

Huilin, L. and Gidaspow, D., 2003, "Hydrodynamic simulations of gas-solid flow in a riser", *Ind. Eng. Chem. Res.*, 42, 2390-2398.

Issangya A.S., Bai D.R., Grace J.R. and Zhu J.X., 1998, "Solids radial flux profiles in a high density circulating fluidized bed riser", *Fluidization IX*, Ed. L.S. Fan and T.M. Knowlton, Engineering Foundation, New York, 197-204.

Issangya, A. S., Bai, D., Bi, H. T, Lim, K. S, Zhu, J., and Grace., J. R., 1999, "Suspension densities in a high-density circulating fluidized bed riser", *Chemical Engineering Science*, 54, 5451-5460.

Issangya, A. S., Grace., J. R., Bai, D., and Zhu, J., 2000, "Further measurements of flow dynamics in a high-density circulating fluidized bed riser", *Powder Tech.*, 111, 104-113.

Ishii, H., Nakajima, T. and Horio, M., 1989, "The clustering annular flow model of circulating fluidized beds", *J. Chem. Eng. Japan*, 22, 484-490.

Jaworski, A. J. and Dyakowski., T., 2001, "Application of electrical capacitance tomography for measurement of gas-solids flow characteristics in a pneumatic conveying system", *Measurement Science Technology*, 12, 1109-1119.

Kak, A. C. and Slaney, M., 1988, "*Principles of computerized tomographic imaging",* Ch.3, IEEE Press.

Kato, K., Takarada, T., Tamura, T. and Nishino, K., 1991, "Particle hold up distribution in a circulating fluidized bed", *Circulating Fluidized Bed Technology III*, P.Basu, M.Horio and M.Hasatani, Eds., Pergamon press, New York, 145-150.

Kiared, K, Larachi, F., Guy, C. and Chaouki, J., 1997, "Trajectory length and residence time distributions of the solids in three phase fluidized beds", *Chem. Eng. Sci.*, 52-21/22, 3931-3939.

Kim, S. W., Kirbas, G., Bi, H, Lim, C.J., Grace, J.R., 2004, "Flow structure and thickness of annular downflow layer in a circulating fluidized bed riser", *Powder Tech.*, 142, 48-58.

King, D., 1992, "Fluidized catalytic crackers. an engineering review" *Fluidization VII*, Eds. O.E. Potter and D.J. Nicklin, Engineering Foundation, New York.

Knoll, G. F., 1989, "Radiation detection and measurement", John Wiley and Sons, NY.

Koenigsdorff, R. and Werther, J., 1995, "Gas-solids mixing and flow structure modeling of the upper dilute zone of a circulating fluidized bed", *Powder Tech.* 82, 317-329.

Kojima, T., Ishihara, K., Guittlin, Y., & Furusawa, T., 1989, "Measurement of solids behaviour in a fast fluidized beds", *J. of Chemical Engg. Japan*, 22, 341-346.

Kondukov, N.B., Kornilaev, A.N., Skachko, I.M., Akhromenkov, A.A. and Kurglov, A.S., 1964, "An investigation of the parameters of moving particles in a fluidized bed by a radioisotope method", *Int. Chem. Eng.*, 4, 43-47.

Kuroki, H. and Horio, M., 1994, "The flow structure of a three dimensional circulating fluidized bed observed by the Laser sheet technique", *Circulating Fluidized Bed Technology IV*, A.A.Avidan, Ed., AIChE, New York, 77-84.

Kumar, S. B., 1994, *Computed tomographic measurements of void fraction and modeling of the flow in bubble columns*, Ph.D. Thesis, Florida Atlantic University.

Kumar, S. B., N. Devanathan, D. Moslemian and M. P. Dudukovic, 1994, "Effect of scale on liquid recirculation in bubble columns", *Chem. Engg. Sci*., 49(24B), 5637-5652.

Kumar, S. B., Moslemian, D., and Dudukovic, M. P., 1995, A gamma ray tomographic scanner for imaging void fraction distribution in bubble columns, *Flow Meas. Instr.*, 6(1), 61-73.

Kumar, S. B., D. Moslemian and M. P. Dudukovic, 1997, "Gas holdup measurements in bubble columns using computed tomography", *AIChE J*., 43(6), 1414-1425.

Kumar, S.B. and Dudukovic, M.P., 1997, "Computer assisted gamma and X-ray tomography: applications to multiphase flow systems", Chapter 2, In J. Chaouki, F. Larachi and M.P. Duduković, Non-Inavsive Monitoring of Multiphase Flows, Elsevier Science.

Kunii, D. and Levenspiel, O., 1991, "Fluidization engineering", Butterworth- Heinemann series in Chemical Engineering, Ch.8.

Kwauk, M., Wang, N., Li, Y., Chen, B. and Shen, Z., 1986, "Fast fluidization at ICM", in Circulating fluidized bed technology, P. Basu, Ed., Pergamon Press, Oxford, 33-62.

Lange, K. and Carson, R., 1984, "EM reconstruction algorithms for emission and transmission tomography", *J. of Computer Assisted Tomography*, 8-2, 306-316.

Larachi, F., Kennedy, G.; Chaouki, J., 1994, "A γ-ray detection system for 3-D particle tracking in multiphase reactors", *Nucl. Instrum. Methods Phys. Res., Sect. A*, 338 (2-3), 568-76.

Larachi, F., Chaouki, J., Kennedy, G., Dudukovic, M. P., 1997, "Radioactive particle tracking in multiphase reactors: principles and applications", in Non-Invasive Monitoring of Multiphase Flows, J. Chaouki, F. Larachi, and M. P. Dudukovic, Eds., Elsevier, New York.

Lee, N. and Duckler, A.E., 1976, "Lagrangian simulation of dispersion in turbulent shear flow with a hybrid computer", *AIChE J.*, 22, 449-456.

Leung, L.S., 1980, "The ups and down of gas-solid flow – a review", *Fluidization*, Eds. T.R. Grace and J.M. Matsen, Plenum Press, New York, 25.

Levenspiel, O., Bischoff, K. B., 1963, "Patterns of flow in chemical process vessels", *Advan. Chem. Eng.,* 4, 95-198.

Levenspiel, O., 1999, "Chemical reaction engineering", John Wiley & Sons, Third Ed.

Li, H. and Tomita, Y., 2000, "Measurements of particle velocity and concentration for dilute swirling gas-solid flow in a vertical pipe", *Particulate Sci. and Tech.*, 20, 1-13.

Li, J., Reh, L. and Kwauk, M., 1991, "Application of the principle of energy minimization to the fluid dynamics of circulating fluidized beds", in *Circulating Fluidized Bed Technology III*, Eds. P.Basu, M.Horio and M.Hasatani, Pergamon Press, Oxford, 105-111.

Li, J., Cheng, C., Zhang, Z., Yuan, J., Nemet, A., and Fett, F.N., 1999, "The EMMS model – its applications, development and updated concepts", *Chem. Eng. Sci.*, 54, 5409-5425.

Li, Y. and Kwauk, M., 1980, "The dynamics of fast fluidization", *Fluidization*, Eds., J.R. Grace and J.M. Matsen, Plenum Press, New York, 537-544.

Limtrakul, S., 1996, *Hydrodynamics of liquid fluidized beds and gas-liquid fluidized beds*, D.Sc. Thesis, Washington University, Saint Louis, Missouri.

Lin, J.S., Chen, M.M., and Chao, B.T., 1985, "A novel radioactive particle tracking facility for measurement of solids motion in gas fluidized beds", *AIChE J.*, 31, 465-473.

Lin, W., Weinell, C.E., Hansen, P.F.B., and Dam-Johansen, K., 1999, "Hydrodynamics of a commercial scale CFB boiler-study with radioactive tracer particles", *Chem. Eng. Sci.*, 54, 5495-5506.

Liu, J. and Huan, B., 1995, "Turbine meter for the measurement of bulk solids Flowrate", *Powder Technology*, 82, 145-151.

Louge M., 1997, "Experimental techniques", In J.R. Grace, A.A. Avidan, and T.M. Knowlton, *Circulating Fluidized Beds*, Ch.9.

Lyngfelt, A. and Leckner, B., 1992, "Residence time distributions of sorbent particles in a circulating fluidized bed boiler", *Powder Technol.*, 70, 285-292.

Malcus, S., Chaplin G., and Pugsley., T., 2000, "The Hydrodynamics of the high-density bottom zone in a CFB riser analyzed by the means of electrical capacitance tomography (ECT)", *Chemical Engineering Science*, 55, 4129-4138.

Mann, U. and Crosby, E.J., 1973, "Cycle time distribution in circulating systems", *Chemical Engineering Science,* 28, 623-627.

Martin, M.P., Turlier, P., Bernard, J.R. and Wild, G., 1992, "Gas and solid behavior in cracking circulating fluidized beds", *Powder Technology*, 70, 249-258.

Marzocchella, A., Zijerveld, R.C., Schouten, J.C. and van den Bleek, C.M., 1997, "Chaotic behavior of gas-solid flow in the riser of a laboratory scale circulating fluidized bed", *AIChE J.*, 43, 1458-1468.

Mastellone, M. L. and Arena, U., 1999, "The effect of particle size and density on solids distribution along the riser of a circulating fluidized bed*", Chemical Engineering Science*, 54, 5383-5391.

MATLAB, 2003, Version 6.5, The MATH WORKS Inc., Boston, MA.

Mei, R., Adrian, R.J. and Hanratty, T.J., 1991, "Particle dispersion in isotropic turbulence under stokes drag and Basset force with gravitational settling", *J. Fluid Mech.*, 225, 481-495.

MFDRC website, http://www.mfdrc.org as of August 23, 2003.

Miller, A. and Gidaspow, D., 1992, "Dense, vertical gas-solid flow in a pipe", *AIChE Journal*, 38, 11, 1801-1815.

Milne, B.J. and Berruti, F., 1990, "Modeling the mixing of solids in circulating fluidized beds", in: Basu, P., Horio, M, and Hasatani, M. (Eds.), *Circulating Fluidized Bed Technology III*, Pergamon Press, New York, 235-242.

Monceaux, L., Azzi, M., Molodtsof, Y. and Large, J.F., 1986, "Overall and local characterization of flow regimes in a circulating fluidized bed", *Circulating Fluidized Bed Technology*, P.Basu, Ed., Pergamon Press, New York, 185-191.

Monin, A.S. and Yaglom, A.M., 1971, "Statistical fluid mechanics: mechanics of turbulence (Vol.1)", The MIT Press, Cambridge.

Moslemian, D., 1987, "*Study of solids motion, mixing and heat transfer in gas-fluidized beds*", Ph.D Dissertation, University of Illinois at Urbana-Champaign, Urbana, Illinois.

Naumann, E.B., 1981, "Transient response functions and residence time distributions in open systems", *AIChE Symp. Ser.*, 202 (77), 87-93.

Nauman, E.B. and Buffham, B.A., 1983, "Mixing in continuous flow systems" John Wiley & Sons Pubs.

Nieuwland, J.J., Van Sint Annaland, M., Kuipers, J.A.M., and VanSwaaji, W.P.M., 1996, "Hydrodynamic modeling of gas/particle flows in riser reactors", *AIChE J.*,42, 1569-1582.

Trujillo, S.M., O' Hern, T.J., Shollenberger, K., Grasser, T., Torczynski, J., 2001, "Summary of the Sandia National Laboratories efforts in multiphase fluid dynamics research consortium", SAND report.

O'Hern, T.J., Trujillo, S.M., Tortora, P.R., 2003, "Gamma tomography system for determination of solids loading in gas-solid flows: comparison with axial pressure gradient method", *Proceedings of the 3rd World Congress on Industrial Process Tomography*, Banff, Canada.

Ong, B. C., 2003, "*Experimental investigation of bubble columns hydrodynamics: effect of elevated pressure and superficial gas velocity"*, D.Sc. Thesis, Washington University, Saint Louis, Missouri.

Osseo, L.S. and Donsi, G., 1999, "Pressure analysis along a transport riser", In J. Werther, *Circulating Fluidized Bed Technology VI*, Germany:DECHEMA e.V., 77-82.

O'Sullivan, J. and Benac, J., 2001, "Alternating minimization algorithms for transmission tomography", *Submitted to IEEE Trans. On Medical Imaging*.

Park, D.W. and Gau, G., 1986, "Simulation of ethylene epoxidation in a multitubular transport reactor", *Chem. Eng. Sci.*, 41, 143-150.

Parker, D.J., Broadbent, C.J., Fowles, P., Hawkesworth, M.R. and McNeil, P., 1993, "Positron emission particle tracking – a technique for studying flow within engineering equipment", *Nuclear Instruments and Methods in Physics Research A*, 326, 592-607.

Parssinen, J.H. and Zhu, J.X., 2001[a], "Axial and radial solids distribution in a long and high-flux CFB riser", *AIChE J.*, 47-10, 2197-2205.

Parssinen, J.H. and Zhu, J.X., 2001[b], "Particle velocity and flow development in a long and high-flux circulating fluidized bed riser", *Chemical Engineering Science*, 56**,** 5295-5303.

Patience, G. S., Chaouki J., and Grandejean, B. P. A., 1990, "Solids flow metering from pressure drop measurement in circulating fluidized beds", *Powder Technology*, 61, 95-99.

Patience, G. S., Chaouki J., and Kennedy, G., 1991, "Solids residence time distribution in CFB reactors", *Circulating Fluidized Bed Technology III*, P.Basu, M.Horio and M.Hasatani, Eds., Pergamon Press, New York, 627-632.

Patience, G.S. and Chaouki, J., 1992, "Solids hydrodynamics in the fully developed region of CFB risers", In O.E.Potter and D.J.Nicklin, *Fluidization VII*, New York: Engineering Foundation, 33-40.

Pita, J.A. and Sundaresan, S., 1993, "Developing flow of gas-particle mixture in a vertical riser", *AIChE J.*, 39, 541-555.

Pugsley, T. and Berruti, F., 1995, "A core-annulus solids interchange model for circulating fluidized beds and FCC risers", *Fluidization VIII*, Tours, France.

Pugsley, T., Lapointe, D., Hirshberg B., and Werther, J., 1997, "Exit effects in circulating fluidized bed risers", *The Canadian Journal of Chemical Engineering*, 75, December, 1001-1010.

Qian, C. and Li, J., 1994, "Particle velocity measurement in CFB with an integrated probe", *Circulating Fluidized Bed Technology IV*, A.A.Avidan, Ed., American Institute of Chemical Engineers, New York, 274-278.

Rados, N., 2003, "*Slurry bubble column hydrodynamics: experimentation and modeling"*, D.Sc., Thesis, Washington University, Saint Louis, Missouri.

Ramirez, R., Poschel, T., Brillinatov, N. and Schwager, T., 1999, "Coefficient of restitution of colliding viscoelastic spheres", *Physical Review E*, 60-4, 4465-4572.

Rammohan, A., Kemoun, A., Al-Dahhan, M., Dudukovic, M. and Larachi, F., 2001[a], "CARPT dynamic bias studies: evaluation of accuracy of position and velocity measurements", *Recents Prog. Genie Procedes,* 2001; *Tracers and Tracing Methods*, 79, 59-67.

Rammohan, A., Kemoun, A., Al-Dahhan, M. and Dudukovic, M., 2001[b], "A Lagrangian description of flows in stirred tanks via computer automated radioactive particle tracking (CARPT)", *Chem. Engg. Sci., 56,* 2629-2639.

Ran, X., Wei, F., Wang, Z., and Jin, Y., 2001, "Lateral solids dispersion in a high-density riser with swirling air flow", *Powder Technology*, 121, 123-130.

Ranade, V.V., 1999, "Modeling of gas-solid flows in FCC riser reactors: fully developed flow", *Second Int. Conference on CFD in Minerals and Process Ind.,* CSIRO, Melbourne, Australia.

Reh, L., 1971, "Fluid bed processing", *Chem. Engg. Progr.*, 67, 58-63.

Reh, L., 1986, "The circulating fluid bed reactor- a key to efficient gas/solid processing", *Circulting Fluidized Bed Technology*, Ed. P. Basu, Pergamon Press, Oxford, 105-118.

Reh, L., 1995, "New and efficient high- temperature processes with circulating fluidized bed reactors", *Chem. Engg. Technol.*, 18, 75-89.

Rhodes, M.J. and Geldart, D., 1986, "The hydrodynamics of re-circulating fluidized beds", *Circulating Fluidized Bed Technology*, Ed. P.Basu, Pergamon Press, New York, 193-200.

Rhodes, M.J., Laussmann, P., Vilain, F. and Geldart, D., 1988, "Measurement of radial and axial solids flux variations in the riser of circulating fluidized bed" in *Circulating Fluidized Bed Technology II"*, P.Basu and J.F. Large Eds., Pergamon Press, New York, 155-164.

Rhodes, M., 1990, "Modeling the flow structure of upward-flowing gas-solids suspensions", *Powder Tech.*, 60, 27-38.

Rhodes, M.J., Zhou, S., Hirama, T. and Cheng, H., 1991, "Effects of operating conditions on longitudinal mixing in a circulating fluidized bed riser", *AIChE J.*, 1450-1458.

Rhodes, M.J., Wang, X.S., Cheng, Hirama, T., 1992, "Similar profiles of solids flux in circulating fluidized bed risers", *Chem. Eng. Sci.*, 47, 1635-1643.

Rhodes, M.J. and Laussmann, P., 1992, "A simple non-isokinetic sampling probe for dense suspensions", *Podwer Technol.*, 70, 141-151.

Rhodes, M.J., Sollaart, M., and Wang, X.S., 1998, "Flow structure in a fast fluid bed", *Powder Tech.*, 99, 194-200.

Rhodes, M., 2003, "An analysis of choking and fast fluidization", *AIChE Annual Meeting*, San Francisco.

Richardson, J.F. and Zaki, W.N., 1954, "Sedimentation and fluidization: Part 1", *Trans. Instn. Chem. Engrs.*, 32, 35-53.

Roy, S., 2000, "*Quantification of two-phase flows in liquid-solid riser"*, D.Sc. Thesis, Washington University, Saint Louis, Missouri.

Roy, S., Kemoun, A., Al-Dahhan, M. H., and Dudukovic, M. P., 2001, "A method for estimating the solid circulation rate in a closed-loop circulating fluidized bed", *Powder Technology*, 121, 213-222.

Roy, S., Larachi, F., Al-Dahhan, M. H., Dudukovic, M. P., 2002, "Optimal design of radioactive particle tracking experiments for flow mapping in opaque multiphase reactors", *Applied Radiation and Isotopes* , 56(3), 485-503.

Roy, S., Kemoun, A., Al-Dahhan, M.H., Dudukovic, M.P., Skourlis, T.B., Dautzenberg, F.M., 2004, "Countercurrent flow distribution in structured packing via computed tomography", *Chemical Engineering and Processing*, 44, 59-69.

Roy, S., Kemoun, A., Al-Dahhan, M.H. and Dudukovic, M.P., 2005, "Experimental investigation of the hydrodynamics in a liquid-solid riser", *AIChE J.*, 51-3, 802-835.

Saxton, A.L. and Worley, A.C., 1970, "Modern catalytic cracking design", *Oil Gas J.*, 68, 82-99.

Schoenfelder, H., Hinderer, J., Werther, J. and Keil, F., 1994, "Methanol to olefins, prediction of the performance of a circulating fluidized bed reactor on the basis of kinetic experiments in a fixed bed reactor", C*hem. Engg. Sci.*, 49, 5377-5390.

Schoenfleder, H., Kruse, M., and Werther, J., 1996, "Two dimensional model for circulating fluidized bed reactors", *AIChE J.*, 42(7), 1875-88.

Schlichthaerle, P. and Werther, J., 1999, "Axial pressure profiles and solids concentration distributions in the CFB bottom zone", *Chem. Eng. Sci.*, 54, 5485-5493.

Schuurmans, H.J.A, 1980, "Measurements in a commercial catalytic cracker unit", *Ind. Eng. Chem. Process Des. Dev.*, 19, 267-271.

Senior, R.C., and Brereton, C., 1992, "Modeling of circulating fluidized-bed solids flow and distribution", *Chem. Eng. Sci.*, 47(2), 281-296.

Shingles, T. and McDonald, A.F., 1988, "Commercial experience with Synthol CFB reactors", *Circulating Fluidized Bed Technology II*, Eds. P.Basu and J.F. Large, Pergamon Press, Toronto, 43-50.

Shinnar, R., Naor, P., & Katz, S., 1972, "Interpretation and evaluation of multiple tracer experiments", *Chemical Engineering Science*, 27(9), 1627- 1642.

Shinnar, R., and Naor, P., 1967, "Residence time distribution in systems with internal reflux", *Chemical Eng. Sci.*, 22, 1369-81.

Smolders, K. and Baeyens, J., 2000, "Overall solids movement and solids residence time distribution in a CFB-riser", *Chemical Engineering Science*, 55, 4101-4116.

Sinclair, J.L. and Jackson, R., 1989, "Gas particle flow in a vertical pipe with particle-particle interaction", *AIChE J.*, 35, 1473-1486.

Sinclair, J.L, 2000, "CFD for Multiphase Flow: Research codes and commercial software", *AIChE Symposium Series*, 323, 138-146.

Slaughter, M.C., Zhu, C. and Soo, S.L., 1993, "Measurement of local statistical properties of particle motion in a dense gas-solid suspension", *Advanced Powder Technol.*, 4, 169-178.

Snyder, D.L. and Cox, Jr. J.R., 1977, "An overview of reconstructive tomography and limitations imposed by a finite number of projections", In M.M. Ter-Pogossian, Reconstruction Tomography in Diagnostic Radiology and Nuclear Medicine.

Snyder, D.L., Schulz, T.J. and O'Sullivan, J., 1992, "Deblurring subject to nonnegativity constraints", *IEEE transactions on signal processing*, 40 (5), 1143-1150.

Snyder, D.L., 2003, "Tomographic systems", Course E65 554A, Washington University, St.Louis, MO, USA.

Snyder, W.H. and Lumley, J.L., 1971, "Some measurements of particle velocity autocorrelation functions in a turbulent flow", *J. Fluid Mech.*, 48, 41-71.

Stellema, C.S., 1998, "*Radiotracers for gas/solids flows in (Interconnected) fluidized beds*", Ph.D Dissertation, Delft University of Technology, Delft, Netherlands.

Squires, A.M., 1986, "The story of fluid catalytic cracking: The first circulating fluid bed", *Circulating Fluidized Bed Technology*, Ed. P. Basu, Pergamon Press, Oxford, 1-19.

Sun, B. and Gidaspow, D., 1999, "Computation of circulating fluidized-bed riser flow for the Fluidization VIII benchmark test", *Ind. Eng. Chem. Res.*, 38, 787-792.

Sureshkumar, R., 2001, "Turbulent transport processes", Course E63 516, Washington University, St.Louis, MO, USA.

Suzuki, S., Kunitomo, K., Hayashi, Y., Egashira, T. and Yamamoto, T., 1990, "Iron ore reduction in a circulating fluidized bed", *Proceedings 2nd Asian Conference on Fluidized Bed and Three phase Reactors,* 118-125.

Tanner, H., Li, J. and Reh, L., 1994, "Radial profiles of slip velocity between gas and solids in circulating fluidized beds", *AIChE Symposium Series*, 301, 105-113.

Tartan, M. and Gidaspow, D., 2004, "Measurement of granular temperature and stresses in risers", *AIChE J.*, 50-8, 1760-1775.

Tmenov, D.N., Svintson, N.I., Shapovalova, L.P., Tabakov, A.V., Dvoretskii, M.L., Vasil'ev, G.I., and Shestovkii, G.P., 1980, "Unsaturated hydrocarbons", German Patent DE 2902220 assigned to Institute of Physical-Organic chemistry and coal chemistry, July 31.

Tsoulfanidis, N., 1983, "Measurement and detection of radiation", McGraw Hill, New York.

Tsuji, Y., Morikawa, Y. and Shiomi, H., 1984, "LDV measurements of an air-solid two phase flow in a vertical pipe", *J. Fluid Mech.*, 139, 417-434.

Van Breugel, J.W., Stein, J.J.M. and de Vries, R.J., 1969, "Isokinetic sampling in a dense gas-solid stream", *Proc. Instn. Mech. Engrs.*, 184, 18-23.

Van den Moortel, T., Azario, E., Santini, R. and Tadrist, L., 1998, "Experimental análysis of the gas-particle flows in a circulating fluidized bed using a phase Doppler particle analyzer", *Chem. Eng. Sci.*, 53-10, 1883-1899.

Viitanen, P.I., 1993, "Tracer studies on a riser reactor of a fluidized catalyst cracking plant", *Ind. Eng. Chem. Res.*, 32, 577-583.

Villermaux, J., 1996, "Trajectory Length Distribution (TLD), A novel concept to characterize mixing in flow systems", *Chem. Eng. Sci.*, 51(10), 1939-1946.

Wang, T., Lin, Z.J., Zhu, C.M., Liu, D.C. and Saxena, S.C., 1993, "Particle velocity measurements in a circulating fluidized bed", *AIChE J.*, 39, 1406-1410.

Wang, Y., Wei, F., Wang, Z., Jin, Y. and Yu, Z., 1998, "Radial profiles of solids concentration and velocity in a very fine particle riser", *Powder Tech.*, 96, 262-266.

Wainwright, M.S. and Hoffman, T.W., 1974, "The oxidation of *o*-xylene in a transported bed reactor", C*hem.. Reaction Engg. II, Advances in Chemical Sciences,* Ed. H.M.Hulburt, American chemical society, Washington DC, 669-685.

Wei, F., Cheng, Y., Jin Y., Yu, Z., 1998, "Axial and lateral dispersion of fine particles in a binary-solid riser", *The Canadian Journal of Chemical Engineering*, 76, 19-26.

Weinell, C.E., Dam-Johansen, K., and Johnsson, J.E., 1997, "Single-particle behaviour in circulating fluidized beds", *Powder Technology*, 92, 241-252.

Weinell, C.E., Dam-Johansen, K., and Johnsson, J.E., 1994, "Single particle velocities and residence times in circulating fluidized beds", in Avidan, A.A. (Ed.), *Circulating Fluidized Bed Technology IV*, AIChE, New York, 571-576.

Weinstein, H., Shao, M. and Schnitizlein, M., 1986, "Radial variation in solid density in high velocity fluidization", *Circulating Fluidized Bed Technology II*, P.Basu, Ed., Pergamon Press, New York, 201-206.

Werther, J. and Hirschberg, B., 1997, "Solids motion and mixing" In J.R. Grace, A.A. Avidan, and T.M.Knowlton, Circulating Fluidized Beds, Ch.4.

Wilcox, D.C., 1994, "Turbulence modeling for CFD", DCW Industries, La Canada, California.

Wirth, K.-E., Seiter, M. and Molerus, O., 1991, "Concentration and velocities of solids in area close to walls in circulating fluidized bed systems", VGB Kraftwerkstechnik 10, 824-828.

Wong, R., Pugsley, T. and Berruti, F., 1992, "Modeling the axial voidage profile and flow structure in risers of circulating fluidized beds", *Chem. Eng. Sci.*, 47, 2301-2306.

Wu, W., Gerhart, A. L., Chen, Z., Dellenback P. A., and Agarwal P. K., 2001, "A device for measuring the solids flow rate in a circulating fluidized bed", *Powder Technology*, 120, 151-158.

Xu, G., Sun, G., Nomura, K., Li, J. and Kato, K., 1999, "Two distinctive variational regions of radial particle concentration profiles in circulating fluidized bed risers", *Powder Tech.*, 101, 91-100.

Yang, Y., Jin, Y., Yu, Z., Wang, Z. and Bai, D., 1991, "The radial distribution of local particle velocity in a dilute circulating fluidized bed", *Circulating Fluidized Bed Technology III*, P.Basu, M.Horio and M.Hasatani, Eds., Pergamon Press, New York, 201-206.

Yang, Y., 1997, "Monte carlo simulations for CARPT calibrations", Chapter 4 in Novel Techniques for Slurry Bubble Column Hydrodynamics, *Annual Tech. Report*, 2 (July 1996-June 1997) to DOE from Chemical Reaction Engineering Laboratory (DOE-FG2295 PC 95212), 20-39.

Yates, J.G., and Simons, S.J.R., 1994, "Experimental methods in fluidization research", *Int. J. Multiphase Flow*, 20, Suppl., 297-330.

Yerushalmi, J., Turner, D.H., Squires, A.M., 1976, "The fast fluidization bed", *Ind. Eng. Chem. Process Des. Dev.*, 15, 47-53.

Yerushalmi, J., 1986, "High velocity fluidized beds", Ch.7 in Gas Fluidization Technology, D.Geldart, Ed., John Wiley & Sons, Chichester, UK, 155-196.

Yester M.W. and Barnes, G.T., 1977, "Geometrical limitations of computed tomography (C.T.) scanner resolution", *Appl. Opt. Instr. in Medicine*, Vol.VI 127, 296-303.

Yousfi, Y. and Gau, G., 1974, “Aerodynamique de l”ecoulement vertical de suspensions concentrees gaz-solides—I. Regimes d’ecoulement et stabilite aerodynamique”, *Chemical Engineering Science,* 29, 9, 1939-1946.

Zhang, W., Tung, Y. and Johnsson, F., 1991, “Radial voidage profiles in fast fluidized beds of different diameters”, *Chem. Eng. Sci.*,46, 3045-3052.

Zhang, W., Johnson, F., and Leckner, B., 1997, “Momentum probe and sampling probe for measurement of particle flow properties in CFB boilers*”, Chemical Engineering Science*, 52, 4, 497-509.

Zhang, Y, and Arastoopour, H., 1994, “Experimental and theoretical analysis of gas and particles dispersion in large scale CFB”, in Avidan, A.A. (Ed.), *Circulating Fluidized Bed Technology IV*, American Institute of Chemical Engineers, New York, 473-478.

Zhang, M.; Qian, Z.; Yu, H.; Wei, F., 2003, “The solid flow structure in a circulating fluidized bed riser/downer of 0.42-m diameter”, *Powder Technology*, 129(1-3), 46-52.

Zhou, J., Grace, J.R., Lim, C.J. and Brereton, C.M.H., 1995, “Particle velocity profiles in a circulating fluidized bed riser of square cross-section”, *Chem. Eng. Sci.*, 50-2, 237-244.

Zhu, J.-X., Salah, M. and Zhou, Y., 1997, “Radial and axial voidage distributions in circulating fluidized bed with ring-type internals”, *J. of Chem. Eng. of Japan*, 30-5, 928-937.

LIST OF PUBLICATIONS

Publications

Quantification of Solids Flow in a Gas-Solid Riser: Single Radioactive Particle Tracking, S. Bhusarapu, M. H. Al-Dahhan and M. P. Duduković, *Chemical Engineering Science,* **59/22-23**, 5381-5386, 2004.

Measurement of Overall Solids Mass Flux in a Gas-Solid Circulating Fluidized Bed, S. Bhusarapu, P. Fongarland, M. H. Al-Dahhan and M. P. Duduković, *Powder Technology*, **148/2-3,** 155-168, 2004.

Solids Flow Mapping in a Gas-Solid Riser: Velocity and Holdup Profiles, S. Bhusarapu, M. H. Al-Dahhan and M. P. Duduković, To be published in a special issue in *Powder Technology*, 2005, In review.

Experimental Study of the Solids Velocity Field in Gas-solid Risers, S. Bhusarapu, M. H. Al-Dahhan, M. P. Duduković, S. Trujillo and T.J. O'Hern, To be Published in a special issue in *Ind. & Eng. Chem. Res.*, 2005, In review.

Solids Residence Time Distributions at High and Low Fluxes in Gas-Solid Risers, S. Bhusarapu, S. Trujillo, T.J. O'Hern, M. H. Al-Dahhan and M. P. Duduković, *In preparation.*

Proceedings and Presentations

Application of an Alternating Minimization Algorithm for Image Reconstruction in Computed Tomography, S. Bhusarapu, M.H. Al-Dahhan, M.P. Duduković, To be published in the *Proceedings of 4th World Congress on Industrial Process Tomography*, Aizu, Japan, 2005.

Solids Flow Mapping in a Gas-Solid Riser: Mean Holdup and Velocity Fields, S. Bhusarapu, M. H. Al-Dahhan and M. P. Duduković, *Proceedings of WCCE7*, Glasgow, 2005.

Experimental Study of the Solids Velocity Field in Gas-solid Risers, S. Bhusarapu, M. H. Al-Dahhan, M. P. Duduković, S. Trujillo and T.J. O'Hern, *Oral Presentation,* To be Presented at CAMURE 5 & ISMR 4 symposium, Slovenia, 2005.

Solids Flow Mapping in a Gas-Solid Riser, S. Bhusarapu, M. H. Al-Dahhan and M. P. Duduković, *Oral Presentation*, AIChE Annual Meeting 2004, Austin.

Quantification of Solids Flow in a Gas-Solid Riser: Single Radioactive Particle Tracking, S. Bhusarapu, M. H. Al-Dahhan and M. P. Duduković, *Oral Presentation,* ISCRE 18, Chicago.

Flow Visualization of Pilot-Plant Cold Flow FCC Unit via Advanced Non-Invasive Measurement Techniques, S. Bhusarapu, M. H. Al-Dahhan and M. P. Duduković, *Oral Presentation,* ISAHOF 2004, Oaxaca, Mexico.

Measurement and Modeling of Solids RTD in a Circulating Fluidized Bed (CFB) Riser, S. Bhusarapu, M. H. Al-Dahhan and M. P. Duduković, *Oral Presentation,* AIChE Annual Meeting 2003, San Francisco.

Solids Eulerian Flow Field from Lagrangian Information in a Gas-Solid Riser using Computer Automated Radioactive Particle Tracking, S. Bhusarapu, M. H. Al-Dahhan and M. P. Duduković, *Oral Presentation,* AIChE Annual Meeting 2003, San Francisco.

A Non-Invasive Method for Overall Solids Flux Measurements in a Circulating Fluidized Bed (CFB), S. Bhusarapu, P. Fongarland, M. H. Al-Dahhan and M. P. Duduković, *Oral Presentation,* AIChE Annual Meeting 2002, Indianapolis.

A Non-Invasive Method for Overall Solids Flux Measurements in a Circulating Fluidized Bed (CFB), S. Bhusarapu, P. Fongarland, M. H. Al-Dahhan and M. P. Duduković, *Poster Presentation*, CFB7 Conference, Niagara Falls, 2002.

Flow Mapping In Gas-Solid Risers via Computer Automated Radioactive Particle Tracking (CARPT) Current Progress, S. Bhusarapu, M. H. Al-Dahhan and M. P. Duduković, *Oral Presentation,* MFDRC meeting, Aug.'01, Sept.'02, June '03.

May, 2005